Olivine-hosted MIs as recorders of processes and conditions of slab dehydration and magmatic differentiation in the subduction zones of northern Japan

A thesis presented in partial fulfilment of the requirements for the degree of

Doctor of Philosophy

In

Earth Science

at Massey University, Palmerston North, New Zealand.

Raimundo Brahm Scott

2021

Abstract

Subduction zones are the controlling mechanisms of geochemical cycling between the Earth's crust and mantle. Transfer of incompatible trace elements and volatile species from the subducted slab to the mantle wedge by an H_2O-rich component triggers hydrous melting of the metasomatized mantle. This mechanism produces the magmatism that gives rise to volcanic arcs across the globe. The analysis of basic volcanic products from arc settings thus provides a window to study the processes involved in arc magmatism, from the mass transfer of slab to mantle wedge, partial melting, transport, differentiation and storage.

In particular, olivine-hosted MIs (OHMIs) provide a window to assess for early magmatic processes without the interference of the crystal cargo, as they are potentially less affected by differentiation processes. OHMIs have the additional advantage of having the potential to retain the volatile signatures (H_2O, CO_2, S, Cl and F) which are usually lost through degassing during ascent and eruption.

The subduction zones of northern Japan make for an excellent natural laboratory for the study of arc variations as they have been well characterized by seismic tomography work, making for more accurate estimations of the geometry and PT conditions of the subducted slab. There is a significant variation in the distance of the volcanic front to the trench, and in addition there is back-arc magmatism, with one volcano located extremely far from the trench. This produces a broad distribution of PT conditions of the slab below each volcano, making it feasible to study across-arc variations related to progressive subduction.

This thesis addresses the problem of post-entrapment processes that can make the recovery of initial OHMI compositions difficult. In particular, the identification of complete Fe-Mg re-equilibration of long stored antecrystic olivine hosts impedes the recovery of the syn-entrapment melt composition from traditional reverse crystallization and diffusion models. The MushPEC algorithm is developed, a novel tool to recover original MI compositions from a set of cogenetic re-equilibrated OHMIs that evolved through simple fractional or equilibrium crystallization.

Next, the storage conditions and differentiation process recorded by MI populations from five arc-front samples of northern Japan are addressed. Homogeneous olivine compositions with a wide range of SiO_2 contents indicate that most olivine-hosts in arc front systems of northern Japan are antecrystic and have been completely re-equilibrated. Application of the MushPEC algorithm shows that the differentiation trends that the MI follow within each sample are incompatible with simple fractional/equilibrium crystallization and require boundary layer fractionation, where interstitial differentiated melts formed in highly crystallized solidification fronts are progressively extracted and incorporated into the main un-differentiated magmatic body. The estimated P-T-H_2O conditions of the MIs agree with boundary layer fractionation processes, promoted in hydrous melts stored at >100 MPa, as proposed by previous studies.

Further, the processes of material release from the slab to the source mantle are addressed, and how they vary with increased P-T conditions across the arc. Across-arc variations of large ion lithophile (LILE), rare earth (REE), high field strength elements (HFSE) and volatile ratios are correlated with the estimated PT conditions of the slab and the expected metamorphic reactions that release components enriched in trace and volatile elements. Constant LILE/HREE and volatile/HREE ratios in the arc front indicate homogeneous slab component compositions along the arc. Progressive enrichment of these ratios towards the back-arc indicates a new liquid source enriched in most LILEs and volatiles. This increase coincides with the expected initiation of the antigorite breakdown reaction in lithospheric serpentinites, providing enriched liquids involved in back-arc magmatism. Constant (Pb, Sr)/HREE from arc to back-arc points to lawsonite breakdown occurring at all depths. Progressive LREE/HREE increase towards the back-arc is explained by increasing LREE mobility with increasing T, which controls the solubility of LREE-rich accessory minerals (e.g., allanite). Finally, the composition of the slab liquid depleted of the LILE and halogen components released by serpentinites when serpentine is exhausted at c. 8 GPa, and strong enrichment of HFSE elements indicates the participation of supercritical liquids at these extreme depths of the slab.

This thesis highlights the importance of assessing the re-equilibration of OHMIs during long storage times, a process that is seldom discussed in the literature, the widespread occurrence of boundary layer fractionation in arc magmatic systems that needs to be taken into account when modelling differentiation processes in hydrous magmas, as application

of simple fractional crystallization models will result in estimations of inaccurate magmatic conditions. This work also highlights the importance of the hydrated lithospheric mantle on the production of back-arc magmatism in island arc systems and the potential of halogen volatile phases on the tracking of slab fluid compositions.

Acknowledgements

I would like to acknowledge all the people that had an impact on the production of this thesis. To my supervisory team, led by Georg, and constituted by Karoly at Massey University, and Kuritani-san and Sakamoto-san at Hokkaido University.

Georg gave me the opportunity to start this project and he has been an excellent guide during my whole study. His constant trust and support has helped me get to this point. I also want to thank him for his concern beyond his obligations as a supervisor.

Kuritani-san provided many of the studied samples, facilities access and guidance during my initial work and support during the production of all the manuscripts. Sakamoto-san provided all his expertise to obtain high quality data from the SIMS.

Thanks to Prof. Hisayoshi Yurimoto who provided access to the Isotope Imaging Laboratory for SIMS and FE-SEM work, and to Prof. Mitsuhiro Nakagawa for his help with laboratory and sample access, and useful information on volcanoes of Japan.

To Prof. Mark Kendrick, who was extremely helpful by providing glass standards for volatile analysis. Further, to Prof. Vadim Kamenetsky for his valuable input on MI studies.

Special thanks to Hajime Taniuchi, for all his help during my work in Hokkaido, especially for organizing and helping me with fieldwork in Rishiri and Tokachi-dake. Thank you to the group of petrology postgraduate students at Hokkaido University and the team at IIL for giving me a space in their office and for helping me enjoy my stay in Japan.

To the geochemistry group in the VRS and to the infamous geochemistry meetings. Special thanks to Daniel Couldhard Jr., with whom we had long research discussions.

To the “Coffee club” which provided the necessary caffeine and much needed fun breaks during the whole PhD journey. To my old flatmates of Glasgow street and “The Mansion”, which made my PhD journey a lot more fun. To my office mates that also provided some laughs on those busy days.

To my family, who always supports me from the distance on the other side of the Pacific.

And last but not least, to Arantzasu “Chacha” Morales, who accompanied me during the whole adventure in this strange land, who had to overcome her own struggles to get that much deserved reward. She helped me to cope with those difficult times to get to this point, including this bizarre last year caused by the pandemic and the stressful last months of this journey. Love you.

Table of Contents

List of Tables

List of Figures

Chapter 1

Introduction

1.1 Motivational background

1.1.1 Differentiation processes in subduction settings

Crustal differentiation processes are commonly thought to be the key to understanding the compositional diversity of arc magmas. Fractional crystallization (FC) has been invoked as the main process of magma differentiation at crustal depths (e.g., Bowen, 1915; Brahm et al., 2018; Forni et al., 2016; Gavrilenko et al., 2016b; Gelman et al., 2013; Grove and Kinzler, 1986; Kimura and Ariskin, 2014; Mollo et al., 2015; Portnyagin et al., 2015; Watanabe et al., 2006; Yoshida and Aoki, 1984; Zen, 1986). Most attempts to model FC are based on Rayleigh fractionation, which assumes that the crystallization process occurs homogeneously throughout the magmatic body (homogeneous FC; HFC). For its simplicity, this approach is commonly preferred over more complex fractionation models. Nonetheless, several studies have proposed that crystallization of magma reservoirs dominantly operates in solidification fronts at their boundaries, where the magma is expected to cool most effectively (Kuritani, 1999b; Kuritani, 2009; Langmuir, 1989; Marsh, 1996; Marsh, 2007; Nielsen and DeLong, 1992; O'Hara and Fry, 1996; Simura and Ozawa, 2011). The chemical evolution of the magma can then be modelled by mixing of the central melt with increments of differentiated magma from the boundary layer (in situ crystallization or boundary layer fractionation; BLF; Langmuir, 1989; Nielsen and DeLong, 1992). The compositional path generated by BLF is substantially different to the one produced by HFC, meaning the application of HFC or BLF models can result in strong discrepancies in the interpretation of magmatic conditions. Discriminating between these processes is thus of crucial importance. BLF has been

`

proposed to explain the compositional evolution observed in some volcanic suites (Kuritani, 1999b; Kuritani, 2009) in arc magmas, where higher H_2O contents promote BLF over HFC. Crustal differentiation processes operating in arc magmas need to be fully understood before the generation of primary magmas by partial melting processes in the underlying mantle wedge can be considered.

1.1.2 Volatile elements and their role in arc magmatism

Volatile elements in magmatic systems consist mainly of H, C and S, with lower concentrations of halogens (Cl, F, Br and I). Volatiles have an important role in magma genesis and evolution, and in arc settings, they are thought to be a dominant factor that allows for mantle melting and thus the generation of magmatism. In a subduction zone, the slab, constituting of serpentinized lithospheric mantle, basaltic oceanic crust and sediment cover, is subducted deep into the mantle (Figure 1.1). This subducted slab carries volatile and mobile elements that are released as a fluid phase into the mantle wedge (Grove et al., 2012). The H_2O-rich fluids metasomatize the mantle, reducing its solidus temperature and consequently triggering the partial melting of the mantle in a melting process known as fluid-flux melting (Grove et al., 2006).

Each volatile phase has a particular behaviour and effect on the magma. Most of the volatile budget is composed of H_2O. The H_2O content has a direct effect on the crystallization path of the magma during differentiation, inhibiting crystallization (Sisson and Grove, 1993). At higher H_2O concentrations, the magma can stay in a liquid state (or at lower crystallinity) at lower temperatures than a magma with low H_2O content. Hence, “wet” magmas are usually colder than “dry” magmas, and water exsolution due to decompression during ascent of these cold, H_2O-rich magmas triggers crystallization, resulting in their emplacement at greater depths compared to dry and hot magmas (Zellmer et al., 2016).

CO_2 is the second most abundant volatile species in magmas, and the one with the lowest solubility (Dixon et al., 1997; Dixon and Stolper, 1995). Hence, it is usually exsolved

before magma reaches shallow crustal levels. Deeply exsolved CO_2 can ascend and interact with shallower stored magmas, re-equilibrating the melt with this CO_2-rich vapour phase (CO_2-fluxing or flushing) (Caricchi et al., 2018; Oppenheimer et al., 2011a).

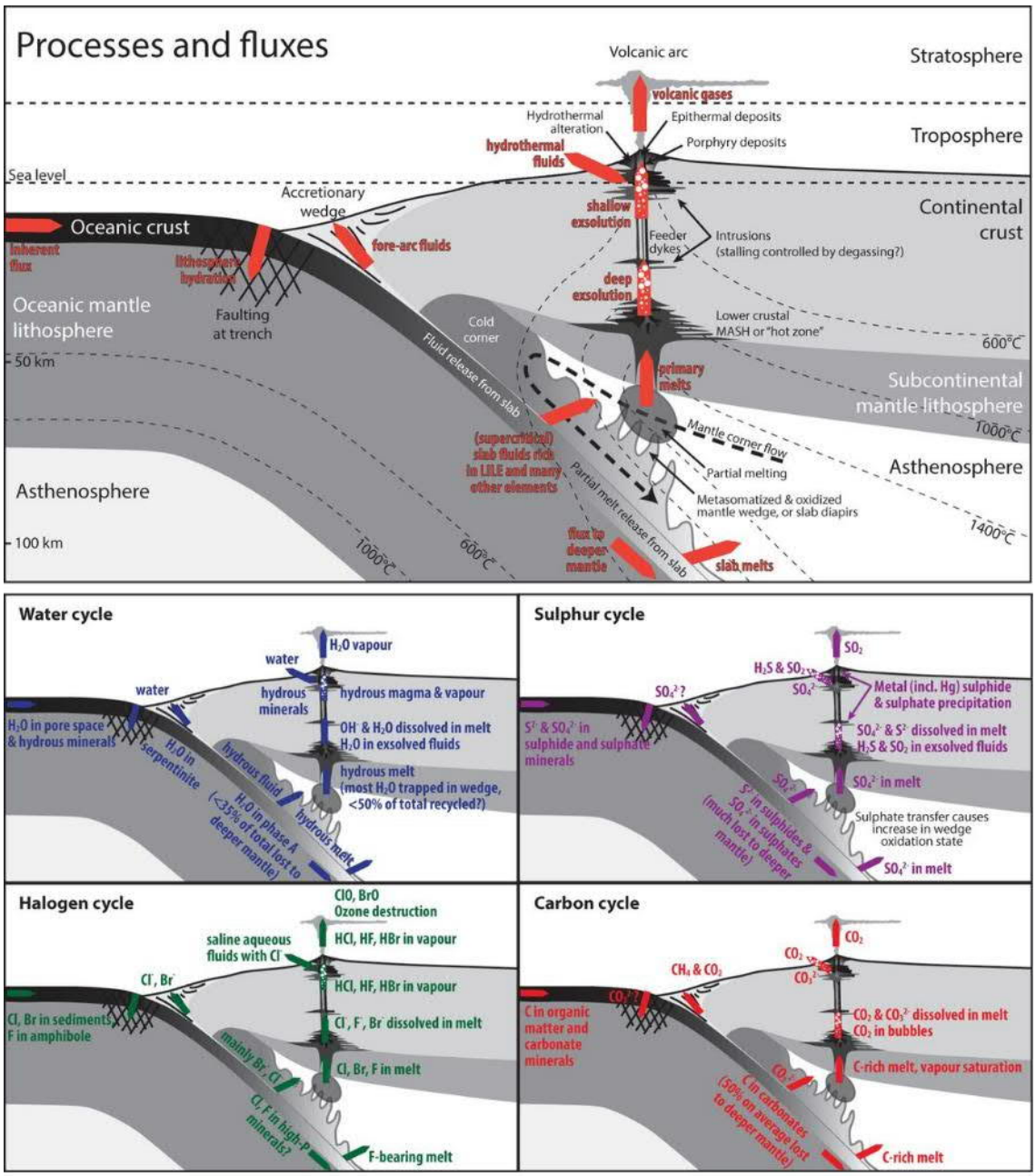

Figure 1.1. Schematic of a subduction setting indicating the stages of volatile cycles involved in arc magma generation, transport and eruption (from Zellmer et al., 2015).

The behaviour of sulphur is highly dependent of the oxidation state of the magma, because it can be present as SO_4^{2-} and S^{2-}, which have very different solubilities (Wallace and Carmichael, 1992). S can be separated from the silicate melt into an S-rich immiscible liquid (Moretti and Baker, 2008), it can crystallize into sulphates or sulphides (Ariskin et

`

al., 2013) and/or it can be exsolved as H_2S and SO_2 during decompression and eruption (Oppenheimer et al., 2011b). S species have an important role in the transport of metals and formation of mineral deposits of economic interest (Vaughan and Corkhill, 2017).

Cl and F are usually highly soluble in the melt and incompatible with the crystallizing mineral phases (Alletti et al., 2014; Zhang et al., 2012). A small portion of these halogens can be incorporated into hydrous mineral phases or exsolved during eruption, but a considerable portion can stay dissolved in the quenched volcanic glass (Pyle and Mather, 2009; Wallace, 2005).

1.1.3 Olivine-hosted MIs

Obtaining volatile contents in magmatic samples is not a straightforward process. Most of the volatile budget in magmas is released as exsolved gas during ascent and eruption (Alletti et al., 2014; Berlo et al., 2010; Edmonds and Woods, 2018; Witham et al., 2012). Hence, groundmass or whole rock compositions of volcanic samples do not record pre-eruptive volatile compositions.

A more straightforward way to obtain volatile data is through the direct measurement of MI (MI) compositions (Hauri, 2002; Métrich and Wallace, 2008; Rose-Koga et al., 2014; Vigouroux et al., 2012). MIs are small pockets of melt trapped in minerals during growth (Figure 1.2) and have the potential to record the magmatic composition during the process of entrapment (Kelley et al., 2006; Kelley et al., 2010; Kent, 2008). Unlike groundmass glass, glass compositions of MIs may, under certain circumstances, retain the volatile species trapped inside still dissolved in the glass or exsolved into a gas bubble.

Thus, analyses of MIs hosted in early-crystallized phases (e.g. olivine) of mafic magmas may yield a precious record of unevolved compositions (Blundy et al., 2010; Métrich and Wallace, 2008; Reubi and Blundy, 2009), whereas mineral phases in equilibrium with later storage conditions can record the evolution of the volatile budget during transport and differentiation (post-entrapment crystallization or PEC; Kent, 2008; Kress and Ghiorso, 2004).

MI analysis is not exempt of difficulties. There are a number of processes that can occur after MI entrapment, which may change the initial composition of the MI glass and are needed to be assessed. In many cases, melt inside an inclusion may crystallize around the walls of the host crystal or as newly nucleated crystals inside the MI (post-entrapment crystallization or PEC; Kent, 2008; Kress and Ghiorso, 2004). MIs can also form a 'shrinkage bubble' (Figure 1.2) due to differential volume changes of the melt inside the inclusion and the mineral host, where the bubble may or may not have an exsolved gas phase (Wallace et al., 2015). To reconstruct the initial entrapment compositions, a combination of experimental and modeling methodologies are usually applied. These consist in re-heating the MI-bearing crystal to magmatic temperatures to re-melt crystals or resorb the shrinkage bubble, and application of thermodynamic equilibrium calculations to track back processes of PEC and diffusion (Cannatelli et al., 2016; Danyushevsky et al., 2002a; Danyushevsky and Plechov, 2011).

In recent years, studies have shown that post-entrapment processes are more complex than previously understood. Corrections for bubble formation might be obscured by precipitation of sulphide and carbonate minerals in the shrinkage bubble walls (Venugopal et al., 2020), diffusion of H^+ through the olivine host might re-equilibrate the H_2O content of the MI with the outside melt in a matter of hours (Hartley et al., 2015; Hartley et al., 2017; Turner et al., 2017b), and long residence times of the hosts might impede the recovery of original compositions at the moment of entrapment (Gaetani and Watson, 2000; Gaetani and Watson, 2002).

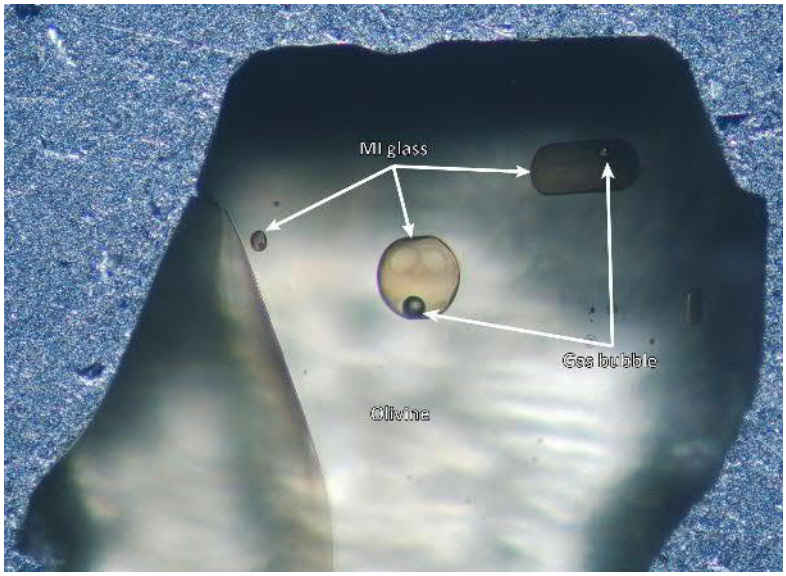

Figure 1.2. Optical microscope image of an olivine-hosted glassy MI with a shrinkage bubble from a basaltic tephra of Rishiri volcano (North Japan).

1.1.4 The subduction setting of northern Japan

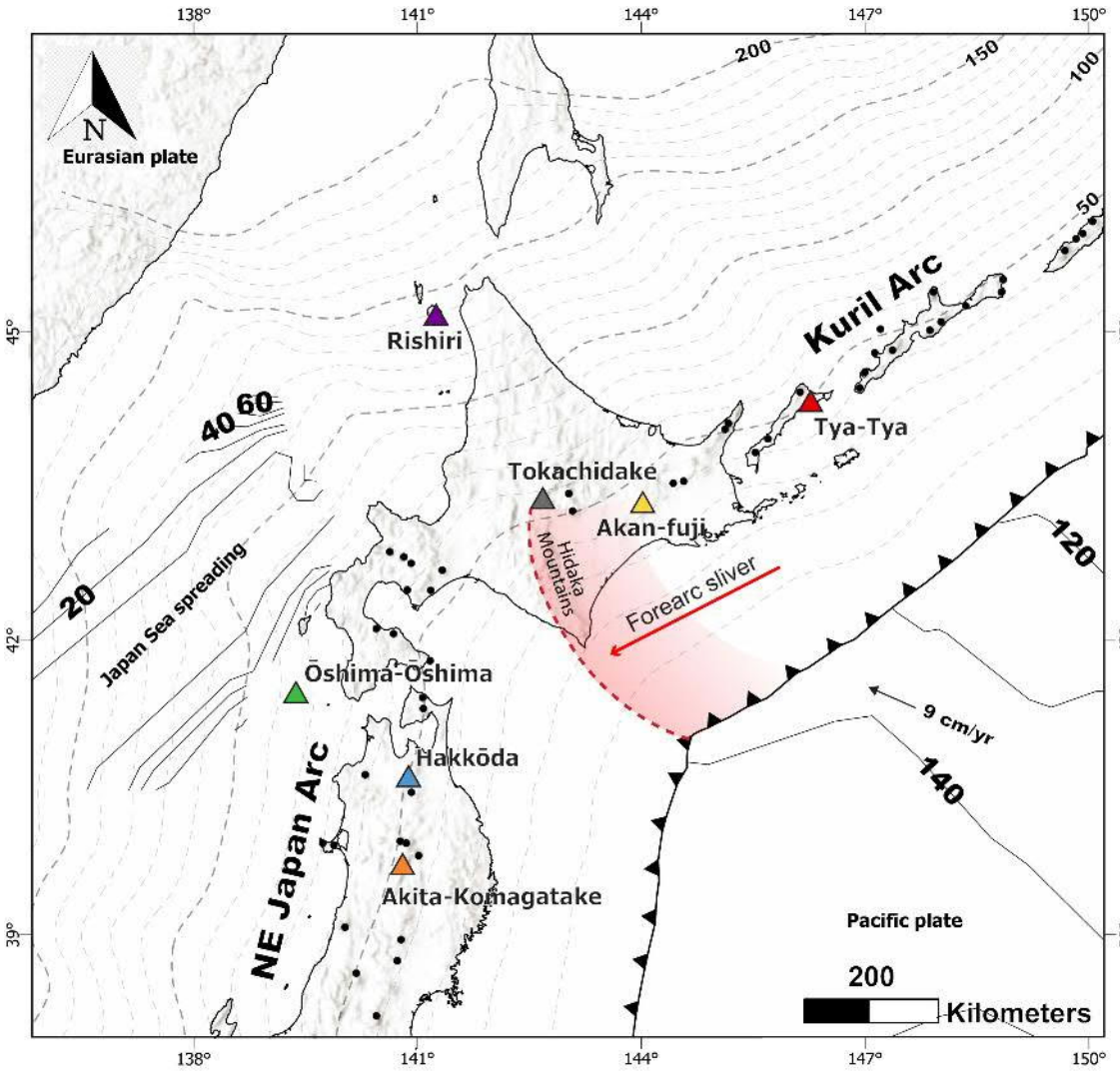

Figure 1.3. Topographic map of NE Japan. Triangles with names are the volcanic systems of interest in this study. Black dots are other volcanoes of the NE Japan and the Kuril arcs. The black line with triangles marks the subduction trench. Red area indicates the collision zone of the Kuril arc forearc sliver over the NE Japan arc, and the red arrow indicate the direction of movement of the forearc sliver. Grey dashed lines indicate the depth of the slab (km). Black contour lines with numbers indicate the age of the oceanic crust in Myr.

The subduction zone of the Japanese Islands is a particularly good natural laboratory to study arc magmatism from genesis to eruption, including along and across arc variations in slab fluid input, melting conditions and crustal level processes (e.g., transport, storage, differentiation and eruption). This area contains one of the best-understood subduction settings, thanks to the dense network of seismic stations, allowing the generation of many high-resolution seismic tomography models (e.g., Abdelwahed and Zhao, 2007; Chen et

al., 2018a; Huang and Zhao, 2013; Huang et al., 2010; Kita et al., 2014; Liu and Zhao, 2016; Nakajima et al., 2013; Tong et al., 2012; Tsuji et al., 2008; Wang and Zhao, 2013; Zhao et al., 2017). In particular, the Tohoku and Hokkaido regions present a great opportunity to analyse changes in subduction and relate them to variations in volcanic volatile compositions. The southernmost Kuril arc and the northernmost NE Japan arc collide in Central Hokkaido (Figure 1.3), where a forearc sliver of the Kuril arc is pushed SW over the NE Japan forearc (Kimura, 1986; Kita et al., 2012; Kita et al., 2014; Kusunoki and Kimura, 1998). The orientation of the trench in the arc-arc junction changes from N10E in the NE Japan arc to N56E in the Kuril arc, producing a change of the subduction rate between both arcs, while the slab age and composition continues to be similar in both sides of the junction. Therefore, sharp changes in some slab parameters, while other parameters are kept more or less constant, makes it possible to identify the effect that these changes have on the composition of the generated arc magmas, and the associated volatile cycles.

1.2 Objectives

1.2.1 General objective

The aim of this thesis is to identify along- an across-arc variations in magmatic signatures of generation and differentiation processes in a subduction setting and relate them to known variations in the subduction architecture.

NE Japan was used as natural laboratory for this study, encompassing the northern NE Japan arc and southern Kuril arc, around the arc-arc collision zone, taking advantage of the well-studied subduction architecture of this particular subduction setting.

Olivine-hosted MIs (OHMIs) of seven basic tephra sample from seven volcanoes in the arc front and back-arc of northern Japan are investigated for this purpose. As pointed out above, newly identified post-entrapment processes makes interpretating OHMI compositions very complex. In addition, the need of novel analytical techniques (e.g., synchrotron source techniques like XANES or XRT) and more common methods (e.g.,

`

EPMA, FTIR, SIMS) to get a full picture of post-entrapment processes, makes MI studies less accessible. This study focuses on the interpretation of the standard battery of MI glass data (major, trace and volatile elements). Emphasis is on the identification of post-entrapment processes that make correction and interpretation of MI data difficult, especially for volatile components, but this is necessary for accessing deeper processes such as melt generation in the mantle.

1.2.2 Specific objectives

To achieve the main objective of this thesis, the work is divided into three specific objectives, each one tackled in a separate scientific article, which are provided here as chapters 4 to 6. These specific objectives are:

1) Develop a correction scheme for completely re-equilibrated olivine-hosted MIs.

   Many studies have relied in PEC-corrected olivine-hosted MI data as direct evidence of syn-entrapment melt compositions and in some cases also as starting points for reverse crystallization models to estimate primary magma compositions, which in turn are used to estimate melting conditions. PEC corrections usually consist in reverse crystallization of olivine in equilibrium with the melt, sometimes coupled with an Fe-loss correction that assesses for Mg – Fe exchange between melt and olivine during olivine crystallization in the MI walls (Danyushevsky et al., 2000; Danyushevsky et al., 2002b).

   These correction methods estimate the melt composition at the last MI equilibration stage, which is often assumed to be the moment of entrapment. As suggested by (Gaetani and Watson, 2000; Gaetani and Watson, 2002), long residence times of olivine host crystals will cause host and MI magnesium number to be completely re-equilibrated with the carrier melt, and classic post-entrapment corrections applied to these MIs will recover these storage equilibrium conditions. This is especially true for antecrystic hosts, which may have been stored for long times in mush reservoirs prior to their remobilized by the new carrier melt.

A set of MIs from a basaltic tephra sample of the Akita-Komagatake volcano is used to identify the geochemical signatures of re-equilibrated MIs during long residence times, and a new methodology is proposed to attempt to recover the original MI compositions at the moment of entrapment. A program called MushPEC is developed in Matlab®, which finds the best fit of the MI liquid line of descent to homogeneous fractional crystallization models produced with rhyolite-MELTS (Asimow and Ghiorso, 1998; Ghiorso and Sack, 1995; Gualda et al., 2012).

2) Estimation of magmatic conditions and identification of common differentiation mechanisms in arc magmas of northern Japan through OHMI populations.

Whole rock compositional trends have been widely used to generate differentiation models of volcanic suites. In many cases the crystal cargo can substantially alter the compositions of whole rocks by crystal accumulation and entrainment of antecrysts and xenocrysts (e.g., Jerram and Martin, 2008; Zellmer et al., 2016; Zellmer et al., 2014). Compositional trends of PEC-corrected OHMI compositions have the potential of being a better representation of the differentiation processes as they are not affected by the crystal cargo.

In addition, the combination of PEC correction schemes with newly developed thermodynamic models of gas bubble formation (Rasmussen et al., 2020) and olivine – melt H_2O equilibrium (Gavrilenko et al., 2016a) allows for estimation of original volatile contents (H_2O – CO_2). These estimations allow for more reliable magmatic P – T conditions to be calculated using H_2O – CO_2 solubility models (e.g., Papale et al., 2006) and olivine – melt thermometry (e.g., Putirka et al., 2007).

A collection of olivine-hosted MIs from tephra samples from five arc front volcanoes in NE Japan are used to characterize intrinsic magmatic properties and to identify the most likely differentiation mechanism in arc magmas from NE Japan.

3) Correlation of along and across variations in trace and volatile elements with conditions of the slab below each volcanic system.

Magma generation in subduction zones is an interplay of fluid component release from the slab and the composition and conditions of the overlaying mantle wedge. Volatile and fluid mobile trace elements compositions of arc magmas can elucidate the slab component contributions during mantle melting, whereas immobile trace

`

elements are usually related to the mantle wedge source (Pearce et al., 2005). Olivine-hosted MIs have been used to estimate primary magma compositions and melting conditions. However, this is not achievable when the MIs are hosted in olivine crystals that have been re-equilibrated during long crustal residence. In these cases, element ratios of incompatible elements in olivine may be used provide insights into source component and melting condition variations.

Olivine-hosted MI populations of seven volcanoes located in the arc-front and back-arc of the northernmost NE Japan arc and the southernmost Kuril arc are studied with the aim of identifying compositional trends related to variations in conditions of magma generation along and across the arc setting. The analysis relies on elemental ratios of a selection of trace elements incompatible in olivine and including halogens elements (F and Cl), which are neither lost to the MI bubble nor through diffusion These ratios are compared to the progressive change of the estimated PT conditions of the slab and the expected mineralogy and dehydration metamorphic reactions occurring with progressive subduction.

Chapter 2 provides the literature review related to the subduction system in northern Japan and the volcanic systems of interests, plus the literature related to olivine-hosted MI studies and subduction magmatism. Chapter 3 describes the analytical methodologies used in this study. Chapter 4 to 6 each correspond to a scientific manuscript tackling one of the specific objectives described above. Chapter 7 provides a synthesis of the main discussion points of each manuscript and Chapter 8 summarizes the conclusions and provides an outlook.

Chapter 2

Literature Review

2.1 Geologic background

2.1.1 Current tectonic setting of the Japanese Islands

The Japanese Islands comprise four main islands and a series of smaller islands. Form north to south the main islands are Hokkaido, Honshu, Shikoku and Kyushu. These islands are located in a highly seismically active area, with an interplay of at least four tectonic plates (Figure 2.1), which combined with a dense high-sensitivity seismic network makes this region one of the best studied subduction zones in the world.

Hokkaido and Tohoku (NE Honshu) regions are located in the Okhotsk Plate, whereas SW Japan belongs to the Eurasian (or Amur) Plate. East of Hokkaido and NE Honshu, the Pacific Plate is subducted beneath the Okhotsk Plate (7 – 11 cm/yr; Bird, 2003; Northrup et al., 1995), at the Kuril (to the north) and Japan (to the south) trenches. In the south, the Philippine Sea Plate is subducted northward below the Okhotsk Plate in the Sagami Trough and to the NW under the Eurasian Plate, in the Nankai Trough, beneath the central and SW Honshu, respectively (4-5 cm/yr; Bird, 2003; Zhao, 2015).

These subduction systems are associated with volcanic arcs along the whole extension of the main Japanese islands (with the exception of Shikoku). The SW Japan Arc comprises the volcanoes associated with the subduction in the Nankai Trough, along Kyushu and SW Honshu. The NE Japan Arc is associated with the Japan Trench comprising the volcanoes from NE Honshu and SW Hokkaido. In south-central Hokkaido an arc-arc collision is occurring, where the NE Japan Arc meets the southernmost part of the Kuril

Arc. The Kuril Arc, related to the Kuril Trench, begins in central Hokkaido, extending to the NE through the Kuril Islands.

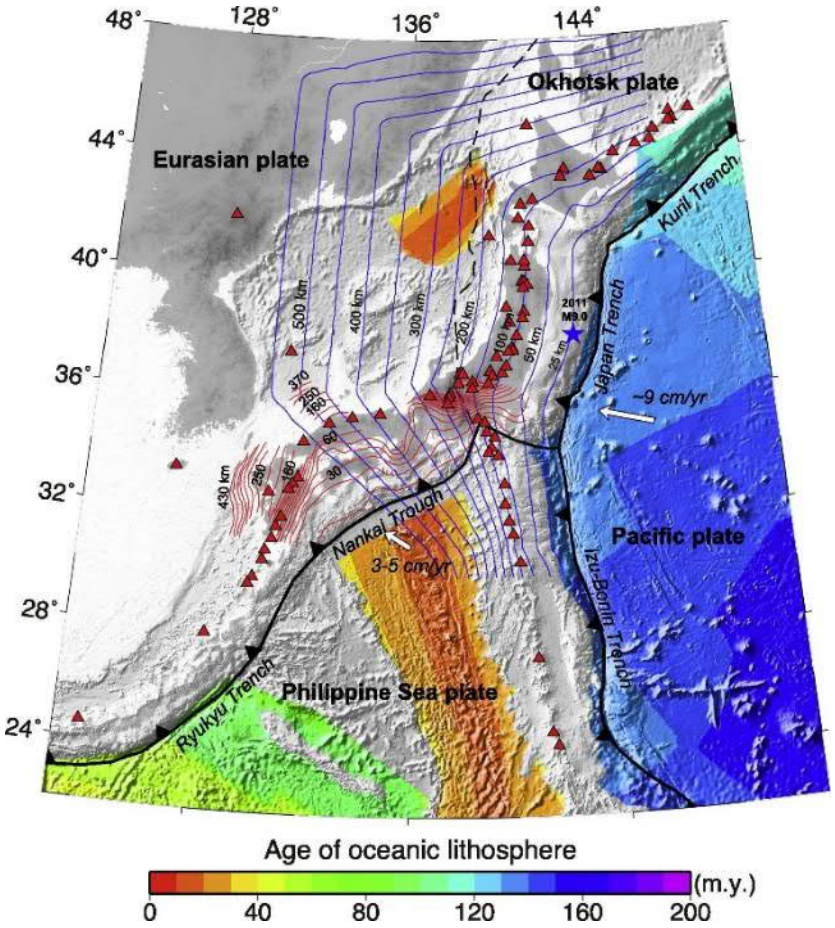

Figure 2.1. Tectonic setting of Japan (Liu and Zhao, 2016). The red triangles mark the Quaternary volcanoes. Solid sawtooth lines and dashed lines indicate plate boundaries. Blue and red contour lines denote the depths of the subducting Pacific and Philippine Sea plates, respectively.

2.1.2 Tectonic and Magmatic evolution of the Japanese Islands

The Cenozoic evolution of the Japanese Islands can be divided into three main periods in relation to its magmatism and tectonic settings (Ohguchi et al., 1989; Yoshida, 2001; Yoshida et al., 2014):

(1) Continental margin period (66 – 21 Ma)
(2) Back-arc basin period (21 – 13.5 Ma)
(3) Island-arc period (13.5 – 0 Ma)

`

Even though the arc magmatism in the Japanese Islands is catalogued as island arc magmatism, the basement of the main island is composed of continental crust that initially belonged to the eastern margin of the Eurasian continent, from where proto-Japan detached during the opening of the Japan Sea during the Oligocene (Maruyama and Send, 1986; Tamaki et al., 1992; Van Horne et al., 2017). In the last stage of the continental margin period and the whole back-arc basin period (around 23 - 13 Ma) the opening of the Japan Sea occurred. The Japan Sea is interpreted to have formed by the extension and thinning of the proto-Japan arc, which was part of the eastern margin of the Eurasian continent.

In NE Japan, extension during the opening of the Japan Sea generated a series of tectonic segments of horst and graben-like structures. They can be divided in two main rift systems: the Yamato Basin rift to the west and the Northern Honshu rift to the east. The Yamato Basin developed half-grabens, bounded by westward-dipping normal faults during early Miocene times. There is a decrease in the thickness of the crust westward, produced by stretching related to the opening of the Japan Sea. The Northern Honshu rift developed later (Middle Miocene) as a deep sedimentary basin developed by simple shear.

During the Cenozoic evolution of the Japan Arc, the arc front migrated from a position in the current back-arc that shifted to the forearc during the change from the continental margin to the back-arc basin period, reaching the current arc position at around 5 Ma (Figure 2.2) (Martin, 2011; Yoshida et al., 2014). The arc-front shift was slightly different between NE and SW Japan, with a delayed migration of the arc to the current forearc in SW Japan.

The island-arc period started when the opening of the Japan Sea ceased (*c.* 13.5 Ma). A neutral stress regime started and lasted until 10 Ma (Yoshida et al., 2014). During this stage, lithospheric cooling led to thermal subsidence of the back-arc region. Crustal felsic magmatism at 13.5 – 8 Ma, related to igneous underplating during the back-arc basin period, likely produced the uplift of the axial zone of the volcanic arc. The weak compressional phase can be divided in two stages (10 – 8 Ma and 8 – 3.5 Ma). Volcanism of the island-arc period occurred in the eastern rift zones and was mainly characterized by caldera forming felsic volcanism at 8 – 1.7 Ma (Yamada and Yoshida, 2002; Yamada

and Yoshida, 2011; Yoshida et al., 1999a), with subordinate basaltic to andesitic volcanism (Acocella et al., 2008). Two peaks of caldera activity are divided by a period of quiescence during 4 – 5 Ma. The neutral stress field during the beginning of the island-arc period would have helped the rising of felsic magmas through the lower and upper crust. Then, the change to a weak compressional stress regime would have led to the development of shallow reservoirs in the upper crust (Aizawa and Yoshida, 2000; Sato and Yoshida, 1993). During the island-arc period, the collision of the Kuril arc with the NE Japan arc started in the Hidaka Collision Zone, central Hokkaido (12 Ma). The change to a NE-SW compression stress field, related to the collision of the Kuril Arc in central Hokkaido (Kimura, 1986), would have triggered felsic eruptions in localized areas of extension (Acocella et al., 2008).

There was an increase in the westward motion of the Pacific Plate around 4 Ma (Pollitz,

Figure 2.2. Volcanic arc-front migration during the Cenozoic. Image and data taken from (Martin, 2011) and references therein.

1986), which generated an increase in compression across the arc at 3.5 – 1 Ma, producing the uplift of the volcanic arc in the Ou Backbone through inversion of Miocene normal

`

faults. The change from caldera forming felsic eruptions to basaltic to andesitic stratovolcanoes that happened around 2 Ma was synchronous with a tectonic change from a NE–SW oriented compression to an ENE–WSW oriented compression (Acocella et al., 2008).

2.1.3 Arc-arc collision between NE Japan arc and Kuril arc

Figure 2.3. Tectonic setting of Hokkaido from Kita et al. (2014), after Kimura (1994), showing the tectonic division. Green- and purple-shaded areas show the Hidaka metamorphic belt and the Kamuikotan metamorphic belt, respectively. Red dotted line and thick grey lines mark, respectively, the boundary of the Kuril and NE Japan arcs and active faults. Triangles are active and/or Quaternary volcanoes.

In Hokkaido, the NE Japan arc meets the southernmost Kuril arc in an arc-arc collision zone (Kimura, 1996; Kita et al., 2014), known as the Hidaka collision zone. Oblique subduction of the Pacific plate produces a southward migration of the Kuril forearc sliver

(Figure 2.3), which has been colliding with the NE Japan arc in south-central Hokkaido since Miocene times, uplifting the Hidaka Mountains.

The compressional stress of this collision generates a series of N-S deformation structures that can be divided in a series of tectonic belts as shown in Figure 2.3 (Kita et al., 2012), which are (from west to east): (1) the Oshima belt, (2) the Ishikari low land, (3) the Sorachi-Yezo belt, (4) the Idonappu belt, (5) the Hidaka belt, (6) the Yubetsu belt, (7) the Tokoro belt and (8) the Nemuro belt.

There is a volcanic gap of *c.* 120 km between the volcanoes in the SW of Hokkaido (NE Japan Arc) and central Hokkaido (southern Kuril Arc) that coincides with the zone of collision of the Kuril forearc sliver and includes the tectonic zones (2), (3), (4) named above (Figure 2.3).

Wave velocity (V_p and V_s) and attenuation (Q_p) tomography studies (Kita et al., 2012; Kita et al., 2014; Zhao et al., 2012) allow the identification of the subduction architecture in this arc-arc collision setting. SW and E Hokkaido show an elongated low-V and low-Q zone in the core of mantle wedge, subparallel to the subducting slab. As seen in the NE Japan arc beneath Honshu, this elongated low velocity zone reaches the Moho just below the arc-front (*c.* 40 km deep) and is interpreted as the mantle wedge upwelling flow. There is also a low-V and low-Q zone just above the slab at depths of 90 – 100 km, which has been interpreted as hydrated mantle material like serpentinite and chlorite, generated by the release of fluid from the slab (Kita et al., 2014).

The elongated low-V and low-Q zone of the upwelling flow of the mantle wedge disappears beneath central Hokkaido in the collision zone. Also, the low-V zone just above the slab that indicates the dehydration depth is recognized at depths of 110 – 130 km, 10 – 40 km deeper than in SW and NE Hokkaido. Kita et al. (2010) identified the existence of deep crustal materials immediately above the Pacific slab (Figure 2.4). The colder hydrated crust hinders the heating of the slab, reducing the temperature of the slab in the collision zone and, in consequence, deepening the slab dehydration depth, where partial melting of the mantle is not sufficient to form magma, thus generating the volcanic gap of central Hokkaido.

`

Figure 2.4. Model of the Hidaka collision zone from Kita et al. (2012). The crust from the NE Japan Arc is subducted, reaching the Pacific slab.

2.1.4 Quaternary NE Japan

2.1.4.1 Crustal structure

The basement of NE Honshu and SW Hokkaido is represented by the accretionary complexes and granitic intrusives of the Kitakami and Abukuma massifs, related basement of SW Hokkaido, and the Ashio belt further south, separated by near N-S fault systems (Figure 2.5). The Kitakami Massif is intruded by Cretaceous to Paleogene granitoids designated as the Kitakami zone granitoids (Kagami, 2005; Kagami et al., 2000), which are isotopically depleted compared to the granitoids intruding metamorphic complexes further south.

The composition of the lower crust and upper mantle is interpreted to be represented by the Ichino-megata xenoliths (Aoki, 1971). The *c.* 15 km thick lower crust is believed to be composed of hornblende gabbro generated as fractionated cumulates from calc-alkaline magmas (Fukuyama, 1985; Sakuyama, 1983; Yoshida et al., 1997), and amphibolite generated from the same calc-alkaline magmas (Zashu et al., 1980). Using

Figure 2.5. Simplified geologic map of Japan (modified from Van Horne et al., 2017). Ab: Abukuma massif, As – Ashio belt, Ch: Chichibu belt, Hd: Hida belt, Ki: Kitakami massif, Mt: Mino Tamba belt, Ry: Ryoke belt, Sb: Sanbagawa belt, Sh: Shimanto belt, TTL: Tanakura Tectonic Line, HTL: Hatagawa Tectonic Line, MTL: Median Tectonic Line, ISTL: Itoigawa-Shizuoka Tectonic Line.

V_p and V_s tomographic images at the depth of 25 km, Zhao et al. (2011) recognized nine velocity anomalies and made estimations of the lithologies composing the lower crust (Figure 2.6). The dominant crustal rock would be hornblende gabbro and amphibolite, mainly distributed along the central axis of the NE Japan arc (C, E and F in Figure 2.6). Hornblende pyroxene gabbro to gabbrodiorite and/or pyroxene amphibolite are dominant in the rifted back-arc basin (B and D in Figure 2.6) (Nishimoto et al., 2008). The zones of rifted continental crust, west of the Tanakura Tectonic Line (TTL), are composed of mainly granitic rocks (I in Figure 2.6) (Tamaki et al., 1992), while granodioritic lower crust is present to the east of the TTL (H in Figure 2.6).

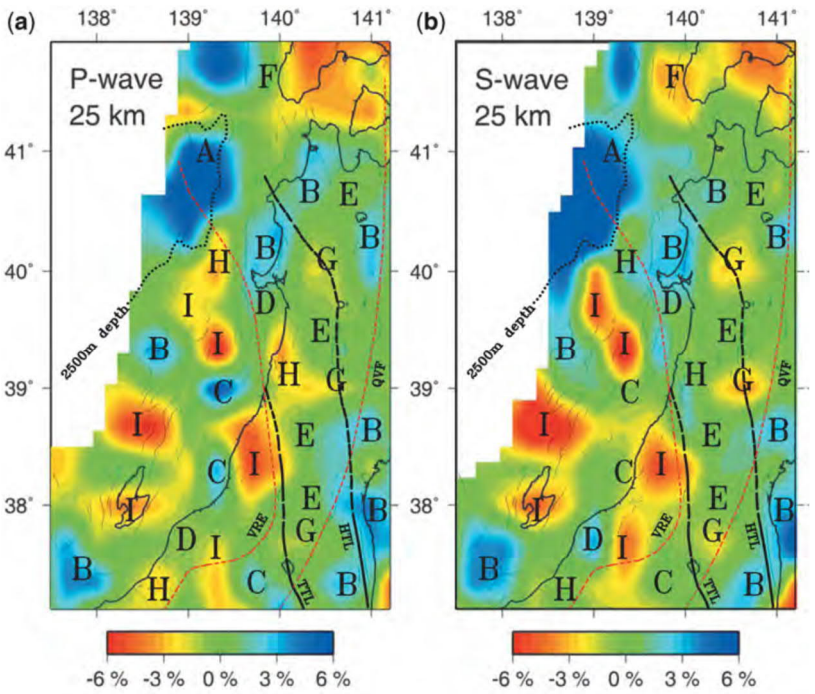

Figure 2.6. P-wave (a) and S-wave (b) velocity images at 25 km depth in NE Japan back-arc region. From Yoshida et al. (2014), after Zhao et al. (2011). Velocity anomalies: (A) (high V_p, high V_s, low V_p/V_s) as peridotites; (B) (high V_p, high V_s, medium V_p/V_s) as hornblende pyroxene gabbro; (C) (high V_p, medium V_s, high V_p/V_s) as hornblende gabbro to amphibolite; (D) (medium V_p, high V_s, low V_p/V_s) as gabbronorite to amphibolite; (E) (medium V_p, medium V_s, medium V_p/V_s) as pyroxene hornblende gabbro to amphibolite; (F) (medium V_p, low V_s, high V_p/V_s) as hornblende gabbro to hornblendite/amphibolite; (G) (medium V_p, low V_s, high V_p/V_s) as partially molten lower crust; (H) (low V_p, medium V_s, low V_p/V_s) as granodiorite; and (I) (low V_p, low V_s, low V_p/V_s) as granite.

In the forearc (Figure 2.7a), a low velocity anomaly belt is interpreted to be a remnant of the middle Miocene magma plumbing system positioned in the eastern limit of the Northern Honshu rift (Okada et al., 2010), which is a seismically active NS elongated structure that marks the location of the Miocene arc. Another anomaly belt to the west of the Northern Honshu rift is observed in the Ou Backbone, which is another NS elongated seismically active structure located along the current volcanic arc. This anomaly reflects the current magma plumbing system. In an along arc section of the velocity anomaly map (Figure 2.7b), three level of low velocity are recognized (lower, middle and upper crust) and may be reflecting a lower level of partially molten crust, a level of magma reservoirs in the middle crust and the shallow caldera-fill pyroclastic rocks with occasionally central plutonic bodies (Yoshida et al., 2014).

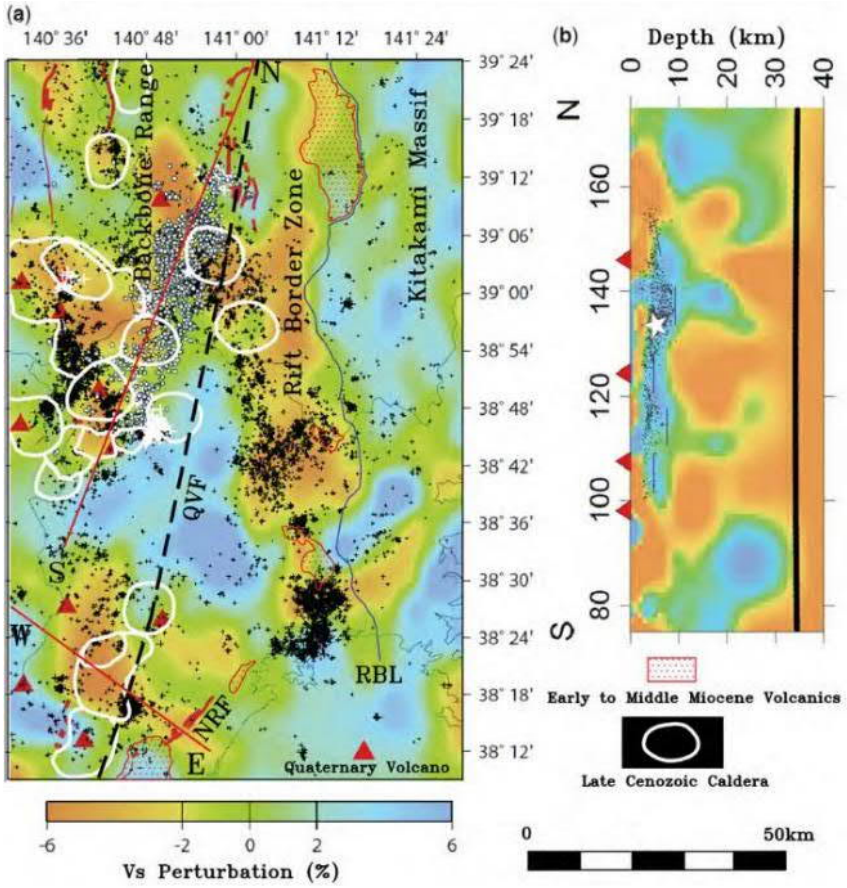

Figure 2.7. (a) Vs tomography map of NE Japan at a depth of 24 km from Yoshida et al. (2014) after Okada et al. (2010). The Vs perturbation (%) scale is shown at the bottom. Epicenter of shallow seismicity (depth of 45 km) is denoted by a small black cross. Triangles and bold red lines denote Quaternary volcanoes and active faults, respectively. The white cross denotes low-frequency micro-earthquakes. White circles denote late Cenozoic calderas (Yoshida et al., 1999a). (b) Vs tomographic vertical cross section of N – S section showed in (a).

2.1.4.2 Mantle and slab structure

Wave velocity tomography of the mantle wedge under the NE Japan arc shows a low-V_p, low-V_s, low-V_p/V_s elongated zone in the middle of the mantle wedge, which is subparallel to the subducted slab (Figure 2.8) (Nakajima et al., 2001; Nakajima et al., 2005; Sato and Hasegawa, 1996). This low velocity zone represents a melt-rich high-temperature zone in the core of the mantle wedge. Where this hot zone reaches the lower crust, a high concentration of low-frequency earthquakes occurs, which is located just below the arc. This suggest a zone of coalescence and migration of the melt from the partially molten mantle (Hasegawa and Nakajima, 2004). The inferred temperature structure of the mantle wedge from wave attenuation tomography shows that the high temperature zone at 40 km

depth corresponds to the distribution of Quaternary volcanoes at the surface (Nakajima and Hasegawa, 2003). Higher temperatures are inferred further south, west of the TTL. This difference indicates a heterogeneity in the mantle that Yoshida et al. (1999b) explained as being produced by the counter-clockwise rotation of the continental hydrous lithosphere during the back-arc opening of the Japan Sea.

The slab shows a relatively high V_p/V_s at *c.* 80 km depth, where it is interpreted that significant dehydration of the slab starts and dehydration is thought to be largely completed at depths of about 70 – 90 km (Tsuji et al., 2008). The released hydrous fluids enter the mantle peridotite producing a layer of serpentinite, which can reach a depth of *c.* 120 – 150 km (Kawakatsu and Watada, 2007).

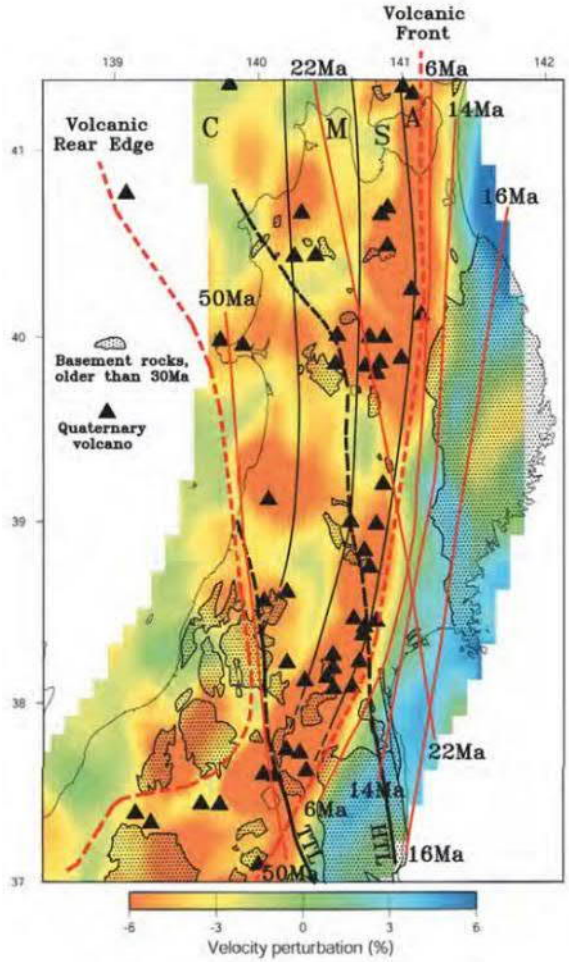

Figure 2.8. Vs tomography map along the inclined low-velocity zone in the mantle wedge of the NE Japan Arc from Yoshida et al. (2014) after Yoshida et al. (2005). Continuous red lines indicate the position of the arc front with time. Dashed red lines indicate the west and east limit of the rear-arc and arc front. Black triangles are the Quaternary volcanoes and black lines indicates the main tectonic structures.

In Figure 2.8 a heterogeneous distribution of low-V anomalies can be distinguished along the arc, with hot asthenospheric zones separated by colder zones. This finger- or branch-like structure was first noted by Tamura et al. (2002). Honda and Yoshida (2005) developed a 3D mantle corner flow model that reproduces this unstable 3D convection structure similar to what is observed in Figure 2.8.

2.1.4.3 Magmatism

Plumbing systems between the upper mantle and the crust appear to be directly connected, evidenced by the correlation between low-Vs anomalies of the mantle wedge and the Quaternary volcanic arc (Figure 2.9) (Chen et al., 2018a; Niu et al., 2018; Zellmer et al., 2019). The mantle velocity anomalies also show a heterogeneous structure of branches or "hot fingers" (Tamura et al., 2002), associated with the location of the volcanic systems in the arc (with some exceptions, e.g., Zao volcano; Zellmer et al., 2019)).

Figure 2.9. Sr and Nd isotopic ratios for the Quaternary volcanic front (QVF) samples classified as I (north), II (central) and III (south) and the rear-arc (QRA) (from Kimura and Yoshida, 2006). The isotopic ratios of the basement granitoids are also shown and a correlation between the volcanic products and their respective basements can be clearly distinguish. BE = bulk earth.

`

The volcanic products from the Quaternary volcanic arc follow the same isotopic trend as the basement granitoids (Figure 2.9), indicating that lower crustal assimilation plays an important role in magma generation in the NE Japan arc, with the northernmost volcanic centers (QFV-I in Figure 2.9) being the least contaminated by crustal melts (<10%, Kimura and Yoshida, 2006).

There is a gradual compositional variation of volcanic products from the arc front to the back-arc, which was first notice by Kuno (1959) in the Japanese Arc system and it has since then been found to be a common feature in arc settings. Increase of K_2O and incompatible elements towards the rear-arc was explained by Kimura and Yoshida (2006) as produced by partial flux melting of a common depleted mantle with different fluxes of slab fluids. Slab flux is higher at the volcanic front and lower in the back-arc, producing larger extents of partial melting beneath the arc front than in the back-arc. Magma segregation depths were estimated to be *c.* 1 GPa for volcanic front magmatism, and *c.* 2 GPa for rear-arc magmatism (from mantle melting models). In contrast to the front-arc magmas, isotopic signatures of the rear-arc volcanic products show little involvement of the crust.

2.1.4.4 Relevant volcanic systems

This study focuses on seven volcanic system along and across the arc-arc collision setting of the northernmost NE Japan arc and the southernmost Kuril arc. From the NE Japan arc there is Akita-Komagatake and Hakkoda volcanic systems in the arc front, and Oshima-Oshima volcano in the back-arc. In the collision zone between the two arcs there is Tokachidake volcano in the arc front. In the Kuril arc there is Akan-fuji and Tya-Tya volcanoes in the arc front, and Rishiri volcano in the back-arc. One basic tephra sample from each volcanic system is studied here, with primary focus on the OHMIs. A brief description of each system is provided here.

a) Akita-Komagatake (AK)

Akita-Komagatake is the southernmost volcano in this study, it is located in the Tohoku region and it belongs to the arc front section of the NE Japan arc. Its activity started at about 74 ± 15 ka (Itaya et al., 1984) and its eruptive history can be divided into three main

stages (Sutō and Ishii, 1987): (1) stratocone formation stage, (2) syn-caldera stage, and (3) post-caldera stage. The compositions of Akita-Komagatake products range from basaltic to andesitic (Fujinawa et al., 2004; Nakagawa, 1985; Sutō and Ishii, 1987; Ueki and Iwamori, 2017). The selected sample (AK) is from the second Hokubu pyroclastic cone deposits, believed to be associated with the *c.* 7 ka "AK-6" tephra layer (Fujinawa et al., 2004; Kuritani et al., 2019; Wachi and Koshiya, 1997), which is the unit with the highest MgO content found in this volcanic system (Fujinawa et al., 2004; Kuritani et al., 2019).

b) Hakkoda (HK)

Hakkoda (or Kita-Hakkoda) is the northernmost volcano from the arc front of the NE Japan volcanic arc and is located south of Mutsu Bay in northern Tohoku. It is part of the Hakkodasan volcanic area that comprises at least 17 stratovolcanoes and lava domes, divided into the Kita-Hakkoda volcanic group (north) and Minami-Hakkoda volcanic group (south). Hakkodasan products range from basalts to dacites (49.4 and 63.2 wt% SiO_2) (Sasaki, 1986; Sasaki, 1987; Sasaki et al., 1985). The current volcanic activity is located into Kita-Hakkoda, which has been active since 0.4 Ma (Kudo et al., 2004; Takarada and Muraoka, 2004). Historic activity of Kita-Hakkoda has only involved seismic swarms (1986) and volcanic gas emanations (1997 and 2010) (Kudo and Hoshizumi, 2006). Past eruptions include five magmatic to phreatic eruptions of Odake volcano from (4.8 ka to 1.5 ka) and three phreatic eruptions of Jigokunuma crater from 0.7 to 0.4 ka. The tephra sample in this study (HK) corresponds to tephra fall from the 2 ka Odake phreatomagmatic eruption HK-2 (Kudo et al., 2003; Kudo et al., 2000; Kudo et al., 2004).

c) Tokachidake (TK)

This volcanic system is the southernmost volcano in the Kuril arc. It is located in the south-westward collision zone of the Kuril forearc sliver over the NE Japan arc forearc, generating a 120 km volcanic gap between the Kuril and NE Japan arcs (Kita et al., 2012). The eruptive history of TK is divided into Older (1.0 to 0.5 Ma), Middle (300 to 70 ka) and Younger (60-50 ka to present) stages (Ishizuka et al., 2010). Tokachi Dake is the central stratovolcano where most of the activity of the Younger stage occurred, starting with andesitic to dacitic products. Later activity was dominated by fall deposits and lava flows, with lesser amounts of pyroclastic flow deposits. Historic eruptions in the 20th

century occurred in 1926, 1962 and 1988-1989. The TK sample from this study belongs to a proximal fall deposit of the 1962 sub-plinian eruption.

d) Akan-fuji (AKN)

Akan-fuji is located in NE Hokkaido in the south Kurile arc front. It is one of the eight small stratovolcanoes that compose Meakandake (Yokoyama et al., 1976), located on the SW flank of the Akan caldera. Activity of Akan-fuji started around 1.0 to 2.5 ka ago, forming basaltic lavas and scoria fall deposits (Wada, 1997; Wada et al., 1998). The AKN sample was collected from fall deposits of the cone.

e) Tya-Tya (TT)

This stratovolcano is located in the north of Kunashir Island, the southernmost Kuril island. Its development can be divided into the construction of an old and a young volcanic edifice (Nakagawa et al., 2002), with the later partially overlying the former. Both volcanic edifices are compositionally distinct, with the old composed of low-K products and the young of medium-K products. The last known activity occurred in 1973 forming two maars in the northern flank of the edifice through phreatic eruptions (Markhinin et al., 1974), followed by the formation of two scoria cones in the southern flank. The largest scoria cone was the last one produced in a sub-plinian eruption, representing the most active period of the 1973 eruptive sequence and within the southern Kuril arc in the 20th century. Whole rock compositions of the young edifice of Tya-Tya range from tholeiitic basalt to dacite (49 to 63 wt% SiO_2) (Nakagawa et al., 2002). Products from the 1973 eruption are crystal-poor, with a narrow compositional range of about 53 to 54 wt% SiO_2 (Nakagawa et al., 2002). The selected sample (TT) was collected from the 1973 eruption scoria fall deposit (locality 6 in Nakagawa et al., 2002).

2.2 MIs

2.2.1 Generation and significance

MIs are small pockets or parcels of silicate melts trapped inside crystals within a magmatic system, during the process of crystal growth (Kent, 2008; Lowenstern, 1995; Wallace, 2005). These small portions of trapped magma represent 'snapshots' of the magma during its evolution (Danyushevsky et al., 2004), making them particularly useful to get information on primitive magma composition and especially volatile compositions (H, C, Cl, S, F), because MIs trapped at high pressures have the potential to preserve the original volatile contents of the melt during entrapment, without releasing them during degassing cause by depressurization during eruption (Kent, 2008).

Olivine is by far the most widely used host mineral phase for MI studies (e.g., Dalou et al., 2014; Hartley et al., 2017; Kamenetsky and Gurenko, 2007; Kamenetsky et al., 2017; Kelley et al., 2010; Le Voyer et al., 2008; Le Voyer et al., 2010; Moore et al., 2018; Portnyagin et al., 2007; Reubi et al., 2013; Rose-Koga et al., 2014; Rose-Koga et al., 2017; Rowe et al., 2009; Straub and Layne, 2003a; Wehrmann et al., 2014b; Weller and Stern, 2018). Olivine is usually the first mineral phase to crystallize from primary basaltic magmas, so the olivine-hosted MIs have the potential to record melt compositions closer to the primary magma. Another advantage of MIs in olivine is that most lithophile trace elements of petrologic interest (except for transition metals such as Ni, Mn, Co, Cr, V) are incompatible in olivine, so post-entrapment recrystallization of olivine from the MI walls (see below) have a small effect on the trace element contents (Kent, 2008) and calculations to correct post-entrapment processes is fairly easy to apply, without the need of re-homogenization. On the other hand, MI H_2O analyses in OHMIs needs to be treated carefully, because they are open to H-loss by diffusion through the crystal host (see below).

Plagioclase-hosted MIs have also been widely used for volatile analysis (e.g., Blundy and Cashman, 2001; Donovan et al., 2018; Johnson et al., 1996; Sours-Page et al., 2002). Plagioclase has the advantage of crystallizing almost throughout the entire crystal fractionation process and the MIs are common in plagioclase phenocrysts. Plagioclase is

`

less reliable for determining MI compositions mainly because formation of MI by resorption-regrowth is a very common process in plagioclase (e.g., sieve and mantled textures). This process produces MIs that are mainly composed of melted plagioclase and do not represent the magma composition at the time of entrapment. Pyroxenes have also been analysed for MIs, but less widely (Ferriss et al., 2016; Kress and Ghiorso, 2004; Reubi et al., 2013; Rowe and Lassiter, 2009; Rowe et al., 2011b)

2.2.2 MI composition correction hosted in olivine crystals

After the entrapment of a OHMI, its composition can be (and usually is) affected by:

(1) Crystallization of olivine at the host-inclusion interface during cooling or decompression of the system. This process is commonly known as post-entrapment crystallization (PEC) of the host mineral.
(2) PEC of other daughter mineral phases from the OHMI volume.
(3) Volatile loss to the shrinkage bubble formed inside the OHMI (e.g., Wallace et al., 2015).
(4) Volatile loss by exsolution and inclusion rupture (decrepitation; e.g., Maclennan, 2017).

Diffusive exchange of elements (re-equilibration) between inclusion and host. These processes are minimized in the case of explosive volcanic products (e.g., tephra) in contrast to effusive products, because their considerably faster cooling hampers recrystallization and diffusion. Nonetheless, diffusion can occur during differentiation and storage.

After entrapment, the cooling of the magma will probably generate crystallization in the MI, reflected as the presence of small crystals inside the inclusion. In addition, pressure cause by magma ascent can cause volatile exsolution, generating gas bubbles inside the MI. These processes are easily identified by microscopy analysis of the inclusion (Figure 1.2 and Figure 2.10).

Crystallization of the host mineral from the MI boundaries is a common process. It is usually identified by rims of different composition at the crystal-melt boundary of the inclusion (usually Fo poorer rims in olivine crystals; Figure 2.10). Two types of corrections can be applied for this case. The first one is to use the same procedure of homogenization by heating, until the re-grown rims are resorbed. The problem with this procedure is that it is hard to assess the temperature required to melt only the re-grown rims; as a result more or less olivine than needed can be melted in the process. The other option is to numerically model the addition of olivine composition to the melt until equilibrium between melt and the host mineral is reached. The latter procedure has been

Figure 2.10. Possible post-entrapment modification processes of MI (from Wallace, 2005).

widely used in OHMIs because the Fe-Mg equilibrium between melt and olivine is well known (e.g. Ford et al., 1983) and, as said above, most trace elements are not affected by olivine crystallization, meaning that the trace element composition is also easily corrected by this method.

The process of diffusive exchange between the MI and host crystal is harder to assess. In the case of OHMIs, the assessment of diffusion of two elements are the most relevant: H^+ and Fe^{2+}. Recent studies have shown that H^+ diffusion is fast, with $D^{H^+}_{[001]} = 10^{-1.4} \exp^{-258/RT}$ (Demouchy and Mackwell, 2006), making it possible to re-equilibrate the water content of a MI with the magma in timescales of days to weeks (Hartley et al., 2015). This means that H_2O concentrations measured in MIs from slowly cooled lava samples will record lower values, due to re-equilibration with the fully degassed host-lava (Hartley et al., 2015), and have no relevance for volatile contents of the source magma. Even MI

`

analyses in quenched tephra samples will probably record the last storage conditions of the magma and not necessarily the conditions during MI trapping. Turner et al. (2017b) showed that water loss in OHMIs is identified when compared with the water contents in clinopyroxene phenocrysts. H^+ diffusion has also been proposed to alter f_{O_2} conditions, oxidizing the inclusion by the excess of O_2 produced due the loss of H^+. Hartley et al. (2017) demonstrated that the effect of f_{O_2} caused by H^+ diffusion is irrelevant, because OHMIs are also open to f_{O_2} re-equilibration with the host magma, and this re-equilibration appears to be even faster than H^+ diffusion. The fast diffusion of H^+ in olivine has important implications for the interpretation of homogenized OHMIs. If H_2O are required, the homogenization procedure must be done as quickly as possible to avoid H^+ loss through diffusion.

Danyushevsky et al. (2000) identified the re-equilibration of the Fe content through diffusive exchange as a common process between the MIs and the olivine host crystals, which they referred to as “Fe-loss”. During cooling, after the formation of an OHMI, new olivine crystallizes from the trapped melt, forming a rim on the walls of the inclusion. This rim is progressively depleted in Mg (or enriched in Fe). The compositional gradient between this rim and the host olivine produces re-equilibration through diffusion of Fe to the host olivine and Mg to the newly formed olivine rims. The re-equilibration between the trapped melt and the re-equilibrated rim produces a rapid loss of Fe in the melt. The Fe-loss process is promoted during slow cooling, as Fe-Mg diffusion progresses faster than crystallization (Figure 2.11). During re-homogenization of the MI, the olivine rims grown during PEC will melt producing a re-homogenized MI depleted in FeO_T. With enough heating time, Fe-Mg diffusion between melt and olivine will increase FeO_T of the MI, approximating the composition of the melt during entrapment. To avoid the complications of the re-homogenization process (e.g., H^+ diffusion, melting of part of host olivine) Danyushevsky et al. (2000) defined a numeric model that simulates the process of Fe regain during re-homogenization. This model is implemented in the software Petrolog3, which can correct the OHMI composition for PEC of olivine rims and for the Fe-loss, given the uncorrected composition of the MI, the Fo content of the host olivine, the initial FeO_T content of the MI during entrapment (see below for how to estimate this variable) and a model of olivine-melt equilibrium (e.g., Ford et al. 1983). The olivine-melt equilibrium model needs to have information about the oxidation state

Figure 2.11. Variation diagram of FeO_T with MgO illustrating the process of Fe-loss (Wallace et al., 2021). The blue line indicates the fractional crystallization path from olivine fractionation. The blue circle indicates the syn-entrapment MI composition. Red circles are example compositions of measured MIs representing different post-entrapment processes suffered by the initial MI composition. Each black line indicates different paths of post-entrapment evolution with different levels of Fe-loss caused by different rates of cooling.

to be able to calculate the content of Fe^{2+} from FeO_T. An alternative way was developed by Danyushevsky et al. (2002b), which consists of modelling the diffusion process by fitting the Fe-Mg compositional profile of the MI.

A way to identify if Fe-loss has occurred in a set of OHMIs is to compare the MI compositions with the whole rock compositions of the same suite. Many studied MIs show major element compositions that fall within the differentiation trend of the whole rock suite, except for FeO_T, which is usually depleted in the MIs, which can be interpreted as evidence of Fe-loss (Figure 2.12a). Another way to visualize this Fe-loss is by plotting FeO_T vs Fo content of the MI and its host olivine, respectively (Figure 2.12b). The whole rock FeO_T content vs Fo in equilibrium with the whole rock composition is also plotted, using an olivine-melt equilibrium model (e.g., Ford et al., 1983). MIs that suffered Fe-

`

Figure 2.12. Example of Fe-loss in OHMIs (from Danyushevsky et al., 2000). (a) FeO_T vs MgO of MIs (circles) and whole rock (crosses). (b) FeO_T vs Fo in olivine of the same MIs and whole rock compositions. All circles below the whole rock trend are interpreted as Fe-loss. In (b), Trend I indicates that MIs in Fo-richer host olivines can suffer larger extents of Fe-loss, and Trend II indicates the process of Fe-loss for each MI.

loss plot below the whole rock trend, and the FeO_T content of the MI without Fe-loss can be estimated from the whole rock composition at a specific Fo value. In some cases, the estimation of FeO_T content during entrapment of the MI is harder, because of the heterogeneity of the whole rock samples, for example in the case of magma mixing.

The Fe-loss process is caused by the re-equilibration effect of the MI with the olivine in its vicinity, but it does not consider the effect of diffusion interaction when the composition of the olivine-host near the MI is affected by the composition of the interstitial melt. Long timescales of diffusion can affect the olivine and MI compositions, rewriting the Fe-Mg distribution and the amount of PEC due by the liquidus temperature change that caused by the changes in Mg# of the melt (Gaetani and Watson, 2000; Gaetani and Watson, 2002).

After the formation of a shrinkage bubble, volatile phases can diffuse from the melt to the bubble exsolving, hence, reducing their concentration in the melt. Studies of shrinkage bubble formation have shown that usually the only relevant volatile phase found in the shrinkage bubble is CO_2 (Hartley et al., 2014; Moore et al., 2015; Moore et al., 2018; Wallace et al., 2015), mainly because it is the first volatile to exsolve from them melt. If CO_2 is required for the study, there are different ways to correct for the initial CO_2

composition. First, the shrinkage bubble can be resorbed into the melt during reheating experiments under high pressure, which may be problematic due to the uncertainties in calculating a proper temperature of homogenization, and the possibility of decrepitation of the shrinkage bubble. The second possibility is to measure the CO_2 content in the bubble and add it to the glass. CO_2 in the shrinkage bubble can be directly measured using micro-Raman spectroscopy or estimated using bubble growth models (e.g., Aster et al., 2016; Fall et al., 2011; Hartley et al., 2014; Moore et al., 2015; Moore et al., 2018; Rasmussen et al., 2020). The main source of uncertainties of this method is the estimation of the bubble and MI volumes, which are needed for the mass balance.

2.3 Thermodynamic tools

In this section a series of examples of available thermodynamic model are described. These models provide quantification of parameters involved in mantle melting of subduction zones (flux melting) and evaluation of saturation pressures and degassing paths from volatile data.

2.3.1 Modeling hydrous melting

2.3.1.1 Overview of the melting models in subduction zones

The identification of a somewhat constant depth for the high seismicity zone below arc front volcanoes (c. 100 km) (Gill, 1981) led to the interpretation that melt production in arc magmatism is controlled by pressure-dependent reactions (Tatsumi, 1986; Tatsumi, 1989; Tatsumi et al., 1986) associated with the solidus temperature of hydrated peridotite. The basaltic slab was thought to be dehydrated at the hornblende breakdown limit (2.0 – 2.5 GPa), with fluids being released to the forearc mantle wedge, forming hydrous minerals at the mantle wedge base (e.g., chlorite, serpentine, amphibole, talc). This hydrated mantle is then dragged down until pressure-dependent mineral breakdown reactions occur near the depth below the arc front, releasing H_2O which generates the

`

volcanic front magmatism. Some of the H_2O in the hydrated mantle was thought to be transported further down in phlogopite, being later released to form the back-arc magmatism. Subsequent experimental and geodynamic studies indicated that the subducted oceanic lithosphere remains hydrous until greater depths (250 km) and is continuously dehydrated beyond the amphibole breakdown reaction (e.g., Poli and Schmidt, 1995; Schmidt and Poli, 1998).

These studies proposed that melts where generated and accumulated above the location of the solidus temperature, increasing in volume and degree of melting as ever more H_2O is added to the source. From the top of the magmatic column, a diapir can begin to rise, passing through the hot core of the mantle wedge and releasing primary melts when the diapir stalls at shallower depth.

An alternative model for hydrous melting of the mantle wedge was later proposed: the hydrous flux-melting model (Gaetani et al., 2003; Grove et al., 2006). The initial high H_2O partial melts produced above the slab percolate through the mantle wedge, which has an inverted geotherm below the central hot zone. The melts progressively react assimilating more peridotite, resulting in decreasing bulk H_2O content. Flux melting models of Grove et al. (2006) assumed that the fluids are sourced from chlorite-bearing peridotite (*c.* 2 wt% H_2O), which produced an H_2O rich melt (*c.* 25 wt% H_2O) after chlorite breakdown at the base of the melting region. As the melt ascends and reacts, progressively increasing T and decreasing P, the H_2O content is reduced to *c*. 4 wt% and the degree of melting increases to 10 – 15 % in the hot core of the mantle wedge. Beyond this point the melt can further react as temperature drops towards lower depths, increasing its H_2O content (Grove et al., 2002), or it may rise as diapirs, reducing reaction with the mantle and allowing for further adiabatic melting.

2.3.1.2 Tracking back primary magma major elements composition from primitive melts

To model the flux melting conditions that generated the studied magmatic rock, the first step is to estimate the primary magma composition, which is the composition of the melt generated from the partial melting of the mantle without subsequent changes due to fractional crystallization and differentiation.

In the case of primitive melt compositions that appear to only have suffered olivine fractionation, the primary magma composition can be estimated by a reverse olivine crystallization calculation until the melt is in equilibrium with mantle olivine. The procedure consists of adding olivine compositions in equilibrium with the melt using an olivine-melt equilibrium model (e.g. Ford et al., 1983) back into the liquid in small steps (usually in increments of 0.1%) until the new liquid is in equilibrium with a olivine composition of Fo_{90} (Kelley et al., 2006; Kelley et al., 2010; Stolper and Newman, 1994). This back calculation can be rapidly applied using Petrolog3 (Danyushevsky and Plechov, 2011), where back calculation scheme and the equilibrium models are already programmed into the software.

This procedure is usually used for primitive glass composition in olivine-hosted MIs. In more differentiated compositions, it is harder to back-calculate the primary magma composition due to the involvement of other mineral phases with more complex equilibrium models (e.g. plagioclase, pyroxene), which involve higher uncertainties.

2.3.1.3 PRIMACALC2 to calculate primary magma compositions

PRIMACALC2 (Kimura and Ariskin, 2014) is an Excel based software for Windows that estimates primary magma basaltic compositions of whole rock or glass compositions. It uses forward calculations fractional crystallization models with COMAGMAT3.72 (Ariskin, 1999; Ariskin and Barmina, 2004; Ariskin et al., 1993), which is applied iteratively to adjust and identify the primary basalt major elements composition, followed by back calculations to obtain the primary trace elements composition. PRIMACALC2 uses 11 major elements (SiO_2, TiO_2, Al_2O_3, FeO, MnO, MgO, CaO, Na_2O, K_2O, P_2O_5 and H_2O) and 26 trace elements (Ni, Rb, Ba, Th, U, Nb, Ta, K, La, Ce, Pb, Pr, Sr, Nd, Sm, Zr, Hf, Eu, Gd, Tb, Dy, Y, Ho, Er, Tm, Yb and Lu).

Major elements, Ni and H_2O are used to calculate the phase equilibria melt/mineral compositions during fractional crystallization using COMAGMAT3.72 to identify the primary basalt. A provisional primary basalt composition is chosen, and the forward crystallization calculations result is compared with the studied sample composition. Then, the primary magma composition is adjusted, and calculations are repeated iteratively until the sample composition is reproduced. Fitting parameters for the fractional crystallization

`

calculations are P, T, f_{O_2} and H_2O. Next, the source mantle conditions in equilibrium with the primary basalt are calculated using petrogenetic grids modified from PRIMELT2 (Herzberg and Asimow, 2008), extending this model to wet conditions using the parametrization of Katz et al. (2003). Finally, back-tracking calculations of trace elements are made, using the mineral/melt partitioning of each trace element following the fractionation sequence calculated in the first step. The model of the NiO content in olivine with the mantle peridotite is used to test the equilibration of the primary basalt with the mantle conditions (Herzberg, 2011; Takahashi, 1986).

2.3.1.4 Batch melting models for hydrous melting parameters

Kelley et al. (2006) compiled global OHMI data from different back-arc basin localities and used major element and volatile measurements to calculate the degree of melting (F) and the water content in the mantle source (H_2O_0). This procedure has been also applied to arc settings, using OHMIs (Kelley et al., 2010) and whole rock and mineral compositions in basaltic rocks (Kuritani and Nakagawa, 2016; Kuritani et al., 2016).

After the calculation of the primary magma composition, following the methodologies stipulated above, the TiO_2 content of a primary magma ($TiO_{2(Fo90)}$) can be used as a proxy for F. Because of its incompatibility during mantle melting, TiO_2 concentrations decrease with increasing F and are independent of the amount of slab-derived component in the mantle (Kelley et al., 2006). The batch melting equation is used to calculate F, with known source TiO_2 content (C_{Ti}^0; commonly depleted MORB for arc and back arc settings) and the bulk distribution coefficient (D_{Ti}):

$$F = \frac{\left(C_{Ti}^0/C_{Ti}^l\right)-D_{Ti}}{(1-D_{Ti})}, \qquad \text{(Eq. 2.1)}$$

where C_{Ti}^l equivalent $TiO_{2(Fo90)}$.

The calculated melt fraction is then used to re-solve the batch melting equation in terms of H_2O:

$$C^0_{H_2O} = C^l_{H_2O}\left[F\left(1 - D_{H_2O}\right) + D_{H_2O}\right], \quad \text{(Eq. 2.2)}$$

where $C^0_{H_2O}$ is the water content in the source mantle, $C^l_{H_2O}$ (equivalent to $H_2O_{(Fo90)}$) is the water content of the primary magma and D_{H_2O} is the bulk distribution coefficient of water during mantle melting.

Melting models can also be applied to trace element compositions of MIs. The addition of slab fluid produced an enrichment of fluid-mobile trace elements (e.g., Ba, Sr), the degree of this enrichment is related to the degree of slab-fluid addition, while immobile trace elements will be related only to the source mantle material (e.g. Nb).

From data measured in OHMIs, Rowe et al. (2009) uses the batch melting model of the trace elements Sr, Ba and Nb in primary magmas (Sr_{90}, Ba_{90}, Nb_{90}) to provide general observations on the mantle source fertility, degree of melting (F) and amount of subduction component (SC) added to the mantle-wedge. Because Rowe et al. (2009) do not have measurements of H_2O, it was not possible to get a direct relation between slab-fluid addition and F (as in Kelley et al., 2006; 2010). They use an isenthalpic model to relate the F calculated from batch melting with the degree of enrichment of the slab liquid (Reiners et al., 2000). Isenthalpic melting produced a decrease of mantle temperature as melting progresses, reducing the efficiency of each melting step. The isenthalpic model is generated from an isothermal model parameterization of Hirschmann et al. (1999):

$$\frac{dF}{dSC} = 3 \times 10^{-6} e^{0.012T}, \quad \text{(Eq. 2.3)}$$

which is combined with the equation that relates the progressive melting with a decrease in temperature:

$$T = T_0 - F\frac{\Delta H_f}{C_p}, \quad \text{(Eq. 2.4)}$$

where the latent heat fusion (ΔH_f) and the heat capacity (C_p) are 753 J/g and 1.3 J/g K, respectively (Hess, 1992; Langmuir et al., 1992) and T_0 is initial peridotite temperature prior to melting. The combination of both equations yields:

$$\frac{dF}{dSC} = 3 \times 10^{-6} e^{0.012\left(T_0 - F\frac{\Delta H_f}{C_p}\right)}, \quad \text{(Eq. 2.5)}$$

`

,

Figure 2.13. Isenthalpic flux melting model of Cascade Volcanic Arc samples. Modified (from Rowe et al., 2009).

This equation is applied iteratively and results are plotted, showing the relationship between the trace element composition of primary magmas and their melting conditions (F, SC and T_0), for particular mantle and slab-fluid compositions and mantle mode (Figure 2.13). It is important to note that the positive correlations between F and SC observed in every studied subduction setting differ from each other (Kelley et al., 2010).

2.3.1.5 Arc Basalt Simulator

The Arc Basalt Simulator version 5 (ABS5; Kimura, 2017) is an Excel-based software to model the genesis of primary arc magmas. It can be used to examine the element mass balance between the slab materials and the flux melting of mantle-wedge peridotite. It uses a forward model approach to assess the mass balance, whereas an inverse approach

allows the estimation of the geophysical variables in arc magma genesis. The mass balance model is applied to 26 incompatible elements (Rb, Ba, Th, U, Nb, Ta, K, La, Ce, Pb, Pr, Sr, Nd, Sm, Zr, Hf, Eu, Gd, Tb, Dy, Y, Ho, Er, Tm, Yb and Lu) and to $^{87}Sr/^{86}Sr$, $^{143}Nd/^{144}Nd$, $^{176}Hf/^{177}Hf$, $^{206}Pb/^{204}Pb$, $^{207}Pb/^{204}Pb$ and $^{208}Pb/^{204}Pb$ isotopic ratios. It has mainly been applied to whole rock compositional data, and it only models the volatile content as pure H_2O. It also takes into account the possibility of slab melting. ABS5 presents a valuable tool to estimate the initial water content when no direct analysis is possible because of the lack of MIs or because MI water contents suggest late-stage water exsolution.

The first available version of this software was the ABS2 (Kimura et al., 2009), which only considered the fluid-flux mantle melting process with an aqueous slab fluid. ABS3 (Kimura et al., 2010) improved the software by adding the slab melting process. ABS4 (Kimura et al., 2014) introduced a simulation of the steep thermal gradient in the slab with a multi-layered slab model, and it also added a chromatographic reaction model between the slab liquid and the slab solids. The improvements of ABS5 over ABS4 are a refined parametrization of mantle melting and an updated user interface.

The intensive geophysical variables that affect primary magma compositions and that can be modelled with ABS5 are:

(1) Slab dehydration depth (P_{ss}): Indicates the depth (pressure) of the slab where the dehydration and slab fluid release take place.

(2) Slab dehydration temperature (T_{ss}): It is the temperature in the surface of the slab at the depth of dehydration. It is one of the primary controls of the composition of slab liquid released at the P_{ss} depth.

(3) Mantle melting pressure (P_{perid}): pressure where mantle flux melting occurs.

(4) Mantle melting temperature (T_{perid}): temperature at the location of mantle flux melting.

ABS5 also calculates extensive geophysical variables affecting primary magma compositions, which are:

`

(1) Amount of liquid added to the mantle ($F_{slab\ liq}$): It can be aqueous fluid, supercritical liquid or melt. It is composed of a mixture of liquids derived from the topmost slab layers: altered oceanic crust (AOC), ocean floor sediments (SED) and mantle wedge peridotite subducted with the slab (MwP) ($F_{slab\ liq} = F_{liq}(AOC) + F_{liq}(SED) + F_{liq}(MwP)$). This variable defines the entire mass balance for the ABS5 model, which is a common parameter between the slab dehydration process and the fluid-flux melting process.

(2) Degree of melting of the mantle (F_{perid}): It is determined by the experimental parametrization of Katz et al. (2003) and it is dependent on T_{perid}, P_{perid} and XH_2O_{perid}.

(3) Amount of water in the slab liquid ($XH_2O_{slab\ liq}$): for an aqueous slab fluid, the $XH_2O_{slab\ liq}$ is 100%. For a slab melt, a mixture between H_2O with a fixed rhyolitic melt composition is selected based on the average of experimental melts of hydrous SED and MORB (Moyen and Stevens, 2006) is used.

(4) Amount of water in the mantle (XH_2O_{perid}): is derived from the $F_{slab\ liq}$ that is added to the mantle and $XH_2O_{slab\ liq}$, which indicates how much water is in the slab fluid/melt.

(5) Amount of water in the magma (XH_2O_{melt}): is the water content of the primary magma generated during the fluid-flux melting of the mantle peridotite.

The modeling is divided into two main processes. First, the slab dehydration or melting process, which controls the composition and amount of the slab liquid. Second, the flux melting of the mantle-wedge, which controls the final composition of the primary magma.

a. Slab dehydration/melting

ABS5 divides the slab model into eight layers, including (in ascending order): slab peridotite from the lithospheric mantle (SlbP); lower gabbro (LGAB); upper gabbro (UGAB); dikes (DIKE); lower unaltered basalt (LBAS); upper altered basalt (UBAS or AOC); ocean-floor sediment (SED) and mantle-wedge peridotite (MwP).

During subduction, dehydration occurs through different metamorphic reactions, affecting each layer in a different way. In this regard, the P-T path of the slab is a fundamental factor that controls the chemistry of slab liquids, because it affects the mineralogical mode of the residual slab (X_a) and the T-dependent partition coefficient (D) of elements between minerals and liquids (Kimura et al., 2014; Kimura et al., 2016). The thermal structure of the slab results in different deflux profiles in each slab layer, where the released liquid from each layer is affected by the layers above, in 1D vertical chromatographic reaction columns in the slab (Gorman et al., 2006; Kimura et al., 2014; Kimura et al., 2016).

ABS5 uses different slab P-T paths derived from the geodynamic model of 56 present-day subduction regions (Syracuse et al., 2010; Van Keken et al., 2011), which are applied to the eight slab layers. For each layer of the slab, the mode (X_a), $F_{slab\ liq}$ and $XH_2O_{slab\ liq}$ are calculated with Perple_X version 7 (Connolly and Kerrick, 1987; Connolly and Petrini, 2002). The source materials are mid-ocean ridge basalt(MORB; Hacker, 2008; Moyen and Stevens, 2006), terrigenous sediment (SED; Hacker, 2008), and depleted MORB source mantle (DMM; Workman and Hart, 2005a), which are assumed to have been fully hydrated at the beginning of subduction (Hacker, 2008). These calculations are only valid for sub-solidus conditions. For the solidus-liquidus interval (slab melting), X_a and $F_{slab\ liq}$ are generated based on experimental results (Hermann and Spandler, 2008; Schmidt et al., 2004). For the element partitioning, the bulk partition coefficient is calculated from the T-dependent partition coefficients for each mineral phase and X_a as follows:

$$C_L = C_S/[D_{bulk} \times F_{slab}(1 - D_{bulk})], \quad \text{(Eq. 2.6)}$$

$$D_{bulk} = \sum[D_a \times X_a], \quad \text{(Eq. 2.7)}$$

where C_L is the fluid and/or melt composition, C_S is the solid composition, D_{bulk} is the bulk partition coefficient, F_{slab} is the degree of dehydration and/or melting, D_a is the partition coefficient of an element in the mineral phase a and X_a is the modal composition of the mineral.

The degree of the chromatographic reaction between the upwelling liquid and the slab layers is simulated by the "reactivity" between the liquids and solids ($\%R_{slab}$; Kimura et al., 2014). Values of $\%R_{slab}$ <100 a reactive porous flow regime, whereas $\%R_{slab}$ >100

`

simulates fracture flow. The role of $\%R_{slab}$ is subordinate in mass balance calculations, but it is effective for the isotope mass balance.

For the case of dehydration of the slab, it is assumed that the aqueous fluid contains various amounts of trace elements within 100 wt% H_2O liquid. For the case of slab melting, a silicic melt with various amounts of trace elements in a rhyolitic melt of SiO_2 = 72.05, TiO_2 =0.41, Al_2O_3 = 16.76, FeO = 2.40, MgO = 0.29, CaO = 1.24, Na_2O = 3.92 and K_2O = 2.87 wt% is used. This composition is obtained from the average experimental melts of hydrous SED and MORB (Moyen and Stevens, 2006) from ABS3 (Kimura et al., 2010).

b. Mantle-wedge flux melting

ABS5 uses an open-system melting equation from Ozawa and Shimizu (1995) for trace element calculations, which requires the degree of melting of the peridotite (F_{perid}), the residual peridotite mineral mode (X_a), partition coefficients (D_a), and an open system melting parameter β defined as:

$$\beta = a/(a + b), \qquad \text{(Eq. 2.8)}$$

where a is the influx fraction from the slab and b is the fraction of partial melt from the mantle. F_{perid} is determined by the experimental parametrization of Katz et al. (2003), which requires T_{perid}, P_{perid} and XH_2O_{perid}.

The pMELTS thermodynamic model (Ghiorso et al., 2002) with Adiabat_1ph frontend version 1.8 (Smith and Asimow, 2005) is used to calculate the residual mode for the PM and DMM compositions (Sun and McDonough, 1989; Workman and Hart, 2005b). A correction for systematic discrepancies in olivine and orthopyroxene modes between pMELTS and experimental results (Lambart et al., 2012) is applied. The partition coefficients for mantle minerals use D_a values for a water-rich mantle, obtained from Green et al. (2000).

2.3.2 Volatile solubility and degassing

An important application of volatile MI analyses is the measurement of volatile saturation pressures and assessment of volatile degassing paths. The main volatile species in magmas, H_2O and CO_2, have solubilities that are dependent on the liquid and vapour phase compositions (and P-T conditions).

2.3.2.1 Solubility models

There are different solubility models that can be applied to assess saturation pressures and degassing paths. Moore et al. (1998) developed the following empirical H_2O solubility model for silicate melts:

$$2 \ln X_{H_2O}^{melt} = \frac{a}{T} + \sum_i b_i X_i \left(\frac{P}{T}\right) + c \ln f_{H_2O}^{fluid} + d, \qquad \text{(Eq. 2.9)}$$

,where $X_{H_2O}^{melt}$ is the mole fraction of H_2O dissolved in the melt, $f_{H_2O}^{fluid}$ is the fugacity of H_2O in the fluid, P is the pressure (bars), T is temperature (Kelvin), X_i is the anhydrous mole fraction of the oxide component (Al_2O_3, FeO_T and Na_2O) and a, b_i, c and d are the fit parameters (a = 2565, $b_{Al_2O_3}$ = – 1.997, b_{FeO_t} = – 0.9273, b_{Na_2O} = 2.736, c = 1.171, d = – 14.21). This model works under conditions of 700 – 1200 ºC and 1 – 3000 bar in any natural silicate liquid. Because this model uses $f_{H_2O}^{fluid}$ as a parameter, it can successfully calculate H_2O solubility in mixed volatile cases.

There are a few models that assess the equilibria of H_2O and CO_2 between silicate liquids and a vapour phase. Usually, silicic melts contain only molecular CO_2, whereas mafic melts only contain carbonate complex CO_3^{2-} (Blank and Brooker, 1994). In intermediate compositions both species usually coexists (Behrens et al., 2004; King et al., 2002). Dixon et al. (1995) generated a model of H_2O + CO_2 equilibria between a silicate melt and a vapor phase, which was updated by Dixon (1997). This model works only for tholeiitic and alkali basalts. VolatileCalc (Newman and Lowenstern, 2002) is an Excel software that applies the models of Dixon (1997) and (Moore et al., 1998) to calculate saturation pressures and model degassing paths under open or close-system conditions.

Papale et al. (2006) developed a non-linear H_2O + CO_2 saturation model in the H_2O – CO_2 – silicate melt system. This model is a recalibration of the previous model of Papale

`

(1999), adding more compositional data to the calibration. The solubility model works for the whole range of natural silicate melt compositions, pressures, and temperatures. Papale et al. (2006) found a strong dependence of the solubility behaviour of both volatile species with the Fe_2O_3/FeO mass ratio of the magma. An online calculator and an Excel spreadsheet can be found on the website: http://melts.ofm-research.org/CORBA_CTserver/Papale/Papale.php.

Ghiorso and Gualda (2015) produced a new solubility model for the H_2O – CO_2 – silicate melt system, which was implemented in the rhyolite-MELTS software (Gualda et al., 2012), but can be independently used to estimate pressure and saturation conditions from MIs. This model works with any natural silicate composition at pressures of <3 GPa. An online calculator is available at the following website: http://melts.ofm-research.org/CORBA_CTserver/GG-H2O-CO2.html.

The semiempirical H_2O – CO_2 solubility model of Iacono-Marziano et al. (2012) identified an important control of the alkali content of the melt in the solubility of CO_2, showing that previous models sub-estimates CO_2 solubility for alkali-rich melts. Duan (2014) developed a general thermodynamically based H_2O – CO_2 solubility model that reproduced the available calibration data with good accuracy (7.2% for H_2O and 9.7% for CO_2 solubilities) for a wide range of melt compositions.

There are other models available that includes the effect of other volatile species. The program SolEx (Witham et al., 2012) models the solubility behaviour of basaltic melts of the C – O – H – S – Cl volatile system. It assumes that the behaviour of the fluid phase is controlled by the volumetrically dominant volatile species, H_2O and CO_2. S and Cl are controlled by their partitioning behaviour between melt and fluid phases (Churakov and Gottschalk, 2003; Jugo et al., 2010; Lesne et al., 2011). The D-compress software (Burgisser et al., 2015) models the volatile solubilities of the C – O – H – S system for three melt compositions (basalt, rhyolite and phonolite) for systems of f_{O_2} > NNO - 3, temperatures of 790 – 1400 °C and pressures < 300 MPa.

2.3.2.2 Degassing paths

Figure 2.14. CO_2 vs H_2O plot, with examples of isobars and isopleths for a rhyolitic melt in equilibrium with H_2O + CO_2 vapor at 800 ºC (modified from Newman and Lowenstern, 2002). Isobars and Isopleths were calculated with the VolatileCalc software.

Once the battery of CO_2 and H_2O data have been obtained from MI analysis, they can be plotted in a CO_2 vs H_2O plot to assess the equilibrium conditions of each volatile composition using the models from the previous section (assuming saturated conditions during entrapment). For a fixed melt composition and temperature, isobars can be constructed and plotted in the CO_2 vs H_2O graph to indicate all volatile compositions that are in equilibrium at a particular pressure (Newman and Lowenstern, 2002). The models can also calculate the vapour composition in equilibrium with the volatile composition of the melt and isopleths of fixed vapour compositions can be constructed (usually in mol% H_2O; Figure 2.14).

The process of degassing can be then analysed by adjusting the degassing models to fit the MI volatile contents. The degassing can be closed-system, when the vapour exsolved maintains equilibrium with the melt during the whole degassing process, or open-system, when the vapour exsolved is immediately extracted from the melt. Figure 2.15 shows different degassing paths modelled for a basalt at 1200°C. Open-system degassing produces a steeper trend than the closed-system case, with higher CO_2 loss before significant H_2O loss occurs. In the closed-system degassing path, higher CO_2 loss is buffered by equilibration with the extracted vapour, which has a high CO_2/H_2O ratio. The figure shows a third case where the initial basalt has already a 2% exsolved vapour, meaning that the vapour buffering effect starts earlier, and the degassing path is even

`

shallower. This last case can also model changes caused by the influx of CO_2-rich vapours from deeper in the system (CO_2 fluxing), which re-equilibrate with the melt and buffer CO_2 degassing, generating a volatile composition in the melt with lower CO_2/H_2O ratios (e.g., Oppenheimer et al., 2011a).

Figure 2.15. CO_2 vs H_2O plot with modelled degassing paths of a basaltic melt at 1200 ºC with initial 4 wt% H_2O, 3000 ppm CO_2 (modified from Newman and Lowenstern, 2002). Models were calculated using the VolatileCalc software.

Chapter 3

Methodology

3.1 Sample selection and preparation

Basic tephra samples of the seven volcanoes of interest were donated from the storage unit of the Earth and Planetary Science Department of Hokkaido University (Sapporo). Additional samples from Rishiri Volcano were collected during fieldwork in during July 2018.

Tephra samples were washed and dried overnight. A few of the largest tephra fragments were selected for polished thin section preparation. Part of the samples were mildly crushed in a tungsten pestle and sieved to separate two size fractions (710-355 μm and 355-250 μm) to pick olivine crystals (Figure 3.1). Olivine crystals were handpicked and

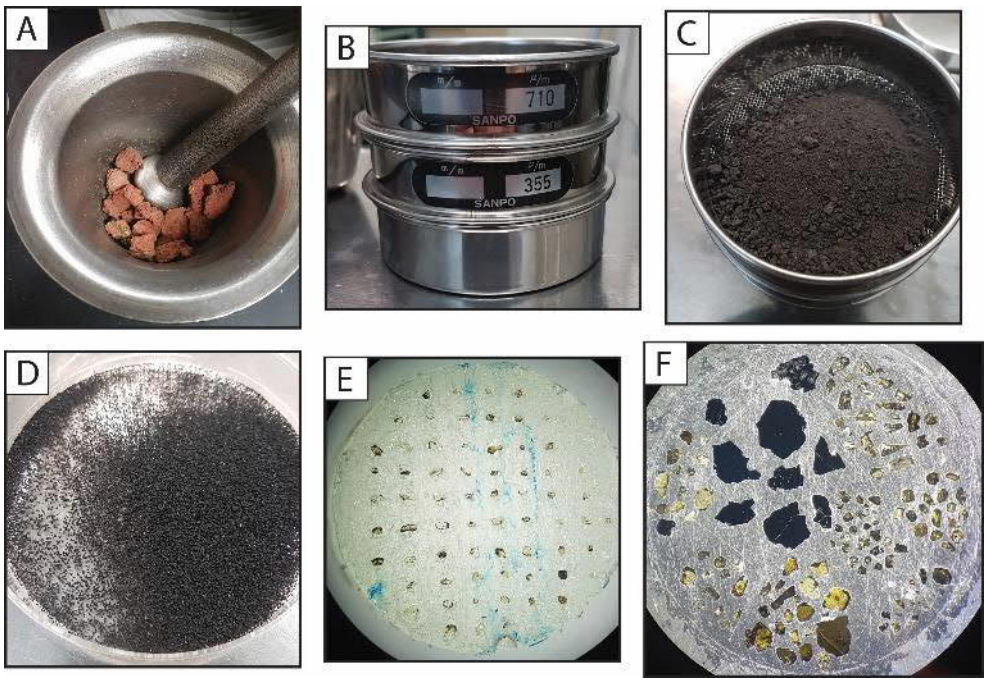

Figure 3.1. Preparation process of exposed olivine-hosted MIs for SIMS and EPMA analysis. (A) Crushing of tephra samples. (B and C) Sieve process. (D) Handpicking of olivines from sieved sample. (E) Epoxy mount of selected olivine crystals with MIs. (F) Final indium mount with exposed MIs and reference glasses.

submerged into water or a high-refractive index immersion liquid (n = 1.6570) to improve visibility of trapped MIs. MI-bearing olivine crystals were then picked and mounted in epoxy and carefully polished on one side, then released from the epoxy with the help of a soldering iron and remounted and polished on the other side to have a clear view of the MI for characterization under the optic microscope (MI are not exposed at this stage). Glassy MI (with or without shrinkage bubbles) with no evidence of the system being opened (cracks, hour-glass shape, decrepitation) were selected for analysis and remounted and polished to expose the glass. The exposed MIs were then remounted in indium. The indium metal is melted and then pressed into a custom-made aluminium disc. Each crystal is carefully pressed into the indium using a hydraulic press. In addition to the exposed MIs, reference glasses for volatile analysis were also polished and pressed into the same indium plug.

3.2 Analytical techniques

The exposed MIs and tin sections of the tephra samples were analysed with different analytical techniques to obtain a battery of textural and geochemical data, which includes whole rock major and trace element compositions of the tephra samples, mineral and glass major element compositions from in-situ geochemical analysis of thin sections and major, trace and volatile compositions of the MIs.

3.2.1 X-ray fluorescence spectrometry

Glass beads were prepared from whole rock powders of each sample to perform X-ray fluorescence spectrometry (XRF) analysis. To prepare the glass beads each sample was first cleaned in ultrasonic bath with distilled water. Samples were then dried in an oven at 100 °C for at least 2 hours or overnight at 45 °C. Samples were then powdered in a tungsten grinding machine and kept in the oven at 100 °C for at least 2 hours. Loss of ignition (LOI) was determining by weighing *c.* 2 g of powder before and after heating in an oven at ca. 900 °C for 3 hours. After heating, *c.* 0.8 g of the powdered sample was

mixed with *c.* 8.0 g of a flux of a lithium metaborate : lithium tetraborate mixture (12 : 22), then fused to produce a glass disc using a XRFuse2 electric fusion apparatus.

Major element concentrations were measured with a 1 kW Bruker Tiger S8 Series II XRF spectrometer at Massey University in Palmerston North, New Zealand. Interference-corrected spectra intensities were converted to oxide concentrations using calibration curves consisting of natural standards closely approximating the mafic matrix of our samples. The long-term reproducibility of Oreas 24c standard reference material is better than ± 1% relative (1σ) for all elements except MnO, for which it is better than ±1.5% relative.

3.2.2 Scanning electron microscope

Backscatter electron (BSE) imaging was used to assess textural features, e.g. formation of daughter crystals in the MI, Fe-rich olivine rims around the MI and Fe-Mg zones of the olivine host. BSE images of the exposed MIs were obtained using the JEOL JSM-7000F Field-Emission scanning electron microscope (FE-SEM) at Hokkaido University, Japan. An acceleration voltage of 15 kV was used, with a beam current of 10 nA.

The FEI Quanta 200 SEM at Massey University (New Zealand) was used to study the textural features of the tephras through BSE imaging of the thin sections. This was done to identify mineral associations, zonation patterns and other disequilibrium features. The BSE images were used to define spots of interest for subsequent microprobe analysis of glass and minerals.

3.2.3 Electron probe microanalyzer

Mineral and glass compositions were analysed with the JXA-8230 SuperProbe electron probe microanalyser (EPMA) at Victoria University, New Zealand. Plagioclase crystals were analysed using a defocused beam of a 10 µm diameter with an accelerating voltage of 15 kV and an electron beam current of 12 nA. Pyroxene crystals were analysed using a focused beam with an accelerating potential of 20 kV and an electron beam current of

30 nA. Counting times were 40 s on peak and 15 s on background for all elements in both mineral phases. Na was analysed first to avoid Na migration.

For olivine crystals, analysis spots were chosen in the vicinity of the MIs to better constrain equilibrium conditions. A focused beam with accelerating potential of 20 kV was used with an electron beam current of 30 nA for Si, Fe, Mg, Mn and Ti, and 100 nA for Al, Ni, Ca and Cr. Counting times were 40 s on peak and 15 s on background for all elements but Ca, with 400 s on peak and 20 s on background. Accuracy and reproducibility of the analyses was constrained by alternating analyses of USNM2566 and JK3 olivine secondary standards with the samples during the session. Concentrations are accurate to <4% for major elements, <35% for Mn, <24% for Ni and <89% for Cr. Accuracy of Ca was <7%. Ti and Al values are usually below the detection limits for both standards. Reproducibility estimates (as 1σ) were <2% for major elements, *c.* 3% for Ni and Ca, *c.* 5% for Mn and *c.* 27% for Cr.

MI and interstitial glass compositions (Si, Ti, Al, Fe, Mn, Mg, Ca, Na, K, and P or Cr) were analysed with an accelerating potential of 15 keV and an electron beam current of 8 nA. A defocused beam of 5 – 10 μm diameter was used and Na was analysed first to avoid Na migration. Basaltic glass secondary standards (VGA99 and BHVO-2G) were analysed periodically throughout the session to test for instrumental drift and to constrain accuracy and reproducibility of the analyses. Reproducibility estimates (1σ) are <1% for SiO_2, Al_2O_3 and CaO, *c.* 2% for FeO and MgO, *c.* 3% for Na_2O and K_2O, *c.* 10% for TiO_2, MnO and P_2O_5. Accuracies are <1% for most SiO_2 and Al_2O_3 secondary standard analyses, <2% for most Al_2O_3, FeO, MgO and CaO analyses, <3% for most K_2O analyses, <10% for most Na_2O and TiO_2 analyses and <20% for most P_2O_5 analyses.

S content for the reference glasses used in the secondary ion mass spectrometry (SIMS) measurements (see below) were measured by repeated high precision analysis with the EPMA. Ten S measurements of each reference glass were performed, where the average result was used as the reference value with the associated standard deviation as the error. Analysis conditions were accelerating voltage of 15 kV, an electron current beam of 8 nA with a 10 μm diameter defocused beam. Primary standard for calibration was the Elba Pyrite. Precision uncertainties (1σ) were <4%, except for the volatile poor glasses (<15

ppm for BIR-1G and BHVO-2G). Accuracy was tested using VG99 and VG2 as secondary standards, showing a relative error of <10% for most analyses.

3.2.4 Secondary ion mass spectrometry

Analysis of volatile contents (H, C, S, Cl and F) of MI glasses were carried out with the Cameca ims-1270 secondary ion mass spectrometer (SIMS) at Hokkaido University, Japan. Exposed MIs were pressed down into an indium plug mounted in an aluminium disk to avoid H and C contamination from epoxy. The plug was then coated with gold and loaded into the SIMS sample chamber to remain under vacuum for three days before analysis to reduce H contamination.

A $^{133}Cs^{+}$ ion primary beam was used to analyse for ^{1}H, ^{12}C, ^{19}F, ^{30}Si, ^{32}S and ^{35}Cl isotopes. Pre-sputtering of a 25×25 µm area was conducted before each analysis with beam current of 1 nA for 100 s, plus a beam centring time of 96 s. Analysis was carried out with a beam current of 0.1 nA over a 3-5 µm wide area of Gaussian shape. Field aperture was set to 2000 µm with an entrance slit of 60 µm, an energy slit of 25 µm, a contrast aperture of 100 µm and an exit slit of 400 µm. Mass resolution was set to 3243 to avoid interference of isotopic signals (mainly $^{34}S^{1}H$ on ^{35}Cl, $^{29}Si^{1}H$ on ^{30}Si, and $^{31}P^{1}H$ on ^{32}S). The isotopes were measured in five consecutive cycles of 10 s of waiting time and 3 s of analysis time for ^{1}H, 4 s waiting time and 5 s analysis time for ^{12}C, and 2 s waiting time and 1 s analysis time for the rest of the isotopes (^{19}F, ^{30}Si, ^{32}S and ^{35}Cl). Including pre-sputtering time, each analysis lasted *c.* 8 min. The reproducibility of counts ratios between each volatile and matrix was obtained from the five cycles per analysis. Maximum uncertainties of reproducibility are <10% for $^{1}H/^{30}Si$, <13% for $^{12}C/^{30}Si$ and <3% for $^{19}F/^{30}Si$, $^{32}S/^{30}Si$ and $^{35}Cl/^{30}Si$.

Reference glasses were polished and mounted in the same indium plug with the MIs and were repeatedly measured during the same analysis session to produce the calibration lines and to check for instrument drift. The reference glasses used were BIR-1G and BHVO-2G synthetic standard glasses (USGS), plus CL DR-1, Gal 1652, LS 427, 2πD43, SAM 76-11, SAM 73-12 and SAM 74-2 natural volcanic glasses (Kendrick et al., 2017). F and Cl values for the synthetic glasses were obtained from Marks et al. (2017) and Kendrick et al. (2018), whereas values for natural samples were obtained from Kendrick

et al. (2017) revised compositions. H_2O and CO_2 compositions for most of the reference materials were measured using a micro-FTIR instrument (see below) and S was remeasured with EPMA (see above).

Calibration of the SIMS analyses was produced using a maximum likelihood linear regression scheme considering the uncertainties related to SIMS analysis precision and

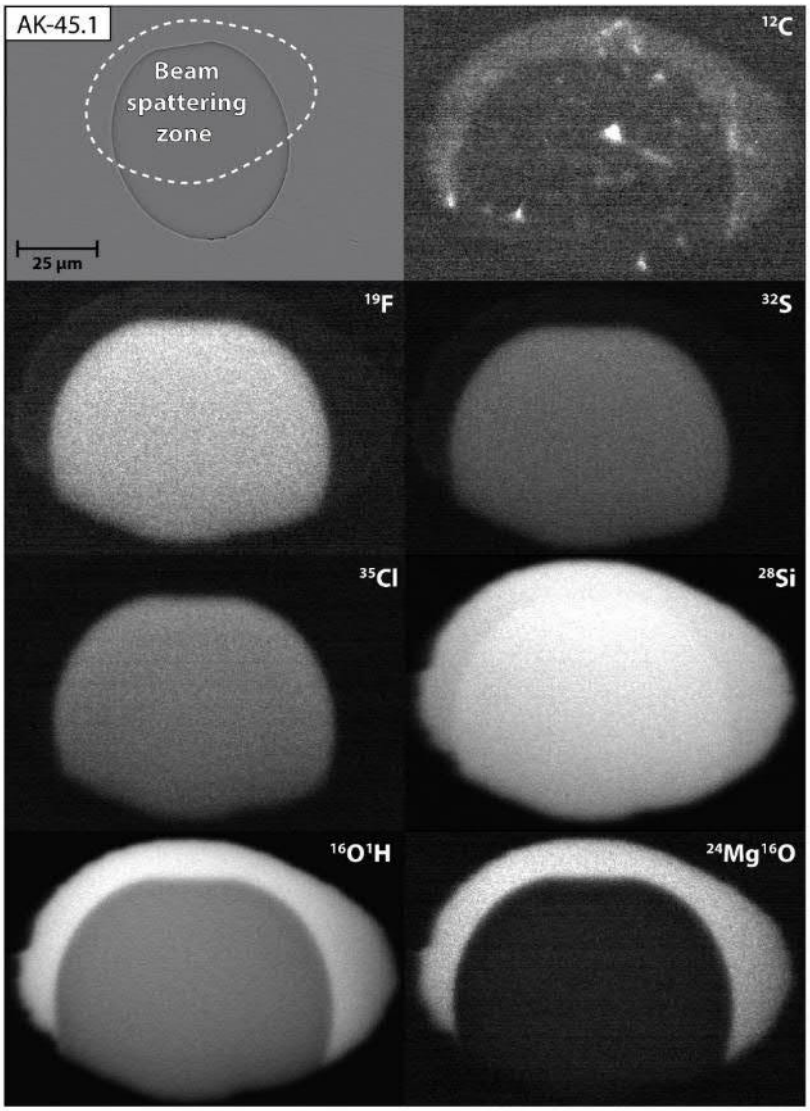

Figure 3.2. Example of BSE image of glassy MI from Akita-Komagatake tephra sample (upper-left image). The other images are isotopographs from SCAPS detector (see below) for the same MI. Bright zones indicate higher secondary ion intensities than dark zones for the same images. Dark signal with bright spots in the ^{12}C image is interpreted as low C contents in the glass, contaminated with C rich epoxy fragments. Lower intensities of $^{16}O^{1}H$ than in the olivine is interpreted as a matrix effect.

uncertainties in the reference values used. After calibration, the uncertainties in accuracy (1σ) for the volatile species in MIs are *c.* 4% for H_2O, <15% for CO_2 (for concentrations above 50 ppm), <8% for most S analyses, *c.* 2% for Cl and <8% for most F analyses.

Homogeneity of volatile distribution of MI glasses was also tested for some MI using the CMOS-type active pixel sensor (SCAPS; Nagashima et al., 2001; Yurimoto et al., 2003) attached to the same SIMS instrument at Hokkaido University. Isotopographs of the olivine-hosted MIs were generated to analyse MI volatile composition and distribution. A ~100 to ~200 pA Cs+ primary beam was used, with a normal incident electron gun to compensate for sample charging. The beam generates an elliptic image of diameters of c. 80 µm and c. 60 µm. The exit slit was narrow enough to eliminate the contribution of interference ions to the isotope images. Isotopograph images of ^{12}C, $^{16}O^{1}H$, ^{19}F, ^{28}Si, ^{32}S, ^{35}Cl and $^{24}Mg^{16}O$ were acquired (Figure 3.2), where a 50-µm contrast aperture was used in order to obtain high lateral spatial resolution. Samples were first exposed to the beam for 50 cycles (each cycle lasts ca. 5 s) to remove the gold coating. Exposure time was 30 cycles for ^{12}C, 20 cycles for ^{19}F, ^{32}S and ^{35}Cl, 5 cycles for ^{28}Si and 1 cycle for $^{16}O^{1}H$ and $^{24}Mg^{16}O$.

3.2.5 Fourier-transform infrared spectroscopy

H_2O and CO_2 compositions for some of the reference glasses were measured using a Nicolet 6700 Fourier-transform infrared (FT-IR) spectrometer attached to a Nicolet Continuµm FT-IR microscope equipped with a KBr beamspitter at Massey University, Palmerston North. Both instruments are attached to a FT-IR purge gas generator (Parker Balstion Model 75-52), which pushes a constant flow of dry air with depleted CO_2 content through the IR beam path, reducing background noise.

Free-standing double polished thin wafers (*c.* 60 to 160 µm thickness) were prepared from the reference glasses and placed on a NaCl disk on the microscope. Six transmission and reflectance spectra with a square beam area of *c.* 50 µm wide were taken for each buffer to test for reproducibility and heterogeneity of the materials. Transmission analysis conditions were 512 scans per analysis and a spectral resolution of 4 cm^{-1}. Reflectance analysis conditions were 128 scans and a resolution of 8 cm^{-1}. Background measurements were taken before each sample analyses, which corresponded to about 1 hr time between

background re-measurements. Reflectance background analysis was done on a gold-coated disk to improve reflectance signal. Total dissolved water (H_2O_T) was measured using the wide absorption peak at wavenumbers of around 3535 cm^{-1} band, whereas CO_2 was measured using the carbonate doublet peak (CO_3^{2-}) at around 1515 cm^{-1} and 1430 cm^{-1}. Baseline definition was performed using OriginLab 2019b. A straight line between both sides of the *c.* 3535 cm^{-1} band peak was defined as baseline for H_2O_T, whereas a curved baseline was constructed for the CO_3^{2-} peak doublet by carefully selecting a few points around the peaks and applying a spline interpolation.

Volatile concentrations were calculated from the absorption peaks using the Beer-Lambert Law(Ihinger et al., 1994):

$$c = \frac{m.w.\times a}{t \times \rho \times \varepsilon} \qquad \text{(Eq. 3.1)}$$

where c is the concentration of the volatile species (wt%), $m.w.$ is the molecular weight of the molecule of interest (g/mol) (H_2O and CO_2), a is the absorption peak (dimensionless), t is the thickness of the glass buffer (m), ρ is the density of the glass (g/m^3) and ε is the absorptivity coefficient of the glass material for the band of interest (L/mol·cm).

The thickness of each analysed point was calculated using the interference fringes of the reflectance spectrum. This method consists of measuring the wavelength of the fringes observed in the reflectance spectrum, which is related to thickness by the following equation:

$$t = \frac{m}{2n(\nu_1 - \nu_2)} \qquad \text{(Eq. 3.2)}$$

where m is the number of waves counted in a section of the reflectance spectrum which shows clear interference fringes (usually between 3000 cm^{-1} and 2000 cm^{-1} bands), $(\nu_1 - \nu_2)$ is the distance between the first and last counted wave (cm^{-1}) and n is the refractive index of the material. In this study, the refractive index of the glass was calculated using the following relationship (Shoji et al., 1993):

$$n = 1.804 - 0.00425 \times SiO_2(wt\%) \quad \text{(Eq. 3.3)}$$

Glass density is iteratively calculated using the density model after Best (2013) at room temperature and atmospheric pressure. Thermodynamic constants where taken from Lange and Carmichael (1990) and Lange (1997), except for H_2O data taken from Ochs III. and Lange (1997). The iteration consisted of choosing an arbitrary initial water content to calculate density, using the density to calculate the water content from the Beer-Lambert equation and then re-calculating the density with the new water content until the water content converges. The absorptivity coefficient for basaltic glasses used were 62.8 ± 0.8 for the 3535 cm^{-1} band (Mercier et al., 2010) and 375 ± 20 for the 1515 cm^{-1} and 1430 cm^{-1} bands (Fine and Stolper, 1985), where the peak value used for CO_2 measurements corresponded to the average of the height of both peaks.

3.2.6 Laser ablation inductively coupled plasma spectrometry

The trace element concentrations of the whole rock glass beads and the MI glasses were measured with a RESOlution-SE Compact 193nm excimer laser ablation system in tandem with an Agilent 8900 Inductively Coupled Plasma – Mass Spectometer (LA ICP-MS) at Waikato University in Hamilton, New Zealand.

After XRF analysis the glass beads were piled up and glued together with epoxy then a slice of the stack was cut, polished and mounted in a glass slide. The same indium mount used for EPMA and SIMS analysis was used for LA ICP-MS analysis. The analysis was conducted by pulsing the laser at 10 Hz with a 100 µm spot size and energy density of 5.0 j/cm^2 with an ablation time of 45 s. Ultra-high purity helium was used as the carrier gas (370 mL/min) to deliver the ablated sample for the LA system to the ICP-MS. The ICP-MS was optimized to maximum sensitivity daily (Table 3.1). Background counts (gas background, measured with the laser off) were collected for 30 s between samples. NIST610 and NIST612 glass standards were analysed after every 10 samples to account for any instrument drift. Analysis conditions for MI glasses were the same as the glass beads, except that the laser size spot varied between 50 to 100 µm depending on the MI

size. Standard glasses were measured with each laser spot size used to be able to obtain the concentrations of trace elements and their precisions at each spot size.

Data processing was performed using Iolite (v3.32, Patton et al., 2011). Background counts were subtracted from the raw data and all data were standardized to the NIST612 glass. NIST610 glass was used as a secondary standard. GeoReM database (Jochum et al., 2005) was utilized for the standard glass values. The whole rock real concentrations where calculated by mass balance calculations using the LA ICP-MS results and the proportion of sample and flux measured when producing the glass beads.

Table 3.1. ICP-MS Operating Conditions

Properties	**Conditions**
Forward (reflected) power (watt)	1550
Gas flows (L/min):	
Plasma	15 (Ar)
Auxiliary	0.90
Carrier (Nebulizer)	1.00
Sampling Depth (mm)	4.0
Detector mode	Pulse counting
Sweep mode	Peak hopping
Dwell time (s)	0.01 - 0.1
Points per peak	1

Chapter 4

MushPEC: Correcting post-entrapment processes affecting MIs hosted in olivine antecrysts

Raimundo Brahm[1], Georg Zellmer[1], Takeshi Kuritani[2], Daniel Coulthard Jr.[1], Mitsuhiro Nakagawa[2], Naoya Sakamoto[3], Hisayoshi Yurimoto[3], Eiichi Sato[4].

[1]School of Agriculture and Environment, Massey University, Palmerston North, New Zealand.

[2]Graduate School of Science, Hokkaido University, Sapporo, Japan.

[3]Isotope Imaging Laboratory, Creative Research Institution, Hokkaido University, Sapporo, Japan.

[4]Hokkaido University of Education, Asahikawa, Japan.

4.1 Abstract

Olivine-hosted melt inclusions (MIs) are widely used as a tool to study the early stages of magmatic evolution. There are a series of processes that affect MI compositions after trapping, including post-entrapment crystallization (PEC) of the host mineral at the MI boundaries, exsolution of volatile phases into a “shrinkage bubble” and diffusive exchange between a MI and its host. Classical correction schemes applied to olivine-hosted MIs include PEC correction through addition of olivine back to the melt until it reaches equilibrium with the host composition and “Fe-loss” correction due to Fe-Mg diffusive exchange. These corrections rely on the assumption that the original host composition is preserved. However, for many volcanic samples the crystal cargo is thought to be antecrystic, and the olivine composition may thus have been completely re-equilibrated during long crystal storage times.

Here, we develop a novel MI correction scheme that is applicable when the original host crystal composition has not been preserved and the initial MI composition variability can be represented by simple fractional crystallization (FC). The new scheme allows correction of MI compositions in antecrystic hosts with long and varied temperature histories. The correction fits a set of MI compositions to modelled liquid lines of descent generated by FC. A MATLAB® script (called MushPEC) iterates FC simulations using the rhyolite-MELTS algorithm.

In addition to obtaining the corrected MI compositions, the application of this methodology provides estimations of magmatic conditions during MI entrapment. A set of MIs hosted in olivine crystals of homogeneous composition (Fo_{77-78}) from a basaltic tephra of Akita-Komagatake volcano was used to test the methodology. The MIs in the tephra sample shows evidence of re-equilibration to a narrow Mg# range equivalent to the carrier melt composition. The correction shows that olivine hosts were stored in the upper crust (*c.* 125 – 150 MPa) at undersaturated H_2O contents of *c.* 1 – 2 wt% H_2O.

4.2 Introduction

Melt inclusions (MIs) have been widely used in the study of magmatic processes, as they can constitute snapshots of primary to pre-eruptive magmatic conditions (Cannatelli et al., 2016; Danyushevsky et al., 2004; Danyushevsky et al., 2002a; Kelley et al., 2006; Kelley et al., 2010; Kent, 2008; e.g., Lowenstern, 1995). MIs have been the focus of many studies due to the belief that their volatiles can be retained in the melt that would otherwise be exsolved and lost from the melt during eruption (Blundy and Cashman, 2001; Blundy et al., 2010; Donovan et al., 2018; Hauri, 2002; e.g., Johnson et al., 1996; Métrich and Wallace, 2008; Reubi and Blundy, 2009; Rose-Koga et al., 2014; Sours-Page et al., 2002; Vigouroux et al., 2012) and that glassy MIs closely represent the melt composition at a particular stage of magmatic evolution, without contamination by the crystal cargo of the magma, which can affect the whole rock composition by phenocryst (± antecryst ± xenocryst) accumulation. Nonetheless, MIs are subjected to a series of post-entrapment processes that affect their compositions, and careful assessment is required to identify and correct for these processes. Olivine-hosted MIs are especially valuable for the study of primary magma compositions. This mineral phase is usually the

first to crystallize from mafic melts, and the post-entrapment processes are well understood. These processes are easy to correct for because of the simplicity of the olivine structure and because relevant diffusion of major elements is reduced to Fe-Mg exchange (Danyushevsky et al., 2000). The use of these MIs for studies of primary magmas has typically been restricted to primitive olivine compositions (Fo >80) where the original olivine composition is thought to be preserved and MI compositions are close to that of the primary magma.

A detailed summary of the post-entrapment processes suffered by MIs can be found in Kent (2008). The processes that can change the compositions of MIs after trapping in olivine crystals can be summarized as:

(1) Crystallization of olivine at the host-inclusion interface during cooling or decompression of the system. This process is commonly known as post-entrapment crystallization (PEC) of the host mineral.
(2) PEC of other daughter mineral phases from the MI volume.
(3) Volatile loss to the shrinkage bubble formed inside the MI (e.g., Wallace et al., 2015).
(4) Volatile loss by exsolution and inclusion rupture (decrepitation; e.g., Maclennan, 2017).
(5) Diffusive exchange of elements (re-equilibration) between inclusion and host.

The focus of this study is glassy MIs, so the formation of daughter minerals is not considered here. It has been demonstrated that the main volatile exsolved to the shrinkage bubble in MIs trapped at elevated pressures is CO_2, and there are methods available to measure or to estimate the CO_2 content of the bubble (e.g., Aster et al., 2016; Fall et al., 2011; Hartley et al., 2014; Moore et al., 2015; Moore et al., 2018). Nonetheless, significant amounts of H_2O (and S) have been detected in MIs trapped at upper crust pressures (e.g., Robidoux et al., 2018). The most important diffusion reactions occurring during olivine re-equilibration are H^+ diffusion between inclusion and magma through the olivine walls (Demouchy and Mackwell, 2006; Roedder, 1979) and the “Fe-loss” process (Danyushevsky et al., 2000), which involves an interplay between PEC and Fe-Mg interdiffusion. High H^+ diffusivity in olivine implies that water can be lost very quickly through diffusion. Usually, the H_2O contents of MIs are expected to be lower than

their initial concentrations, due to outward H^+ diffusion caused by H_2O vapor exsolution during magma ascent (Hartley et al., 2015; Turner et al., 2017b). It has also been shown that H^+ could diffuse into the MI when H_2O is concentrated in the magma (Hartley et al., 2017). Regarding magma H_2O contents, the ability of H^+ to diffuse through olivine means that inferences made from olivine-hosted MI analysis are not straightforward. Compositional changes in the MI due to PEC or diffusive exchange can produce compositional heterogeneities in the MI glass when not enough time is available for melt diffusive re-equilibration (e.g., Danyushevsky et al., 2000; Newcombe et al., 2014). Major and trace element zoning generated by diffusion with the depleted boundary layer in the MI wall is likely to occur during post entrapment processes triggered during ascent and eruption, when there is not enough time for diffusive re-equilibration within the MI.

Here, we consider the processes that change the major element composition of the MI through olivine crystallization and Fe-Mg diffusion. In the rest of the text, PEC will be used to refer only to the post-entrapment crystallization of the host mineral in the MI rims. The classical view on how these processes affect olivine-hosted MI compositions after trapping and how to correct for them are described in detail by Danyushevsky et al. (2000), and the correction calculations can be performed using the software Petrolog (Danyushevsky and Plechov, 2011). During entrapment, the MI composition should be in equilibrium with its host olivine crystal. PEC occurs on the wall of the MI, where the newly formed olivine is progressively more Fe-rich as melt Fe/Mg increases by olivine fractionation. By knowing the host crystal composition and the final melt composition, the original major element composition can be backtracked by stepwise addition of equilibrium olivine to the MI until it reaches equilibrium with the host crystal. Danyushevsky et al. (2000) showed that the PEC corrected MI total FeO (FeO_T) contents for a set of MIs were usually lower than the trend defined by the whole rock data. This is thought to be caused by Fe-Mg diffusion between the host olivine and the newly formed olivine from the PEC. If the rate of PEC is slow enough, the newly formed olivine that is higher in Fe will lose Fe and gain Mg through diffusion with the host olivine and Mg will also diffuse into (and Fe out of) the MIs. This exchange increases the olivine liquidus temperature of the MI, triggering additional olivine crystallization. The process is known as “Fe-loss”, and Danyushevsky et al. (2000) designed a methodology for correcting its effect on the MI composition, which are incorporated in the Petrolog software. If total re-equilibration of the MI with the host has not been achieved, the original MI composition

can be reconstructed from the shape of the diffusion profile of the MI (Danyushevsky et al., 2002b), or in case that no profiles are available or no clear profile is distinguishable in the MI, the original MI composition can be calculated by assigning an estimated original FeO_T content of the MI before PEC and Fe-loss. These methodologies are usually applied assuming that the olivine host composition is preserved and that the corrected MI composition is an estimation of the original composition during entrapment. If the olivine-hosts have been stored in steady state conditions for enough time, its composition and the composition of its hosted MI will have reached an equilibrium composition with the carrier melt. Then, later post-entrapment processes displace the MI from equilibrium during remobilization and eruption, when applying the PEC and Fe-loss corrections, the corrected MI composition would be an estimation of the storage conditions, not necessarily equivalent to the composition at entrapment. This would mainly affect the MgO and FeO estimation of the melt and give erroneous estimations of parental magma compositions

In this paper, we develop a novel approach for PEC and Fe-Mg diffusion correction of olivine-hosted glassy MIs, which can be applied to a genetically related population of MIs that have been entrapped during co-crystallization of other mineral phases (e.g. pyroxene, plagioclase) and that have suffered widespread Fe-Mg diffusive re-equilibration. The methodology relies on fitting the MI trend to fractional crystallization (FC) models iteratively generated using the rhyolite-MELTS algorithm (Asimow and Ghiorso, 1998; Ghiorso and Sack, 1995; Gualda et al., 2012) via the alphaMELTS2 front end (Smith and Asimow, 2005). A MATLAB® script (called MushPEC) was written to automate FC model generation and PEC correction calculations. We then use the MushPEC script to correct a population of olivine-hosted MIs from a volcanic sample derived from the NE Japan arc (Akita-Komagatake volcano) as a worked example.

4.3 Post -entrapment processes for antecrystic olivine-hosts

In many cases it has been proposed that much of the crystal cargo observed in volcanic samples is antecrystic (e.g., Jerram and Martin, 2008; Zellmer et al., 2016; Zellmer et al.,

2014). This means many crystals that are stored at depth in highly crystalline magmatic mushes get remobilized and picked up by newly intruded magma batches, which carry the crystals to the surface. During long residence times at elevated temperatures, olivine crystals and the MIs they host may thus be re-equilibrated to the Fe/Mg ratio of the surrounding interstitial melt, where the "Fe-loss" suffered by the MI is overprinted by total re-equilibration during storage. Gaetani and Watson (2000) have previously discussed the possibility of diffusion re-equilibration affecting FeO and MgO systematics in olivine-hosted MIs subjected to slow cooling rates. Thomson and Maclennan (2013) performed a statistical model of olivine compositions in Icelandic basalts and picrites. They explain the homogeneous olivine populations, which are more magnesian than the ones in equilibrium with their carrier melts, were stored for long times and re-equilibrated in mush piles before being picked-up and erupted. Long storage time of olivine mush piles have also been identified in the Kilauea volcano plumbing system (Wieser et al., 2019).

With remobilization of the stored olivine crystals, a second stage of PEC can occur before eruption. As the original host composition and the "Fe-loss" signal of the MI have been overwritten, any constraints needed to apply the classical correction scheme of Danyushevsky et al. (2000) to recover the original melt compositions at the moment of entrapment are lost. Using this methodology would recover the storage conditions just before ascent and eruption. The processes of PEC and Fe-Mg interdiffusion can be differentiated from each other by studying the MI compositions in mol% instead of wt%. This way, the concentrations of every element but MgO and FeO_T are affected only by olivine fractionation and not by Fe-Mg exchange. The total FeO_T+MgO is also not affected by Fe-Mg exchange or olivine composition.

Figure 4.1 shows an example of the processes that MIs in antecrystic olivine hosts may have suffered and how this affects the FeO_T vs MgO trends in comparison to simple PEC and Fe-loss for quickly extruded phenocrysts. These compositions were generated by modelling the post-entrapment processes on a set of melt compositions produced by a FC model using rhyolite-MELTS. This forward model of post-entrapment processes is based on the calculations of Danyushevsky et al. (2000) and a detailed explanation of these equations are found in Appendix 1. The model is divided into three phases. In phase 1 (P1), PEC and Fe-loss processes occur as MIs are trapped and the magma is slowly

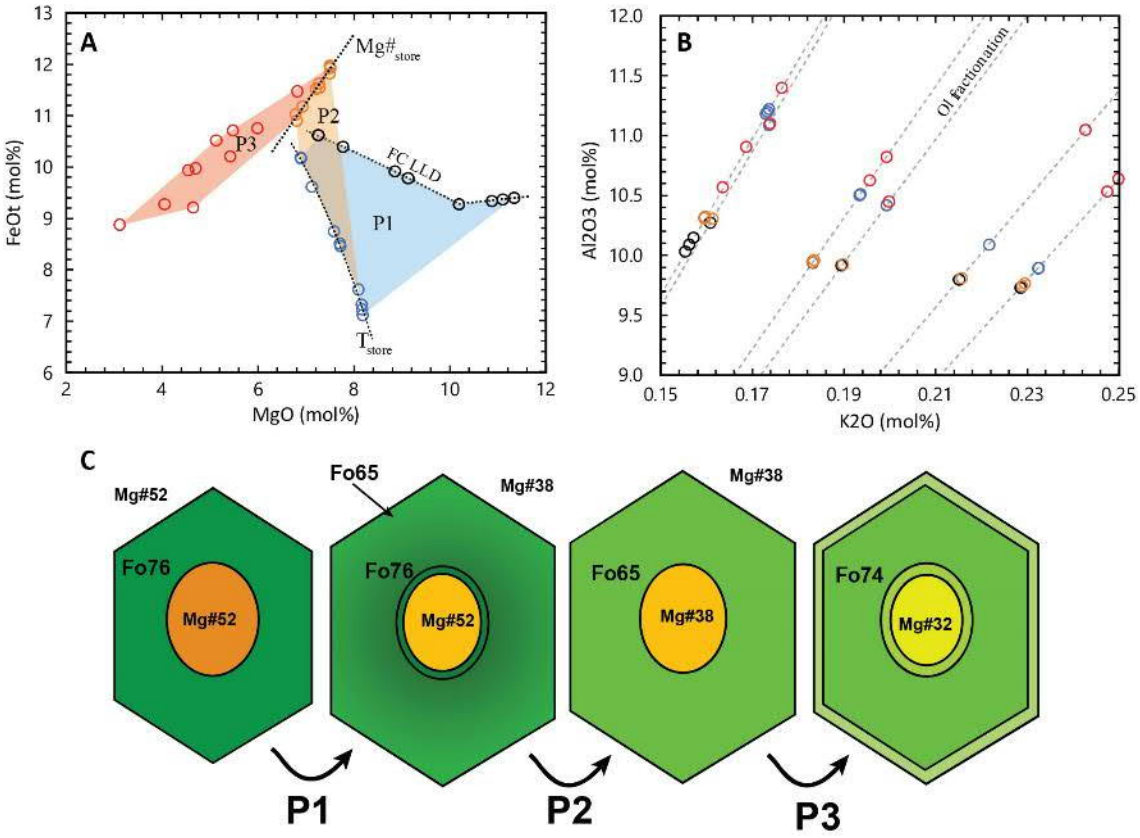

Figure 4.1. Forward model of post-entrapment compositional changes in long stored MIs. (a) MgO vs FeO_T variation diagram for the MIs. Black circles are the original MI compositions trapped during the fractional crystallization differentiation process of a magma batch. Blue circles are the composition of the MIs after P1 (PEC and Fe-loss during slow cooling) at storage temperature, T_{store}. Orange circles are the MI compositions after P2 (re-equilibration to $Mg\#_{store}$) and red circles are the final MI compositions after P3 (PEC and Fe-loss during ascent and eruption). (b) K_2O vs Al_2O_3 variation diagram for the MIs. Grey dashed lines indicate the olivine addition/subtraction trend of the MIs. Symbol colours are the same as (a). (c) Schematic cartoon of the evolution of one of the MIs with each phase of the post-entrapment history.

cooling, and FC is progressing in the melt. As cooling is slow, the Fe-loss process is expected to be near its maximum, maintaining the MI equilibrium with the olivine host composition. P1 is stopped when at a temperature 10 °C below that of entrapment of the most differentiated MI (T_{store} in Figure 4.1A). During phase 2 (P2) the olivine hosts are stored in steady state conditions at constant temperature, T_{store}, and Mg# of the interstitial melt. As Fe-Mg re-equilibration of the olivine reaches MI vicinity, Fe is incorporated into the MI and Mg is lost to the olivine. The Fe increase decreases the liquidus temperature of olivine, triggering melting of olivine in the MI walls. This process continues until the

MI reaches Fe-Mg equilibrium with the new olivine and the interstitial melt compositions. As diffusivities in melts are faster than in olivine, a flat profile of Fe-Mg in olivine cores means that the olivine-hosted MI should have been completely re-equilibrated to the same Fe-Mg conditions during storage. At this stage, all MIs have the same Mg# ($Mg\#_{store}$ in Figure 4.1A). These equilibrium conditions are disrupted during remobilization and eruption, and the final MI MgO/FeO_T ratios are affected by a second stage of post-entrapment processes occurring just before eruption (P3). During P3, variable amounts of PEC and Fe-loss are expected as observed in natural samples. Figure 4.1C shows a schematic illustration of the variation of composition and texture of a single olivine and its hosted MI during these processes. For glassy MIs trapped in olivine antecrysts it can still be assumed that the only processes changing the major element composition of the MI after trapping are olivine subtraction via crystallization (or addition via melting in some particular cases) and Fe-Mg exchange through diffusion from the outside melt, through the crystal and into the MI. This is clearly evidenced by the forward model in Figure 4.1B. All compositional changes suffered by each MI during the modelled post-entrapment processes follow a single path of olivine fractionation and addition, which is observable in variation diagrams (in mol%) of all major elements with the exception of FeO and MgO.

4.4 Geologic background

To develop and test the novel PEC-correction methodology, olivine-hosted MIs collected from Akita-Komagatake (AK) volcano were analysed. AK is an arc-front volcano in the Tohoku region of the NE Japan arc. The volcano is situated on the Okhotsk Plate. To the east, the Pacific Plate is subducted beneath the Okhotsk Plate (7 – 11 cm/yr; Bird, 2003; Northrup et al., 1995), at the Japan trench. Arc volcanism in NE Honshu has been located in the same position since *c.* 5 Ma (Martin, 2011; Yoshida et al., 2014). Caldera-dominated felsic volcanism related to NE – SW oriented compression shifted at *c.* 2 Ma to a stratovolcano-dominated basaltic to andesitic volcanism associated with a change to a current ENE – WSW oriented compression in NE Honshu (Acocella et al., 2008). The activity of AK began *c.* 74 ± 15 ka (Itaya et al., 1984), and its eruptive history can be divided into three main stages (Sutō and Ishii, 1987): (1) stratocone formation stage, (2) syn-caldera stage and (3) post-caldera stage. The compositions of AK products range

from basaltic to andesitic (Fujinawa et al., 2004; Nakagawa, 1985; Sutō and Ishii, 1987; Ueki and Iwamori, 2017).

The AK sample investigated here are fragments of tephra from the second Hokubu pyroclastic cone deposits, believed to be associated with the *c.* 7 ka "AK-6" tephra layer (Fujinawa et al., 2004; Kuritani et al., 2019; Wachi and Koshiya, 1997). This unit has the highest MgO content found in this volcano (*c.* 6.6 wt% MgO; Fujinawa et al., 2004; Kuritani et al., 2019).

4.5 Methods

4.5.1 Analytical methods

4.5.1.1 Whole rock major element composition

A glass bead was prepared from whole rock powder of the sample to perform the XRF analysis. The sample was first cleaned in an ultrasonic bath with distilled water and dried in an oven at 100 °C for at least 2 hours. The sample was then powdered in a tungsten grinding machine and kept in the oven at 100 °C for at least 2 hours. Loss on ignition (LOI) was determined by weighing *c.* 2 g of powder before and after heating in an oven at *c.* 900 °C for 3 hours. After heating, *c.* 0.8 g of the powdered sample was mixed with *c.* 8.0 g of lithium metaborate : lithium tetraborate (12 : 22) flux mixture, followed by fusion to produce a glass disc using a XRFuse2 electric fusion apparatus.

Major element concentrations were measured with a 1 kW Bruker Tiger S8 Series II XRF spectrometer at Massey University in Palmerston North, New Zealand. Interference-corrected spectra intensities were converted to oxide concentrations using calibration curves consisting of natural standards, closely approximating the mafic matrix of our samples. The long-term reproducibility of Oreas 24c standard reference material is better than ± 1% relative (1σ) for all elements except MnO, for which it is better than ± 1.5% relative.

4.5.1.2 Mineral and MI glass major element compositions

BSE imaging was used to assess textural features, e.g. formation of daughter crystals in the MIs, Fe-rich olivine rims around the MIs and Fe-Mg zoning in the olivine host. BSE images of the exposed MIs were obtained using the JEOL JSM-7000F Field-Emission scanning electron microscope (FE-SEM) at Hokkaido University, Japan. An acceleration voltage of 15 kV was used, with a beam current of 10 nA.

Mineral compositions were analysed with the JXA-8230 SuperProbe Electron Probe Microanalyser (EPMA) at Victoria University, New Zealand. Plagioclase crystals were analysed using a defocused beam of a 10 µm diameter with an acceleration voltage of 15 kV and a beam current of 12 nA. Pyroxene crystals were analysed using a focused beam with an acceleration potential of 20 kV and a beam current of 30 nA. Counting times were 40 s on peak and 15 s on background for all elements in both mineral phases. Na was analysed first to avoid Na migration. Precision and accuracy evaluation for these two mineral phases can be found in the Appendix 3.

For olivine crystals, analysis spots were chosen in the vicinity of the MIs to better constrain equilibrium conditions even though most olivine crystals showed homogeneous cores with narrow rims of higher Fe content in the BSE images. A focused beam with an acceleration voltage of 20 kV was used with a beam current of 30 nA for Si, Fe, Mg, Mn and Ti, and 100 nA for Al, Ni, Ca and Cr. Counting times were 40 s on peak and 15 s on background for all elements except Ca, with 400 s on peak and 20 s on background. Accuracy and reproducibility of the analyses was constrained by alternating analyses of USNM2566 and JK3 olivine secondary standards during the session. Concentrations are accurate to <4% for major elements, <35% for Mn, <24% for Ni and <89% for Cr. Accuracy of Ca was usually <4% with a couple of analyses with *c.* 7%. Ti and Al values are usually below the detection limits for both standards. Reproducibility estimates (as 1σ) were <2% for major elements, *c.* 3% for Ni and Ca, *c.* 5% for Mn and *c.* 27% for Cr.

MI and interstitial glass compositions (Si, Ti, Al, Fe, Mn, Mg, Ca, Na, K, and P or Cr) were analysed with an accelerating voltage of 15 keV and a beam current of 8 nA. A defocused beam of 5 – 10 µm diameter was used and Na was analysed first to avoid Na migration. Basaltic glass secondary standards (VGA99 and BHVO-2G) were analysed

periodically throughout the session to test for instrumental drift and to constrain accuracy and reproducibility of the analyses. Reproducibility estimates (1σ) are <1% for SiO_2, Al_2O_3 and CaO, *c.* 2% for FeO and MgO, *c.* 3% for Na_2O and K_2O, *c.* 10% for TiO_2, MnO and P_2O_5. Accuracies are <1% for most SiO_2 and Al_2O_3 secondary standard analyses, <2% for most Al_2O_3, FeO, MgO and CaO analyses, <3% for most K_2O analyses, <10% for most Na_2O and TiO_2 analyses and <20% for most P_2O_5 analyses.

4.5.2 Development of the MushPEC algorithm

In the following sections, a group of MIs from a sample thought to be genetically related will be referred to as a MI set. The original (corrected) MI compositions within a set are expected to follow the same liquid line of decent (LLD) representative of the melt differentiation path.

The new PEC correction scheme relies on fitting the compositions of a MI set to LLDs generated by crystallization models. The script allows for the selection of fractional crystallization (FC) or equilibrium crystallization (EC) models. In this study we applied the FC model as it better represents the fractionation behaviour of plagioclase, which is the main phase being crystallized during the magmatic differentiation of the studied sample (see below). This is due to the coupled NaSi – CaAl substitution, which hampers diffusive re-equilibration of plagioclase composition. However, we note that the effect of choosing EC instead of FC modeling on the resulting LLD compositions is very small for the level of differentiation along the tested differentiation trend.

Iterative FC simulations are modelled using the alphaMELTS2 front end (Smith and Asimow, 2005), which implements the rhyolite-MELTS algorithm version 1.2.0 (Asimow and Ghiorso, 1998; Ghiorso and Sack, 1995; Gualda et al., 2012). For each simulation, the MI compositions are adjusted by olivine addition in an attempt to get their composition as close as possible to the LLD of the FC model. The corrected MI compositions for each simulation are then compared and the best fit solutions are identified. This methodology has the advantage of not only providing corrected MI compositions, but also an estimation of the conditions of the fractional crystallization process (P, T, f_{O_2}, H_2O, and crystallizing phase assemblage) during their entrapment.

To automate the alphaMELTS2 runs and the output analysis, a MATLAB® script called MushPEC was developed. The methodology typically involves the production of a few thousand FC simulations, which can be time consuming. The script includes the application of machine learning techniques to reduce the number of FC iterations needed by running FC models in cycles to make predictions of how the system behaves.

In Appendix 1, the rhyolite-MELTS model is compared to crystallization experiments of a low-alkali tholeiitic basalt of similar composition to the MIs analysed in this study (Takagi et al., 2005). This comparison shows that the rhyolite-MELTS model is remarkably accurate in reproducing the cotectic crystallization behaviour of hydrous tholeiitic basalts at upper to middle crustal pressures.

4.5.2.1 Selection of initial parameters

Modified compositions of the most primitive MI in a set are selected as starting compositions for the FC simulations. The most primitive composition corresponds to the MI for which the olivine fractionation trend is located the furthest to the left in a variation diagram with SiO_2 or K_2O on the abscissa. This MI has suffered the same post-entrapment processes as the rest of the MIs in the set, and for each iteration its composition is modified to simulate different degrees of PEC and Fe-Mg redistribution suffered by the initial MI. All FC simulations are derived using a 5-dimensional grid of initial parameter combinations. Three of the parameters are related to the initial composition of the most primitive MI. The first parameter is the olivine addition (in mol%) to the initial MI, within a range of estimated amounts of PEC suffered by this MI. The second parameter corresponds to a value within an estimated range of the MgO/FeO_T ratio of the initial MI, prior to PEC and Fe-Mg diffusion processes. The last compositional parameter is the H_2O content of the initial MI composition. H_2O concentration in the melt has a major effect on the crystallization path of the melt, especially on the liquidus temperature and composition of plagioclase, as evidenced in the Appendix 1. As explained above, MIs are susceptible to important changes of H_2O concentrations (exsolution and diffusive exchange), making concentrations measured in the MI unreliable as a record of magmatic H_2O contents. To make the initial H_2O parameter independent of the olivine addition and initial MgO/FeO_T parameters, the H_2O concentration is set in mol% to the uncorrected MI composition. This way, the initial H_2O parameter is comparable between models of

different degrees of PEC and Fe-Mg diffusion of the initial MI. The other two parameters are pressure (P) and oxygen fugacity (f_{O_2}). The FC simulations are run at isobaric conditions. The f_{O_2} conditions are set as $\Delta \log(f_{O_2})$ to a chosen oxygen buffer (e.g. QFM, NNO).

4.5.2.2 FC model evaluation

After each FC model run, the output is used to calculate a best fit PEC correction solution for the MI set. This is done by finding the amount of olivine addition/subtraction required to bring each MI composition as close as possible to the modelled LLD (i.e. find the minimum compositional distance between the FC trend and the olivine addition trend for each MI in the set).

The definition of the Aitchison distance (Aitchison, 1986) is used for a D-dimensional compositional space or simplex (S^D) to quantify the similarity of two compositions. This definition of compositional distance complies with the properties of scale invariance, perturbation invariance, permutation invariance and sub-compositional dominance. The Aitchison distance is defined as:

$$\mathrm{d}_A(x,y) = \sqrt{\sum_{i=1}^{D}\left(\ln\frac{x_i}{\mathrm{g}(x)} - \ln\frac{y_i}{\mathrm{g}(y)}\right)^2} = \mathrm{d}_E\big(\mathrm{clr}(x), \mathrm{clr}(y)\big), \qquad \text{(Eq. 4.1)}$$

where $\mathrm{d}_A(x,y)$ is the Aitchison distance between compositions x and y, D is the number of components or dimensions of S^D, $\mathrm{g}(x)$ is the geometric mean of x defined as $(\prod_{i=1}^{D} x_i)^{1/D}$, d_E is the Euclidean distance in the D-dimensional real space ($\mathbb{R}^D$) and $\mathrm{clr}(x)$ is the centered log-ratio transformation of x (Aitchison, 1986), defined as:

$$\mathrm{clr}(x) = \left[\ln\frac{x_1}{\mathrm{g}(x)}, \ldots, \ln\frac{x_D}{\mathrm{g}(x)}\right], \qquad \text{(Eq. 4.2)}$$

The clr transformation converts a composition from S^D geometry to one that is represented in $\mathbb{R}^D$. (Eq. **2.1** states that the Aitchison distance between two compositions in S^D is equivalent to the Euclidian distance of their clr transformations in $\mathbb{R}^D$.

To find the minimum distance between the two compositional trends, the sub-composition defined by the SiO_2, Al_2O_3, CaO, K_2O and (FeO_T+MgO) components

measured in mol% units is used. As explained earlier, the changes of FeO_T and MgO contents of the MIs due to Fe-Mg exchange are not yet constrained, but it is known that the sum of both oxides is only dependent on the amount of PEC. The term PEC is used here to define total olivine crystallization/melting that occurs due to post-entrapment processes, including extra amounts due to liquidus temperature changes triggered by Fe-Mg exchange. These major elements are selected as they (with the exception of K_2O) are the stochiometric components of the mineral phases crystallized from basaltic melts and their compositions are better modelled with rhyolite-MELTS. K_2O is chosen as its high incompatibility makes its concentration representative of the mass subtraction during the FC process. MnO and P_2O_5 are minor oxides and not used in the calculation because of their scattered behaviour and because of the limitations of modelling their partitioning behaviour with rhyolite-MELTS. TiO_2 is not used to avoid uncertainties associated with TiO_2 incorporation in pyroxenes and the crystallization of Fe-Ti oxides by rhyolite-MELTS. Also, Na_2O is omitted because of analysis errors due to possible Na_2O migration during EPMA glass analysis and uncertainties generated by Na_2O incorporation in pyroxene in rhyolite-MELTS models.

The minimum Aitchison distance from the FC trend to the olivine trend provides the amount of PEC needed by each MI in the set to reproduce the particular FC trend as closely as possible in subcompositional space. The combination of the minimum distances for all the MIs in the set can be used as a goodness of fit measurement to compare how well each trend generated from the FC simulations explains the MI set compositions. The root of the average squared Aitchison distance is taken as measurement of "goodness of fit", GoF:

$$\mathrm{GoF} = \sqrt{\frac{1}{n}\mathrm{SSE}} = \sqrt{\frac{1}{n}\sum_{i=1}^{n} \mathrm{d}_A{}^2(x_i, y_i)}, \qquad \text{(Eq. 4.3)}$$

Here, n is the number of fitted MI compositions, which is the number of MIs in the set minus one (the starting composition for the models). SSE stands for "sum of square errors", which is the parameter to be minimized during linear regression calculations for compositional data (Pawlowsky-Glahn et al., 2015). SSE is equivalent to the sum of the square Aitchison distances of each composition to the trend. x_i is the PEC-corrected composition of the i^{th} MI and y_i is the closest composition of the FC trend to x_i. The

SSE parameter divided by the number of corrected MI is used, to make the goodness of fit of different MI sets with different number of MIs comparable.

Figure 4.2 illustrates an example of the process of PEC correction for the AK MI set to a particular FC model. The 5-dimensional sub-compositions are represented with four variation diagrams of the main four components against K_2O. The diagrams show the raw and corrected compositions of each MI connected through the olivine addition trends. The position of the corrected composition for each MI correspond to the closest point of the olivine addition trend to the FC model trend in 5-dimensional space.

MushPEC automatically identifies initially water-saturated models and for models with the same combination of initial parameters besides H_2O content, identifies the first time that initial water-saturation is reached and its solubility. All consecutive models with the same combination of parameters and water contents higher than the melt solubility are discarded to avoid redundancies. After correction, each model output is evaluated with a series of filters, to discriminate the possible solutions from discarded models. The first filter excludes all FC simulations that do not crystallize any olivine during fractionation. The second filter excludes models that need amounts of post-entrapment melting (PEM) during correction that are higher than a limit defined by the user. PEM is represented by negative values of PEC in the output. A third filter excludes model trends that evolve outside the area defined by the 2σ limits of the linear regression of the MI set trend in a CaO/K_2O vs Al_2O_3/K_2O variation diagram, in which the differentiation trend observed is not affected by olivine fractionation (see below). A fourth filter exclude models that start crystallizing plagioclase or pyroxene at the beginning of the model in absence of olivine. Models that are equivalent after reaching the cotectic crystallization, for example of olivine + plagioclase can be reproduced by different initial compositions that starts from a plagioclase-only or olivine-only crystallization, but it is known that for natural basalts in arc systems, olivine is the first phase to crystallize. Only models that pass all these filters are taken as possible solutions.

Finally, the complete composition of the corrected MI is obtained by adding the corresponding mol% of olivine to the original MI composition and then adjusting the MgO and FeO_T content by getting the MgO/FeO_T from the closest point of the FC model LLD to the corrected MI composition. Olivine composition is taken as an ideal Fe-Mg solid solution, not including any minor or trace elements (e.g. Ca, Mn).

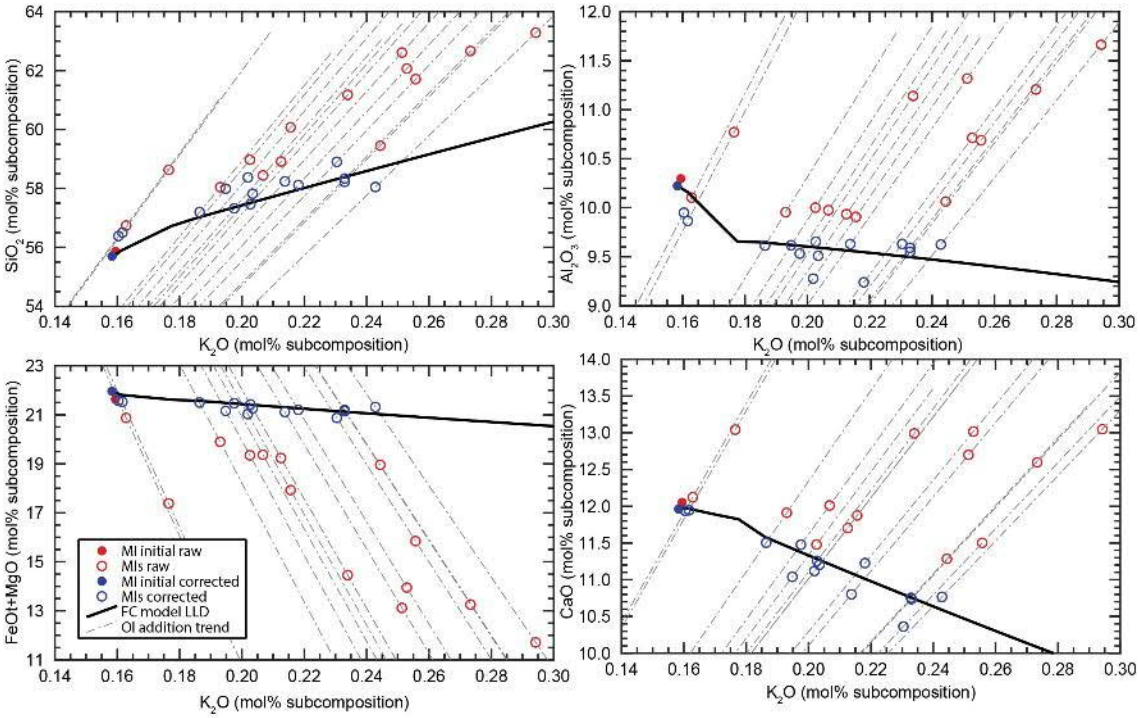

Figure 4.2. Variation diagrams (in mol%) as an example of potential PEC correction for one FC simulation. Components are re-normalized to the sub-composition defined by SiO_2, Al_2O_3, FeO_T+MgO, CaO and K_2O. Blue circles represent the raw MI compositions, and red circles are the PEC corrected MI compositions. Filled circles indicate the composition of the MI used as initial composition of the FC model. Dashed grey lines indicates the trend of olivine addition-subtraction, and the black line is the LLD of one of the FC simulations generated in the rhyolite-MELTS iterations. The corrected compositions correspond to the closest point of each olivine addition trend to the FC model LLD, which is measured as the smallest Aitchison distance between the two compositional trends.

4.5.2.3 Machine learning algorithms

Machine Learning algorithms were implemented in MushPEC in order to optimize the number and density of FC simulations. To apply these algorithms, the models are run in grouped iterations or grids of initial parameters to make predictions after each group. First, minimum and maximum values for each of the five parameters (olivine addition,

MgO/FeO_T initial ratio, f_{O_2}, pressure and initial H_2O content) are assigned. The first grid is generated by assigning a node in the middle between the maximum and minimum nodes. The consecutive grids are generated by assigning nodes between the nodes of the previous grid until no more nodes can be added without making the distance between nodes smaller than the minimum step assigned. The last grid is generated by using the closest value to the minimum steps chosen that can evenly distribute the nodes in the grid. The f_{O_2} parameter nodes are assigned differently, using the same number of nodes in each grid.

Each FC model has two values that indicate its probability of being a possible positive result: (1) binary output of success or failing in passing the three filters described in the previous section and (2) the GoF value calculated from the distances of the corrected MIs to the FC model. These results are used as the response of the models during the training stage of the machine learning algorithms to predict the results of the next iteration of models.

First, the logistic regression method is employed. A logistic regression uses a logistic function to model a binary dependent variable. Figure 4.3A illustrates how a logistic regression fits the logistic function for the simple case of one independent variable (input parameter) with a binary dependent variable (0 or 1). Using the first grid as the training set, where the five initial parameters are taken as the input parameters and the binary output of the filters is used as the response (true or false). To avoid most of the false negatives, the cut-off or limit of the logistic regression for positive predictions (the model is predicted to pass all filters) is set to a probability of 5%.

In a second step, the models of the first grid that pass all filters are selected to train a regression tree model. A regression tree is trained to predict the behaviour of a system that contains a single numerical output variable (response) and multiple numerical or categorical input variables (predictors). The construction of a regression tree uses a binary recursive partitioning method applied to a training data set. The training data set is split into branches until the last partition reaches a minimum size defined by the user or when the sum of squared deviations from the mean is zero. The last branches with no partitions are known as nodes or leaves. The leaf size is the number of elements in the training set that belong to the particular leaf. Figure 4.3B illustrates a simple example of a regression

tree. In MushPEC, the GoF values for the previous iterations are used as the response or output variable, with the aim to predict the GoF values of the next iteration. As with the logistic regression, the five input parameters are used as the input variables to train the regression tree. A fine tree is used, with a minimum leaf size of 4. There are no overfitting issues with the application of the regression tree algorithm for this particular use as the compared outputs are all generated by the same modelling algorithm (rhyolite-MELTS).

After both machine learning models are trained, the second grid is evaluated with both models to predict models that pass the filters and have low GoF values. Only the models that are predicted to pass the filters and that are predicted to have GoF values between a percentage of the lowest values of the grid are run. After each grid is completed, the

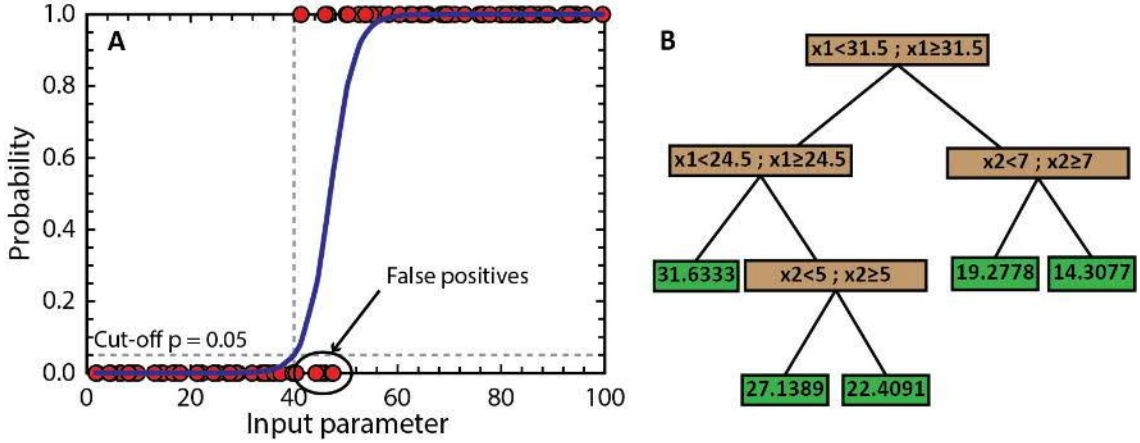

Figure 4.3. Schematic examples of the machine learning methods used in MushPEC. (a) Logistic regression of a simple one variable system. Filled red circles correspond to the observations used as training set. Blue line is the logistic function modelled to explain the data. The cut-off probability is set to 0.05 to minimize false negatives, which in turn maximizes false positives. (b) Example of regression tree modified from MathWorks documentation from a system with 2 variables (x1 and x2). Brown boxes correspond to the branches that define the partitioning conditions, and the green boxes correspond to the leaves or nodes that assign the response value.

percentage of lowest GoF values is reduced as models converge towards the best solutions. After the second iteration the logistic regression and the regression tree models are updated by adding the new results. The models from the second grid that did not pass the predictions in the previous iterations are re-evaluated with the updated models and models that are now predicted to pass the filters are run. This process is repeated until no more models of the second grid are predicted to pass the filters. The process is repeated for each grid until the final grid is completely evaluated. The first grids, which have less nodes and wider steps, have a higher probability to define models far away from the

solution, which may cause a low number of models pass the filters , producing few to no models predicted by the machine learning algorithms. To avoid this, the filter evaluation is deactivated when more than 95% of the run models of a grid fail the filtering process.

4.5.2.4 Testing MushPEC in a synthetic MI set

Before using the MushPEC algorithm on a natural MI set, the method was tested on the modelled MI set of Figure 4.3. The resulting MI compositions after phase P3 were loaded into the MushPEC script to test if the methodology could successfully recover the original compositions of the MI set under ideal conditions (i.e. it was known that the MI set represented a perfect FC LLD reproducible with rhyolite-MELTS, and there was no scatter in the compositional data). The initial compositions of the MIs and the conditions of the FC model are listed in Table 4.1. A first run was tested using a wide grid of initial parameters (0 to 8 mol% olivine addition, 0.8 to 1.6 MgO/FeO_T ratio, 0 to 400 MPa, -2 to 2 ΔQFM and 2 to 10 mol% H_2O). A second finer grid was run around the conditions that showed the best fits (2 to 4 mol% olivine addition, 0.9 to 1.22 MgO/FeO_T, QFM to QFM -2, 50 to 250 MPa and 5.4 to 8.6 mol% H_2O).

Figure 4.4A and B show how the minimum GoF behaviour as a function of P and H_2O and as a function of olivine addition and MgO/FeO_T ratio and Figure 4.4C shows the LLD and corrected MI compositions for the best 10 fit models. The results show that MushPEC can accurately find the FC models that fit best the corrected MI data. Convergence of P, H_2O and f_{O_2}conditions is clear and agrees with the values used to generate the MI set (200 MPa and 6.8 mol% H_2O at QFM -1), but there are a few issues in finding the proper initial composition of the trend. MIs trapped when olivine was the only phase being fractionated cannot be corrected to the exact initial composition as they LLD is parallel to the olivine addition trend. However, as usually the aim is to be able to correct the MIs to the parental magma composition, this can still be easily done by olivine addition from any point in this section of the LLD. A second issue is that even though the minimum GoF is found on the proper FC model from which the synthetic MI set was generated, similar GoF values are found for other models. In Figure 4.4B the convergence towards a particular combination of olivine addition and MgO/FeO_T is less strong. A wave-shaped

surface for QFM -1 indicates that good fits can be found at very different MgO/FeO_T ratios. Thus, it may be difficult to discriminate the proper MgO/FeO_T values for a natural MI set, when scatter of data can obscure the proper minimum. External information on the initial MgO/FeO_T conditions of the magma will likely be required to properly estimate

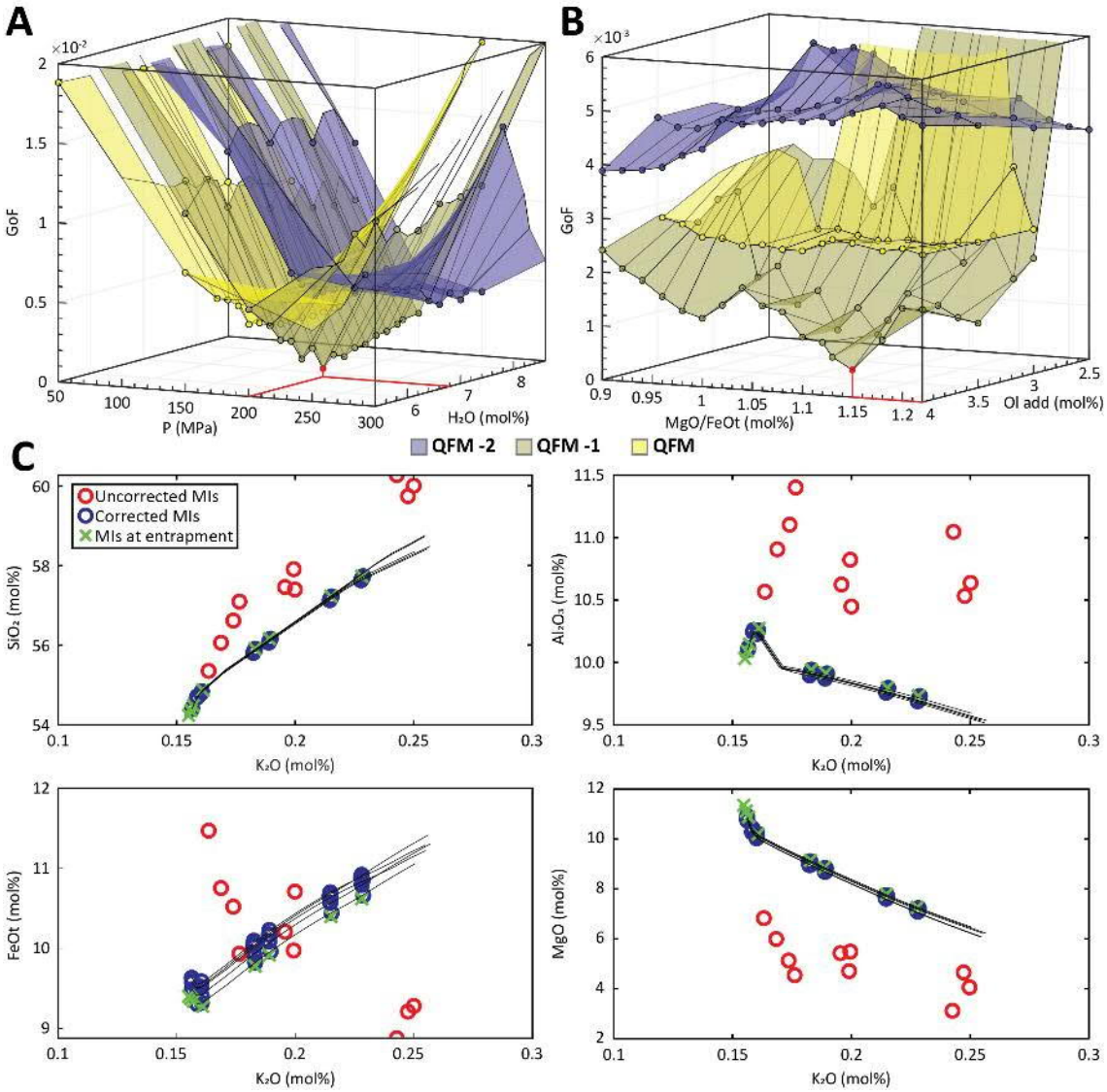

Figure 4.4. MushPEC output of the test on the synthetic MI set of Figure 4.1 of the main text. (a) Minimum GoF behaviour with changes in P and H_2O content. Each coloured surface corresponds to a f_{O_2} condition as indicated in the figure. Minimum GoF is marked in red and it is found at 200 MPa and 6.8 H2O in the QFM -1 surface. (b) Minimum GoF behavior with changes in olivine addition and MgO/FeO_T ratio. Minimum GoF is marked in red and it is found at 4 mol% olivine addition and 1.15 MgO/FeO_T in the QFM -1 surface. (c) Variation diagrams of the 10 best fit models found. Red circles are the uncorrected MIs loaded into the MushPEC script, and blue circles are the corrected compositions for each of the 10 bet fit models. Black lines are the LLD's of the best fit FC models and the green crosses are the original MI compositions before modification by the forward post-entrapment model

the initial compositions of the MI set, whereas convergence of P, H_2O and f_{O_2} conditions of the MI set can be readily identified.

Table 4.1. Initial composition (wt%) and conditions of the FC rhyolite-MELTS model used as test for the MushPEC algorithm.

Initial composition				Initial conditions	
SiO_2	50.43	**MgO**	8.27	**P (MPa)**	200
TiO_2	0.826	**CaO**	9.92	**f_{O_2} (ΔQFM)**	-1
Al_2O_3	15.42	**Na_2O**	2.11	**Initial H_2O (mol%)**	6.8
FeO	10.81	**K_2O**	0.221		
MnO	0.140	**P_2O_5**	0.096		

4.6 Results

4.6.1 AK sample petrography and geochemistry

The tephra sample has a vesicularity of *c.* 52 vol% (Figure 4.5A and B). The rest of the sample is constituted of *c.* 75 vol% groundmass and *c.* 25 vol% crystals. Plagioclase is the most abundant mineral phase (*c.* 87 vol% of crystals), followed by olivine (*c.* 12 vol%) and scarce clinopyroxene. Plagioclase compositions are within $An_{69\text{-}92}$, olivine compositions have a very narrow range of $Fo_{77\text{-}79}$ and clinopyroxene compositions are $En_{51\text{-}55}Fe_{10\text{-}14}Wo_{32\text{-}39}$ (detailed results of the mineral chemistry can be found in the Appendix 3). The groundmass is glass-rich with microlites of plagioclase, olivine, less pyroxene. Groundmass glass analyses show compositions of similar degree of differentiation (SiO_2 and K_2O concentrations) than some of the analysed olivine-hosted

and the plagioclase-hosted MIs. However, FeO_T contents of the groundmass glass are higher.

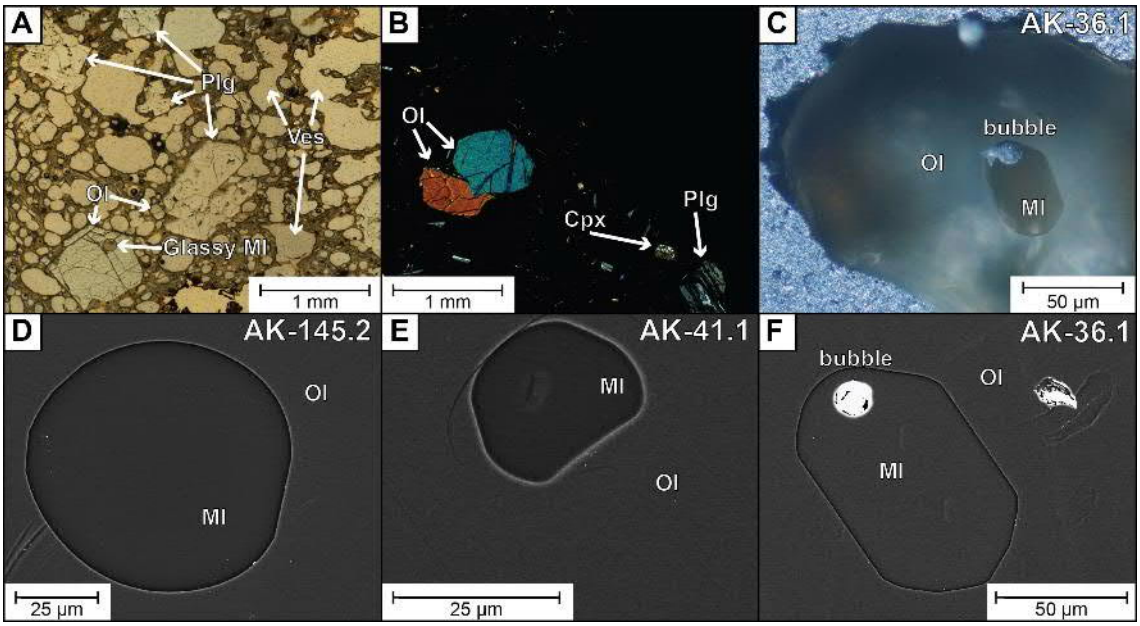

Figure 4.5. Photographs of the AK sample. (A) Thin section parallel polarized light microphotograph. (B) Thin section cross-polarized light microphotograph. (C) Oblique light microphotograph of olivine-hosted MI. (D) to (G) BSE images of olivine-hosted MIs. (C) and (G) correspond to the MI used as initial composition during modelling, and (D) and (F) are MIs with evidences of low and high PEC, respectively (see text). Plg = plagioclase, Ol = olivine, Cpx = clinopyroxene, MI = MI, Ves = vesicle.

Olivine crystals are euhedral to subhedral, with unzoned cores and narrow Fe-rich rims likely generated during ascent and eruption. Olivine-hosted MIs are glassy, some with shrinkage bubbles that comprise < 6 vol% of the MI (Figure 4.5C to F). MI diameters range from *c.* 15 to 150 µm. Some plagioclase-hosted MIs were also analysed from the thin section of sample AK, hosted in plagioclases of An_{80-90} (see Appendix 3). Olivine-hosted MI, sample whole rock and estimated melt fraction compositions are shown in Table 4.2 in wt%, whereas the compositions are plotted in mol% in the variation diagrams of Figure 4.6. The composition of the melt fraction of the sample was estimated by subtracting the composition of the crystal cargo from the whole rock composition, using the measured volume abundances and average compositions and densities of the mineral phases.

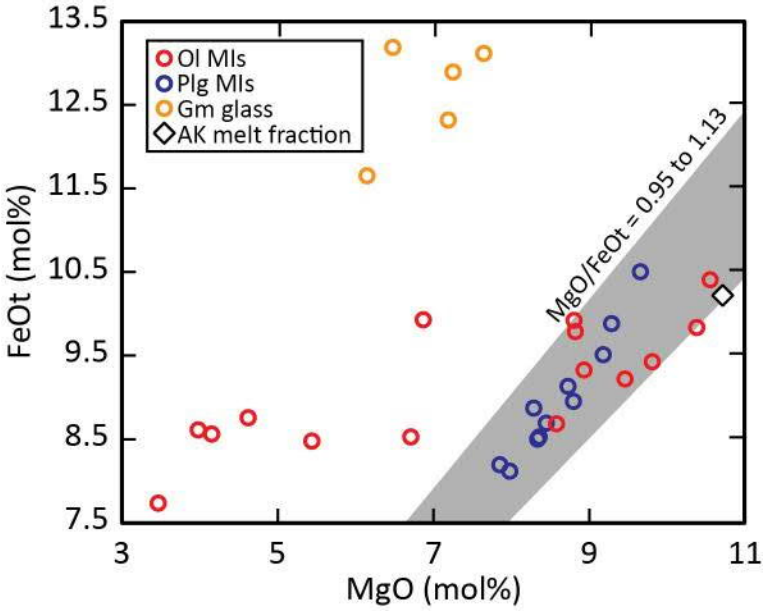

Figure 4.6. MgO vs FeO_T variation diagram of all glass analyses of the AK sample. The red circles are the uncorrected olivine-hosted MIs, the blue circles are the plagioclase-hosted MIs, the yellow circles are the groundmass glass analyses and the less PEC affected olivine-hosted MIs, the plagioclase-hosted MIs and the estimated AK melt fraction composition follows a path of narrow MgO/FeO_T ratios between 0.95 and 1.13, marked by the grey area.

4.6.2 Application of MushPEC to the AK sample

4.6.2.1 Pre-assessment of the MI set

We used the AK MI set to test MushPEC, but first the set needed to be evaluated to identify the antecrystic origin of the hosts. The main geochemical evidence for the antecrystic nature of these host olivine crystals and their re-equilibration of Fe-Mg is:

(1) All MIs in the set are more differentiated than the estimated melt fraction of the whole rock sample (higher SiO_2 and K_2O contents; Figure 4.7A). In addition, even though the melt fraction composition is similar to the most primitive MIs, the lower CaO contents of the melt fraction indicates that this melt is not equivalent to the one that produced the MIs.

(2) All olivine crystals have flat zonation patterns, and their compositions fall between a narrow range ($Fo_{77.4-78.5}$), whereas the silica range of their hosted MIs is wide (51.5-56.1 wt% SiO_2).

(3) TiO_2 increase and FeO_T decrease with differentiation in the MIs (Figure 4.7D and E). The TiO_2 trend indicates absence of Fe-Ti oxides fractionation. For a basaltic melt that does not fractionate Fe-Ti oxides, FeO_T is expected to increase with fractionation of an olivine + pyroxene + plagioclase assemblage. As this is accompanied by MgO decrease, re-equilibration to a fixed Fe/Mg ratio will produce a decreasing trend of FeO_T without affecting TiO_2.

(4) Half of the MI compositions have FeO_T concentrations higher than the whole rock tephra sample. The classical model of trapping followed by quick transport and eruption of MIs should only produce a decrease in FeO_T concentrations, resulting in a MI trend of depleted FeO_T compared to the whole rock trend.

(5) Plagioclase-hosted MIs form a clear trend in the MgO vs FeO_T variation diagram (Figure 4.6) with narrow MgO/FeO_T range, which overlaps the MgO/FeO_T ratios of the olivine-hosted MIs less affected by PEC and the estimated AK melt fraction composition. Fe and Mg diffusion in plagioclase have been shown to be fast enough to affect MI compositions (Costa et al., 2003; Drignon et al., 2019), and as MgO/FeO_T ratios in the plagioclase MIs are not affected by PEC, plagioclase-hosted MIs should preserve their MgO/FeO_T ratios during storage. This suggests that olivine- and plagioclase-hosted MIs were re-equilibrated to a constant MgO/FeO_T ratio with interstitial melt, comparable in composition to the estimated melt composition of the AK sample, prior to ascent and eruption. The groundmass glass composition has a similar degree of differentiation indicated by its SiO_2 and K_2O contents, and most major element contents overlap with the olivine-hosted MI compositions with the exception of FeO_T. The groundmass glass is enriched in FeO for MgO concentrations similar to those in the olivine-hosted MIs indicating a crystallization path consistent with the absence of Fe-Ti oxides and the presence of FeO-rich olivine rims. In Figure 4.7, the effects of PEC on some of the MIs that displace them from the differentiation trend of the melt can be identified. Black lines with circles in the variation diagrams indicate the compositional change produced by olivine addition (in mol%) to one of the MIs. As stated above, this trend is independent of olivine composition for all components except for MgO, FeO_T and MgO/FeO_T (Figure 4.7E, F and H).

Table 4.2. Uncorrected MI major element compositions from EPMA and major element whole rock compositions from the AK sample in wt%. AK melt fraction was calculated with mass balance, using the mineral compositions and abundances measured in the thin section. Forsterite composition of olivine-hosts calculated from the EPMA olivine analyses. MI and bubble sizes were estimated by using the measured diameters.

Ol MIs	SiO_2	TiO_2	Al_2O_3	FeO_T	MnO	MgO	CaO	Na_2O	K_2O	P_2O_5	Total	Fo host	Size (mm^3)	Bubble (vol%)
AK-36.1	50.29	0.843	15.73	11.56	0.144	6.57	10.13	2.15	0.225	0.098	97.74	78.3	8.6×10^{-4}	3.9
AK-153	51.44	0.971	15.50	11.05	0.179	6.30	10.07	1.86	0.205	0.133	97.71	78.5	2.8×10^{-3}	b.f.
AK-43.1	51.71	0.960	16.12	10.82	0.172	4.20	10.74	2.17	0.244	0.158	97.30	77.4	6.3×10^{-3}	2.4
AK-47.1	51.99	0.960	15.13	10.44	0.151	6.09	9.96	2.26	0.271	0.091	97.35	77.8	9.2×10^{-4}	3.6
AK_144	52.12	0.929	15.10	10.93	0.168	5.45	10.00	2.23	0.289	0.105	97.32	77.5	2.0×10^{-4}	b.f.
AK_149	52.17	1.026	14.93	10.70	0.221	5.42	9.67	2.02	0.295	0.124	96.58	77.5	1.4×10^{-4}	b.f.
AK-38.1	52.75	0.941	15.18	10.21	0.153	5.88	9.59	2.36	0.284	0.135	97.48	78.1	9.4×10^{-3}	b.f.
AK-135	52.98	1.086	14.83	9.50	0.191	5.27	9.77	2.42	0.298	0.152	96.49	78.0	3.4×10^{-4}	b.f.
AK-42.1	53.24	1.096	15.29	10.36	0.139	5.57	9.43	2.46	0.343	0.190	98.12	77.8	9.6×10^{-4}	b.f.
AK-39.1	54.18	1.168	15.87	9.52	0.123	2.82	10.61	2.72	0.346	0.178	97.54	77.7	5.9×10^{-4}	n.m.
AK-151	54.35	1.078	15.98	9.33	0.189	4.12	9.46	2.54	0.353	0.144	97.53	77.9	-	-
AK-43-53	54.56	1.117	16.56	9.29	0.136	2.53	10.24	2.74	0.373	0.188	97.72	77.4	9.9×10^{-5}	b.f.
AK-41.1	54.68	1.077	16.78	9.36	0.102	2.43	10.35	2.76	0.344	0.123	98.00	77.4	4.8×10^{-5}	b.f.
AK-143	55.16	1.302	17.25	8.42	0.162	2.12	10.62	2.81	0.402	0.148	98.39	78.0	5.4×10^{-5}	5.6
AK_137b	54.90	1.171	16.97	9.44	0.136	3.40	10.88	2.51	0.329	0.121	99.85	77.4	5.1×10^{-6}	b.f.

Whole rock	SiO_2	TiO_2	Al_2O_3	FeO_T	MnO	MgO	CaO	Na_2O	K_2O	P_2O_5	LOI	Total
AK	50.05	0.81	18.70	9.63	0.18	6.60	10.40	1.86	0.20	0.10	1.64	101.24
AK melt	52.37	1.08	16.26	11.58	0.22	6.81	9.25	2.03	0.26	0.13		100

To show the approximate behaviour of olivine addition for those two components and their ratios, the trend was calculated using a Mg olivine-host composition of Fo_{78}. Al_2O_3 and CaO variation diagrams show that higher PEC results in higher concentrations of these incompatible components in the MI. The MI set can be divided in two groups of high- and low-PEC on basis of their Al_2O_3 and CaO concentrations. This separation is also consistent with the MgO + FeO_T plot (Figure 4.7G) and the SEM images of the MIs (Figure 4.5) where low Al_2O_3 MIs have less bright olivine rims indicative of low PEC. The division of both groups is less clear in the SiO_2, TiO_2 and Na_2O diagrams (the latter not shown), as the olivine fractionation trends in these diagrams are less oblique relative to the MI set (subparallel for TiO_2).

The trend followed by the low-PEC group might approximate the original differentiation trend of the magma batch before PEC effects if the PEC of those MIs are negligible, but it may also be affected by different degrees of PEC within the low-PEC group generating a "pseudo-LLD". A way to study the LLD of the MI set without the effect of PEC (olivine fractionation) is by analysing trends of ratios of components that are conservative during olivine fractionation against a conservative element for the whole system. Figure 4.7I shows CaO/K_2O plotted against Al_2O_3/K_2O. Here, the trends are not affected by olivine (and orthopyroxene) fractionation, but are affected by plagioclase, clinopyroxene and spinel. From the TiO_2 variation diagram it is clear that spinel is not part of the crystallization assemblage for the MI set considered, so it can safely be assumed that the trend is caused by the combination of plagioclase and clinopyroxene fractionation. The TiO_2 trend break indicative of the start of Fe-Ti oxide fractionation occurs around 0.3 K_2O wt% in the whole rock data which is at more evolved compositions than the MI set (Figure 4.7D). Arrows in Figure 4.7I indicate the approximate direction of evolution during fractionation of these phases, which are shifted slightly with anorthite composition (for high An contents expected in basaltic magmas) and Ca and Al contents in clinopyroxene. From this plot, it can be hypothesized that the trend formed by the four most primitive MIs indicate that plagioclase starts crystallizing before clinopyroxene. As the correction scheme relies on fitting a differentiation trend and not just one MI composition, it is crucial to select a MI set where the MIs can successfully represent the LLD of the melt they were formed in. Extensive PEC and Fe-Mg diffusion can obscure a clear LLD for the MI set.

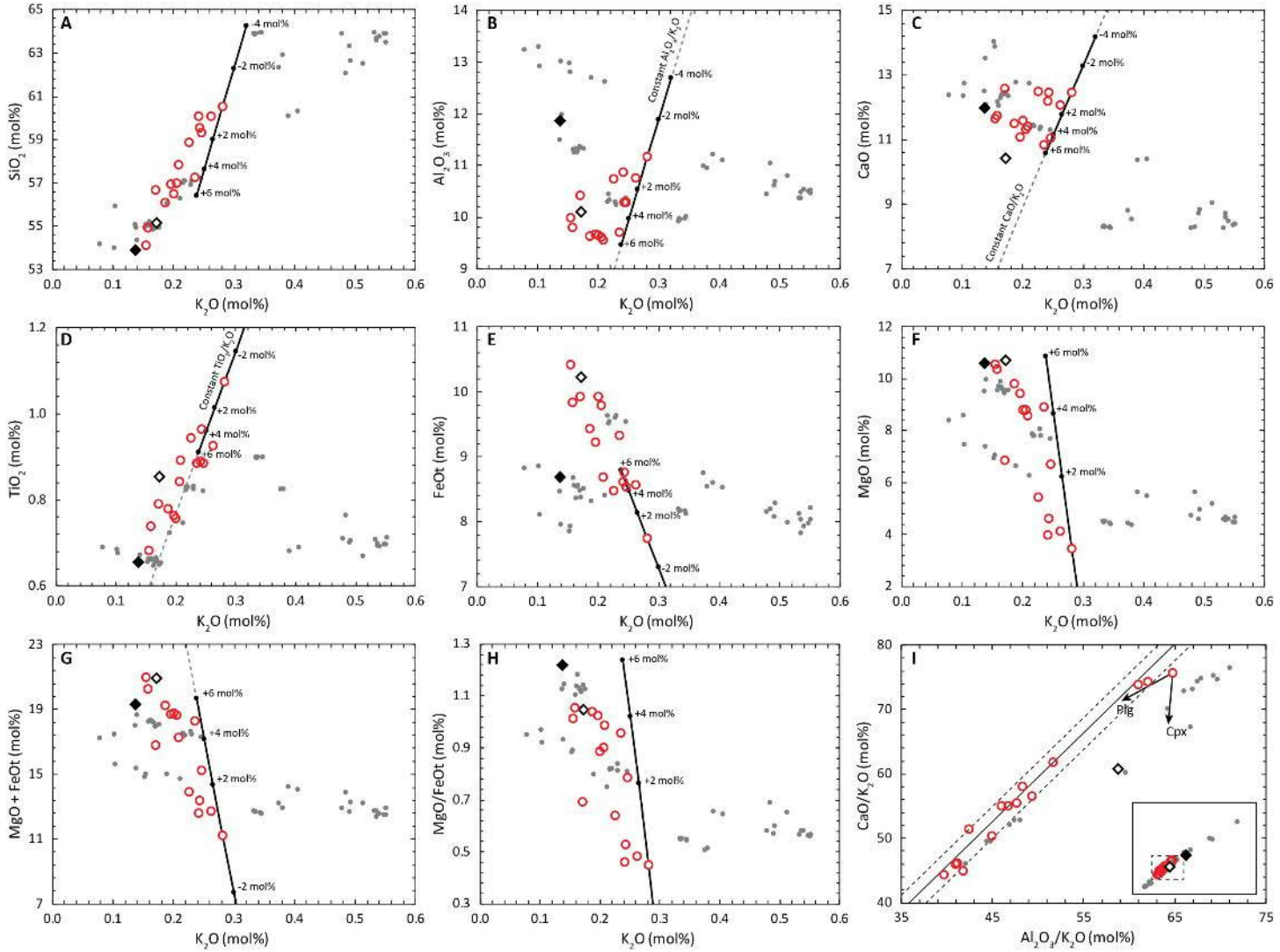
A
SiO2 (mol%)
K2O (mol%)
-4 mol%
-2 mol%
+2 mol%
+4 mol%
+6 mol%
B
Al2O3 (mol%)
Constant Al2O3/K2O
C
CaO (mol%)
Constant CaO/K2O
D
TiO2 (mol%)
Constant TiO2/K2O
E
FeOt (mol%)
F
MgO (mol%)
G
MgO + FeOt (mol%)
H
MgO/FeOt (mol%)
I
CaO/K2O (mol%)
Al2O3/K2O (mol%)
Plg
Cpx

Figure 4.7. Variation diagrams of major elements (in mol%) in the MIs of the AK sample. Red circles are the uncorrected MI compositions, the filled black diamond indicates the whole rock composition of the sample from which the MIs were collected, the hollow diamond corresponds to the AK melt fraction composition estimated through mass balance, and the grey dots are whole rock data of the AK volcanic system from the compilation found in Kuritani et al. (2019). The black line with circles is the trend of olivine addition for one of the MIs, where proportions of addition are indicated for -4, -2, 2, 4 and 6 mol%. The composition of the olivine has no effect on the olivine addition trend for (A) to (D) and (G), whereas an olivine composition of Fo_{78} was used to calculate the trends in (E) and (F). Fractional crystallization trends in (I) are unaffected by olivine fractionation, i.e. they do not change with PEC of olivine in the MI rims. Grey continuous line in (I) is the linear regression of the MI data and the dashed lines mark the standard deviation (±1σ). Arrows in (I) indicate approximated trends of fractionation of plagioclase and clinopyroxene. Dashed grey lines indicate constant ratios of conservative elements during olivine addition/subtraction.

A linear relationship of highly incompatible elements that approximate a line that crosses through the origin is a good indication that the MIs are associated with the same parental magma. Using K_2O concentrations and available trace or volatile elements like F and Cl are very useful for this purpose, as F, Cl and K_2O are highly incompatible in basalts and are expected to behave conservatively in MIs. This means that their concentrations during differentiation vary in the same way and are inversely proportional to the mass fractionated during crystallization. Due to the lack of trace element and volatile data, the conservative element comparison is done only with major elements. As mentioned above, the clear and steady increase of TiO_2 with increasing K_2O is indicative of the absence of Fe-Ti oxides during the FC process, and TiO_2 should behave almost conservatively, with small amounts being incorporated in pyroxene. In Figure 4.7D, a linear regression forced through the origin in the TiO_2 vs K_2O plot for the MI data, has an R-squared (R^2) of 0.99. P_2O_5 should also exhibit conservative behaviour if there is no evidence of apatite fractionation, but scatter may obscure the trends. The clear break of the behaviour of TiO_2 at K_2O contents >0.3 mol% for the whole rock data from the literature is consistent with the idea that the main process of differentiation for the Akita-Komagatake volcanic system is fractional crystallization. Other processes like magma mixing or boundary layer fractionation (Kuritani, 2009; Nielsen and DeLong, 1992) should produce straight mixing lines or smoothed curves in variation diagrams of oxides affected by changes in the fractionated phases during differentiation.

4.6.2.2 Initial parameter selection

The AK-36.1 MI is used as the initial composition of the set as it is the most primitive(Figure 4.5). A first run of MushPEC was used to find the initial parameter space where the solutions could be found. In this run pressures of 0.1 to 400 MPa, and initial H_2O contents from 0 to 8 mol% and f_{O_2} conditions between QFM -2 to QFM +2 were tested. It was found that the solution strongly converged towards pressures of *c.* 100 to 200 MPa, H_2O contents of 3 to 7 mol% and f_{O_2} conditions of QFM -0.5 and QFM +0.5. After this preliminary run, a finer space of initial conditions was tested within these ranges. Table 4.3 summarizes the values used to define the grid of initial parameters. In the preliminary run, the olivine addition parameter (initial guess of PEC for AK-36.1) was set between 4 and -4 (negative values correspond to amount of PEM). High PEC values crystallize olivine-only assemblage in the beginning until reaching compositions equivalent to low PEC conditions, making these models redundant. High PEM are discarded by the MushPEC filter as they start by crystallizing plagioclase. In the finer grid olivine addition is set between 2 and -1.2 mol%. MgO/FeO_T ratio values are set between 0.78 and 1.42, overlapping the values observed for all data in Figure 4.7H at low K_2O contents.

Table 4.3. Values used to define the grids of initial parameters.

Parameter	Min	Max	Grid 1 step	Grid 2 step	Grid 3 step	Grid 4 step	Units
Ol addition	-1.2	2.0	1.6	0.8	0.4	0.4	mol%
MgO/FeO_T	0.78	1.42	0.32	0.16	0.08	0.04	mol%
f_{O_2}	-0.5	+0.5	0.5	0.5	0.5	0.5	ΔQFM
Pressure	100	250	50	25	25	25	MPa
H_2O content	3.2	6.4	1.6	0.8	0.4	0.2	mol%

4.6.2.3 Solution convergence and sensitivity analysis

Figure 4.8 shows the convergence behaviour of GoF with respect to the initial parameters for the AK MI set. The different colours correspond to surfaces that show the behaviour

of minimum GoF values for each particular f_{O_2} condition at each particular combination of initial parameters. There is a clear convergence towards a narrow P – H_2O condition for each f_{O_2} buffer condition in Figure 4.8A, with best fit values ranging from 3.5 to 5.5 mol% H_2O at pressures between 125 to 150 MPa (undersaturated conditions). The sensitivity of the minimum GoF values with respect of these two initial parameters can be observed in the sharp decrease of GoF towards the minimum value of each surface with the changes of P and H_2O content. For example, in the surface for the QFM buffer there is an increase of *c.* 2.3×10^{-3} in the GoF value from the minimum point in this surface when decreasing the pressure by 50 MPa, whereas an increase of *c.* 1.2 mol% H_2O from the QFM surface minimum generates an increase of *c.* 1.4×10^{-3} in the GoF value. GoF values stays somewhat invariant between 4 to 5.2 mol% H_2O. Because the mineral assemblage being fractionated controls the LLD of the FC models, parameters that exert the highest effects on changes in the mineral assemblage will have higher sensitivity. In addition, as olivine fractionation is being adjusted so the MIs fit the FC models, the amount and composition of the olivine generated in the models have little to no effect on the GoF values of each FC model. The sensitivity of H_2O content is explained by the effect of H_2O on plagioclase stability (e.g., Lange et al., 2009; Waters and Lange, 2015). Pressure mainly affects the stability of pyroxene and olivine, with olivine being more stable at low pressures. The oxidation state also has a strong effect on the stability of orthopyroxene over olivine, where the latter is preferred over the former under more reducing conditions. In addition, highly oxidized models will usually fractionate Fe-Ti oxides earlier, which also has a strong effect on the LLD.

The GoF value is a lot less sensitive to changes in the MgO/FeO_T ratio and olivine addition parameters (Figure 4.8B). In agreement with Figure 4.8A, the minimum GoF values are generally lower at the QFM buffer (at 0.4 mol% olivine addition and 0.88 MgO/FeO_T ratio), slightly higher at more reduced conditions (QFM -0.5) and converging to similar minimum to another QFM +0.5 (at -0.4 mol% olivine addition and 1.38 MgO/FeO_T ratio). The steep increase in GoF values towards negative PEC and low MgO/FeO_T values is related to the filtering of models reaching the cotectic from the plagioclase-only crystallization side, as discussed in the test results of the synthetic MI set. Along the high PEC and high MgO/FeO_T corner, GoF values are stable and similar between the three f_{O_2} surfaces. The two different minimums for QFM and QFM +0.5 shows the strong dependence that the f_{O_2} has on the MgO/FeO_T estimations. Other runs

of MushPEC made for f_{O_2} values between these two surfaces show the transition of the minimum from low MgO/FeO_T at QFM to high MgO/FeO_T at QFM +0.5 (not shown). It is seen in the QFM surface that the minimum GoF is part of a "valley" of low GoF values that follows a positive relationship between olivine addition and MgO/FeO_T ratios. This "valley" corresponds to redundant models where higher amounts of olivine addition produce the models that crystallize olivine until the low PEC compositions before the olivine-plagioclase cotectic are reached.

The main problem of using the Aitchison distance as a measure of compositional similarity is that the significance of the difference in GoF values between FC models cannot be easily interpreted. What is the smallest difference in GoF between two models that can be interpreted as one model yielding a significantly better fit than the other? This is particularly important to identify if the small "valleys" observed in the olivine addition vs MgO/FeO_T plot are significantly better fits than the other conditions. The main source of uncertainty on the GoF value is attributable to the arbitrariness of the MI set used in the fitting process. The natural scatter of geochemical data has an effect on the final GoF values obtained by the method and is dependent on the quality and quantity of the MI data used. To analyse how the relative values of GoF can vary with the use of different MI sets, the correction method was applied to random subgroups of the MI set, and statistical analysis of the same surfaces of minimum GoFs was used to estimate uncertainties, which in turn helped to assign a minimum GoF difference that may be interpreted as a significant difference in GoF. The correction scheme was applied to 200 randomly generated subgroups (with no repetitions) of the 14 MIs in the set (without counting the initial composition) using a total of 7 to 13 MIs. To compare the relative differences between GoF values of the different subgroups, a relative GoF (GoF*) was calculated by setting the minimum GoF obtained for each subgroup to GoF* = 0. Histograms with all the GoF* values for each point in each surface of minimum GoF* were constructed and the 68.2% confidence interval around the median (equivalent to the confidence interval of 1σ in a normal distribution) was identified for each histogram. The two planes that define the confidence interval were plotted as the uncertainties of the GoF* values (Figure 4.8C and D). There is an overlap of uncertainties for the three oxygen buffers. The distance from the median to the upper uncertainty limit of the minimum GoF point is 2.5×10^{-4}, which defines the range of possible solutions above the

minimum GoF. The green line around the boxes of Figure 4.8A and B indicate the uncertainty limit for probable solutions.

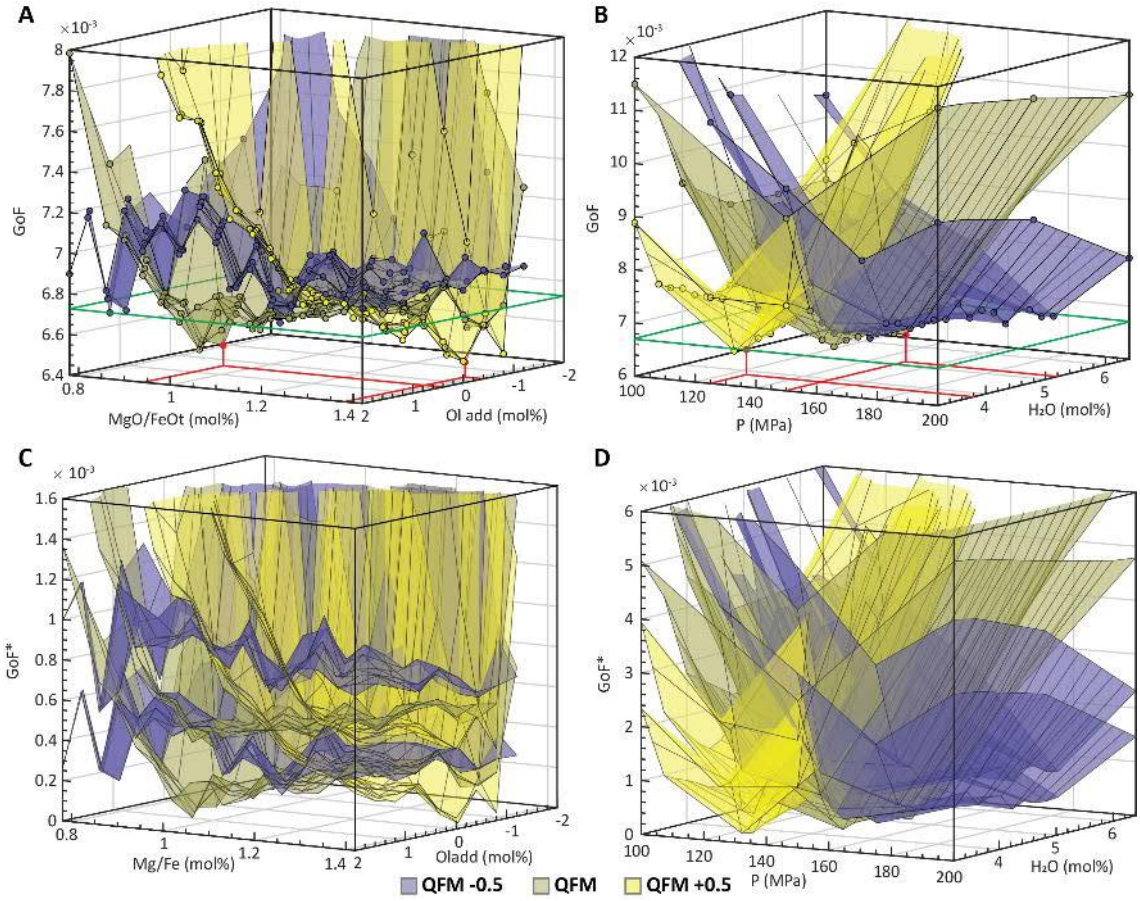

Figure 4.8. (A) and (B) show the convergence behaviour of the GoF parameter with respect to the initial parameters of the MushPEC run for the AK MI set. Each coloured surface represents the minimum GoF values for a fixed f_{O_2} buffer expressed as ΔQFM from -0.5 to +0.5. The red lines indicate the minimum GoF values for the QFM and QFM +0.5 surfaces. The green line around the plots indicates the 1σ limit estimated from the results in (C) and (D). (C) and (D) plot the surfaces defining the 1σ confidence interval for the GoF*.

4.7 Discussion

4.7.1 Initial limitations

As this method relies on FC simulations using the alphaMELTS2 front end, it has the same limitations as the rhyolite-MELTS algorithm. Rhyolite-MELTS is unable to model

some hydrous phases (e.g., amphibole, biotite), but for most basaltic MI sets it is expected that such phases are not present. The success of modelling the crystallization and composition of Fe-Ti oxides is uncertain, and any evidence of fractionation of these minerals in the MI set (e.g. TiO_2 fractionation) would indicate that the validity of the model output will have to be carefully considered. Fe-Ti oxides are absent in the AK sample and the incompatible behaviour of TiO_2 shown by the increasing TiO_2 with differentiation indicates that Fe-Ti oxides are not involved during fractionation while the MIs are being trapped. The whole rock trend from literature indicates that Fe-Ti oxide fractionation starts at *c.* 0.3 wt% K_2O.

Another limitation of this methodology is that cotectic crystallization of olivine with another mineral phase is required. The algorithm relies on finding the closest point between two compositional trends (the LLD of the FC model and the olivine addition trend of a MI), and both trends must be oblique to each other. This means that the crystallization phase assemblage of the FC simulation must include mineral phases like plagioclase or pyroxene in addition to olivine. This makes the methodology applicable to high silica basaltic and basaltic andesitic MI glass compositions, where olivine is not the only phase being fractionated at the time of MI trapping.

4.7.2 External constraints on MgO/FeO_T and magmatic implications for the AK sample

The weak convergence of the GoF values with respect to MgO/FeO_T ratios and the strong dependence of this parameter with the f_{O_2} conditions make it necessary to independently constrain the initial MgO and FeO_T concentrations and/or accurately constrain the f_{O_2} conditions of the melt for accurate MgO and FeO_T estimates. An option is to compare the FeO_T and MgO concentrations of the PEC corrected MIs generated by solution candidate FC models with other available compositions, such as available whole rock or melt data for the same volcanic system or genetically related MIs hosted in a different mineral phase. As identified in this study, plagioclase-hosted MIs experience fast Mg-Fe re-equilibration through diffusion to the carrier melt composition as for olivine-hosted MIs. Slower Fe-Mg diffusion is found in clinopyroxene crystals (Müller et al., 2013) making

them a good candidate to look for the original MgO and FeO_T contents when olivine crystals have re-equilibrated. An indication that clinopyroxene-hosted MIs have preserved their MgO/FeO_T ratios is the presence of sharp zoning in clinopyroxene hosts. Clinopyroxene-hosted MIs have not been found in the AK sample due to the scarcity and small size of available phenocrysts, but clear zoning in observed phenocrysts may indicate that storage times where not long enough to re-equilibrate clinopyroxene-hosted MIs.

Even though the genetic relationship between the carrier melt and the MIs is unlikely to be due to discrepancies in CaO contents (see above), the compositional similarity of the other oxides makes it probable that the FeO_T and MgO contents are close to the original MI contents at the moment of entrapment. The probable solutions found in the previous section were filtered so that probable models fall close to the carrier melt FeO_T vs K_2O. Figure 4.9 shows variation diagrams with the filtered solutions (LLDs) and corrected MI compositions. As predicted by the variation diagrams of the uncorrected MIs, low Al_2O_3 MIs are almost unaffected by PEC, but their FeO_T concentrations are corrected towards an increasing trend with differentiation, in agreement with what is seen for the groundmass glass compositions and with what is expected for tholeiitic basalts that have not started fractionating Fe-Ti oxides. Table 4.4 shows the range of compositions and PEC predicted by MushPEC. Results show similar amounts of PEC in mol% of olivine at the QFM oxygen buffer, but consistently higher in *c.* 0.3 to 1.3 mol% of olivine in the Petrolog results. As olivine compositions are very similar and no detailed compositional profiles were produced for the MIs in this study, the FeO_T value for the correction was set to the highest FeO_T in the set (11.56 wt% for AK-36.1). This generated a horizontal trend for MgO and FeO_T in the variation diagrams, contrasting with the increasing and decreasing trends estimated with MushPEC for FeO_T and MgO, respectively. This result suggests that complete re-equilibration during storage had little effect on the amount of total PEC before ascent and eruption; similar to what is shown by the model in Figure 4.1, where PEC during slow cooling is compensated by PEM, which is triggered by re-equilibration during storage.

Table 4.4. Compositional range of corrected MIs from AK using the MushPEC algorithm.

MIs	SiO_2	TiO_2	Al_2O_3	FeO_T	MnO	MgO	CaO
AK-36.1	50.9 - 51.2	0.9	15.9 - 16.1	10.5 - 11.2	0.2	6.9 - 7.4	10.3 - 10.4
AK-153	51.5 - 51.8	0.9	15.5 - 15.7	10.6 - 11.2	0.2	6.7 - 7.0	10.2 - 10.3
AK-43.1	51.6 - 51.9	0.9	15.4 - 15.5	10.6 - 11.3	0.2	6.6 - 7.0	10.2 - 10.4
AK-47.1	52.0 - 52.3	1.0	14.9 - 15.1	11.3 - 12.0	0.2	6.1 - 6.4	9.8 - 9.9
AK_144	52.1 - 52.4	0.9	14.8 – 15.0	11.6 - 12.4	0.2	5.7 - 6.2	9.8 - 9.9
AK_149	52.4 - 52.7	1.0	14.7 - 14.9	11.7 - 12.5	0.2	5.5 – 6.0	9.6 - 9.7
AK-38.1	52.5 - 52.8	0.9	14.9 - 15.1	11.5 - 12.2	0.2	5.6 - 6.1	9.4 - 9.5
AK-135	52.8 - 53.1	1.1	14.3 - 14.5	11.6 - 12.4	0.2	5.4 - 5.9	9.5 - 9.6
AK-42.1	52.2 - 52.6	1.1	14.7 - 14.9	12.3 - 13.1	0.1	5.0 - 5.4	9.1 - 9.2
AK-39.1	52.4 - 52.8	1.1	14.2 - 14.4	11.9 - 12.7	0.1	5.3 - 5.8	9.5 - 9.6
AK-151	52.8 - 53.2	1.0	14.7 – 15.0	12.2 - 12.9	0.2	4.9 - 5.4	8.7 - 8.9
AK-43-53	52.3 - 52.7	1.0	14.6 - 14.8	12.3 - 13.1	0.1	5.0 - 5.4	9.1 - 9.2
AK-41.1	52.5 - 52.8	1.0	14.8 - 15.0	11.9 - 12.7	0.1	5.3 - 5.8	9.1 - 9.3
AK_137b	51.9 - 52.3	1.1	14.7 - 14.9	12.6 - 13.4	0.1	4.8 - 5.3	9.1 - 9.2
AK-143	52.0 - 52.3	1.0	14.9 - 15.1	11.7 - 12.4	0.1	5.7 - 6.1	9.6 - 9.7

	Na_2O	K_2O	P_2O_5	H_2O	Total	PEC (ol mol%)	Δmass (wt%)
AK-36.1	2.2	0.2	0.1	1.1 - 1.3	100	-0.4 - 0.0	-1.5 - -0.2
AK-153	2.1	0.2	0.1	1.2 - 1.3	100	-0.1 - 0.4	0.0 - 1.1
AK-43.1	2.1	0.2	0.2	1.2 - 1.4	100	2.4 - 2.8	5.2 - 6.4
AK-47.1	2.2	0.3	0.1	1.4 - 1.5	100	0.5 – 1.0	1.5 - 2.7
AK_144	2.2	0.3	0.1	1.4 - 1.6	100	0.8 - 1.3	2.1 - 3.3
AK_149	2.0	0.3	0.1	1.5 - 1.7	100	0.7 - 1.2	1.9 - 3.2
AK-38.1	2.3	0.3	0.1	1.4 - 1.6	100	0.6 - 1.1	1.8 - 3.1
AK-135	2.4	0.3	0.2	1.5 - 1.7	100	1.4 - 1.9	4.2 - 5.5
AK-42.1	2.4	0.3	0.2	1.6 - 1.9	100	0.8 - 1.3	2.7 - 4.10
AK-39.1	2.5	0.3	0.2	1.5 - 1.8	100	4.3 - 4.9	10.9 - 12.4
AK-151	2.4	0.3	0.1	1.6 - 1.9	100	2.7 - 3.3	7.6 - 9.1
AK-43-53	2.4	0.3	0.2	1.6 - 1.9	100	4.7 - 5.3	12.1 - 13.7
AK-41.1	2.4	0.3	0.1	1.5 - 1.8	100	4.8 - 5.4	12.2 - 13.6
AK_137b	2.4	0.3	0.1	1.7 - 1.9	100	5.8 - 6.4	15.3 - 16.9
AK-143	2.2	0.3	0.1	1.5 - 1.6	100	4.2 - 4.8	10.8 - 12.2

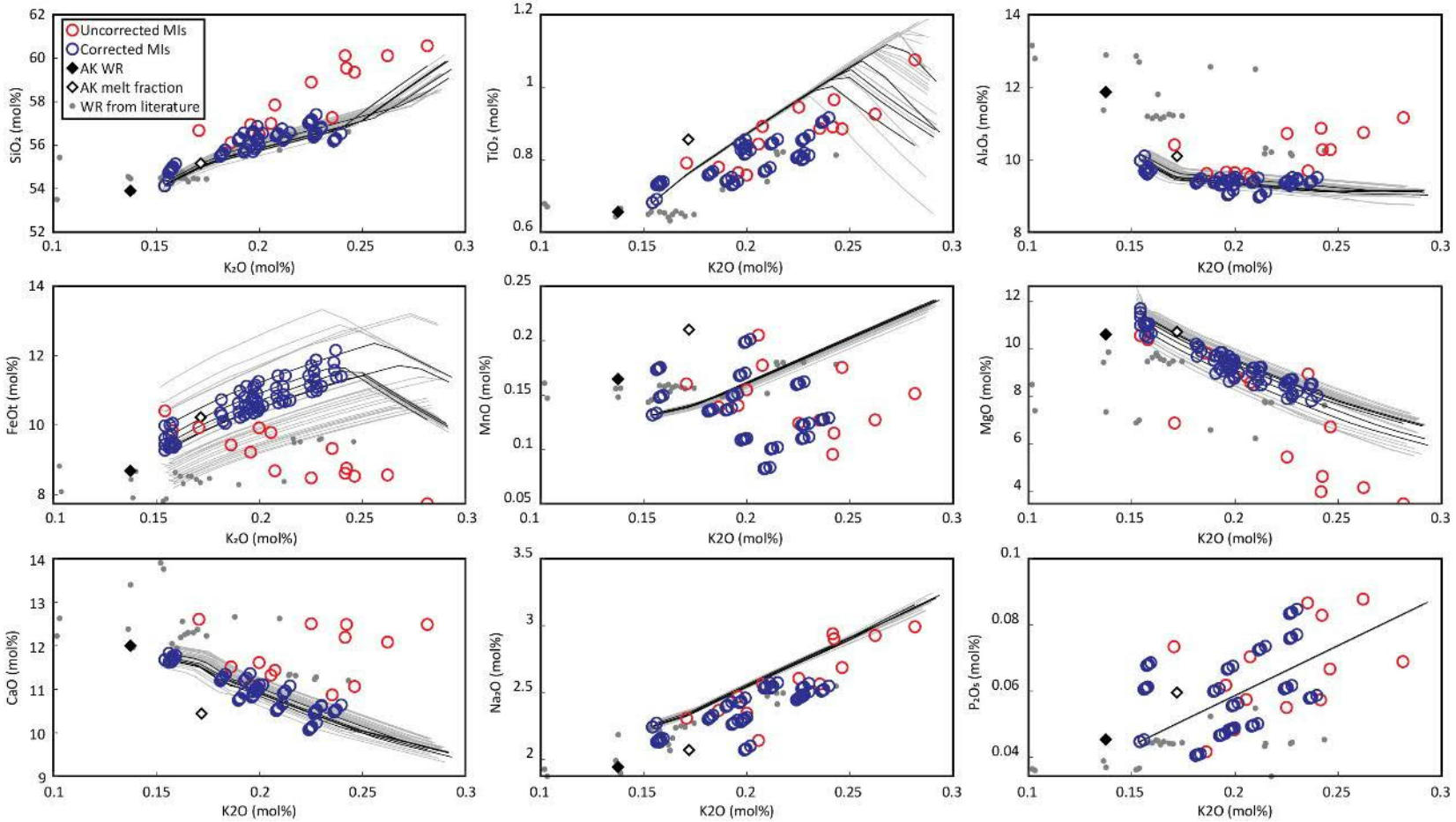

Figure 4.9. Variation diagrams of the corrected MIs. Red circles are the uncorrected MI compositions. The grey lines indicate the FC models that are below the GoF 1σ limit of Figure 4.8. Black lines are the FC models filtered by their intersection with the estimated melt fraction composition (white diamond). Blue circles are the corrected MI compositions for each of the models defined by the black lines.

Water contents and temperatures of entrapment for the most primitive MI in the set (at *c.* 51 wt% SiO_2) predicted by MushPEC are *c.* 1.2 wt% H_2O and *c.* 1150 °C, reaching *c.* 1.8 wt% H_2O and *c.* 1100 °C at the most differentiated MIs (*c.* 52.3 wt% SiO_2). However, the presence of some plagioclase compositions greater than An_{90}, significantly higher than those predicted by MELTS (up to An_{84}), suggests that some plagioclase antecrysts are grown at higher H_2O contents and pressures within the Akita-Komagatake plumbing system, as envisaged by Kuritani et al. (2019). They predicted considerably higher H_2O contents and lower temperatures for the same Akita-Komagatake unit using MIs trapped in high-Ca plagioclase (*c.* An_{90}), estimating *c.* 4.4 wt% H_2O and *c.* 990 °C at *c.* 52.8 wt% SiO_2. These anorthitic plagioclases could have been carried up to the shallow mush storage region where the MIs we modelled were entrapped. Therefore, the water contents of the magmas estimated by Kuritani et al. (2019) may represent those at deeper levels before the equilibration at the shallow levels at *c.* 120-150 MPa.

The mineral assemblage fractionated during crystallization of the melt can be estimated from the mineral assemblage fractionated in the FC models. Figure 4.10 shows the behaviour of the GoF with respect to the mineral assemblage fractionated from the most primitive to the most differentiated MI in the set. The best fit solutions are found at *c.* 50-55 wt% plagioclase, with *c.* 30-40 wt% clinopyroxene and *c.* 10 to 20 wt% olivine, without any orthopyroxene or Fe-Ti oxides. The mineral phases present in the AK sample are the same as the phases appearing in the model, but the low clinopyroxene : olivine ratio of the AK sample contrasts with the high abundance of clinopyroxene over olivine in the modelled mineral assemblage. This discrepancy could be generated by different magmatic processes. For example, preferential clinopyroxene melting during infiltration of the accumulated crystals by the new magma batch can deplete the crystal cargo of clinopyroxene. The FC models show that plagioclase starts crystallizing before clinopyroxene suggesting that during magma recharge, clinopyroxene would be the most unstable mineral phase. Other explanations include mush zone phase assemblage heterogeneity or preferential uptake of plagioclase and olivine during remobilization and ascent.

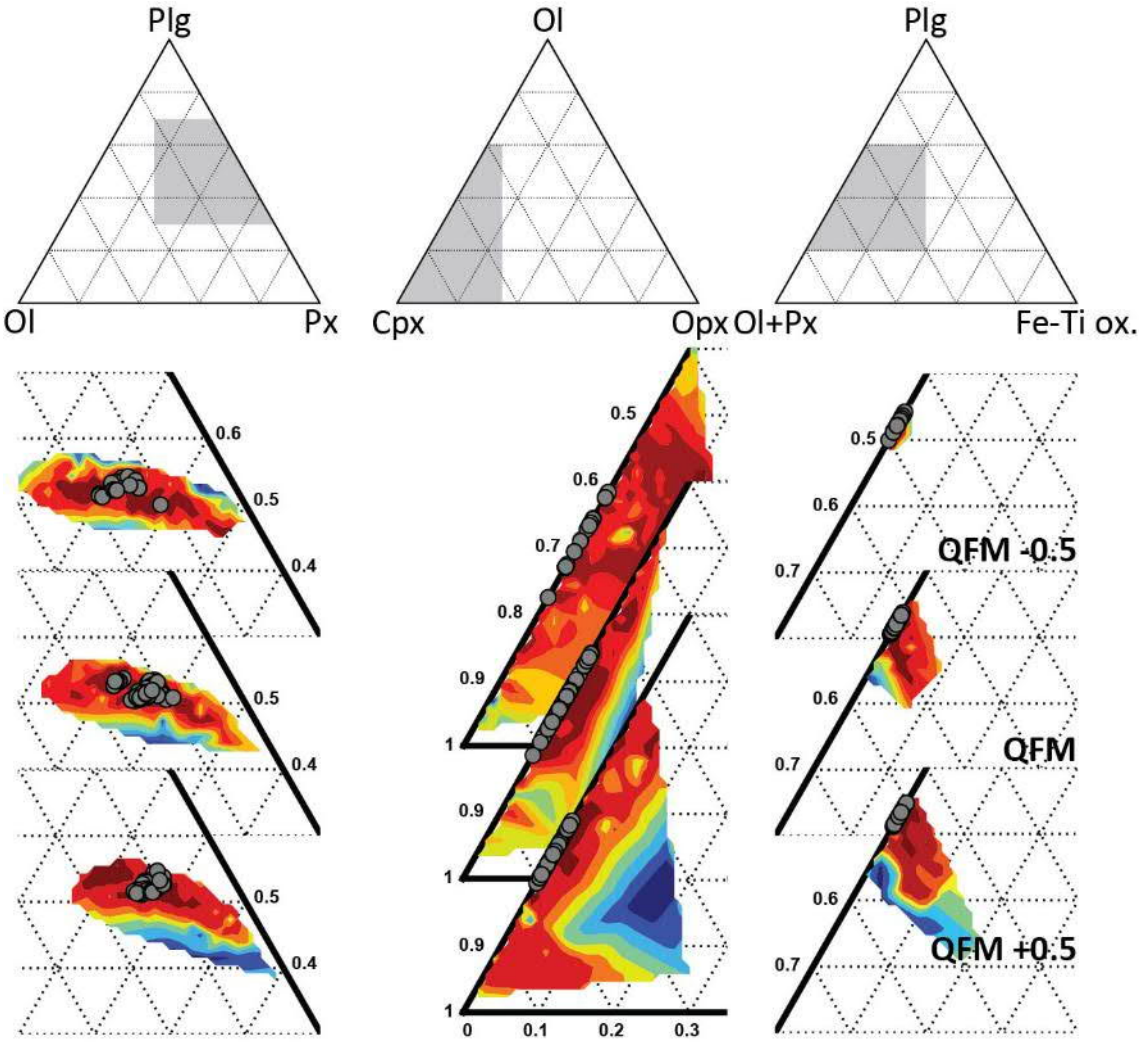

Figure 4.10. Proportions of fractionated phases of the FC models at different f_{O_2} conditions. Coloured areas indicate the GoF value behaviour of the FC models with changes in the mineral proportions. Red colours indicate lower GoF values (good fits), whereas blue colours indicate high GoF values (bad fits). Grey circles indicate the mineral assemblage of the solutions of the PEC corrections before filtering by the FeO_T content of the AK melt fraction. Plg = plagioclase, Ol = olivine, Px = clinopyroxene + orthopyroxene, Cpx = clinopyroxene, Opx = orthopyroxene, Sp = spinel.

4.8 Conclusions

MushPEC can be used to successfully estimate PEC-corrected MI compositions from a set of genetically related MIs hosted in antecrystic olivine by fitting the MI compositions to FC models. A major implication of the development of this methodology is that it expands the number of MI data that can be used for studying the compositions of primary magmas and their volatile contents.

The strong dependency of the MgO/FeO_T of the corrected MI compositions on small changes in f_{O_2} and the weak convergence of the solution with respect to MgO/FeO_T values make it necessary to externally constrain the MgO/FeO_T of the MIs at the moment of entrapment.

MushPEC takes advantage of the rhyolite-MELTS algorithm to estimate crystallization conditions of the magma batch that fractionated the studied antecrysts, including pressure, H_2O content and f_{O_2} conditions. Estimations of the mineral assemblage produced during the differentiation path of the MIs can also be recovered from the output.

The olivine-hosted MIs from the AK sample were trapped during fractional crystallization at shallow depths (*c.* 125-150 MPa), low water contents (*c.* 1 – 2 wt% H_2O) and f_{O_2} conditions near the QFM buffer.

MushPEC is limited in its applicability to natural systems. It is applicable to magmatic systems where FC is the dominant differentiation process, where crystallization conditions can be reproduced with the rhyolite-MELTS algorithm and where external constrains on the MgO/FeO_T ratio or f_{O_2} conditions are available. This study also highlights the importance of assessing the antecrystic nature of some olivine-hosted MIs to make accurate interpretations of the magmatic conditions.

Chapter 5

Olivine MI constraints on some intensive properties of subvolcanic crystal mushes and their evolution through boundary layer fractionation in northern Japan

Raimundo Brahm[1], Georg Zellmer[1], Takeshi Kuritani[2], Naoya Sakamoto[3], Hisayoshi Yurimoto[3], Mitsuhiro Nakagawa[2], Eiichi Sato[4].

[1]School of Agriculture and Environment, Massey University, Palmerston North, New Zealand.

[2]Graduate School of Science, Hokkaido University, Sapporo, Japan.

[3]Isotope Imaging Laboratory, Creative Research Institution, Hokkaido University, Sapporo, Japan.

[4]Hokkaido University of Education, Asahikawa, Japan.

5.1 Abstract

Magma differentiation in arc settings has usually been attributed to an interplay of processes (fractional crystallization, assimilation and magma mixing). Homogeneous fractional crystallization has been widely used to model the magmatic evolution of volcanic systems in arc settings due to its simplicity, even though boundary layer fractionation has been proposed as a preponderant process of differentiation in hydrous magmatic systems. Both models produce distinct compositional paths and the application of the wrong model yields erroneous estimates of parameters like pressure-temperature-H_2O conditions and primary melt compositions. MI populations corrected for post-entrapment processes have the potential to help discriminate between these two types of fractional crystallization, as their compositions are not affected by crystal accumulation and should capture the magmatic evolution as crystallization occurs. In this study, OHMIs

are used to assess the differentiation trends of basic arc magmas in northern Japan. Differentiation trends from five arc volcanic systems in northern Japan show that boundary layer fractionation is ubiquitous. Homogeneous fractionation models are unable to explain the liquid lines of descent of minor elements, like TiO_2 and P_2O_5. To reproduce these differentiation trends, the presence of accessory phases like titanomagnetite or apatite are required, which in many cases are not equilibrated by the melt or need to be fractionated in amounts that are incompatible with homogeneous fractionation. The prevalence of boundary layer fractionation in all studied arc magmas of northern Japan indicates that solidification fronts are key environments in the crustal evolution of hydrous subduction zone magmas in general.

5.2 Introduction

The differentiation mechanisms of magmatic systems in the crust has been a crucial point of interest for many studies in igneous petrology and geochemistry (Bowen, 1928; Dufek and Bachmann, 2010; Harker, 1909; Nielsen, 1990; Wilson, 1995). These studies are particularly relevant in volcanic settings, as understanding the mechanisms involved in magmatic evolution can shed light into conditioning and triggering processes involved in hazardous volcanic eruptions (e.g., magma transport, pressure build-up, viscosity increase, volatile concentration and volatile exsolution; Blake, 1984; Gonnermann, 2015; Petrelli et al., 2018; Wotzlaw et al., 2014). In general, from a geochemical perspective, the mechanisms of magma differentiation have been broadly described as an interplay of three main processes: fractional crystallization (FC), assimilation and magma mixing.

In most cases, FC has been invoked as the main process of magma differentiation at crustal depths (e.g., Bowen, 1915; Brahm et al., 2018; Forni et al., 2016; Gavrilenko et al., 2016b; Gelman et al., 2013; Grove and Kinzler, 1986; Kimura and Ariskin, 2014; Mollo et al., 2015; Portnyagin et al., 2015; Watanabe et al., 2006; Yoshida and Aoki, 1984; Zen, 1986), with small to negligible amounts of wall-rock assimilation and sporadic mixing events. Most attempts to quantify FC have been performed by applying Rayleigh fractionation, which assumes that the crystallization process occurs homogeneously throughout the magmatic body (homogeneous FC; HFC), usually using thermodynamic models of mineral-melt equilibrium (e.g., MELTS, COMAGMAT, Petrolog3; Ariskin

and Barmina, 2004; Ariskin et al., 2018; Danyushevsky and Plechov, 2011; Ghiorso et al., 2002; Ghiorso and Sack, 1995; Gualda et al., 2012). For its simplicity, this approach is commonly preferred over more complex fractionation models. However, HFC modeling does not assess for dynamic processes occurring within the magmatic body that can have strong effects on the compositional path of the melt, and it relies on a simplistic view of chamber-wide convection and/or crystal settling.

In contrast, several studies have proposed that crystallization of magma reservoirs dominantly operates in solidification fronts at their boundaries, where the magma is expected to cool most effectively (Kuritani, 1999b; Kuritani, 2009; Langmuir, 1989; Marsh, 1996; Marsh, 2007; Nielsen and DeLong, 1992; O'Hara and Fry, 1996; Simura and Ozawa, 2011). Abundant crystallization in this boundary layer generates a mushy wall isolating the magma body from the wall-rock. The differentiated liquids generated in the boundary layer may be continuously transported to the main magma body through extraction processes from the boundary crystal mush (Bachmann and Bergantz, 2004; Bachmann and Bergantz, 2006; Pistone et al., 2017). The chemical evolution of the magma can then be modelled by mixing of the central melt with increments of differentiated magma from the boundary layer (in situ crystallization or boundary layer fractionation; BLF; Langmuir, 1989; Nielsen and DeLong, 1992). The compositional path generated by BLF is substantially different to the one produced by HFC, mainly because the boundary layer crystallizes mineral phases that are not expected to be fractionated by the central melt. Hence, the application of HFC or BLF models can have strong discrepancies in the interpretation of magmatic conditions and discriminating between these processes is thus of crucial importance. BLF has been proposed to explain the compositional evolution observed in some volcanic suites (Kuritani, 1999b; Kuritani, 2009) and has been shown to be compatible with field observations of sheet-like intrusive bodies (Simura and Ozawa, 2011).

As many volcanic rocks are crystal-rich, their compositions are usually affected by crystal accumulation processes and by entrainment of antecrysts and xenocrysts (e.g., Jerram and Martin, 2008; Zellmer et al., 2016; Zellmer et al., 2014). This makes it hard to identify from whole rock compositions the liquid line of decent of evolving magmas. MIs (MIs) have the potential to preserve the melt composition along the differentiation path as they

are trapped in the crystalizing mineral phases, unaffected by contamination of other crystals. Nonetheless, there are a series of processes known to change MI composition after entrapment, such as post-entrapment crystallization (PEC) of daughter crystals or the host mineral from the MI boundary, diffusion of elements between MI and host, exsolution of volatile phases into a gas bubble, among others (Danyushevsky et al., 2000; Hartley et al., 2015; Maclennan, 2017; Roedder, 1979; Turner et al., 2017b; Wallace et al., 2015). Olivine-hosted MIs have been widely used due to their potential to preserve early stage compositions, and their post-entrapment processes are comparatively well characterized (e.g., Danyushevsky et al., 2004; Danyushevsky et al., 2002a; Kelley et al., 2006; Rowe et al., 2011a).

In the present study, olivine-hosted MIs from five arc-front volcanic centres in northern Japan are analysed to study their differentiation paths and to identify the prevalence of HFC or BLF in each magmatic system. Results show that BLF is the most common process of magma differentiation in mafic arc-front magmas throughout northern Japan, suggesting that it may in fact be the dominant process of differentiation for most mafic to intermediate hydrous magmatic systems in arc settings.

5.3 Tectonic and geologic setting

The Hokkaido and Tohoku regions of Japan are located on the Okhotsk Plate, whereas SW Japan belongs to the Eurasian (or Amur) Plate. At the eastern margins of Hokkaido and NE Honshu, the Pacific Plate is subducted beneath the Okhotsk Plate (7 – 11 cm/yr; Bird, 2003; Northrup et al., 1995), forming the Kuril (to the north) and Japan (to the south) trenches. In Hokkaido, the NE Japan arc meets the southernmost Kuril arc in an arc-arc collision zone (Kimura, 1996; Kita et al., 2014), known as the Hidaka collision zone. Oblique subduction of the Pacific plate produces a southward migration of the Kuril forearc sliver (Figure 5.1), which has been colliding with the NE Japan arc in south-central Hokkaido since Miocene times (*c.* 12 Ma), resulting in uplift of the Hidaka Mountains. There is a volcanic gap of *c.* 120 km between the two arcs, coincident with the collision zone. The orientation of the trench in the arc junction changes from N10E in the NE Japan arc to N56E in the Kuril arc, which leads to bending of the subducted slab. This bending has been associated with higher thermal inputs from the underlying mantle,

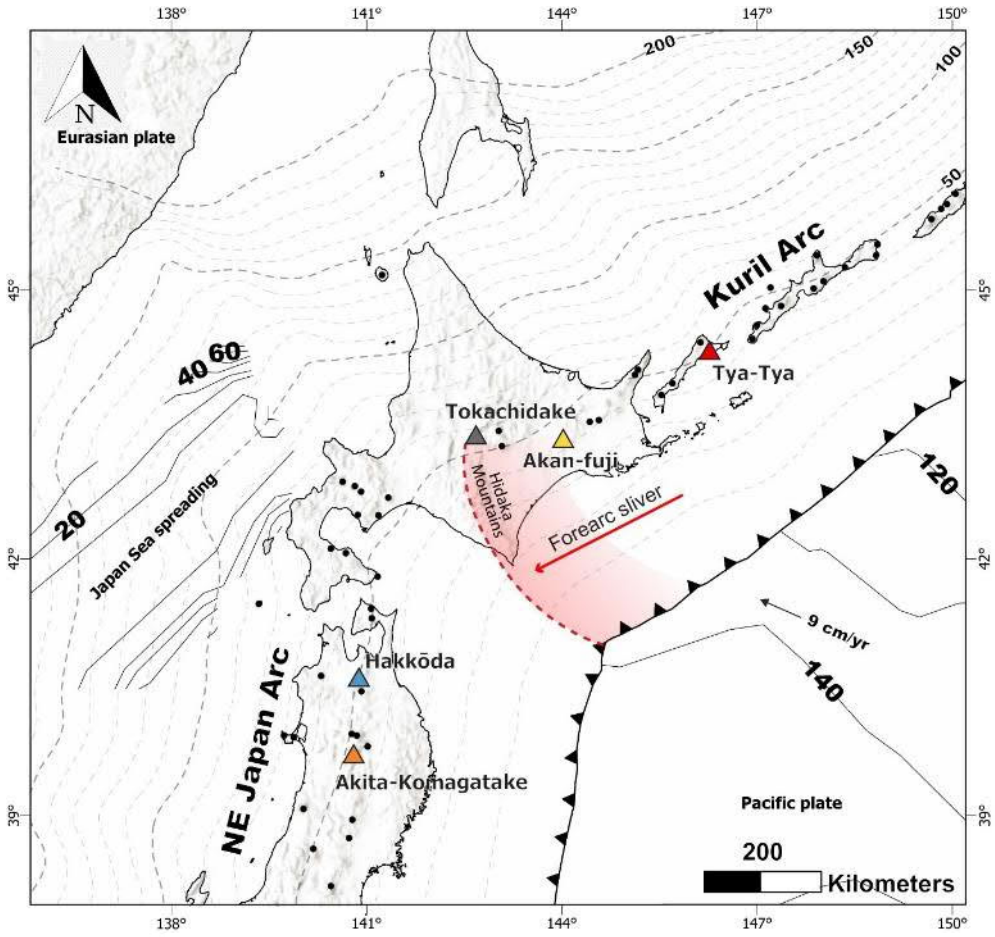

Figure 5.1. Topographic map of NE Japan. Triangles with names are the volcanic systems of interest in this study. Black dots are other volcanoes of the NE Japan and Kuril arcs. The black line with triangles marks the trench. The red area indicates the collision zone of the Kuril forearc sliver over the NE Japan arc, and the red arrow indicates its direction of movement. Grey dashed lines indicate the depth of the slab (in km). The thin black lines indicate the age of the sea floor (in Ma).

caused by cracking or thinning of the subducted oceanic crust, which is thought to affect the slab-fluid input of magmatism generated above the slab-bending zone (Kuritani et al., 2016; Kuritani et al., 2008). Arc volcanism in NE Honshu and Hokkaido has been located in the same position for the last *c*. 5 Ma (Martin, 2011; Yoshida et al., 2014). Caldera-dominated felsic volcanism related to NE-SW oriented compression shifted *c*. 2 Ma to a stratovolcano-dominated basaltic to andesitic volcanism associated with a change to a current ENE – WSW oriented compression in NE Honshu (Acocella et al., 2008).

Five Holocene volcanic systems distributed along the Kuril and NE Japan arc fronts were chosen for this study (Figure 5.1). These volcanic systems were selected to represent a wide distribution of magma generation along the arc front, with the condition that they

have basic tephra products with olivine-hosted glassy MIs. The selected volcanic systems are Akita-Komagatake, Hakkoda, Tokachidake, Akan-fuji and Tya-Tya. One tephra sample for each of these volcanic systems was analysed for the present study.

5.3.1 Akita-Komagatake (AK)

Akita-Komagatake is the southernmost volcano in this study, it is located in the Tohoku region and it belongs to the arc front section of the NE Japan arc. Its activity started at about 74 ± 15 ka (Itaya et al., 1984) and its eruptive history can be divided into three main stages (Sutō and Ishii, 1987): (1) stratocone formation stage, (2) syn-caldera stage, and (3) post-caldera stage. The compositions of Akita-Komagatake products range from basaltic to andesitic (Fujinawa et al., 2004; Nakagawa, 1985; Sutō and Ishii, 1987; Ueki and Iwamori, 2017). The selected sample (AK) is from the second Hokubu pyroclastic cone deposits, believed to be associated with the *c.* 7 ka "AK-6" tephra layer (Fujinawa et al., 2004; Kuritani et al., 2019; Wachi and Koshiya, 1997), which is the unit with the highest MgO content found in this volcanic system (Fujinawa et al., 2004; Kuritani et al., 2019).

5.3.2 Hakkoda (HK)

Hakkoda (or Kita-Hakkoda) is the northernmost volcano from the arc front of the NE Japan volcanic arc and is located south of Mutsu Bay in northern Tohoku. It is part of the Hakkodasan volcanic area that comprises at least 17 stratovolcanoes and lava domes, divided into the Kita-Hakkoda volcanic group (north) and Minami-Hakkoda volcanic group (south). Hakkodasan products range from basalts to dacites (49.4 and 63.2 wt% SiO_2) (Sasaki, 1986; Sasaki, 1987; Sasaki et al., 1985). The current volcanic activity is located in Kita-Hakkoda, which has been active since 0.4 Ma (Kudo et al., 2004; Takarada and Muraoka, 2004). Historic activity of Kita-Hakkoda has only involved seismic swarms (1986) and volcanic gas emanations (1997 and 2010) (Kudo and Hoshizumi, 2006). Past eruptions include five magmatic to phreatic eruptions of Odake volcano from (4.8 ka to 1.5 ka) and three phreatic eruptions of Jigokunuma crater from 0.7 to 0.4 ka. The tephra

sample in this study (HK) corresponds to tephra fall from the 2 ka Odake phreatomagmatic eruption HK-2 (Kudo et al., 2003; Kudo et al., 2000; Kudo et al., 2004).

5.3.3 Tokachidake (TK)

This volcanic system is the southernmost volcano in the Kuril arc. It is located in the south-westward collision zone of the Kuril forearc sliver over the NE Japan arc forearc, generating a 120 km volcanic gap between the Kuril and NE Japan arcs (Kita et al., 2012). The eruptive history of TK is divided into Older (1.0 to 0.5 Ma), Middle (300 to 70 ka) and Younger (60-50 ka to present) stages (Ishizuka et al., 2010). Tokachi Dake is the central stratovolcano where most of the activity of the Younger stage occurred, starting with andesitic to dacitic products. Later activity was dominated by fall deposits and lava flows, with lesser amounts of pyroclastic flow deposits. Historic eruptions in the 20th century occurred in 1926, 1962 and 1988-1989 (Nakagawa et al., 2019). The TK sample from this study belongs to a proximal fall deposit of the 1962 sub-plinian eruption.

5.3.4 Akan-fuji (AKN)

Akan-fuji is located in NE Hokkaido in the south Kurile arc front. It is one of the eight small stratovolcanoes that compose Meakandake (Yokoyama et al., 1976), located on the SW flank of the Akan caldera. Activity of Akan-fuji started around 1.0 to 2.5 ka ago, forming basaltic lavas and scoria fall deposits (Wada, 1997; Wada et al., 1998). The AKN sample was collected from fall deposits of the cone.

5.3.5 Tya-Tya (TT)

This stratovolcano is located in the north of Kunashir Island, the southernmost island in the Kuril arc north of Hokkaido. Its development can be divided into the construction of an old and a young volcanic edifice (Nakagawa et al., 2002), with the later partially overlying the former. Both volcanic edifices are compositionally distinct, with the old

composed of low-K products and the young ofmedium-K products. The last known activity occurred in 1973 forming two maars in the northern flank of the edifice through phreatic eruptions (Markhinin et al., 1974), followed by the formation of two scoria cones in the southern flank. The largest scoria cone was the last one produced in a sub-plinian eruption and represents the most active period of the 1973 eruptive sequence and within the southern Kuril arc in the 20th century. Whole rock compositions of the young edifice of Tya-Tya range from tholeiitic basalt to dacite (49 to 63 wt% SiO_2) (Nakagawa et al., 2002). Products from the 1973 eruption are crystal-poor, with a narrow compositional range of about 53 to 54 wt% SiO_2 (Nakagawa et al., 2002). The selected sample (TT) was collected from the 1973 eruption scoria fall deposit (locality 6 in Nakagawa et al., 2002).

5.4 Analytical methods

5.4.1 Whole rock major element analysis

Glass beads were prepared from whole rock powder of each tephra sample to perform x-ray fluorescence (XRF) analysis. The samples were cleaned in an ultrasonic bath with distilled water and dried in an oven at 100 °C for at least 2 h. The samples were then powdered using a tungsten grinding machine and dried again in the oven at 100 °C for at least 2 h. To determine loss on ignition (LOI), *c.* 2 g of powder was weighed before and after heating in an oven at *c.* 900 °C for 3 h. After heating, *c.* 0.8 g of each powdered sample was mixed with *c.* 8.0 g of lithium metaborate : lithium tetraborate (12 : 22) flux mixture and then fused to produce a glass disc using a XRFuse2 electric fusion apparatus.

Major element concentrations were measured with a 1 kW Bruker Tiger S8 Series II XRF spectrometer at Massey University in Palmerston North, New Zealand. Interference-corrected spectra intensities were converted to oxide concentrations using calibration curves consisting of natural standards, closely approximating the mafic matrix of our samples. The long-term reproducibility of Oreas 24c standard reference material is better than ± 1% relative (1σ) for all elements except MnO, for which it is better than ± 1.5% relative.

5.4.2 Mineral and glass textural and compositional analysis

Textural features of the tephra samples were assessed through BSE imaging. BSE images of the exposed MIs were obtained using a JEOL JSM-7000F field emission scanning electron microscope (FE-SEM) at Hokkaido University, Japan. An acceleration voltage of 15 kV was used, with a beam current of 10 nA.

BSE images of thin sections and mineral compositions were obtained using a JXA-8230 SuperProbe Electron Probe Microanalyser (EPMA) at Victoria University, New Zealand. Plagioclase crystals were analysed using a defocused beam of 10 μm diameter with an acceleration voltage of 15 kV and a beam current of 12 nA. Olivine, pyroxene and Fe-Ti oxide crystals were analysed using a focused beam with an acceleration voltage of 20 kV and an electron beam current of 30 nA. Counting times were 40 s on peak and 15 s on background for all elements. Secondary standards were analysed periodically during the runs to constrain precision and accuracy, and to assess for possible drift effects. Drift correction was applied for some of the analysis runs that showed drifting effects. Precision and accuracy evaluation for these mineral phases can be found in the Appendix 3.

For MI olivine host crystals, analysis spots were chosen in the vicinity of the MIs to better constrain equilibrium conditions. A focused beam with acceleration voltage of 20 kV was used with a beam current of 30 nA for Si, Fe, Mg, Mn and Ti, and 100 nA for Al, Ni, Ca and Cr. Counting times were 40 s on peak and 15 s on background for all elements but Ca, with 400 s on peak and 20 s on background. Accuracy and reproducibility of the analyses were constrained by alternating analyses of USNM2566 and JK3 olivine secondary standards with the samples during the session. Concentrations are accurate to <4% for major elements, <35% for Mn, <24% for Ni and <89% for Cr. Accuracy of Ca was usually <4% with a couple of analyses with c. 7%. Ti and Al values are usually below the detection limits for both standards. Reproducibility estimates (as 1σ) were <2% for major elements, c. 3% for Ni and Ca, c. 5% for Mn and c. 27% for Cr.

MI and interstitial glass compositions (Si, Ti, Al, Fe, Mn, Mg, Ca, Na, K, and P or Cr) were analysed with an accelerating voltage of 15 kV and a beam current of 8 nA. A

defocused beam of 5–10 μm diameter was used, and Na was analysed for 10 s first to avoid Na migration. Basaltic glass secondary standards (VGA99 and BHVO-2G) were analysed periodically throughout the session to test for instrumental drift and to constrain accuracy and reproducibility of the analyses. Reproducibility estimates (1σ) are <1% for SiO_2, Al_2O_3 and CaO, c. 2% for FeO and MgO, c. 3% for Na_2O and K_2O, c. 10% for TiO_2, MnO and P_2O_5. Accuracies uncertainties are <1% for most SiO_2 and Al_2O_3 secondary standard analyses, <2% for most Al_2O_3, FeO, MgO and CaO analyses, <3% for most K_2O analyses, <10% for most Na_2O and TiO_2 analyses and <20% for most P_2O_5 analyses.

5.4.3 Glass H_2O and CO_2 analysis by secondary ion mass spectrometry (SIMS)

Volatile element analyses (H and C) of MI glasses were carried out with the Cameca ims-1270 SIMS at Hokkaido University, Japan. Exposed MIs were pressed down into an indium plug mounted in an aluminium disk to avoid H and C contamination from epoxy. The plug was then coated with gold and loaded into the SIMS to remain under vacuum for three days before analysis to reduce potential H contamination on the sample surface.

A Cs^+ ion primary beam was used to analyse for ^1H, ^{12}C and ^{30}Si. Pre-sputtering of a 25×25 μm area was conducted before each analysis with beam current of 1 nA for 100 s, plus a beam centring time of 96 s. Analysis was carried out with a beam current of 0.1 nA over a 3-5 μm wide area of Gaussian shape. Field aperture was set to 2000 μm with an entrance slit of 60 μm, an energy slit of 25 μm, a contrast aperture of 100 μm and an exit slit of 400 μm. Mass resolution was set to 3243 to avoid interference of isotopic signals. The isotopes were measured in five consecutive cycles of 10 s of waiting time and 3 s of analysis time for ^1H, 4 s waiting time and 5 s analysis time for ^{12}C, and 2 s waiting time and 1 s analysis time for ^{30}Si. The reproducibility of counts ratios between each volatile and matrix was obtained from the five cycles per analysis. Maximum uncertainties of reproducibility are <10% for $^1H/^{30}Si$, <13% and for $^{12}C/^{30}Si$.

Reference glasses were polished and mounted in the same indium plug with the MIs and were repeatedly measured during the same analysis session to produce the calibration

lines and to check for instrument drift. The reference glasses used were BIR-1G and BHVO-2G synthetic standard glasses (USGS), plus CL DR-1, LS 427, 2πD43, SAM 76-11 and SAM 73-12 natural volcanic glasses (Kendrick et al., 2017). H_2O and CO_2 compositions for most of the reference materials were measured using a micro-FTIR instrument at Massey University, Palmerston North. Conditions of H_2O and CO_2 analyses, plus the final reference materials compositions used for SIMS calibration can be found in Appendix 2. Calibration of the SIMS analyses was produced using a maximum likelihood linear regression scheme considering the uncertainties related to SIMS analysis precision and uncertainties in the reference values used. After calibration, the uncertainties in accuracy (1σ) for the volatile species in MIs are *c*. 4% for H_2O and <15% for CO_2 (for concentrations above 50 ppm). Detailed information of the SIMS counts results, calibration curves MIs volatile concentrations and associated errors can be found in Appendix 2.

5.5 Results

5.5.1 Petrography and mineral chemistry

5.5.1.1 Akita-Komagatake

The AK tephra sample is composed of a glass-rich groundmass (*c*. 75 vol% on a vesicle free basis) with plagioclase (Pl; *c*. 87 vol% of crystal cargo), olivine (Ol; *c*. 12 vol%) and scarce clinopyroxene (Cpx; <1 vol%) phenocrysts (Figure 5.2a). Present crystal clots are usually composed of a single mineral phase, with the exception of some scarce Ol + Cpx

clots. The AK sample Ol crystals have very homogeneous core compositions ($Fo_{77.4-78.5}$) with narrow less forsteritic rims (AK-Ol1 in Figure 5.3a). These Ol crystals are the hosts of glassy MIs, and are euhedral to subhedral and have sizes of *c*. 100 to 500 µm. They are present as isolated crystals or as small clots of Ol and scarce Cpx. Ol crystals <100 µm in size are found also associated with small Cpx crystals and in contact with the rims of big Pl crystals (AK-Ol2). These smaller Ol crystals have slightly more Fe-rich compositions (Fo_{74-77}).

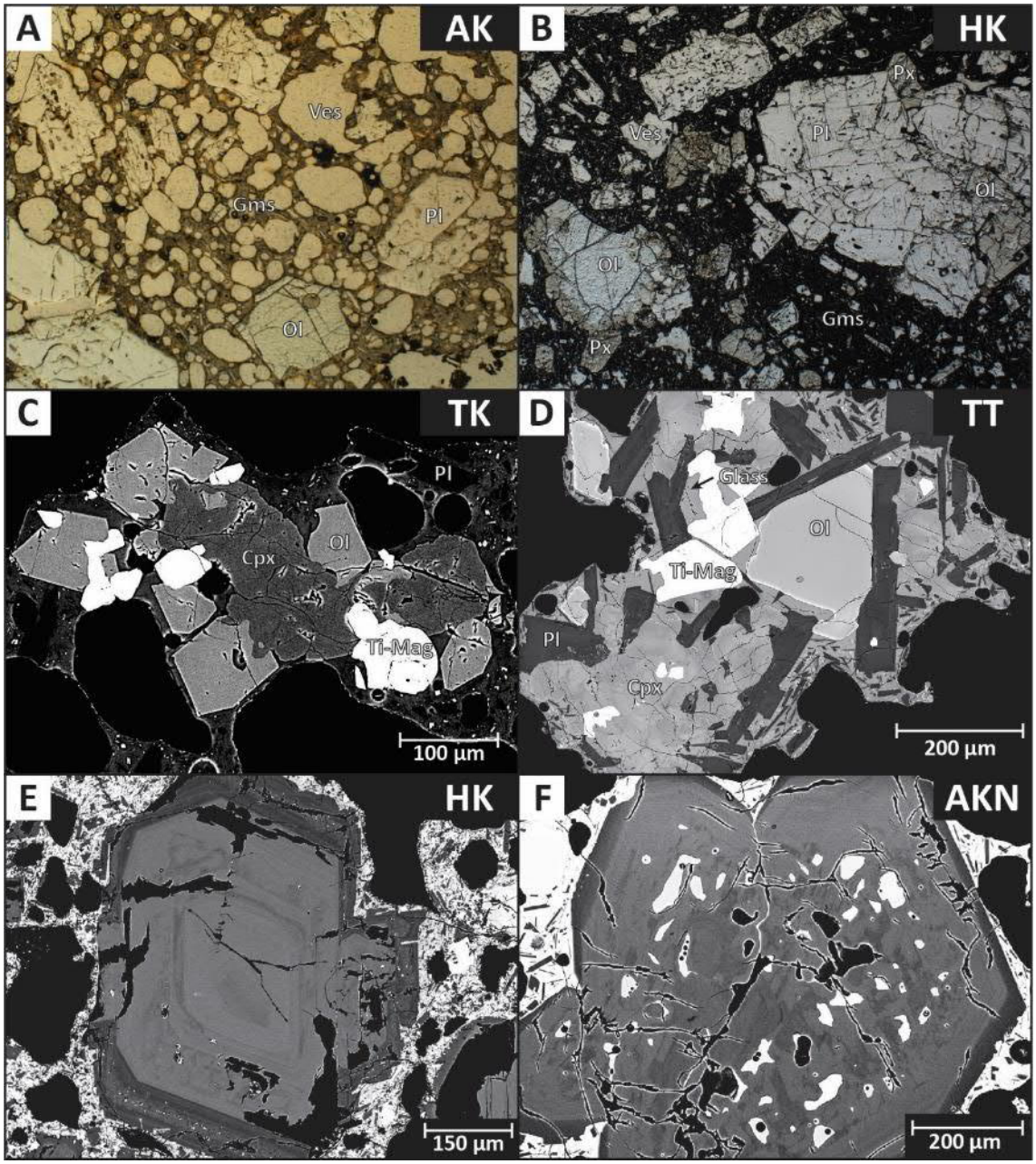

Figure 5.2. (A) and (B) Thin section microphotographs (plane-polarised) of AK and HK tephras. (C) and (D) BSE images of crystal clots from TK and TT sample. (E) and (F) BSE images of characteristic plagioclase texture found in all samples: Wide An-rich core with narrow An-poor rim (see text).

The Pl phenocrysts reach a maximum size of *c.* 2.5 cm and most of them are composed of a wide An-rich core (An_{76-91}; AK-Pl1 in Figure 5.3b) and a narrow less anorthitic rim (An_{65-75}; AK-Pl2). The Pl cores usually present oscillatory zoning and resorption and regrowth textures. Some cores also host MIs or have a sieve texture. Rims display oscillatory or normal zoning. The Cpx crystals are augites (Aug) that are usually small (<100 μm) and found associated with the group of smaller Ol crystals. They are typically zoned with low-Ca compositions towards the rims. The Cpx crystals are then divided into two compositional groups regarding their Ca content: the high-Ca group related to the cores (AK-Px1 in Figure 5.3c) and the low-Ca group related to the rims in zoned crystals (AK-Px2).

5.5.1.2 Hakkoda

The HK tephra sample is composed of a crystal-rich groundmass (*c.* 71 vol% on vesicle free basis), hosting larger Pl (*c.* 84 vol% of the crystal cargo), Ol (*c.* 4 vol%) and pyroxene (Px; *c.* 12 vol%) crystals (Figure 5.2b). Crystal clots formed by all mineral phases present in this rock are very common. HK have two distinct Ol compositional groups. The most abundant group has a composition of $Fo_{76.4-79.7}$ (HK-Ol1 in Figure 5.3a), which consists of normally zoned Ol crystals usually found in big crystal clots with Pl, Cpx and Opx. Most MIs were found on Ol hosts of this group. The second group corresponds to Ol compositions of $Fo_{68.8-73.1}$ (HK-Ol2), which are mostly related to Ol remnants found inside big Opx crystals and Ol crystals with Opx coronas. The largest Pl crystals reach *c.* 3 mm in size and present a texture similar to the Pl phenocrysts of the AK sample (Figure 5.2e). They are composed of a wide core of An_{84-95} (HK-Pl1 in Figure 5.3b) with common resorption textures and oscillatory zoning and a narrow rim of An_{70-81} (HK-Pl2).

Both Opx and Cpx are abundant and common constituents of crystal clots and are also found as isolated crystals. Px crystals are classified into three compositional groups. The most abundant compositional group, HK-Px1 (Figure 5.3c), corresponds to most phenocrysts found in HK, which include the high-Mg and high-Ca Aug and their rims of low-Ca and low-Mg. The HK-Px2 group mainly consists of Opx and scarce Cpx related to crystals associated with coronas and reaction rims around Ol crystals of HK-Ol2 and overlaps in composition with the low-Ca and low-Mg compositions of HK-Px1. The HK-

Px3 group consists of Cpx and Opx crystal cores of higher Fe content, which are surrounded by more Mg-rich regrowth zones represented by HK-Px1.

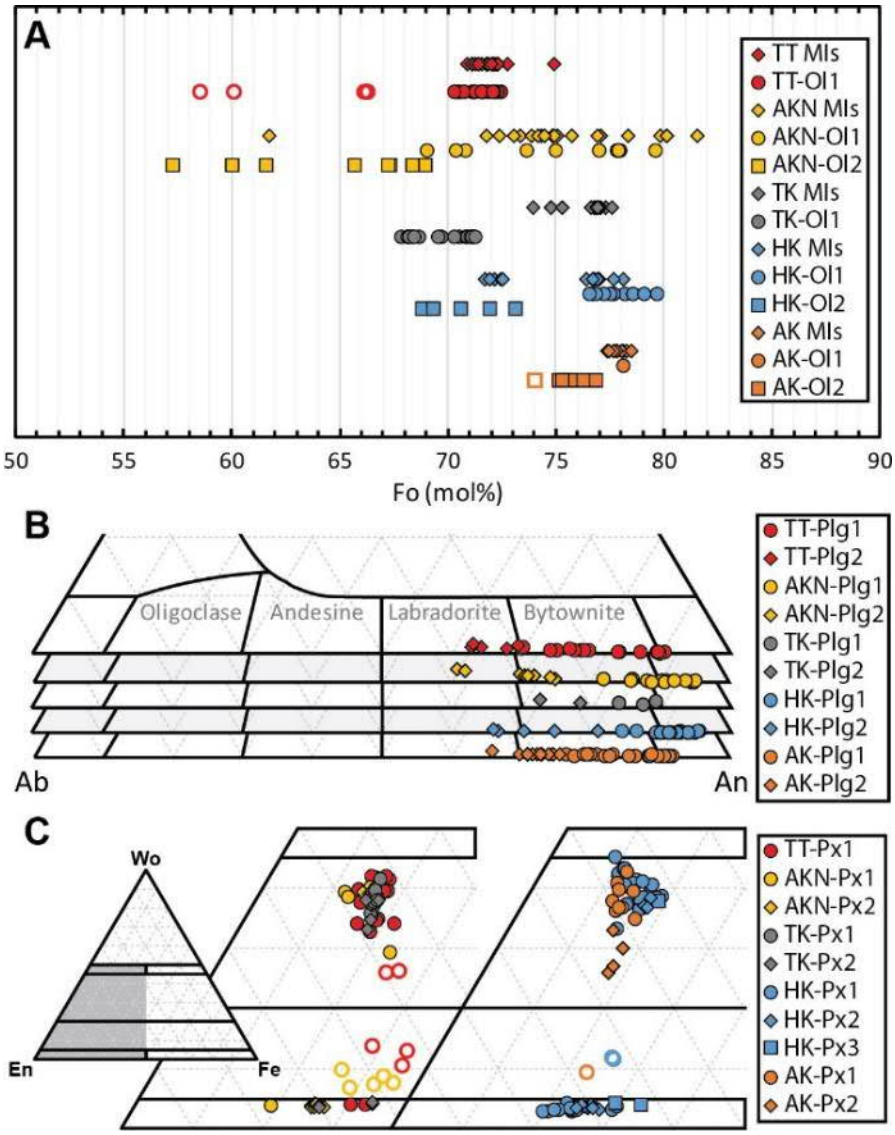

Figure 5.3. Compositions of (A) olivine, (B) plagioclase and (C) pyroxene crystals for the five tephra samples. Each colour represents one of the volcanic systems following the same colour scheme as in Figure 5.1. Hollow symbols indicate groundmass or outer rim compositions related to the ascent and eruption event. Compositional groups are defined in the main text. Diamonds in (A) indicate the olivine compositions of the crystals hosting MIs and can belong to any of the olivine groups defined by the thin sections.

5.5.1.3 Tokachidake

The TK tephra sample is constituted by a glass-rich groundmass (*c*. 61 vol% on a vesicle free basis) and phenocrysts of Pl (*c*. 75 vol% of the crystal cargo), Cpx (*c*. 11 vol%), Ol (*c*. 7 vol%), titanomagnetite (T-Mag; *c*. 6 vol%) and scarce Opx. Crystal clots are very common and can be composed of all mineral phases found in this sample.

As with the previous tephra sample, Pl phenocrysts consist of a wide An-rich core (An_{87-91}; TK-Pl1 in Figure 5.3b) with common sieve texture, oscillatory zoning or resorption and regrowth textures, followed by narrow rims of An_{72-79} (TK-Pl2).

TK also has two distinct Ol compositional groups (Figure 5.3a). The higher forsterite group ($Fo_{74.0-77.6}$) corresponds to the bigger isolated crystals that host the MIs with homogeneous core compositions and narrow normal zoned rims. The second compositional group ($Fo_{67.8-71.3}$) includes smaller euhedral crystals associated with clots that also include pyroxene and Ti-Mag (Figure 5.2c), anhedral crystals with Opx and Cpx coronas, and Ol inclusions in Cpx crystals. Aug is the most abundant pyroxene phenocryst type. It is present as large subhedral crystals with Ol inclusions in Cpx + Ti-Mag crystal clots and small anhedral crystals in Ol + Cpx + Ti-Mag crystal clots (TK-Px1 in Figure 5.3c). Aug crystals with lower Ca content and scarce Opx are present as coronas surrounding anhedral Ol crystals (TK-Px2).

5.5.1.4 Akan-fuji

Two main types of rock fragment types are present in the AKN tephra sample. Fragment type 1 consist of a crystal-rich groundmass (*c.* 48 vol% on a vesicle free basis) mainly composed of Pl, pigeonite (Pgt) and Ti-Mag, with Ol (*c.* 4 vol% of the crystal cargo) and Pl (*c.* 96 vol%) phenocrysts. Fragment type 2 has a glass-rich groundmass (*c.* 75 vol% on a vesicle free basis) with Pl (*c.* 86 vol% of the crystal cargo), Ol (*c.* 13 vol%) and Px (<1 vol%) phenocrysts.

The Pl phenocryst of the AKN sample can also be divided into two main groups (Figure 5.3b). One with a wide An-rich core (An_{81-95}) with common oscillatory zoning and sieve texture that is surrounded by a narrow less anorthitic rim (An_{60-75}) (Figure 5.2f). The other can be found in fragments of type 1, where cores are homogeneous and normally zoned, without displaying any disequilibrium textures. Unlike the other samples, AKN presents a wide range of Ol compositions (Figure 5.3a). The higher Fo group (Fo_{71-82} AKN-Ol1) corresponds to the Ol crystals found in fragments of type 2. They are represented by euhedral to subhedral crystals, isolated or in Ol + Pl clots, and by anhedral crystals in Cpx + Ol clots. Most core compositions of these crystals are homogeneous with slight normal zoning in the rims. A few crystals found in this sample present a normally zoned core

followed by inverse zoning towards the rim. The AKN-Ol2 group consists mainly of low Fo (Fo_{58-71}), normally zoned Ol crystals with Pgt coronas found in fragments of type 1. This Ol group also includes olivine inclusions in big Px crystals.

Px crystals found in type 1 fragments show widespread disequilibrium textures. Cpx and Opx are found making up the same big tabular Px crystals as patches of contrasting Ca content (AKN-Px2 in Figure 5.3c). These crystals have Pgt rims of the composition of groundmass Pgt crystals and Ol inclusions. Opx is also found as reaction patches in some Ol crystals in type 1 fragments. Cpx is found in Cpx + Ol + Pl crystal clots of type 2 fragments (AKN-Px1). Some of these Cpx in clots include scarce and small Opx patches.

5.5.1.5 Tya-Tya

The TT sample has the lowest crystallinity of all 5 tephra samples (*c*. 84 vol% groundmass on a vesicle free basis). The crystal cargo is composed of Pl (*c*. 77 vol% of crystal cargo), Px (*c*. 9 vol%), Ti-Mag (*c*. 8 vol%) and Ol (*c*. 6 vol%). Crystal clots of Ol + Cpx + Pl + Ti-Mag are abundant in this sample.

The Pl phenocrysts of the TT sample have textures similar to those in the other samples. Big plagioclase phenocrysts are composed of a wide An-rich core (An_{74-90}) surrounded by narrow An-poor rims (An_{63-70}). This type of plagioclase is in clots with smaller Ol, Cpx and Ti-Mag crystals growing from their rims in contact with the An-poor section of the Pl crystals. There is another Pl group associated with the crystal clots. This group consists of smaller elongated crystals in clots, similar in sizes to the other mineral phases in the clots (Figure 5.2d). These Pl crystals display oscillatory zoning of An_{63-70}.

Ol phenocrysts found in this sample have a narrow compositional range of $Fo_{70.3-72.8}$, with an outlier of Fo_{75}. Ol phenocrysts are usually present as subhedral crystals in crystal clots, in some cases with embayment textures. Ol core compositions are homogeneous with narrow less forsteritic rims. Few Ol crystals show a wider Fo-rich rim with the development of a Pgt corona.

Px phenocrysts consists mostly of Aug with scarce Opx. They usually are associated with Ol + Pl + Cpx + Ti-Mag clots, but the largest crystals found are associated with Ol-free clots. Px compositions are shown in Figure 5.3c.

5.5.2 MI textures

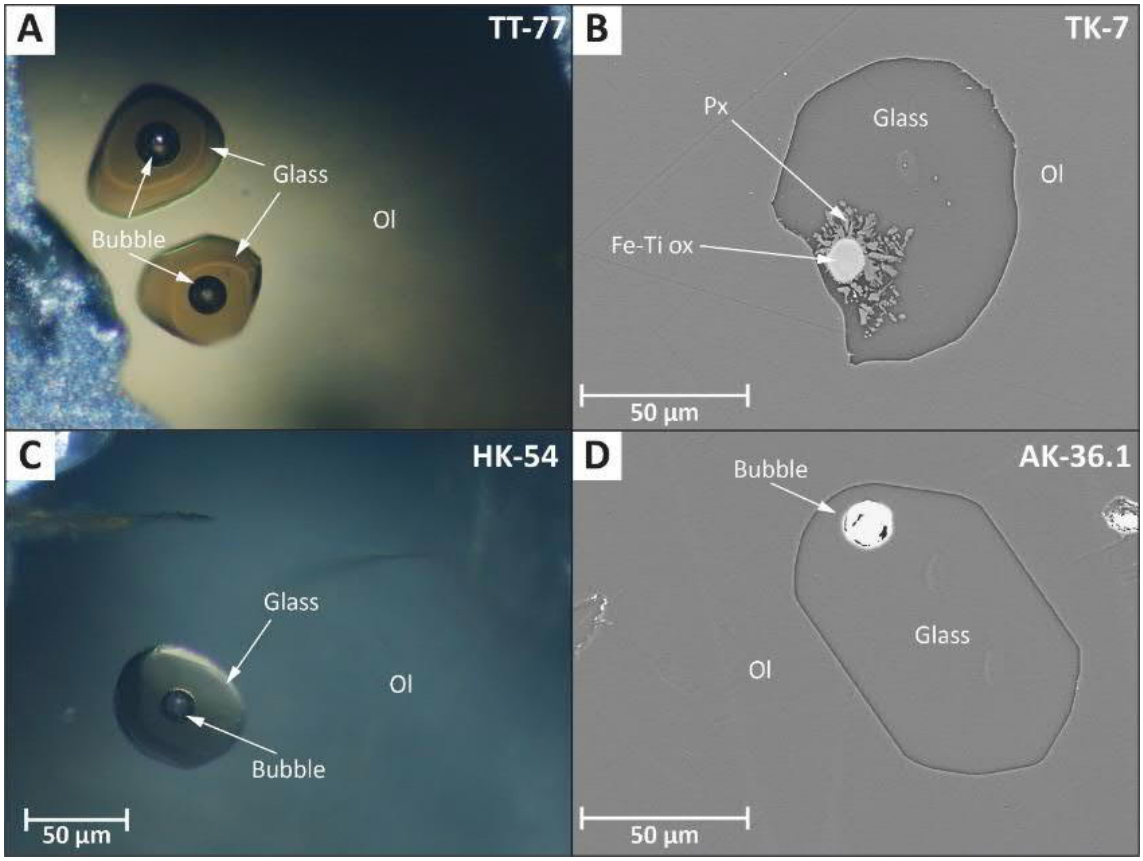

Figure 5.4. (A) and (C) show microphotograph of melt glassy inclusions in an olivine crystal with shrinkage bubbles. (B) BSE image of exposed MI from the TK sample with a Fe-Ti oxide crystal from where daughter pyroxene crystals grew. (D) BSE image of an exposed glassy MI from the AK sample.

Most analysed MIs are glassy with no daughter minerals and with a shrinkage bubble (Figure 5.4). Table 5.1 shows the number of MIs for each sample, the size range for the MIs, their shrinkage bubbles and their Ol hosts.

Unlike the other samples, the TK MI population is not completely glassy. Most of these MIs contain a big Fe-Ti oxide crystal (Figure 5.4b), which given their size, may have been entrapped during MI formation. Some Px daughter crystals have nucleated on and grown from the Fe-Ti oxide walls, which may have affected the glass compositions measured in the TK MIs in some cases. Details of MI dimensions can be found in Appendix 4.

Table 5.1. Number of MIs and their size ranges , together with the size ranges of shrinkage bubbles and their olivine host crystals, in each sample.

	Quantity	Size ranges		
Sample units	**MIs**	**Bubble** % of MI volume	**MI** μm^3	**Ol host** μm^3
AK	19	3.2 - 4.8	2.1×10^3 - 9.4×10^6	2.4×10^8 - 8.6×10^8
HK	13	1.6 - 3.9	2.3×10^4 - 1.0×10^7	1.4×10^8 - 2.5×10^9
TK	20	1.4 - 10.6	1.5×10^4 - 2.7×10^7	6.2×10^7 - 1.2×10^{10}
AKN	27	0.0 - 5.9	1.1×10^4 - 1.1×10^6	4.1×10^7 - 5.5×10^8
TT	26	2.8 - 4.4	1.5×10^4 - 2.3×10^6	2.4×10^7 - 4.0×10^8*

*Except one outlier host at 1.8×10^9 μm^3.

5.5.3 Whole rock and glass geochemistry

All tephra samples are subalkaline and have basaltic to basaltic-andesitic compositions (*c.* 50.8 wt% to *c.* 52.8 wt%; Figure 5.5). The samples from the NE Japan arc (AK and HK) are low in alkalis (c. 2 wt% $Na_2O + K_2O$), with a tholeiitic signature. The available glass compositions of HK and AK (Ol-hosted MIs, Pl-hosted MIs and groundmass) are all richer in SiO_2 than the whole-rocks. The Kuril arc samples have a calc-alkaline signature, with higher alkali concentrations (*c.* 3 wt% and *c.* 3.7 for TT and TK). The

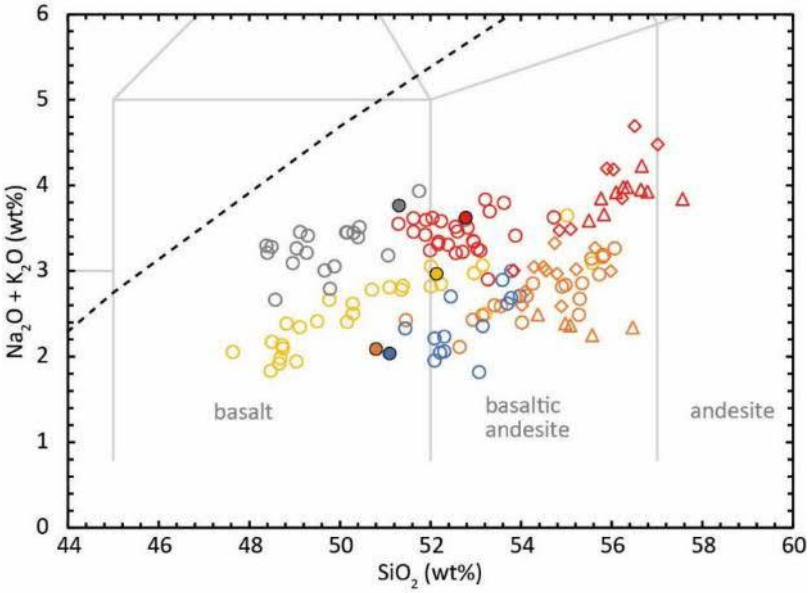

Figure 5.5. Total Alkali Silica (TAS) diagram showing the whole rock and glass compositions of the five tephra samples normalised to 100 on an anhydrous basis. Colour scheme is the same as in Figure 5.1. Filled circles are the whole-rock compositions. Hollow circles are the measured glass compositions of Ol-hosted MIs, diamonds are the glasses from Pl-hosted MIs and triangles are glass compositions from the groundmass.

glass compositions from the Ol-hosted MIs of these samples overlap in composition with the whole-rock, whereas Pl-hosted MIs and groundmass glass of TT are more differentiated. The MI glass major elements compositions are listed in Table 5.2. All compositional data including error estimations can be found in Appendices 2 and 3.

Table 5.2. Glass compositions of the MIs measured with EPMA (in wt%).

Sample	SiO_2	TiO_2	Al_2O_3	FeO_T	MnO	MgO	CaO	Na_2O	K_2O	P_2O_5	Total	Fo[1]
Akita-Komagatake												
AK-135	52.98	1.09	14.83	9.50	0.19	5.27	9.77	2.42	0.30	0.15	96.49	78.0
AK_136	52.54	1.16	16.18	9.47	0.16	2.51	10.48	2.00	0.36	0.19	95.06	78.0
AK-41.1	54.68	1.08	16.78	9.36	0.10	2.43	10.35	2.76	0.34	0.12	98.00	77.4
AK_137b	54.90	1.17	16.97	9.44	0.14	3.40	10.88	2.51	0.33	0.12	99.85	77.4
AK-42.1	53.24	1.10	15.29	10.36	0.14	5.57	9.43	2.46	0.34	0.19	98.12	77.8
AK-38.1	52.75	0.94	15.18	10.21	0.15	5.88	9.59	2.36	0.28	0.14	97.48	78.1
AK-36.1	50.29	0.84	15.73	11.56	0.14	6.57	10.13	2.15	0.22	0.10	97.74	78.3
AK-47.1	51.99	0.96	15.13	10.44	0.15	6.09	9.96	2.26	0.27	0.09	97.35	77.8
AK-143	55.16	1.30	17.25	8.42	0.16	2.12	10.62	2.81	0.40	0.15	98.39	78.1
AK_144	52.12	0.93	15.10	10.93	0.17	5.45	10.00	2.23	0.29	0.11	97.32	77.5
AK-145.2	51.16	0.94	15.28	10.32	0.20	6.19	10.10	2.13	0.22	0.11	96.63	77.5
AK_146	55.44	1.13	16.38	9.96	0.24	3.57	10.45	2.53	0.34	0.15	100.17	77.5
AK_148	54.35	1.12	15.89	9.92	0.17	3.71	10.26	2.28	0.35	0.25	98.28	77.5
AK_149	52.17	1.03	14.93	10.70	0.22	5.42	9.67	2.02	0.30	0.12	96.58	77.5
AK-151	54.35	1.08	15.98	9.33	0.19	4.12	9.46	2.54	0.35	0.14	97.53	77.9
AK-39.1	54.18	1.17	15.87	9.52	0.12	2.82	10.61	2.72	0.35	0.18	97.54	77.7
AK-153	51.44	0.97	15.50	11.05	0.18	6.30	10.07	1.86	0.20	0.13	97.71	78.5
AK-43.1	51.71	0.96	16.12	10.82	0.17	4.20	10.74	2.17	0.24	0.16	97.30	77.5
AK-43-53	54.56	1.12	16.56	9.29	0.14	2.53	10.24	2.74	0.37	0.19	97.72	77.5
Hakkoda												
HK-51	50.60	1.03	15.82	10.57	0.25	4.19	8.57	2.36	0.19	0.17	93.75	71.7
HK_52	50.51	1.01	16.55	11.33	0.18	2.61	9.08	2.27	0.25	0.12	93.90	72.5
HK_54	49.01	0.51	16.29	10.72	0.26	5.38	9.33	1.92	0.17	0.12	93.71	76.7
HK-30.1	50.35	0.95	18.65	9.83	0.14	2.73	10.64	2.38	0.21	0.12	96.00	77.0
HK-23.1	49.53	0.89	16.84	11.46	0.17	5.17	9.89	2.07	0.17	0.10	96.28	76.8
HK_57	49.00	0.86	15.91	11.12	0.19	5.40	9.66	1.69	0.15	0.09	94.07	76.4
HK_58	49.69	0.84	16.33	11.16	0.18	5.17	9.74	1.78	0.17	0.12	95.17	77.1
HK_59	51.63	1.11	17.63	11.05	0.21	2.58	9.22	2.50	0.29	0.13	96.34	72.6
HK_60	50.74	0.91	18.19	9.48	0.20	3.51	10.14	2.04	0.21	0.06	95.47	78.1
HK_61	49.36	0.80	16.39	11.14	0.17	5.05	9.45	1.75	0.20	0.09	94.38	77.0
HK_62	51.88	1.09	16.98	11.52	0.19	2.84	8.93	2.62	0.27	0.13	96.46	72.0
HK-34.1	49.57	0.83	15.99	10.78	0.13	6.18	9.45	1.94	0.17	0.13	95.16	76.7
HK-64	51.35	0.92	18.09	9.71	0.21	3.35	9.39	2.29	0.22	0.11	95.63	77.7
Tokachidake												
TK_01	46.08	1.11	18.17	9.58	0.16	5.02	11.56	2.53	0.59	0.23	95.03	76.9
TK_02	48.51	1.18	19.22	9.94	0.21	3.51	11.90	2.19	0.54	0.25	97.45	76.9

TK_03	48.42	1.16	21.07	7.46	0.16	2.09	12.08	2.76	0.61	0.20	96.01	76.8
TK-04	46.46	1.06	17.91	10.97	0.24	5.43	10.84	2.03	0.53	0.18	95.65	77.3
TK_06	48.04	1.17	19.73	8.65	0.18	2.75	11.72	2.76	0.55	0.23	95.76	77.1
TK-07	46.68	1.07	18.54	10.39	0.22	4.56	11.63	2.59	0.59	0.20	96.49	76.8
TK-08	46.75	1.11	18.55	10.81	0.19	3.86	11.97	2.48	0.63	0.24	96.58	76.8
TK_09	48.07	1.14	19.29	9.71	0.19	2.96	11.84	2.34	0.61	0.23	96.38	76.8
TK-10	47.21	1.13	19.05	9.87	0.19	3.59	11.52	2.73	0.59	0.22	96.11	76.8
TK_11	49.98	1.11	20.03	8.64	0.14	2.16	10.44	2.89	0.91	0.28	96.57	74.8
TK-12	47.63	1.04	18.64	10.25	0.18	3.80	11.64	2.73	0.57	0.15	96.64	76.6
TK_13	48.00	1.15	19.60	8.88	0.21	2.48	11.93	2.70	0.60	0.18	95.73	77.0
TK-14	46.99	1.04	18.77	9.80	0.20	5.15	10.88	2.35	0.61	0.17	95.97	76.8
TK_15	47.56	1.06	18.60	9.80	0.18	3.66	11.82	2.39	0.50	0.20	95.77	76.8
TK-16	51.10	1.44	16.98	10.41	0.22	4.44	8.59	2.34	1.14	0.19	96.85	74.0
TK-17	47.35	1.16	19.07	9.84	0.19	3.70	11.88	2.59	0.56	0.19	96.54	76.7
TK-18	47.71	1.07	18.74	10.43	0.20	3.91	11.41	2.56	0.55	0.27	96.85	76.8
TK-19	48.60	1.08	19.16	9.49	0.18	2.67	11.76	2.70	0.58	0.21	96.42	76.9
TK_23	48.47	1.04	17.60	10.66	0.19	4.93	9.95	2.58	0.75	0.21	96.36	75.3
TK_24	49.18	1.48	19.60	9.30	0.15	2.23	11.06	2.24	0.83	0.25	96.30	75.3
Akan-fuji												
AKN_95	47.05	0.88	16.89	12.18	0.22	4.90	10.59	1.94	0.36	0.06	95.05	74.9
AKN_100	48.00	0.86	18.12	10.46	0.19	5.06	11.11	2.07	0.50	0.08	96.44	79.9
AKN_101	48.41	0.94	15.60	13.68	0.30	4.98	9.78	1.99	0.42	0.17	96.26	73.4
AKN_102a	48.81	0.99	16.59	12.27	0.21	3.21	10.50	2.18	0.50	0.26	95.52	73.4
AKN_112	48.23	0.90	16.48	13.20	0.18	3.93	10.37	2.01	0.50	0.11	95.92	72.4
AKN-117	49.72	0.91	15.72	11.81	0.18	5.07	9.19	2.27	0.65	0.07	95.60	73.1
AKN_118	48.42	0.99	16.61	12.50	0.23	3.73	10.22	2.19	0.47	0.14	95.49	73.1
AKN_123	49.30	0.88	17.41	10.68	0.23	4.41	10.30	2.06	0.62	0.12	95.99	78.4
AKN_124	47.57	0.74	16.32	12.78	0.23	5.16	9.70	1.82	0.46	0.07	94.85	73.9
AKN-94	49.96	0.89	16.54	12.49	0.20	3.57	10.66	2.15	0.60	0.14	97.21	71.8
AKN_97	53.19	1.39	13.68	14.58	0.26	2.28	7.58	2.49	1.04	0.20	96.68	61.8
AKN-99	52.00	0.80	15.96	11.63	0.22	5.17	8.95	2.25	0.74	0.12	97.83	74.4
AKN-105	54.04	1.08	14.57	10.76	0.20	4.75	8.74	2.18	0.82	0.09	97.23	75.1
AKN_106	50.36	0.96	15.66	11.50	0.27	5.19	10.06	2.11	0.62	0.09	96.82	77.1
AKN-116	51.45	0.94	15.52	11.38	0.18	5.16	9.50	2.31	0.58	0.14	97.15	75.8
AKN_122	50.99	0.96	14.93	11.06	0.17	5.17	10.08	1.83	0.56	0.10	95.84	74.9
AKN_132c	51.03	0.98	16.08	12.68	0.24	4.39	10.67	2.36	0.60	0.10	99.13	74.5
AKN_108	47.33	0.85	17.94	10.69	0.19	5.61	11.39	1.90	0.37	0.09	96.36	80.1
AKN_120	45.13	0.84	18.78	9.94	0.14	5.46	12.42	1.71	0.24	0.08	94.74	81.6
AKN_130a	46.69	0.85	16.39	13.58	0.22	4.75	12.03	1.50	0.27	0.05	96.33	74.5
AKN_130b	46.84	0.78	16.58	13.31	0.19	5.04	11.63	1.79	0.31	0.11	96.57	74.5
AKN_130c	47.04	0.87	17.24	13.03	0.23	3.54	12.47	1.78	0.28	0.06	96.54	74.5
AKN_130d	46.30	0.86	16.87	12.49	0.25	4.02	12.33	1.59	0.29	0.09	95.09	74.5
AKN_130e	46.37	0.82	16.50	13.05	0.23	4.74	11.69	1.52	0.31	0.06	95.30	74.5
AKN-131a	46.86	0.86	17.37	12.44	0.20	3.74	12.21	2.01	0.28		95.98	74.5
AKN-132a	46.56	0.79	17.09	12.43	0.25	4.38	11.95	1.72	0.28	0.06	95.51	74.5
AKN_134b	47.20	0.88	18.18	12.16	0.25	3.43	12.21	1.56	0.31	0.07	96.25	74.5
Tya-Tya												
TT-67.10	50.62	1.13	16.11	12.86	0.18	3.71	9.22	2.89	0.62	0.21	97.53	71.6

TT-67.2	52.45	1.22	15.70	12.49	0.19	3.84	8.74	2.98	0.80	0.16	98.58	70.9
TT-68.1	50.44	1.04	15.46	12.42	0.17	4.52	8.87	2.61	0.58	0.19	96.29	71.1
TT-68-75	51.88	1.13	15.52	11.75	0.18	4.20	8.87	2.99	0.61	0.20	97.32	71.1
TT-68-76	50.99	1.18	17.08	12.17	0.20	2.80	9.79	2.91	0.64	0.21	97.97	71.1
TT-71	50.61	1.10	16.13	12.36	0.23	4.17	9.02	2.67	0.54	0.19	97.02	71.9
TT-72	50.13	1.07	15.51	11.17	0.19	4.91	8.82	2.55	0.52	0.25	95.10	72.3
TT-73.2	50.49	1.12	15.61	11.13	0.24	4.44	8.93	2.71	0.49	0.20	95.36	72.3
TT-74	51.27	1.17	16.58	11.62	0.23	3.23	9.32	2.90	0.51	0.24	97.06	72.3
TT-75	51.23	1.12	16.47	11.73	0.22	4.25	9.17	2.60	0.53	0.16	97.47	71.8
TT_76	50.73	1.16	16.60	11.58	0.21	3.50	9.11	2.69	0.65	0.21	96.45	71.8
TT_77	50.26	1.08	15.87	12.20	0.21	4.35	8.98	2.62	0.60	0.17	96.32	71.8
TT-78	50.28	1.07	15.79	11.46	0.26	4.50	8.78	2.78	0.58	0.16	95.67	71.8
TT-79	51.50	1.21	17.46	10.17	0.18	2.07	9.63	3.03	0.62	0.17	96.05	72.8
TT-80	50.19	1.17	16.97	11.95	0.25	3.87	9.73	2.91	0.56	0.25	97.85	72.1
TT-81	50.36	1.11	16.63	12.21	0.23	3.91	9.52	2.85	0.53	0.20	97.55	72.1
TT-82	50.68	1.18	16.08	11.40	0.26	3.31	9.31	2.55	0.56	0.24	95.57	72.2
TT_83	53.17	1.27	16.99	10.09	0.19	2.39	9.35	2.82	0.71	0.19	97.16	72.2
TT-85	50.87	1.12	15.83	11.41	0.23	3.89	9.13	2.59	0.52	0.21	95.79	72.3
TT-86	50.07	1.09	15.73	12.66	0.26	3.90	9.26	2.59	0.54	0.20	96.31	72.3
TT-89	50.60	1.14	16.39	12.34	0.20	4.39	8.92	2.74	0.60	0.20	97.52	71.9
TT_90	49.00	1.26	17.59	11.20	0.20	2.35	9.65	2.74	0.70	0.24	94.92	71.3
TT_91	50.83	1.04	16.30	11.42	0.21	3.62	9.04	2.15	0.62	0.19	95.42	72.0
TT-66.1	50.99	1.07	15.57	11.64	0.18	4.70	8.75	2.61	0.61	0.20	96.29	71.4
TT_92b	51.85	1.10	15.74	11.47	0.25	3.71	8.65	2.60	0.69	0.20	96.23	71.4
TT-65.1	50.60	1.11	19.13	9.33	0.13	2.17	10.75	2.99	0.48	0.20	96.88	75.0

[1]Forsterite content of olivine host

5.6 Discussion

5.6.1 MI corrections

Corrections were performed to each MIs to estimate pre-eruptive compositions of major and volatile components. The term “pre-eruptive” is used here instead of “initial” for the corrected MI compositions because, as discussed below, in most samples the MIs and their host show evidence of being completely re-equilibrated with the surrounding melt to fixed Mg# (magnesium number) in equilibrium with a narrow range of Fo values. As the process of MI correction reconstructs the composition to its last stage of equilibrium,

the results are interpreted as the compositions at storage conditions before remobilization and eruption (Brahm et al., 2021, Chapter 4).

A modified version of the MIMiC program (Rasmussen et al., 2020) was used to apply a combined correction scheme for PEC, Fe-loss, CO_2 loss to the shrinkage bubble and H_2O diffusive loss. MIMiC combines the classic PEC corrections schemes for Ol-hosted MIs (for PEC and Fe-loss) in a similar manner as previously applied with the Petrolog3 program (Danyushevsky and Plechov, 2011): equilibrium Ol is added to the MI composition until reaching equilibrium with the host Ol. Fe-loss is adjusted by iterative steps of Fe-Mg exchange and Ol addition until the iron content defined by the user is reached (see details in Danyushevsky et al., 2000; Rasmussen et al., 2020). The Mg-Fe distribution coefficient ($K_{D\,Ol-melt}^{Mg-Fe}$) is calculated with the Toplis (2005) model and the temperature is estimated using the Ol-melt thermometer of Putirka et al. (2007). The Fe^{3+} content of the melt is treated as an incompatible component during Ol crystallization in a closed system. The biggest MI in each sample, which have flat BSE grey scale profile plateaus and are coincident with the MI predicted to have the least PEC are used to adjust the f_{O_2}conditions of the melt. The Fe speciation of each MI in a sample is set to the value for which 0 wt% of PEC is predicted for the MI expected to have suffered negligible PEC. At higher oxidation conditions PEM would be required, whereas PEC estimates would increase at lower f_{O_2}.

Corrections for CO_2 lost to the bubble are performed by applying a calculated-volume approach to model the vapor-bubble growth that accounts for diffusive limitations of CO_2 addition to the vapor bubble and differential deformation of the melt and host (see details in Rasmussen et al., 2020). Sample dimensions (host, MI and vapor-bubble) or cooling rate estimations are needed for the application of this model. Here estimated dimensions are used, measured using optical microscope and BSE images of the exposed MIs. Vapor bubbles were assumed to be perfect spheres, MIs and Ol-hosts are assumed to be ellipsoids with the dimension perpendicular to the observed plane having a radius equal to the smallest measured radius in the observed plane. Uncertainties (1σ) on these measurements are estimated to be 1.6 vol% for vapor-bubbles, 3 μm for the average diameter of the MIs, and 10 μm for the average diameter of the olivines. These uncertainties were estimated by performing repeated measurements from the images. One of the modifications made to the original MIMiC program was the implementation of the

H_2O-CO_2 solubility model of Papale et al. (2006) instead of the VolatileCalc model (Newman and Lowenstern, 2002). This modification was necessary as many of the MI compositions in this study are outside the SiO_2 range of the VolatileCalc parametrization of basaltic compositions (i.e. their SiO_2 content exceeds 52 wt%). This model was selected because of its versatility of compositions compared to other models restricted to basic or silicic melts. It was also chosen as it does not include other volatile components (e.g., S, Cl), simplifying calculations, and also because it was easy to implement into the MIMiC script.

The original H_2O content of the MIs is estimated using the $D_{CaO}^{Ol-melt}$-dependent hygrometer of Gavrilenko et al. (2016a). This model is implemented in the MIMiC program by performing iterative calculations of the MI corrections followed by H_2O estimations using the corrected MI compositions and the measured host Ol Ca content. The first iteration uses the measured H_2O content, followed by a second iteration where the H_2O content of the uncorrected composition is updated to the new H_2O estimated value, adjusted by the amount of PEC predicted in the previous correction stage. This process is repeated until the estimated H_2O content converges (usually after 3 or 4 iterations). Uncertainties of the H_2O estimations (1σ) are set to 1.1 wt% (Gavrilenko et al., 2016a). Uncertainty estimations of MIMiC results are obtained through Monte Carlo simulation of 50 iterative calculations of each MI correction, applying the defined uncertainties of all input values (melt and olivine compositions, as well as bubble, MI and Ol-host sizes).

Corrections were first applied without any Fe-loss correction and the corrected compositions were assessed for evidence of "Fe-loss" indicators. The MIs of each tephra sample with the exception of AKN are hosted in a very narrow range of olivine compositions, whereas their range in oxides, like SiO_2 or K_2O, indicates substantial amounts of differentiation within the MI compositions. This results in a MgO vs. FeO_T trend at nearly constant Mg#. The Fe-loss correction displaces MI compositions along a constant Mg# line, making Fe-loss difficult to estimate just by observing the MgO vs FeO_T trends. Figure 5.6 shows MgO vs. FeO_T and SiO_2 vs FeO_T compositions of the uncorrected and corrected MI trend. The size of the symbols in these diagrams are proportional to the size of the MI, and the distance between the corrected and uncorrected

MIs (marked by the dotted line) is proportional to the calculated PEC amount (wt%). It is seen that there is no clear correlation between FeO_T content and the MI size as there are small MIs with higher FeO_T contents than bigger MIs with similar SiO_2 contents. This indicates that Fe-loss is negligible during PEC triggered by ascent and eruption, and that

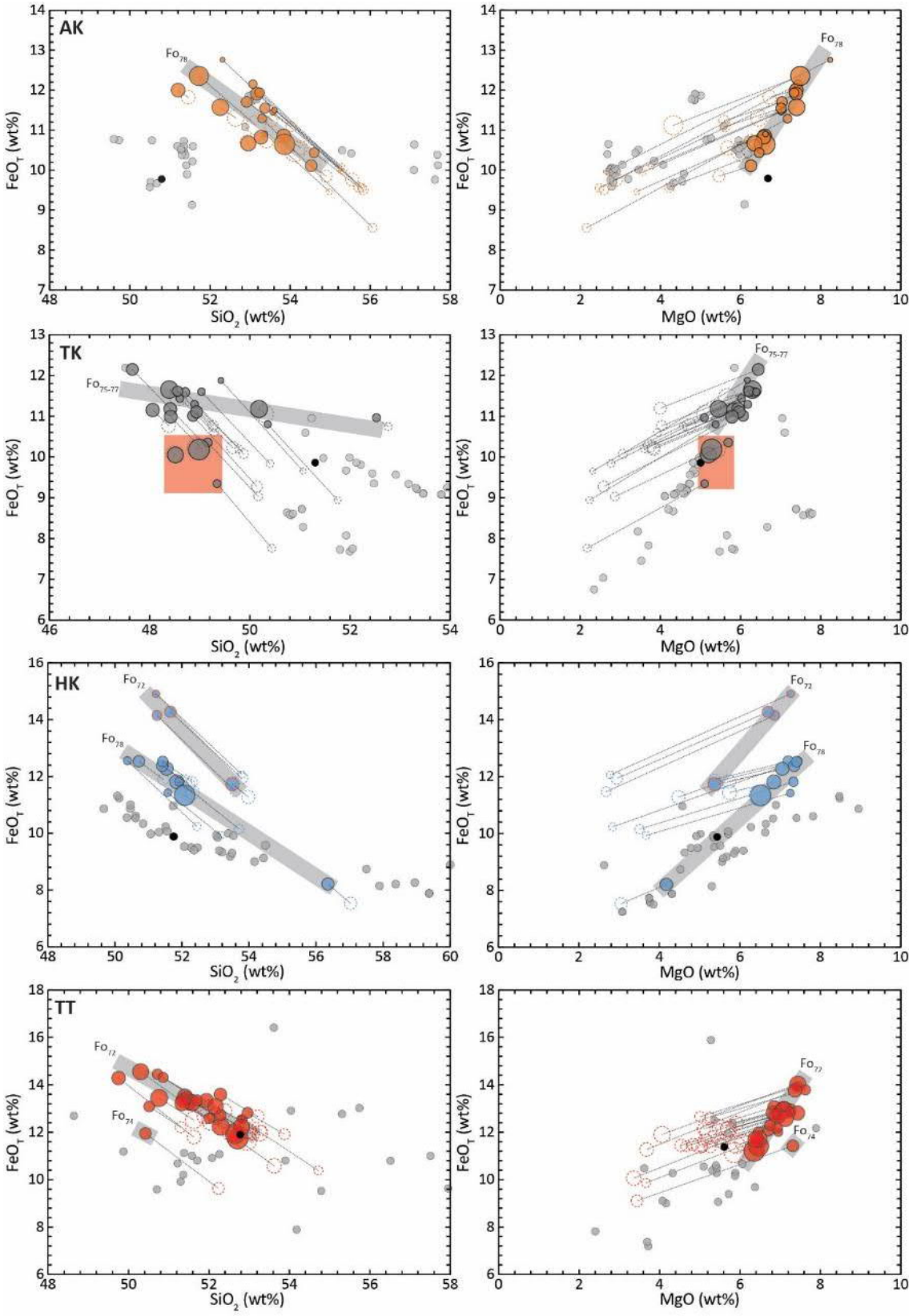

Figure 5.6. Harker diagrams of PEC-corrected MI compositions. Filled circles correspond to the corrected MI compositions, hollow circles correspond to the uncorrected MI compositions. Black small circle is the whole rock composition of each tephra sample and grey small circles are whole rock data from literature. The size of the circles is proportional to the size of the MIs. The dotted black lines connect the corrected and un-corrected MI compositions and the length is proportional to the amount of PEC. The grey bands indicate the trends of different populations of MIs defined by the compositions of their Ol hosts. The red area in the TK sample indicates the MI compositions affected by crystallization of daughter pyroxene crystals.

the constant Mg# trends observed in Figure 5.6 are product of the re-equilibration of MIs trapped at different stages of melt differentiation to a constant #Mg of the surrounding melt during prolonged storage times (, Chapter 4Brahm et al., 2021). As Fe-loss is promoted for slow cooling rates, it can be expected that most Fe-loss occurs through PEC during storage. Since the MIs reached equilibrium before eruption and the PEC triggered during ascent and eruption of tephras is typically fast (0.1 to 3 m/s; compilation in Browne and Szramek, 2015), it is expected that MIs show little to no evidence for Fe-loss. All PEC-corrected MI compositions are available in the Appendix 4.

Akita-Komagatake. All MIs from AK belong to the same Fo group ($Fo_{\sim 78}$) and appear to follow the same FeO_T vs SiO2 trend.

Hakkoda. In the corrected MI from HK (Figure 5.6) two trends can be distinguished with distinct FeO_T concentrations. These trends distinguish two distinct compositional Ol populations ($Fo_{\sim 72}$ and $Fo_{\sim 78}$).

Tya-Tya. In the TT sample, the MI hosted in an outlier Ol of Fo_{74} (interpreted as a xenocryst) can be distinguished from the main trend of constant Fo_{72}.

Tokachidake. During MI corrections of the TK sample, the small amount of daughter crystals that nucleated from the Fe-Ti oxides inside the MIs is assumed to have little effect on the MI composition. Trend analysis of the corrected MIs show a group of four MIs that are depleted in Fe and Mg with respect to the trend that the rest of the MIs in TK. These MIs are interpreted to be the most affected by the crystallization of daughter Px crystals and are excluded from further analysis.

Akan. The analysis of the AKN MIs is more complex. From the petrography of the tephras, it is clear that there must have been mingling (and probably mixing) between two magma batches before eruption, generating two distinct tephra types. The Ol compositional range is very wide in comparison with the other samples and at first glance it is hard to distinguish the provenance of the Ol crystals from the two magma batches. PEC-corrected MI compositions (Figure 5.7) show two distinct behaviours. A clear correlation between SiO_2 increase with Fo decrease is observed for MIs in Ol hosts of Fo_{76-82}, which also follow an increasing trend in FeO_T with SiO_2 and a decreasing trend of MgO and Al_2O_3. This differentiation path is compatible with fractionation of an Ol + Pl (± Px) assemblage. A contrasting behaviour is observed for the MIs hosted in Ol hosts of Fo_{72-75}, where there is no correlation of Fo content with SiO_2, but there is a decrease of

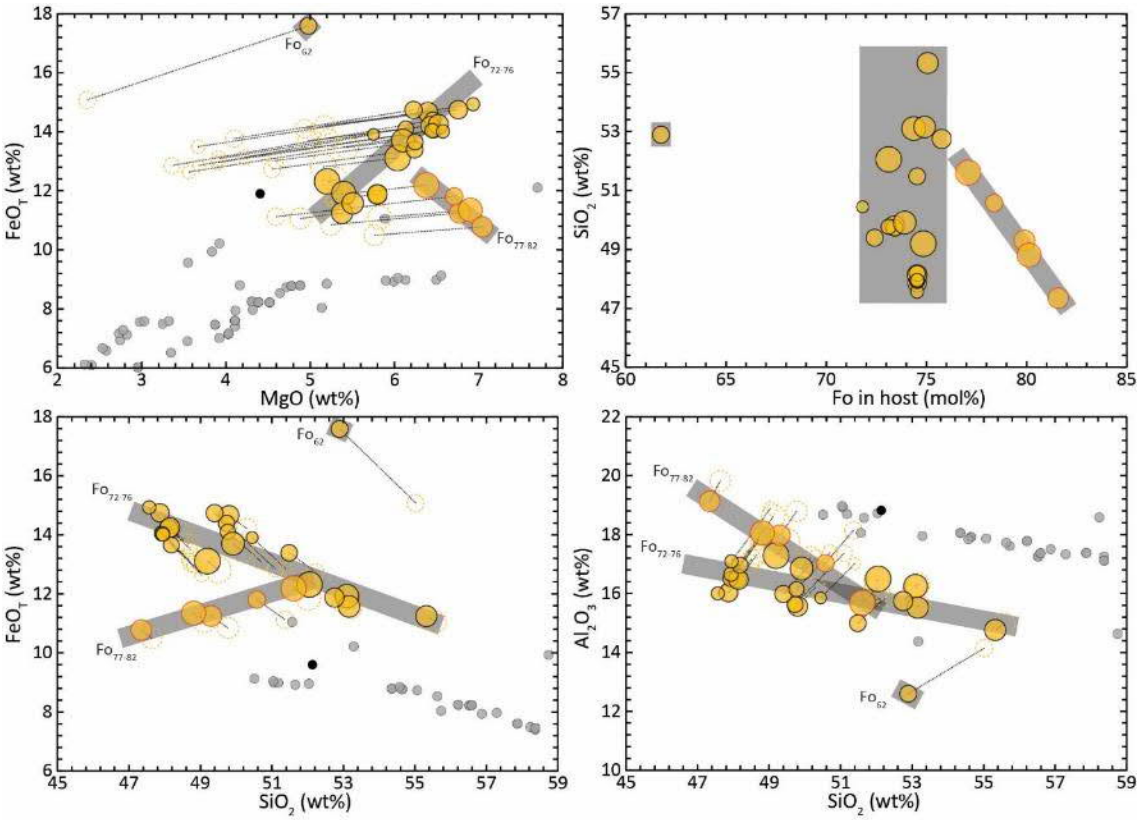

Figure 5.7. Harker diagrams of PEC-corrected MI compositions from the AKN sample. Symbols are the same as Figure 5.6.

FeO_T and MgO with SiO_2, and the Al_2O_3 decrease is less steep than in the other MI group. Here, the latter MI group is interpreted as those hosted in long-stored Ol crystals, which have reached equilibrium with the stored melt, whereas the former MI group is interpreted as MIs recently trapped in Ol crystals coming from the new magma batch. The outlier MI is hosted in an Ol of Fo_{62}, which is interpreted as a xenocryst.

Figure 5.8a shows the corrected H_2O-CO_2 compositions of the MIs with the measured concentrations for comparison. The substantially higher H_2O contents predicted by the hygrometer indicates that all MIs have been significantly dehydrated. Dehydration could have occurred during ascent and eruption by diffusive loss of H^+, as it has been shown that timescales of H^+ diffusion in Ol are faster than for any other element (Hartley et al., 2015; Turner et al., 2017a). Corrected H_2O compositions from hygrometry range from *c.* 3.4 wt% to *c.* 7.4 wt%. The AK sample has the lowest H_2O concentrations (*c.* 3.4 wt% to *c.* 5.2 wt% H_2O), followed by AKN, HK and TT which overlap in H_2O concentrations (from *c.* 4.4 to *c.* 6.2 wt% H_2O, with one HK outlier of *c.* 6.8 wt%). The TK sample H_2O estimations are the highest (*c.* 6.2 wt% to *c.* 7.4 wt% H_2O). Corrected CO_2 compositions are <500 ppm for most MIs in all samples, with some higher concentrations (<1000 ppm) for some MIs of HK and TT. AKN shows the highest variability in CO_2 estimations, with about half of the MIs having concentrations in the range of 500 – 1000 ppm and an outlier of *c.* 1200 ppm.

5.6.2 Thermobarometry

The corrected major and volatile elements contents of the MIs allow the equilibrium temperature (Ol-melt thermometer of Putirka et al., 2007) and H_2O-CO_2 saturation pressures (Papale et al., 2006) to be estimated (Figure 5.8b). These indicate that the magmas where stored at variable depths in the upper crust (*c.* 100 – 300 MPa) at temperatures of *c.* 1030 – 1150 °C.

Available Cpx-Opx pairs from the AKN and HK samples were also used to estimate temperatures, employing the two-pyroxene thermobarometer of Putirka (2008) (equations 36 and 39). Three temperatures calculated for the AKN sample give 1041 to 1054 °C (±56 °C), which overlaps with the 1037-1095 °C range of the Ol-melt thermometry. Pressure estimates of the Px pairs range from 350 to 510 MPa (±320 MPa). Twenty-eight Px pair temperatures from the HK sample yield a 1003 to 1089 °C (±56 °C) range, also overlapping with the 1037-1113 °C range yielded by the corrected MIs. Pressure estimates of the Px pairs of HK define two distinct groups, a low-P group defined by most Px pairs of *c.* 310 – 510 MPa (±320 MPa) and a high-P group defined by a subgroup of

seven Px pairs of *c.* 590 – 660 MPa (±320 MPa). Even though all Px pair pressure estimates are higher than the estimated saturation pressures (<300 MPa) the high uncertainty of the two-pyroxene method makes most of its estimated pressures overlap with the saturation pressures. Higher pressures of the two-pyroxene system, especially in the high-P group of HK, may also be records of storage histories at deeper levels of the crust than the recorded by the saturation pressures of the OHMIs.

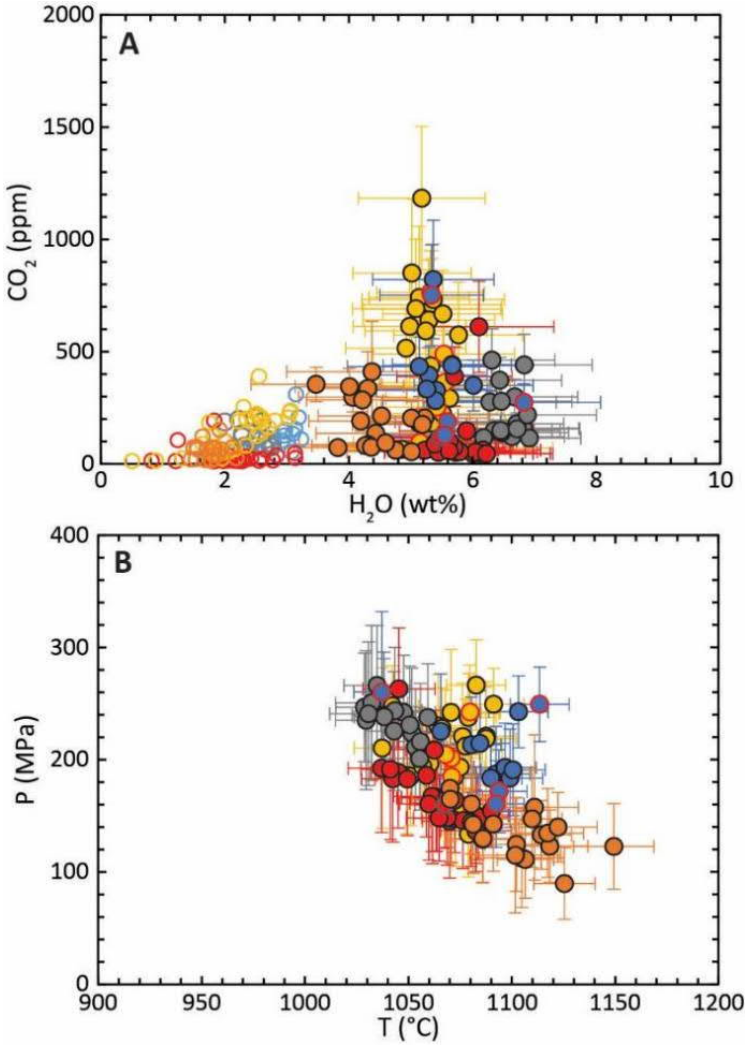

Figure 5.8. (A) Measured (hollow circles) and corrected (filled circles) volatile contents and (B) estimated P-T storage conditions for all MIs. Colour scheme is the same than Figure 5.1. Error bars correspond to 1σ.

5.6.3 Assessing the differentiation process of the MI trends

5.6.3.1 Testing homogeneous fractional crystallization (HFC) using MushPEC

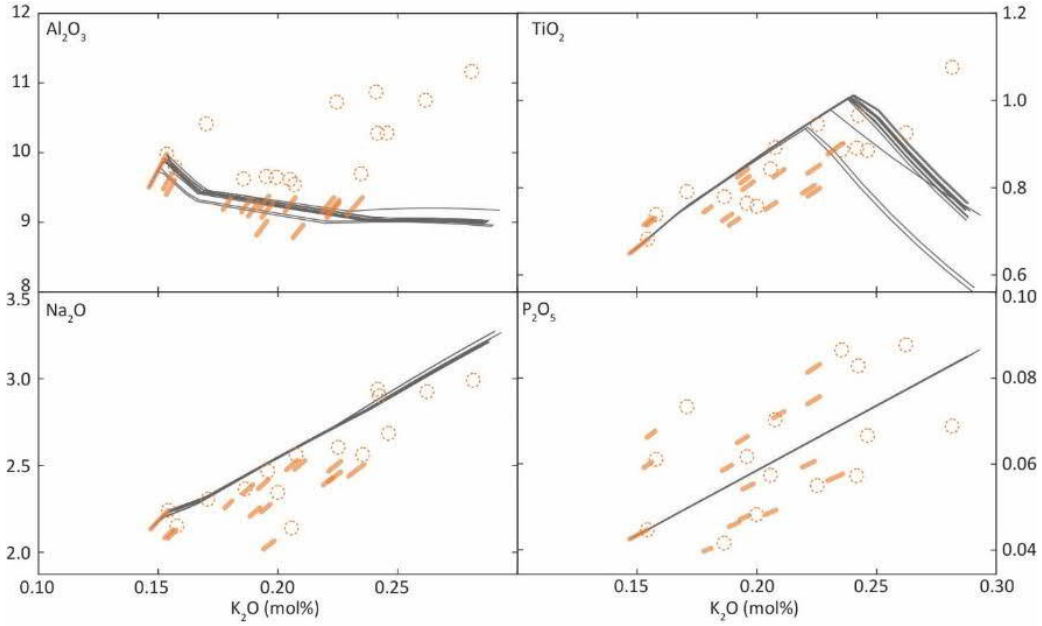

Figure 5.9. K_2O variation diagrams showing the MushPEC results for the AK sample. Dashed circles are the uncorrected MI compositions, the colored short thick lines indicate the ranges of compositions for the MIs corrected by MushPEC assuming that the MIs follow a HFC differentiation path. Black lines correspond to the best fit HFC models calculated with rhyolite-MELTS for the MI set.

As discussed above, most MI populations show evidence of being completely re-equilibrated with the interstitial melt during storage. An attempt to estimate MI compositions at entrapment was done using the MushPEC program (Brahm et al., 2021, Chapter 4). This method finds the best fit of a MI set to a liquid line of decent produced by HFC models generated with the rhyolite-MELTS algorithm (Ghiorso and Sack, 1995; Gualda et al., 2012). It does so by adjusting the Ol amount added/subtracted and Fe-Mg exchange with the Ol host. Iterative HFC models are generated by varying five initial parameters: (1) Ol addition/subtraction, (2) Fe/Mg ratio of the initial MI composition, (3) initial H_2O content, (4) pressure, and (5) f_{O_2} conditions. The fit is found by minimizing the Aitchison distance (Aitchison, 1986) between the corrected MIs and the liquid line of

decent of the HFC models. The major oxides SiO_2, Al_2O_3, FeO_T + MgO, CaO and K_2O (in mol%) are fit.

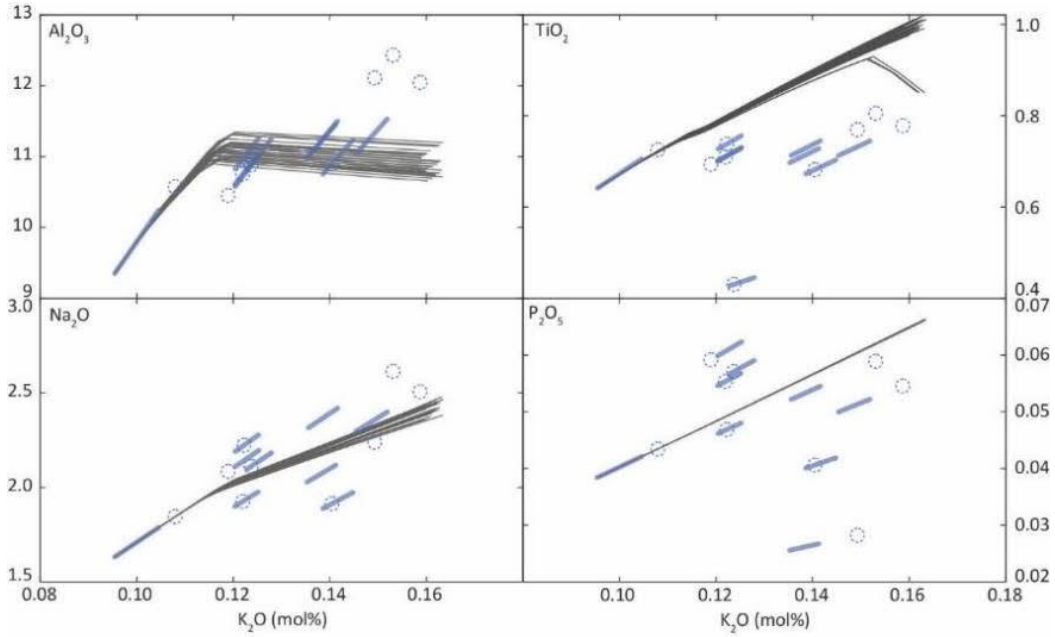

Figure 5.10. K_2O variation diagrams showing the MushPEC results for the HK sample. Figure description as in Figure 5.9.

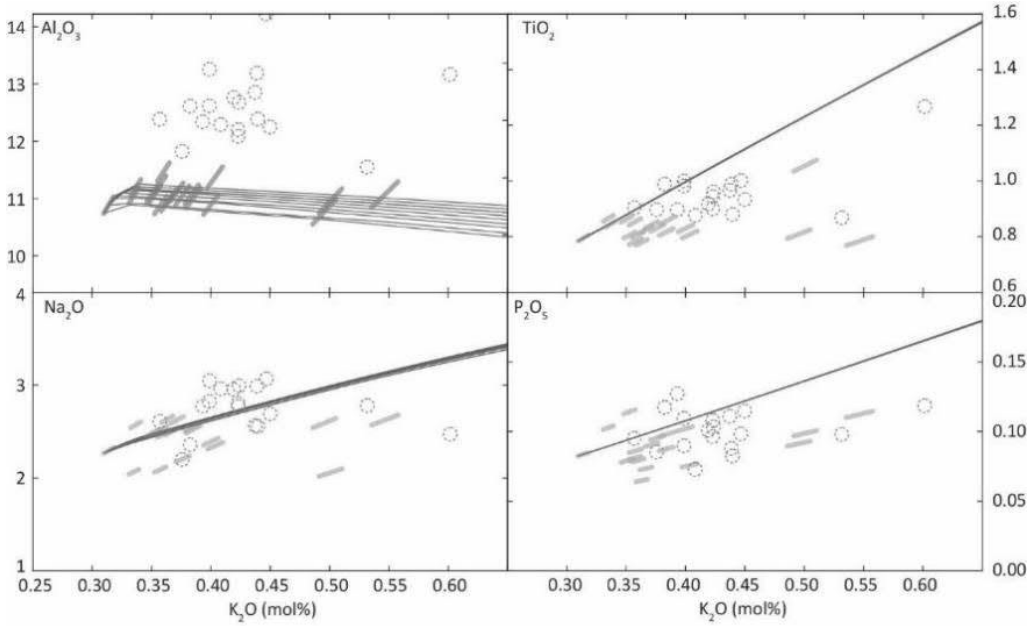

Figure 5.11. K_2O variation diagrams showing the MushPEC results for the TK sample. Figure description as in Figure 5.9

Figure 5.9 to Figure 5.13 show the best fit models produced by MushPEC for each of the samples in terms of the variation of K_2O with Al_2O_3, TiO_2, Na_2O and P_2O_5 (in mol%). The fitting of the major oxides associated with the major mineral phases involved during crystallization of basaltic melts (Ol, Pl and Px) is here represented just by the Al_2O_3 plot.

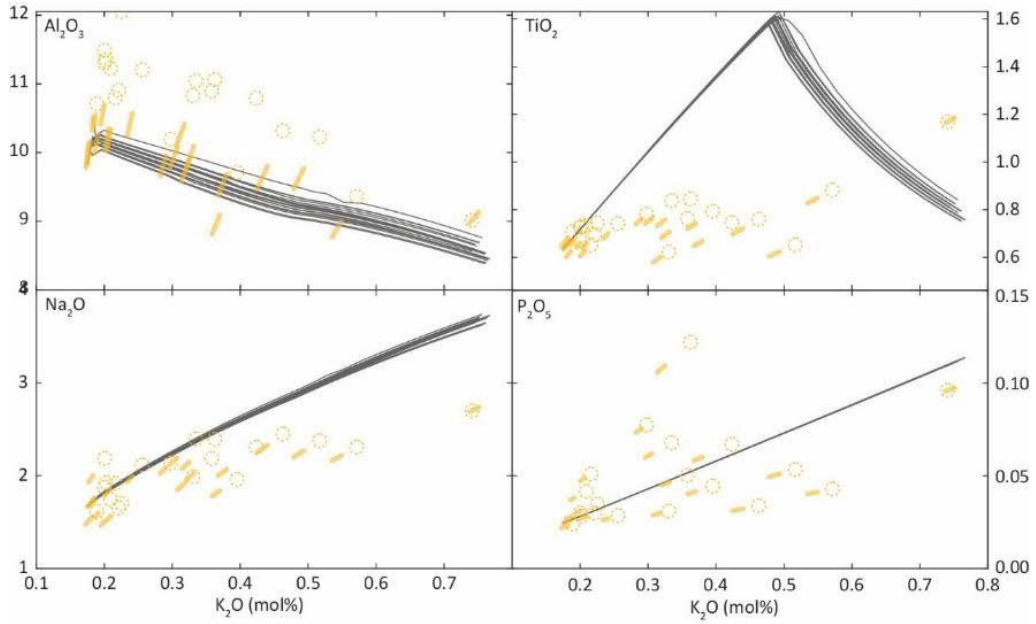

Figure 5.12. K_2O variation diagrams showing the MushPEC results for the AKN sample. Figure description as in Figure 5.9.

MushPEC is able to find good fits for these major oxides that represent the probable HFC trends that the MIs may have followed at entrapment. However, the other three minor elements have significant discrepancies, which are associated with the involvement of Ti-Mag (TiO_2) and apatite (P_2O_5) accessory phases and the composition of Pl. With the exception of AK, the MIs for all samples show a sub-horizontal TiO_2 trend, which indicates that some Fe-Ti oxide phase (probably Ti-Mag) must have been involved during

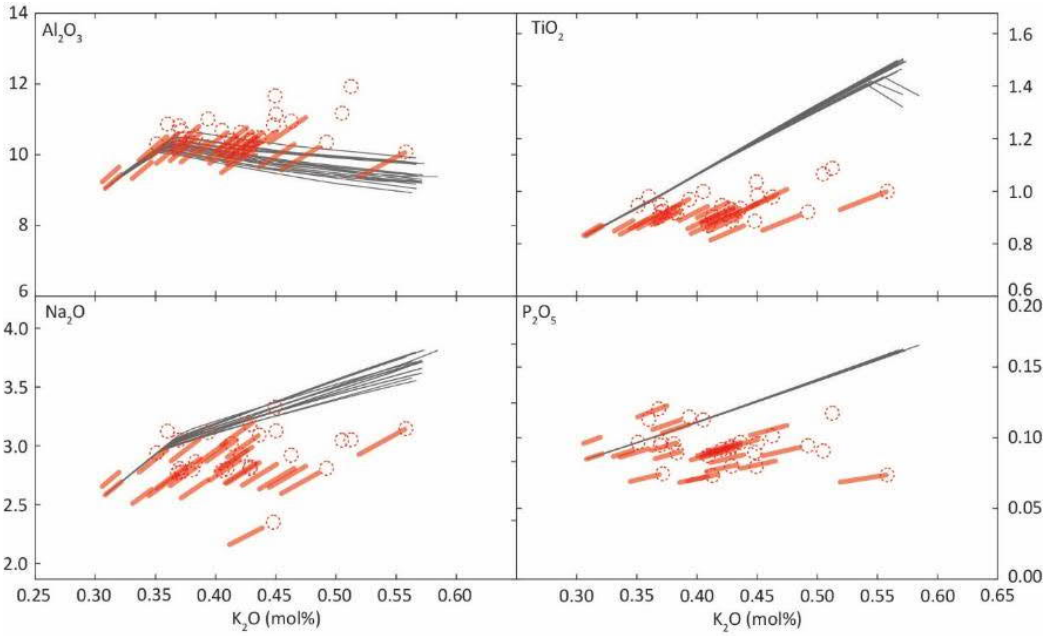

Figure 5.13 K_2O variation diagrams showing the MushPEC results for the TT sample. Figure description as in Figure 5.9.

fractionation. All HFC models produced by MushPEC show conservative behaviour of TiO_2 until Ti-Mag enters the fractionation sequence, generating a sharp change in the trends where TiO_2 starts to decrease strongly during differentiation.

Similar behaviour is observed for Na_2O in the TT and AKN samples and with P_2O_5 in MIs from the TK and TT samples. MIs exhibiting sub-horizontal trends in the P_2O_5 diagrams indicate the involvement of apatite, which is not observed in the samples and furthermore is not expected to be equilibrated in these melt compositions. The flat Na_2O trends shown by the MIs indicate the involvement of a more albitic Pl phase than the ones in equilibrium with the basic melt.

The AK MIs appear to better fit the HFC trends, showing an upward trend in all three minor oxides, but for TiO_2 the MIs follow a slightly lower sloped trend than the HFC models. This sample was the one used in Brahm et al. (2021, Chapter 4) to validate the MushPEC program. Nonetheless, strong discrepancies appear between the H_2O contents of the MIs estimated in this study and the ones predicted with MushPEC.

In addition to the estimated initial MI compositions, MushPEC also provides estimations on the crystallization conditions. Table 5.3 shows the estimated H_2O and P range for the corrected MI populations by MushPEC and the estimations made applying the PEC corrections with MIMiC and the Ol-melt hygrometer. It is seen that all H_2O contents estimated using the Ol-melt hygrometer are significantly higher than the ones determined through MushPEC, where the latter yields undersaturated conditions at the predicted pressures (Table 5.3). These discrepancies also include the AK sample.

Table 5.3. Estimated H_2O and P range of the MIs from the MushPEC results and from the PEC corrections applied with MIMiC and Ol-melt hygrometry.

	MushPEC		**MIMiC**	
Sample	**H_2O (wt%)**	**P (MPa)**	**H_2O (wt%)**	**P (MPa)**
AK	1.3 – 2.2	100 - 150	3.5 – 5.2	90 – 175
HK	2.1 – 3.7	400	5.1 – 6.0	160 – 260
TK	0.5 – 0.9	300 – 400	6.2 – 7.4	200 – 265
AKN	0.7 – 1.8	300	4.4 – 6.1	115 – 275
TT	0.5 – 1.3	300 – 400	5.1 – 6.2	135 – 275

The inability of MushPEC to reproduce the differentiation trends indicates that the mechanism of melt differentiation cannot be assigned as simple HFC. The process of

HFC produces clear ‘kinks’ or breaks in bivariate diagrams associated with the entrance or exit of a mineral phase from the crystallizing assemblage.

5.6.3.2 Assessing mixing of melts with contrasting compositions to produce the MI trends

As early fractionation of Ti-Mag is expected to produce strong depletion of TiO_2 during differentiation, the sub-horizontal to shallow slopes in most TiO_2 trends may indicate mixing of melts of contrasting compositions, e.g., generated by the interaction of two contrasting magmas during injection of a new magma batch (usually hotter and more primitive) into an evolved magma pocket.

The felsic mixing endmembers that generated the MIs of each of the samples should be relatively high in silica to have fractionated Ti-Mag, apatite and/or Na-rich plagioclase to generate the observed shallow sloping TiO_2, P_2O_5 and Na_2O trends. Magma mixing of two compositionally contrasting melts should produce strong disequilibrium textures in the phenocrysts. Further, if a mixing event was responsible for the MI trends, it would have to be an old event that was followed by enough time to completely re-equilibrate the Ol host compositions, rather than mixing just prior eruption (as appears to have occurred in the AKN sample based on its petrography, described in section 5.6.1).

Irrespective of the time since a presumed mixing event, Pl phenocrysts would preserve records of such magma interactions as Ca – Na zoning. The Pl populations of the five samples include a very common pattern of wide high-An cores with oscillatory zoning within a narrow compositional range (*c.* 10% to 15% variation in An content). These perturbations can be generated by temperature perturbances or slight compositional perturbances (particularly H_2O variations), which can be due to convection or thermal interaction with another melt. Mixing of the basic melt with a silica-rich magma would trigger crystallization of Pl growth zones richer in Na within the phenocrysts of the basic melt, but such Na-rich zones are not observed in any of these samples (cf. Figure 5.2).

In addition, several studies examining the mechanics of mixing state that high viscosity and density contrasts between the interacting melts hinder mixing (Blake and Fink, 1987; Frost and Mahood, 1987; Sato and Sato, 2009; Sparks and Marshall, 1986). Thermal

homogenization should occur before chemical homogenization as thermal diffusion is faster than chemical diffusion (Sparks and Marshall, 1986). This means that it is highly probable that Ol crystallization is enhanced before any chemical mixing occurs and the trapped MIs should (at least in part) follow an HFC path.

5.6.3.3 Boundary Layer Fractionation (BLF) to produce the MI trends

Another process that can reproduce trends similar to mixing is BLF, which can be understood as incremental steps of mixing between the main melt body with marginal amounts of differentiated liquids extracted from the highly crystallized boundary layers (Langmuir, 1989; Nielsen and DeLong, 1992). The fact that the liquids are incorporated in small proportions during magma differentiation makes it feasible for them to be assimilated by the mafic melt, in contrast to what is expected for the interaction of two magma batches of contrasting composition and temperature (Frost and Mahood, 1987).

The observed discrepancies between H_2O estimates (Table 5.3) can also be explained by invoking BLF. Is it known that H_2O depresses the liquidus temperature of silicate mineral phases (Almeev et al., 2007; Danyushevsky, 2001; Sisson and Grove, 1993), but it has a stronger effect in the liquidus depression of Pl (Almeev et al., 2012; Médard and Grove, 2008; Waters and Lange, 2015). This means that an increase in H_2O delays plagioclase crystallization with respect to other silicate phases (e.g., Ol and Px). Figure 5.14a illustrates the behaviour of the HFC paths for different water contents, reflected in an Al_2O_3 Harker diagram. Higher H_2O contents delay Pl appearance in the crystallization assemblage, concentrating Al_2O_3 in the melt until Pl begins to fractionate, and Al_2O_3 starts to be depleted. For low H_2O contents the decrease in Al_2O_3 starts earlier, producing lower concentrations of this oxide in less differentiated compositions. The decreasing Al_2O_3 trend at low H_2O contents is similar to a mixing line produced by the mixing of the high H_2O melt with the differentiated composition of the same liquid line of descent, and this is how the BLF process is usually modelled (Nielsen and DeLong, 1992). As the discrepancies between the estimated H_2O contents include the AK sample, it appears that AK was also affected by BLF. The similarity between the trends of the AK MIs with the ones expected for HFC could be due to the late appearance of Ti-Mag and apatite on the

crystallization path and/or the melt extracted from the boundary layer being less differentiated than in the other volcanic systems.

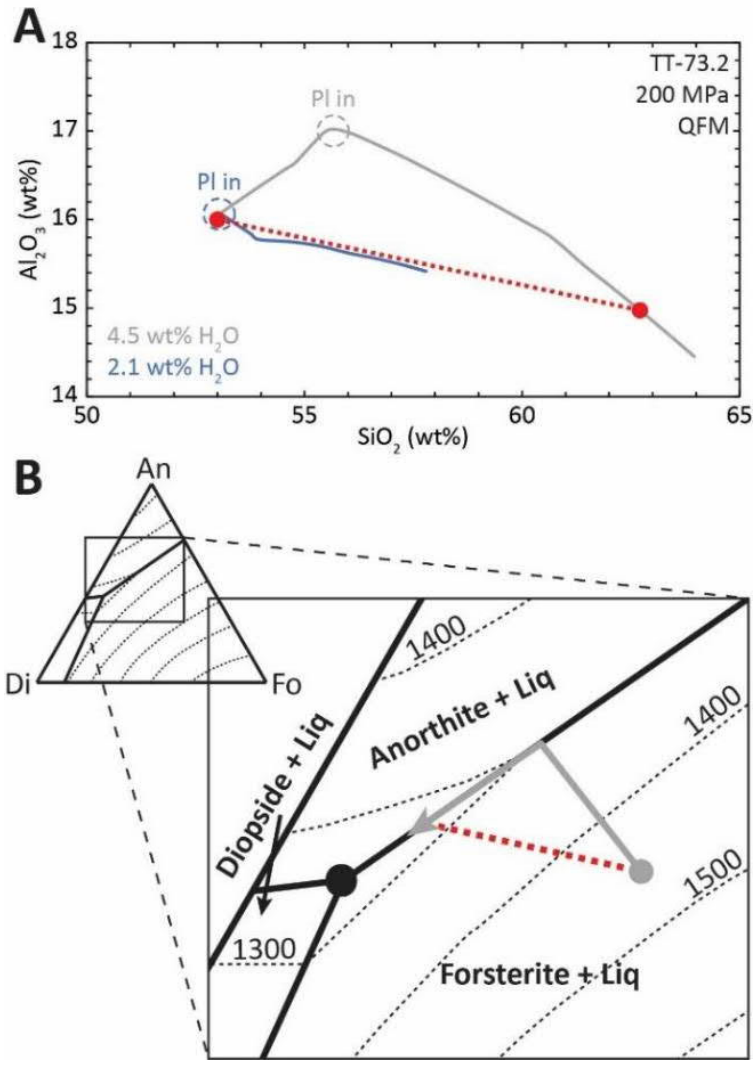

Figure 5.14. (A) Comparison of HFC trends at low-H_2O, high-H_2O and mixing trend of primitive and differentiated melts from the high-H_2O model. The HFC models were calculated with rhyolite-MELTS using the composition of TT-73.2. An Al_2O_3 path similar to an HFC path of a low-H_2O melt can be reproduced by BLF or mixing of a high-H_2O melt. (B) Ternary diagram of the forsterite – diopside – anorthite (modified from Morse, 1994) system showing how BLF produces a melt that evolves towards the eutectic without reaching the Ol-Pl cotectic. Grey line indicates the HFC path and the red dashed line indicates the mixing path for the initial and differentiated melt compositions of the HFC path.

5.6.3.4 BLF versus HFC – further distinguishing characteristics supporting solidification fronts

Another important characteristic observed in the HFC models is that the most primitive MIs are in equilibrium with only Ol or close to the Ol-Pl cotectic (most HFC models start by crystallizing only Ol). The cotectic is not clearly observed by the expected break in the Al_2O_3 trend in the corrected MIs with MIMiC, and it is improbable that for all MI populations found in the tephra samples the most primitive MI reflects the Ol-Pl cotectic. Langmuir (1989) discusses that BLF causes the melt to evolve in the Ol+melt field towards the Ol-Pl-Px cotectic, fractionating all phases in the solidification front but never equilibrating them in the main melt (Figure 5.14b). This indicates that there is a higher probability of the primitive MIs actually being in equilibrium with Ol only in addition to having evolved through a BLF path that resembles Pl fractionation. This particular behaviour can have a strong effect on the estimation of primary melt compositions (Kuritani, 1999b), which for primitive basalts is usually calculated by addition of equilibrium Ol.

Kuritani (2009) analysed the factors that affect the interplay between HFC and BLF as controls on the fractionation process operating. The preponderance of one process over the other is controlled by the efficiency of transport of the differentiated melt in the solidification front to the main magma body (melt extraction). The efficiency of melt extraction is directly proportional to the density contrast between the main melt and the boundary layer liquid and inversely proportional to the effective viscosity. The effect that water has on melt density and viscosity makes magmatic H_2O content crucially important in controlling the main differentiation process. At pressures above 100 MPa, magmas can contain significant amount of H_2O in undersaturated conditions and water is increasingly concentrated in the boundary layer melt due to high volumes of crystallization. This generates high melt density contrasts and reduces the effective viscosity of the boundary layer melt, promoting melt extraction from the solidification front. When the melt is initially saturated, melt extraction efficiency is reduced, because the density contrast decreases as the boundary layer melt does not see a significant increase in H_2O concentrations. Nonetheless, efficiency of melt extraction at saturated conditions may be facilitated by filter-pressing due to bubble formation (Bachmann and Bergantz, 2006).

The increase of water content in the boundary layer melt that is incrementally assimilated by them main melt also hampers crystallization of the main melt by reducing the liquidus temperature as water content increases, further promoting BLF over HFC. In short, the Kuritani (2009) model predicts that boundary layer fractionation is expected to be the main magmatic differentiation process in hydrous basic magmas (>3 wt% H_2O) stored at pressures above 100 MPa, especially at undersaturated conditions. Thus, it can be expected that the pressure-H_2O conditions estimated from the MI data should promote BLF over HFC for all arc melts in northern Japan that are considered in the present study. This is consistent with the behaviour observed for the AK sample. The AK MI trend is closer to a HFC trend than all the other samples and yields the lowest H_2O and pressure estimations of the five samples, which is close to the HFC-BLF transition values modelled by Kuritani (2009).

Another characteristic of volcanic rocks that has been used in support of BLF in solidification fronts is the necessity of fractionation of "ghost phases" to reproduce the evolution of a magmatic suite (Nielsen and DeLong, 1992). This means that to reproduce the magmatic variation, mineral phases that are not observed in the rocks and that are not predicted to be in equilibrium need to be fractionated. This is due to the high amount of crystallization that occurs in the solidification front, which starts fractionating mineral phases that are never equilibrated with the main magma. Nielsen and DeLong (1992) showed how the late appearance of mineral phases like Ti-Mag and apatite in the crystallization assemblage of the solidification front affect the overall TiO_2 and P_2O_5 trends, respectively, while the main magma body does not equilibrate these phases. As discussed above, the TiO_2 trends indicate fractionation of Fe-Ti oxide minerals even for the samples that do not have any Ti-Mag in the mineral assemblage. Further, Na_2O and P_2O_5 sub-horizontal trends in the TT sample indicate fractionation of significant amounts of Na-rich Pl and apatite, which are not observed in the tephra sample and are not expected to be in equilibrium with the TT melt composition.

The presence of compositional signatures of BLF in all the volcanic systems studied here may indicate that BLF is the most common differentiation mechanism occurring in the arc front of northern Japan and potentially all volcanic arcs, where magmas are expected to be H_2O-rich. In volcanic suites where BLF has played a major role during

differentiation, the currently common use of simple HFC models has important negative repercussions on volcanic hazards assessments in subduction zone environments. As shown in this study, HFC models typically result in prediction of substantially lower H_2O contents in the melt, which has a substantial effect on predictions of P-T conditions, viscosity estimations and explosivity potential of future eruptions. Estimates of the conditions of magma generation in subduction settings are also strongly affected, as reverse HFC models are usually applied to backtrack primary magma compositions. More realistic models to estimate primary magma compositions will need to be developed to gain a robust understanding of melt generation in the mantle beneath volcanic arcs.

Conclusions

In this study, Ol-hosted MI populations of five different volcanic systems along the arc in northern Japan were analysed. The compositional trends of PEC-corrected compositions indicate that most MI populations were completely re-equilibrated to storage conditions prior to eruption.

Estimates of corrected MI compositions indicate that the magmas have H_2O contents ranging from *c*. 3 to c. 8 wt%, stored at upper crustal pressures of *c*. 100 to 300 MPa.

An attempt to model the MI differentiation trends by homogeneous fractional crystallization was done using the MushPEC program. Discrepancies between the modelled HFC trends and the minor oxide contents in the MIs indicate the involvement of accessory phases (Ti-Mag and apatite) that are not in equilibrium with the melt. The discrepancies between the H_2O contents using estimated Ol-melt hygrometry and estimated using MushPEC corroborates that the observed liquid lines of descent are produced by the interaction of melts of contrasting compositions.

BLF in solidification fronts is proposed as the most probable mechanism to cause magmatic differentiation consistent with the observed MI trends. Incremental amounts of differentiated liquid are extracted from the crystalline boundary layer and are assimilated into the main melt. These produce differentiation paths that resemble HFC of low H_2O melts, and with features that suggest fractionation of mineral phases that are never equilibrated by the melts represented in the MIs.

These results are also in agreement with model predictions (Kuritani, 2009) that indicate promotion of BLF over HFC in hydrous magmas of >3 wt% H_2O, stored at pressures of >100 MPa.

Given the ubiquity of BLF in solidification fronts at all five arc volcanoes studied, it might be that magma differentiation through this process is common in all arc settings, though more evidence is needed. The application of simple HFC models to understand the magmatic conditions of volcanic systems that suffered BLF will yield inaccurate predictions of P-T-H_2O conditions, which will negatively affect the assessment of volcanic hazards, as well as leading to the derivation of inaccurate primary melt compositions.

Chapter 6

Trace and volatile element variations in slab liquids across the northern Japan arcs

Raimundo Brahm[1], Georg Zellmer[1], Daniel Coulthard Jr.[1], Takeshi Kuritani[2], Naoya Sakamoto[3], Hisayoshi Yurimoto[3]

[1]School of Agriculture and Environment, Massey University, Palmerston North, New Zealand.

[2]Graduate School of Science, Hokkaido University, Sapporo, Japan.

[3]Isotope Imaging Laboratory, Creative Research Institution, Hokkaido University, Sapporo, Japan.

6.1 Abstract

Subduction zone magmatism is generated by the interaction of the hot mantle wedge with liquids released from the subducting slab. These liquids carry geochemical signatures reflecting the partitioning behaviour of elements between mineral phases and the liquid. Studies of natural high grade metamorphic suites from old subduction systems, combined with dehydration/melting experiments of basaltic and pelitic rocks and thermodynamic modelling have helped to predict the mineralogical composition of the slab and the partitioning behaviour of trace elements at PT conditions relevant to subduction systems, whereas geodynamic and seismic models have allowed the estimation of the slab PT paths for many subduction systems around the world.

Tephra samples from seven volcanic systems in northern Japan that cover a wide range of PT conditions of the slab below each volcano (c. 2.8 to 7.9 GPa and c. 710 to 860 °C) are studied to identify geochemical variations related to progressive reactions in the slab. Olivine-hosted glassy MIs are analysed for trace and volatile elements and their compositions are compared to predicted prograde metamorphic reactions occurring in the different layers of the subducting slab (sediment cover, oceanic crust and lithospheric

mantle). Only low degrees of melting are expected in the sediment cover at arc front depths (<10%), and no melting is expected at back-arc depths.

Progressive increases of halogens/HREE and LILE/HREE ratios from arc to back-arc are related to increasing breakdown of serpentine from the hydrated lithospheric mantle. Reduction of most LILE/HREE and Cl/HREE at slab conditions of very high PT in the back-arc indicate exhaustion of lithospheric serpentine, whereas roughly constant inputs of Pb, Sr and F at all PT slab conditions reflect the constant breakdown of lawsonite across the arc. The increasing LREE/HREE with slab surface temperature is the result of the increasing mobility of LREE as the solubility of allanite and monazite decreases with temperature. HFSE enrichment is observed at PT conditions that are expected to generate supercritical fluids (>6 GPa), favoured by their enhanced mobility and the low solubility of accessory minerals (rutile, zircon). Fluid flux models of F and Cl systematics indicate that halogen abundances with similar Cl/F ratios in arc magmas can be explained by a homogeneous slab liquid composition at different fluid amounts added to the mantle wedge and similar degrees of melting. Slab liquid composition varies to the back-arc though enhancement of halogen and H_2O contents provided by serpentine breakdown, producing greater amounts of halogens and similar Cl/F to the arc front samples for lower degrees of melting. Serpentine exhaustion at the highest PT conditions produces decoupling of F and Cl, generating a slab liquid with the lowest Cl/F observed.

6.2 Introduction

It is generally agreed that a slab component is involved in the generation of magmatism in subduction zones (Gaetani et al., 2003; Gill, 1981; Grove et al., 2006; Tatsumi, 1986; Tatsumi, 1989; Tatsumi et al., 1986). The interaction of the hot mantle wedge with H_2O-rich liquids released by the down-going slab triggers partial melting, due to the depression of the mantle solidus temperature through H_2O (Gill, 1981; Tatsumi, 1986). This interaction is responsible for the particular geochemical characteristics of arc magmas, such as their general H_2O enrichment compared to mid-ocean ridge basalts (MORBs) (e.g., Grove et al., 2005), their higher oxidation state (Kelley and Cottrell, 2009) and their

characteristic trace element signatures (enrichment of LILE and LREE elements with respect to MORBs (e.g., Pearce, 1983; Perfit et al., 1980)).
Nonetheless, there is continuing debate regarding the nature of the slab component and the processes that govern its composition. Slab liquids have been interpreted as hydrous fluids generated by dehydration reactions during prograde metamorphism (e.g., Hacker, 2008; Plank and Langmuir, 1998; Schmidt and Poli, 1998), H_2O-rich silicate melts produced by partial melting of the altered oceanic crust (AOC) and/or its sedimentary cover (SED) (e.g., Kimura et al., 2010; Manning, 2004), and supercritical fluids (e.g., Taniuchi et al., 2020).

Further complexities arise from the variable involvement of different sources within the subducted slab on the resulting slab component. The proportions of the AOC and SED components have usually been estimated using radiogenic isotopic data (e.g., Kuritani et al., 2019; Kuritani et al., 2021). Further involvement of fluids percolating through the slab, originating from serpentine (Serp) breakdown of the hydrated subducted lithospheric mantle has also been proposed as an important fluid source (Barnes et al., 2008; Kendrick et al., 2014; Kendrick et al., 2020; Straub and Layne, 2003b). Another source of fluid could be the dehydration of the mantle wedge, hydrated during pore fluid release of the slab in the forearc and dragged downwards by the subducting slab (Tatsumi, 1986; Tatsumi, 1989; Tatsumi et al., 1986).

Different mechanisms of transport of the slab component through the mantle wedge have been proposed. Melting is triggered when the slab liquids reach the solidus as the slab fluids ascend through the mantle wedge with an inverted geotherm from the slab surface to the hot core of the mantle wedge. This hot core is generated by the cooling of the mantle wedge caused by the subducted slab and the corner flow that occurs due to viscous coupling of the mantle wedge with the slab. Less viscous hydrous slab liquids may ascend vertically through percolation, generating an initial H_2O-rich melt when reaching the solidus temperature and reacting continuously with the mantle as the temperature increases and pressure decreases upward, which assimilates more material into the melt, reducing the H_2O content (Gaetani et al., 2003; Grove et al., 2006). If the overlying mantle wedge is not previously saturated in volatiles at forearc depths, the slab liquids will react with the mantle to form hydrated minerals (chlorite, serpentine, phlogopite) that are dragged down by mantle flow and will release fluids deeper, when breakdown

temperatures of these hydrous phases are reached and accumulated mantle melts above the solidus temperature can ascend diapirically producing a component of adiabatic melting (Tatsumi, 1986; Tatsumi, 1989; Tatsumi et al., 1986). Viscous slab-melts can ascend by buoyant diapirs, which might be pushed further away from the trench by the downward corner-flow (Cruz-Uribe et al., 2018; Marschall and Schumacher, 2012; Nielsen and Marschall, 2017). Marschall and Schumacher (2012) proposed that the slab component consists of a diapirically ascending mélange of geochemical and mechanical mixtures of mantle-AOC-SED components.

There is also some debate on the control on and behaviour of trace elements during extraction of liquids from the slab. Partitioning behaviour of trace elements between SED, AOC and mantellic sources with melts or fluids have been studied through analysis of exhumed high-grade metamorphic complexes (e.g., Hermann, 2002; John et al., 2011; Martin et al., 2014; Pagé and Hattori, 2017; Sorensen et al., 1997) and dehydration/melting experiments (e.g., Dalou et al., 2012; Hermann, 2002; Hermann and Green, 2001; Hermann and Rubatto, 2009; Hermann and Spandler, 2008; Kessel et al., 2005; Krenn et al., 2012; Li and Hermann, 2017; Schmidt and Poli, 1998; Spandler et al., 2007; Tsay et al., 2017). Kessel et al. (2005) conducted high-PT experiments on a basaltic eclogite sample, recovering partitioning behaviour for fluids (700 – 900°C at 4 GPa), melt (1000°C at 4 GPa) and supercritical fluids (800 – 1200°C at 6 GPa), based on the partitioning behaviour of major mineral components of the residue, like garnet (Grt) and clinopyroxene (Cpx), and accessory rutile, which retains Nb, Ta and Ti (Foley et al., 2000). Analysis of natural samples and experiments of sediment and basalt melting (Hermann, 2002; Hermann and Rubatto, 2009; Spandler et al., 2007; Tsay et al., 2017) have shown the major importance of accessory phases in controlling the trace element concentrations in the fluid/melt. Allanite and monazite have been shown to carry most of the LREE and Th in eclogitic metasediments and metabasites, whereas phengite (Phen) controls the LILE budget and zircon carries most of the Zr. Saturation of these phases with increasing T controls the slab melt composition. During dehydration, the presence of these accessory phases reduces the capability of the fluid to transport all REE, therefore the systematic increase in mobility from HREE to LREE expected from the presence of a Grt residue is not shown.

As one of the main drivers of arc magmatism is thought to be volatile input from the slab into the mantle source, the study of volatile abundances (H_2O, CO_2, S, Cl and F) in arc magmas is important. However, there is a tendency of volatile records to be lost prior to and during eruption through degassing. Even in melt inclusions (MIs), which are usually analysed with the aim to recover volatile contents, CO_2 is typically degassed because of its low solubility (Hartley et al., 2014; Moore et al., 2015; Moore et al., 2018; Wallace et al., 2015), H_2O is lost because of H^+-permeability of the host crystal (Hartley et al., 2015; Turner et al., 2017b) and S has a complex solubility behaviour affected by f_{O_2} and the fact that it can precipitate in mineral phases, be exsolved as a gas phase or an immiscible liquid (Ariskin et al., 2013; Moretti and Baker, 2008; Oppenheimer et al., 2011b; Wallace and Carmichael, 1992). In contrast, halogens like F and Cl have shown not to be significantly affected by degassing because of their low concentration and high solubility (e.g., Dalou et al., 2014; Webster, 2004). This behaviour, combined with the contrasting partitioning of these two halogens (e.g., Bénard et al., 2017; Dalou et al., 2012), renders these elements capable tracers of the volatile cycle and the processes of slab fluid release in subduction zones. Of additional importance is the effect that F and Cl have in modulating the trace element partitioning of hydrous fluids (e.g., Bali et al., 2011).

Studying the trace and volatile systematics of arc magmas along and across an arc setting can elucidate the processes involved in the release of the slab component. The subduction zones in northern Japan are a particularly good natural laboratory to study variations in slab fluid input, because this area contains one of the best-understood subduction settings due to the dense network of seismic stations, allowing the generation of many high-resolution seismic tomography models (e.g., Abdelwahed and Zhao, 2005; Chen et al., 2018a; Huang and Zhao, 2013; Huang et al., 2011; Kita et al., 2014; Liu and Zhao, 2016; Nakajima et al., 2013; Tong et al., 2012; Wang and Zhao, 2013; Zhao et al., 2017). In particular, the Tohoku and Hokkaido regions provide an opportunity to analyse changes in subduction parameters and relate them to variations in trace element and volatile compositions of the parental magmas because there are volcanic systems in this regions that are distributed along and across-arc, with underlying slab temperatures (T_{slab}) transitioning from low to high arc temperatures (*c.* 710 – 740°C) through anomalously high arc temperatures (*c*, 770°C) and normal back-arc temperatures (*c*. 820°C) to extremely high rear-arc temperatures (*c*. 860°C).

In this study trace elements and volatile contents of well-characterized olivine-hosted MIs from tephra samples of seven volcanoes along and across the northernmost NE Japan arc and southernmost Kuril arc are analysed. The systematics of the variability of trace element and volatile ratios with estimated T_{slab} conditions are investigated to study the across-arc transitions in the composition and nature of the slab component.

6.3 Tectonic and geologic setting

The Tohoku and Hokkaido regions comprise the northernmost section of the NE Japan arc and the southernmost section of the Kuril arc (Figure 6.1). Both arcs have formed by the westward subduction of the Pacific plate beneath the Okhotsk Plate (7 – 11 cm/yr; Bird, 2003; Northrup et al., 1995) at the eastern margin of northern Japan. The arcs meet in central Hokkaido, where the strike of the trench shifts from N56E in the Kuril arc to N10E in the NE Japan arc. This shift in the orientation of the trenches has been associated with higher temperatures in the subducted slab, thought to be caused by the cracking or thinning of the subducted oceanic crust and affecting the nature of the slab-derived fluids (Kuritani et al., 2016; Kuritani et al., 2008)

The two arcs meet in the Hidaka collision zone, where the Kuril forearc sliver has been migrating southward (Kimura, 1996; Kita et al., 2014) and colliding with the NE Japan forearc since the Miocene (*c.* 12 Ma), uplifting the Hidaka Mountains. This collision zone coincides with the position of the southernmost volcano of the Kuril arc (Tokachidake). There is a *c.* 120 km long volcanic gap between Tokachidake and the northernmost active volcano of the NE Japan arc in central Hokkaido.

For the last *c*. 5 Ma the location of the arc front in NE Honshu and Hokkaido has remained in the same place (Martin, 2011; Yoshida et al., 2014). The first *c.* 3 Myr of this period were characterized by caldera-dominated felsic activity. At *c*. 2 Ma the activity changed to stratovolcano-dominated basaltic to andesitic volcanism (Acocella et al., 2008), which was associated with a shift in the compression orientation, from NE-SW to the current ENE-WSW orientation.

The samples analysed in this study belong to seven volcanic systems distributed along and across the northernmost NE Japan arc and the southernmost Kuril arc. In the NE Japan arc, Akita-Komagatake (AK) and Hakkoda (HK) volcanoes at the arc front and Oshima-Oshima (OO) volcano in the back-arc were sampled. In the Kuril arc, Tokachidake (TK), Akan-fuji (AKN) and Tya-Tya (TT) volcanoes at the arc front and Rishiri (RSH) volcano in the back-arc were sampled. These volcanoes where selected as they represent a good geographical distribution along and across these subduction zones and because their products include basic tephras with olivine-hosted MIs.

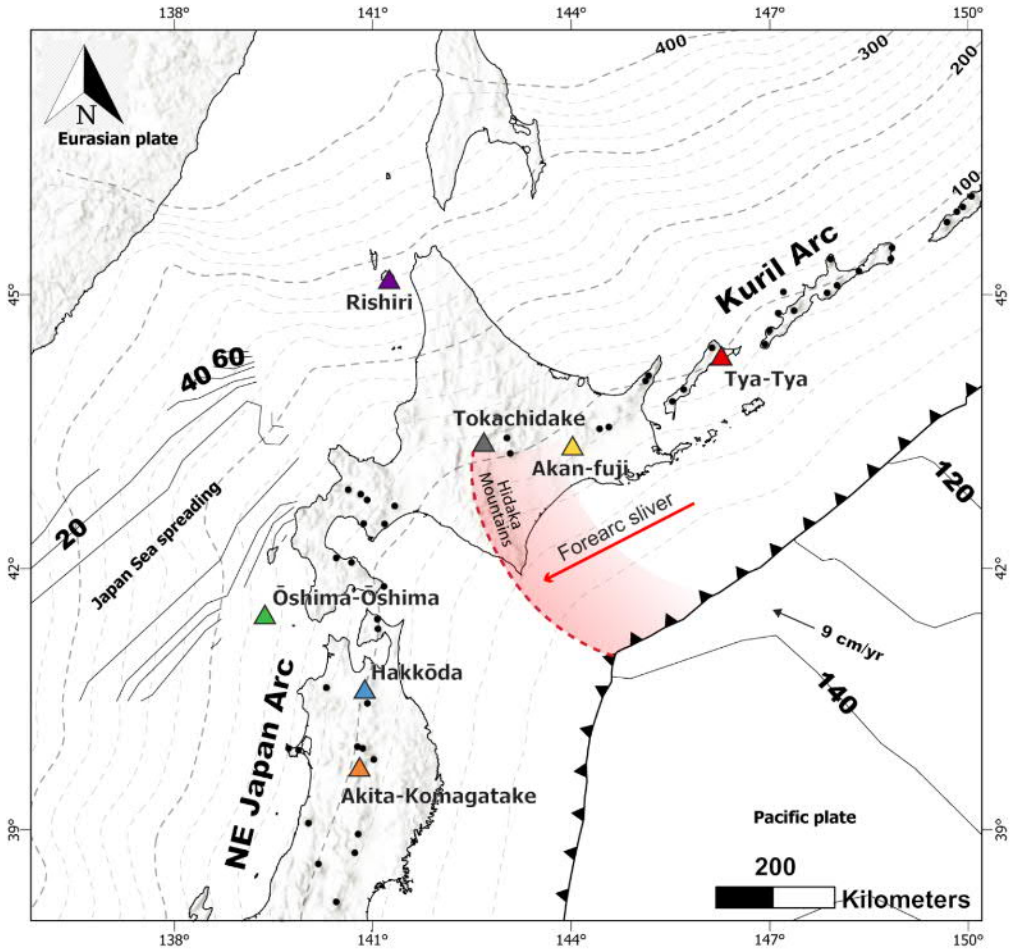

Figure 6.1. Map of the study area comprising north Honshu and Hokkaido regions and the southern islands of the Kuril arc. Triangles with names are the volcanic systems of interest in this study. Black dots are other volcanoes of the NE Japan and the Kuril arcs. The black line with triangles marks the subduction trench. The red area indicates the collision zone of the Kuril arc forearc sliver over the NE Japan arc, and the red arrow indicates the direction of movement of the forearc sliver. Grey dashed lines indicate the depth of the slab (km). Black contour lines with numbers indicate the age of the oceanic crust in Myr.

6.3.1 Slab parameters

The conditions of the slab below each volcanic system can be estimated by combining the information of crustal depth (LITHO1.0; Pasyanos et al., 2014), slab depth (Slab2; Hayes, 2018) and slab surface P-T path (Syracuse et al., 2010; Van Keken et al., 2011) models. Using known values of crustal and mantle densities, the pressure of the slab below each volcanic system is estimated and the slab P-T path model indicates the temperature of the slab surface. Table 6.1 summarizes the slab parameters for each volcanic system.

Table 6.1. Estimated conditions of the slab below each volcanic centre.

Parameter	AK	HK	OO	TK	AKN	TT	RSH
Crust depth (km)	29	29	20	32	33	25	28
Slab depth (km)	94	98	173	127	95	105	254
Distance from trench (km)	296	296	442	341	242	222	568
Subduction angle (degrees)	27	27	30	30	32	37	32
Slab T (°C)	722	713	817	770	707	741	856[a]
Slab P (GPa)	2.81	2.94	5.27	3.83	2.82	3.17	7.88[a]

[a]PT conditions estimated by extrapolating trend beyond (Van Keken et al., 2011) model.

6.3.2 Volcanic systems

A short description of the arc front volcanoes can be found in Brahm et al. (in review) (Chapter 5). Here, a summary is given of the geology of the back-arc volcanoes.

6.3.2.1 Oshima-Oshima (OO)

OO is a volcanic island in the back-arc of the northernmost section of the NE Japan arc, off the SW coast of Hokkaido. The general geology of OO is described by Katsui and Satoh (1970). It consists of three volcanic edifices that overlay one another: Higashi-yama, Nishi-yama and the central cone. Higashi-yama somma is located in the eastern section of the island and it is the oldest edifice. It surrounds a caldera, and it is believed to have formed in the late Pleistocene. Its eruptive history consists of early andesites followed by basalts. The main edifice and the caldera were formed by the basaltic activity. This activity was followed by a period of quiescence and erosion. Nishi-yama formation

started with basaltic and andesitic activity from the western part of the caldera, followed by subsidence of this new edifice to form a second caldera (760 ±70 yr; Katsui and Satoh, 1970) after the eruption of andesitic pumice and basaltic scoria. The central cone is formed by basalts that erupted from the caldera in Nishi-yama somma during historic activity that started with the 1741-1742 eruption. Basaltic lava flows were extruded from flank eruptions, which flowed into the sea at the northern coast. Known historic activity ranges from 1741 to 1790, including ash fall and gas emission events. Most rocks are alkali-rich with high K_2O/Na_2O and MgO/FeO_T ratios. Basalts tend to be silica-undersaturated, whereas andesites are silica-oversaturated and follow a calc-alkaline trend. The selected sample is from the basaltic tephra fall deposit of the 1741-1742 eruption.

6.3.2.2 Rishiri (RSH)

RSH is a volcanic island in the back-arc of the southernmost Kuril arc, offshore to the west of NW Hokkaido. A detailed description of the stratovolcano evolution is given by Kobayashi (1987) and Ishizuka and Nakagawa (1999) The evolution of RSH is divided into three main stages. In the Early stage activity was dominated by andesitic lavas, pyroclastic flows and dacitic lava dome formation. The main stratovolcano was built during the Middle stage with lava and pyroclastic flows, where calc-alkaline andesite was the predominant composition. The Late stage was dominated by the production of alkali lavas, trachytic andesites and minor dacitic and rhyolitic pumice. During the Late stage, a series of scoria cones that erupted lava flows developed on the south-eastern flank of the main cone (Kuritani et al., 2008) at *c.* ≤ 20 ka (Kuritani et al., 2007). The sample analysed in this study was taken from the southern flank of the Senpoushi scoria cone.

6.4 Analytical methods

6.4.1 X-ray fluorescence spectrometry (XRF)

Glass beads were prepared from whole rock powders of the back-arc samples to perform XRF analysis, in the same way that the arc samples were processed for analysis in Brahm

et al. (in review) (Chapter 5). To prepare the glass beads each sample was first cleaned in an ultrasonic bath with distilled water. Samples were then dried in an oven at 100 °C for at least 2 hours or overnight at 45°C. Samples were then powdered in a tungsten grinding machine and kept in the oven at 100°C for at least 2 hours. Loss of ignition (LOI) was determining by weighing *c.* 2 g of powder before and after heating in an oven at *c.* 900°C for 3 hours. After heating, *c.* 0.8 g of the powdered sample was mixed with *c.* 8.0 g of a flux of a lithium metaborate : lithium tetraborate mixture (12 : 22), followed by fusion to produce a glass disc using a XRFuse2 electric fusion apparatus.

Major element concentrations were measured with a 1 kW Bruker Tiger S8 Series II XRF spectrometer at Massey University in Palmerston North, New Zealand. Interference-corrected spectra intensities were converted to oxide concentrations using calibration curves consisting of natural standards closely approximating the mafic matrix of our samples. The long-term reproducibility of Oreas 24c standard reference material is better than ± 1% relative (1σ) for all elements except MnO, for which it is better than ±1.5% relative.

6.4.2 Scanning electron microscope

Backscatter electron (BSE) imaging was used to assess textural features, e.g. formation of daughter crystals in the MI, Fe-rich olivine rims around the MI and Fe-Mg zoning of the olivine host. BSE images of the exposed MIs were obtained using a JEOL JSM-7000F Field-Emission scanning electron microscope (FE-SEM) at Hokkaido University, Japan. An acceleration voltage of 15 kV was used, with a beam current of 10 nA.

The FEI Quanta 200 SEM at Massey University (New Zealand) was used to study the textural features of the tephras through BSE imaging of the thin sections. This was done to identify mineral associations, zonation patterns and other disequilibrium features. The BSE images were used to define spots of interest for subsequent microprobe analysis of glass and minerals.

6.4.3 EPMA (MI, glasses and minerals)

Mineral and glass compositions were analysed with the JXA-8230 SuperProbe electron probe microanalyzer (EPMA) at Victoria University, New Zealand. The analysis of the back-arc samples was done in the same runs as the arc samples which were previously published in Brahm et al. (in review) (Chapter 5). Plagioclase crystals were analysed using a defocused beam of 10 μm diameter with an accelerating voltage of 15 kV and a beam current of 12 nA. Olivine, pyroxene and Fe-Ti oxide crystals were analysed using a focused beam with an accelerating voltage of 20 kV and a beam current of 30 nA. Counting times were 40 s on peak and 15 s on background for all elements.

For MI olivine host crystals, analysis spots were chosen in the vicinity of the MIs to better constrain equilibrium conditions. A focused beam with accelerating voltage of 20 kV was used with a beam current of 30 nA for Si, Fe, Mg, Mn and Ti, and 100 nA for Al, Ni, Ca and Cr. Counting times were 40 s on peak and 15 s on background for all elements but Ca, with 400 s on peak and 20 s on background. MI and interstitial glass compositions (Si, Ti, Al, Fe, Mn, Mg, Ca, Na, K, and P or Cr) were analysed with an accelerating potential of 15 kV and an electron beam current of 8 nA. A defocused beam of 5–10 μm diameter was used, and Na was analysed for 10 s first to avoid Na migration. Secondary standards for all analyses and uncertainties can be found in Brahm et al. (in review) (Chapter 5) and Appendix 2.

6.4.4 Secondary ion mass spectrometry (SIMS) and Fourier-transform infrared spectroscopy (FTIR)

Analysis of volatile contents (H, C, S, Cl and F) of MI glasses were carried out with the Cameca ims-1270 secondary ion mass spectrometer (SIMS) at Hokkaido University, Japan. H and C data from the arc front samples have already been published in Brahm et al. (in review) (Chapter 5). Exposed MIs were pressed down into an indium plug mounted in an aluminium disk to avoid H and C contamination from epoxy. The plug was then coated with gold and loaded into the SIMS sample chamber to remain under vacuum for three days before analysis to reduce H contamination.

A Cs^+ ion primary beam was used to analyse ^{1}H, ^{12}C, ^{19}F, ^{30}Si, ^{32}S and ^{35}Cl isotopes. Pre-sputtering of a 25×25 µm area was conducted before each analysis with a beam current of 1 nA for 100 s, plus a beam centring time of 96 s. Analysis was carried out with a beam current of 0.1 nA over a 3-5 µm wide area of Gaussian shape. Field aperture was set to 2000 µm with an entrance slit of 60 µm, an energy slit of 25 µm, a contrast aperture of 100 µm and an exit slit of 400 µm. Mass resolution was set to *c.* 3240 to avoid interference of isotopic signals (mainly $^{34}S^{1}H$ on ^{35}Cl, $^{29}Si^{1}H$ on ^{30}Si, and $^{31}P^{1}H$ on ^{32}S). The isotopes were measured in five consecutive cycles of 10 s of waiting time and 3 s of analysis time for ^{1}H, 4 s waiting time and 5 s analysis time for ^{12}C, and 2 s waiting time and 1 s analysis time for the rest of the isotopes (^{19}F, ^{30}Si, ^{32}S and ^{35}Cl). Including pre-sputtering time, each analysis lasted *c.* 8 minutes. The reproducibility of counts ratios between each volatile and matrix was obtained from the five cycles per analysis. Maximum uncertainties of reproducibility are <10% for $^{1}H/^{30}Si$, <13% for $^{12}C/^{30}Si$ and <3% for $^{19}F/^{30}Si$, $^{32}S/^{30}Si$ and $^{35}Cl/^{30}Si$.

Reference glasses were polished and mounted in the same indium plug as the MIs and were repeatedly measured during the same analysis session to produce the calibration lines and to check for instrument drift. The reference glasses used were BIR-1G and BHVO-2G synthetic standard glasses (USGS), plus CL DR-1, Gal 1652, LS 427, 2πD43, SAM 76-11, SAM 73-12 and SAM 74-2 natural volcanic glasses (Kendrick et al., 2017). F and Cl reference values for the synthetic glasses were obtained from Marks et al. (2017) and Kendrick et al. (2017), whereas reference values for natural samples were the revised compositions of Kendrick et al. (2017). H_2O and CO_2 compositions for most of the reference materials were measured using a micro-FTIR instrument and S was remeasured by EPMA (see Brahm et al., in review; Chapter 5).

Calibration of the SIMS analyses was produced using a maximum likelihood linear regression scheme considering the uncertainties related to SIMS analysis precision and uncertainties in the reference values used. After calibration, the uncertainties in accuracy (1σ) for the volatile species in MIs are *c.* 4% for H_2O, <15% for CO_2 (for concentrations above 50 ppm), <8% for most S analyses, *c.* 2% for Cl and <8% for most F analyses.

6.4.5 LA ICP-MS

The trace element concentrations of the whole rock glass beads and the MI glasses were measured with a RESOlution-SE Compact 193nm excimer laser ablation system in tandem with an Agilent 8900 Inductively Coupled Plasma – Mass Spectrometer (LA ICP-MS) at Waikato University in Hamilton, New Zealand.

Following XRF analysis, the whole rock glass beads were piled up and glued together with epoxy, then a slice of the stack was cut, polished and mounted on a glass slide. The analysis was conducted by pulsing the laser at 10 Hz with a 100 µm spot size and energy density of 5.0 Jcm^{-2} with an ablation time of 45 s. Ultra-high purity helium was used as the carrier gas (370 mL/min) to deliver the ablated sample from the LA system to the ICP-MS. Background counts (gas background, measured with the laser off) were collected for 30 s between samples. NIST610 and NIST612 glass standards were analysed after every 10 samples to account for any instrument drift. Analysis conditions for MI glasses were the same as for the glass beads, except that the laser size spot was varied between 50 to 100 µm depending on the size of the MI. Standard glasses were measured with each laser spot size used to analyse MIs to obtain trace element concentrations and their precisions at each spot size.

Data processing was performed using Iolite (v3.32; Patton et al., 2011). Background counts were subtracted from the raw data and all data were standardized to the NIST612 glass. NIST610 glass was used as a secondary standard. The GeoReM database (Jochum et al., 2005) was utilized for the standard glass values. The real whole rock concentrations where calculated by mass balance calculations using the LA ICP-MS results and the proportion of sample and flux measured when producing the glass beads.

6.5 Results

The petrography and compositions (except for S, F, Cl, and trace elements) of the arc front samples have already been described in Brahm et al. (in review) (Chapter 5), and thus only the two back-arc samples are described here. Then, the new volatile and trace element compositions of the MIs from all seven samples are provided.

6.5.1 Petrography and mineral chemistry

6.5.1.1 Oshima-Oshima (OO)

The OO tephra (Figure 6.2a, c and e) has a vesicularity of *c*. 39 vol%. The sample is has a glass-rich groundmass (*c*. 65 vol% in a vesicle free basis) with microlites of olivine (Ol) and plagioclase (Pl). The crystal cargo is composed of *c*. 47 vol% Pl, *c*. 32 vol% Ol, *c*. 20 vol% clinopyroxene (Cpx) and <1 vol% chrome-spinel (Cr-Sp). The Pl crystals range from <0.1 mm to *c*. 2.5 mm.

Most Pl crystals have a wide Ca-rich core of An_{83-92} (Figure 6.3a), followed by a narrow rim of An_{68-78} (type OO-Pl1). These Pl crystals are found as isolated crystals or as part of Ol+Cpx+Px(+Cr-Sp) clots. The biggest Pl crystals (type OO-Pl2) contain a mantled zone of An_{72-85}, and sometimes a core with complex oscillatory zoning. Some of these cores include a Ca-rich inner core overlapping in composition with type OO-Pl1 crystals surrounded by very Ca-poor oscillatory zoning (An_{42-52}). In general, the Pl crystals are euhedral to subhedral.

The Ol crystals range between <0.1 mm to 2.4 mm in size and are euhedral to subhedral, with scarce evidence of resorption in some crystals. The most abundant Ol type (type OO-Ol1) consists of normally zoned crystals with high-Fo cores (Fo_{82-92}) (Figure 6.2c and Figure 6.3c). The other Ol type (type OO-Ol2) have Fo-poorer cores (Fo_{74-79}) with inverse zoning (Figure 6.3e). Ol rim compositions reach Fo_{67}, but most rim compositions do not reach Mg contents lower than Fo_{75}. One crystal of type OO-Ol1 crystal was observed with an orthopyroxene (Opx) corona. Both Ol types can be associated with Cpx in clots, and can contain Cr-Sp inclusions and glassy MIs.

The Cpx crystals (<0.1 mm to *c*. 1 mm wide) are mostly diopside to very Ca-high augite (Figure 6.3b). The crystal shapes vary from euhedral to anhedral, with mild concentric oscillatory zoning or sector zoning. Some crystals show a high-Ca core with resorption features followed by regular oscillatory zoning. Crystals can be isolated or in clots with other mineral phases.

Cr-Sp phenocrysts are scarce, but Cr-Sp inclusions are very common in Ol, and Cr-poor spinel inclusions are found in Cpx crystals. Most Cr-Sp inclusions are Fe-poor, with similar cation proportions of Cr and Al (Appendix 3).

6.5.1.2 Rishiri (RSH)

The RSH tephra is composed of *c.* 44 vol% vesicles. The rest of the sample is composed of *c.* 81 vol% groundmass and *c.* 19 vol% crystals (Figure 6.2b, d and f). The groundmass

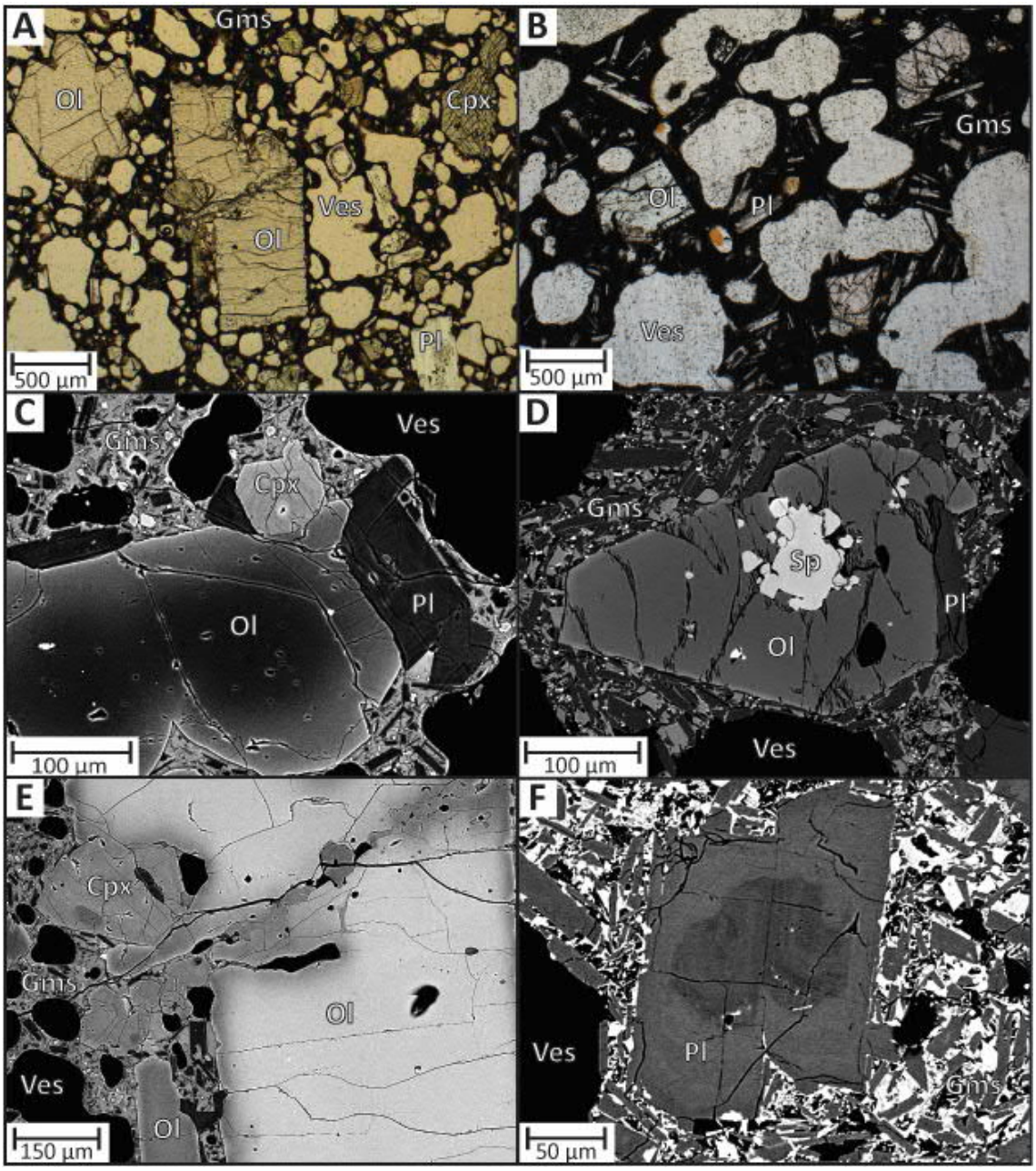

Figure 6.2. Images of OO and RSH tephra samples. Plane-polarized light microphotographs of (A) OO, and (B) RSH samples. BSE images of (C and E) OO, and (D and F) RSH samples.

is crystal-rich with Pl, Ol and Fe-Ti oxide crystals. The phenocryst cargo is composed of *c*. 64 vol% Pl, *c*. 34 vol% Ol and *c*. 2 vol% Cr-Sp. The Ol crystals are euhedral to subhedral and commonly found as isolated crystals or associated with smaller Pl crystals and Cr-Sp inclusions (Figure 6.2d). Core compositions range from Fo_{79} to Fo_{85} and are normally zoned, with the rim compositions reaching Fo_{76} (Figure 6.3c).

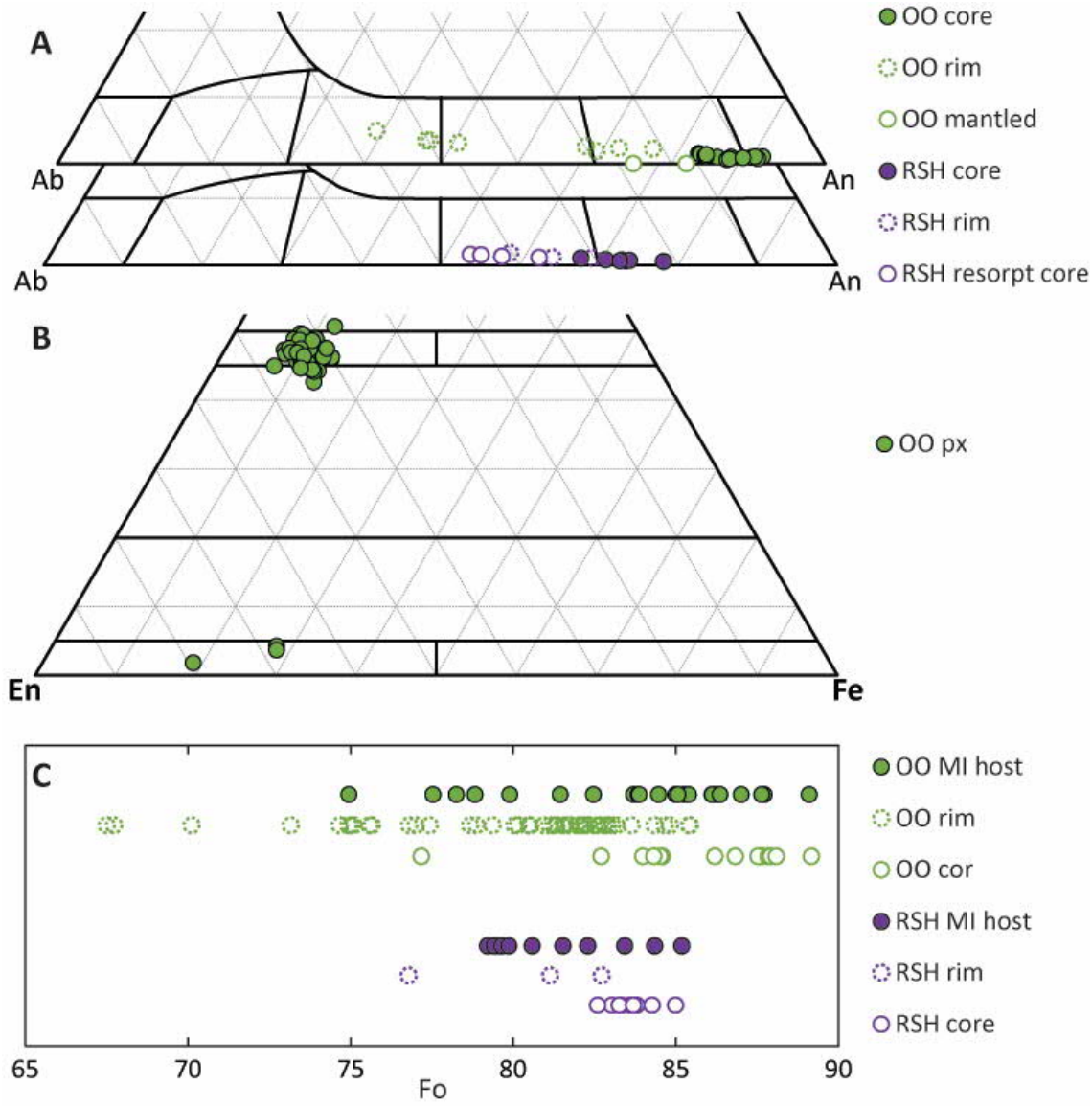

Figure 6.3. Mineral compositions of OO and RSH samples. (A) Pl compositions classified by mineral zone. (B) Px compositions from OO. (C) Olivine compositions for OO and RSJH samples classified by core and rim, with the measured compositions of the MI hosts classified as a different group. for OO and RSJH samples

The Pl crystals of the RSH sample are smaller than the Ol crystals and are euhedral with elongated tabular shape (high aspect ratio). Most Pl crystals are normally zoned with a core of An_{68-78} and rims of An_{54-69} (Figure 6.3a). Some Pl crystals include a resorbed core with an overgrown rim of high An composition. Cr-Sp are abundant as inclusions in Ol crystals, some reaching up to *c*. 100 μm in size (Figure 6.2d). These crystals have a higher Al and lower Cr content than the Cr-Sp inclusions in the OO sample (Appendix 3).

6.5.2 MI glass geochemistry

All MIs are glassy, without daughter minerals but with one or more shrinkage bubbles. Measured compositions of MI glasses (Figure 6.4) show a trend of increasing alkalinity from the NE Japan arc (AK and HK) to the Kuril arc (AKN and TT), with TK, RSH and OO having the highest K_2O concentrations. AK and HK are low-K tholeiites, whereas AKN, TT, TK and RSH follow a calc-alkaline trend. The OO samples have compositions ranging from calc-alkaline to alkaline with most compositions in the high-K calc-alkaline series.

The spider diagrams normalized to primitive mantle for all seven volcanoes (Figure 6.5a, c, e) show the characteristic patterns of arc volcanism related to contamination of the source by a slab component. All samples show LILE enrichment and the common Nb-Ta negative anomaly of subduction zone magmas (Pearce et al., 2005).

The lowest Nb and Ta concentrations are found in HK, AKN and TT, followed by OO and AK, then TK, and the highest concentrations in RSH. LILE general abundances are lower in the NE Japan arc melts, followed by the Kuril arc melts, whereas the highest LILE concentrations are found in the back-arc samples. This increasing trend of LILEs seems to also be followed by increases in Rb/Ba and Th/Ba ratios. The Pb/Ce ratios are similar for all arc melts except TK, which has lower Pb/Ce ratios, followed by the back-arc with the lowest Pb/Ce ratios.

Negative Zr anomalies are seen in all samples but RSH, and negative Ti anomalies are clearly seen in OO, TK and TT. An anomalous Zr positive anomaly is observed for one of the TT MIs. In AK and HK only some of the MIs show slight negative Ti anomalies. One OO MI, which corresponds to the group with very high Cl and F, has a different trace element pattern than the rest of the OO MIs. It is enriched in all trace elements compared to the other OO MIs, and it has a strong positive phosphorus anomaly.

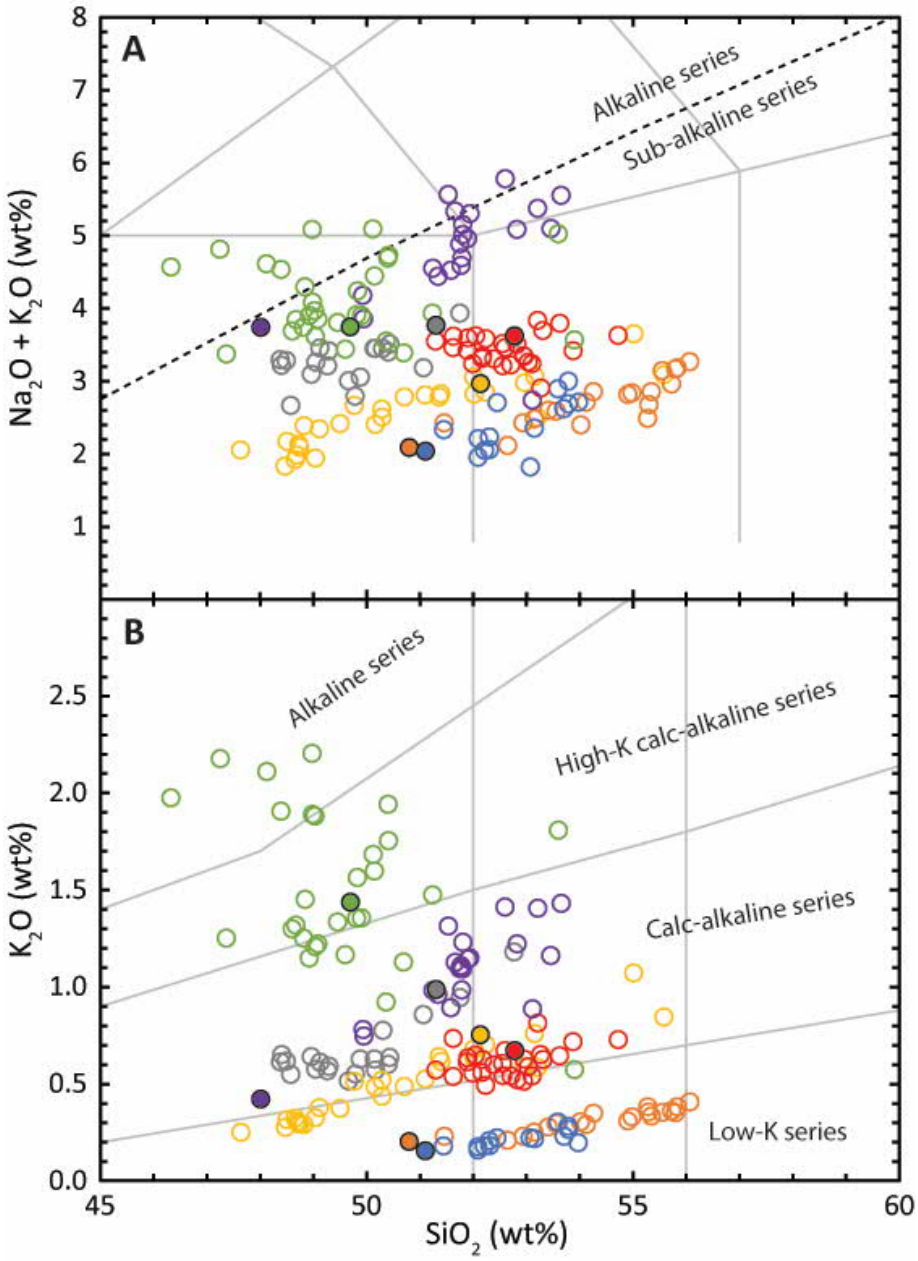

Figure 6.4 Ol-host MIs and whole rock major element compositions of the seven tephra samples. Colour scheme as Figure 6.1. Open circles are the MIs and filled circles are the whole rock compositions. (A) TAS diagram. (B) K2O vs SiO2 plot

The positive Pb and Sr anomalies are not present in this sample as the LREE enrichment is stronger than the Pb and Sr enrichment. The REE plots (Figure 6.5b, d and f) show that LREE enrichment is low in AK, HK and TT samples (La/Yb between 1.7 to 2.1), slightly higher in TK and AKN samples (La/Yb between 2.2 to 3.3) and a lot higher in OO and RSH samples from the back arc (La/Yb between 5.3 to 9.8). Slightly negative Eu anomalies are clear only in TK and TT samples.

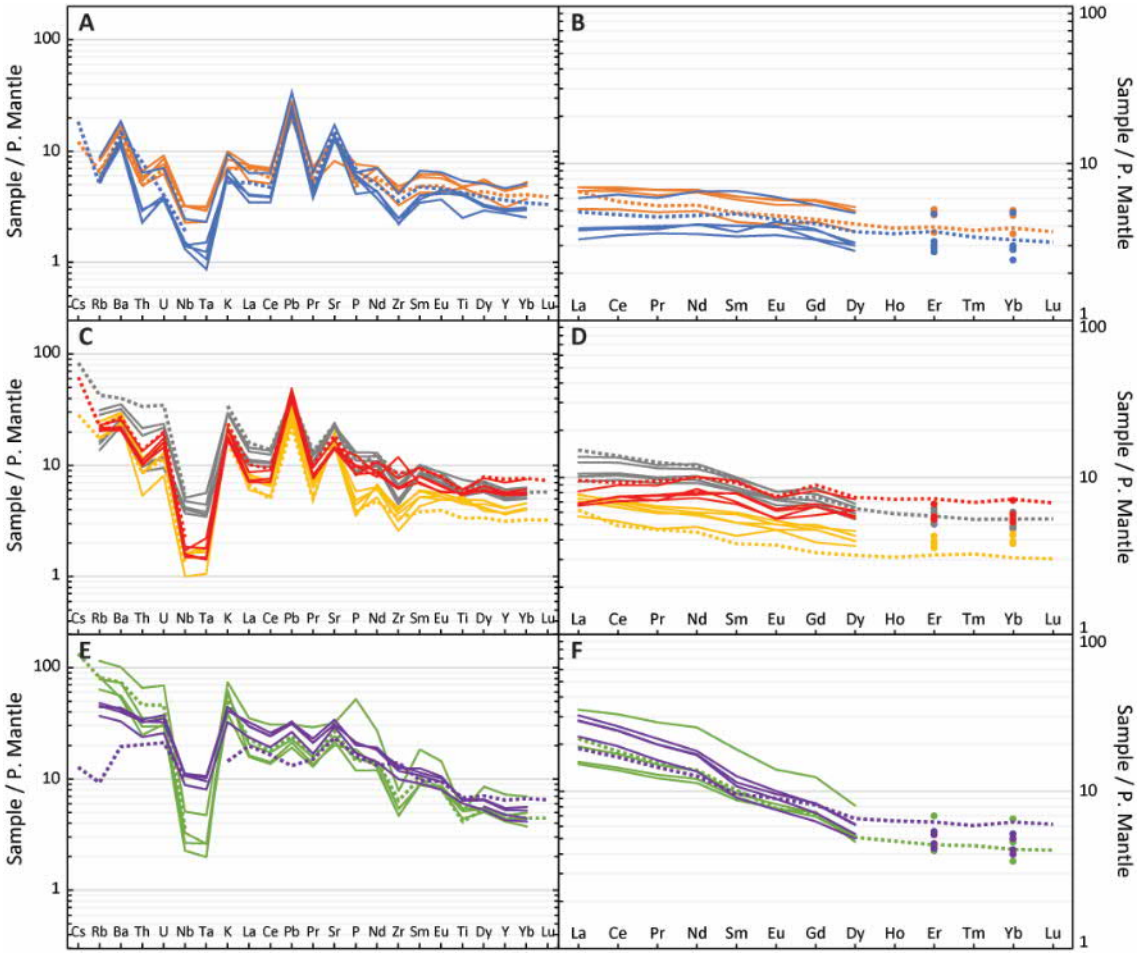

Figure 6.5. Spider and REE diagrams of LA ICP-MS measured MIs (continuous lines) and whole rock samples (dotted lines). Colour scheme as in Figure 6.1.

Measured volatile contents are shown in Figure 6.6 and Figure 6.7a (open circles). As with K_2O, Cl and F contents increase from NE Japan arc to the Kuril arc, with TK and OO showing the highest Cl and F contents and a wider range (*c.* 1500 to *c.* 3800 ppm Cl and *c.* 500 to *c.* 1500 ppm F). RSH compositions have low Cl/F ratios, but with higher F contents than all arc front melts. All H_2O compositions are lower than 3.5 wt% and CO_2 contents are lower than 600 ppm. New back-arc compositions overlap with the arc-front measurements given by Brahm et al. (in review) (Chapter 5), which range between *c.* 0.8

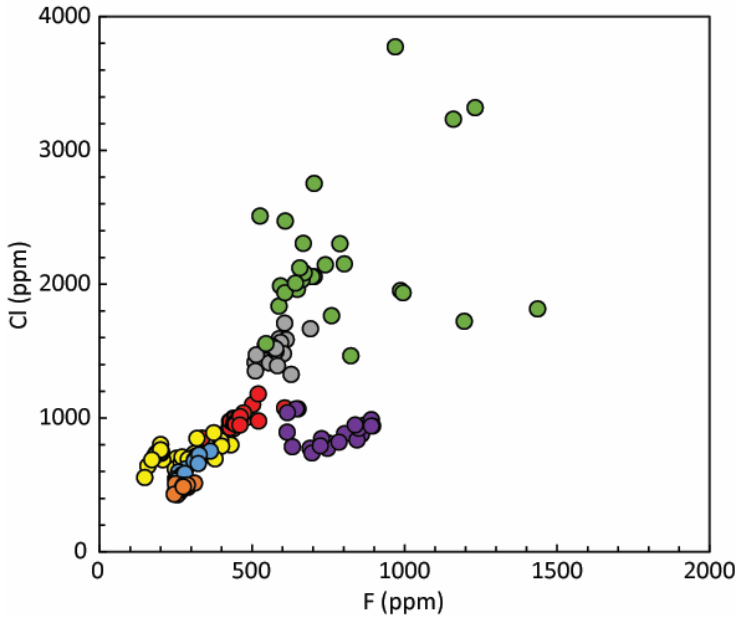

Figure 6.6. F and Cl compositions of the MIs from all seven samples. Colour scheme as in Figure 6.1. Errors (1σ) are about the diameter of the circles.

to *c.* 3.9 wt% H_2O and *c.* 29 to *c.* 426 ppm CO_2 for OO, and between *c.* 0.9 to *c.* 3.4 wt% H_2O and *c.* 15 to *c.* 524 ppm CO_2 for RSH.

As with the halogens, measured sulphur (S) concentrations are generally higher in the arc front samples than the back-arc samples. The arc front samples (excepting TK) range in S contents from *c*. 300 to *c*. 2600 ppm, whereas in the back-arc samples and TK, S contents range from *c*. 1480 to *c*. 2760 ppm. The range of S contents in MIs from each sample are generally wider than for Cl and F.

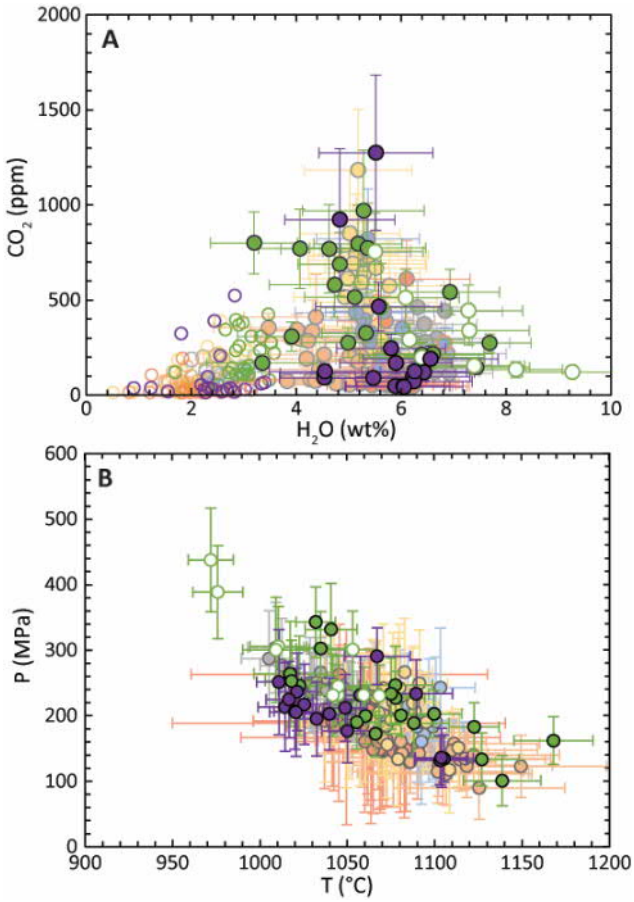

Figure 6.7.(A) Measured (hollow) and corrected (filled) H_2O and CO_2 contents and (B) PT estimated conditions of MIs for OO and RSH, overlayed on values for the arc MIs from Brahm et al. (in review) (Chapter 5). Colour scheme as in Figure 6.1. Error bars are 1σ. White circle with green outline correspond to the Fe-rich melts from xenocryst Ol hosts from OO.

6.6 Discussion

6.6.1 MI corrections and PT conditions

The MIs of the arc front samples (AK, HK, TK, AKN and TT) were already assessed for post-entrapment processes in Brahm et al. (in review) (Chapter 5). Most arc-front MIs show evidence of being completely re-equilibrated to a constant Mg# during long storage histories, and post-entrapment crystallization (PEC) corrections applied reconstruct the compositions at the last equilibrium conditions during storage and not at entrapment. An attempt to apply the MushPEC algorithm to estimate the compositions at entrapment was

made (Brahm et al., 2021, Chapter 4; Brahm et al., in review, Chapter 5), but showed that the main differentiation process is boundary layer fractionation, precluding the derivation of primary MI compositions through MushPEC.

In contrast, the MIs from OO and RSH have Ol-host cores with a wider compositional range and without evidence of re-homogenization. PEC-correction was applied using the following methodology. A modified MIMiC program was used to obtain estimates of CO_2 contents before bubble formation using a calculated-volume approach to model the vapor-bubble growth (Rasmussen et al., 2020; Bram et al., in review , Chapter 5). Host, MI and bubble dimensions were estimated the same way as done by Brahm et al. (in review) (Chapter 5). The modification of MIMiC replaces the VolatileCalc model (Newman and Lowenstern, 2002) with the Papale et al. (2006) H_2O-CO_2 solubility model, to maintain consistency with the corrected MIs from the arc melts.

The reverse Ol crystallization calculations were implemented using the Toplis (2005) model and the Putirka et al. (2007) Ol-melt thermometer. The initial H_2O content was estimated using the Gavrilenko et al. (2016a) hygrometer model iteratively as in Brahm et al. (in review) (Chapter 5).

The iron speciation (Fe^{3+}/Fe^{T}) was estimated by calculating f_{O_2} conditions using the Sp-Ol oxybarometer of Nikolaev et al. (2016) and the iron speciation using Kress and Carmichael (1991). Temperatures used to derive the ΔQFM values were estimated from previous MIMiC runs at QFM. The calculated f_{O_2} conditions for OO are 0.85 ± 0.15 ΔQFM (from 12 Sp-Ol pairs) using temperatures of 1000-1100 °C, and -0.06 ± 0.18 ΔQFM (from 12 Sp-Ol pairs) using temperatures of 1080-1100 °C.

Fe-loss (Danyushevsky et al., 2000) was assessed for the PEC-corrected MIs. Most MIs of the OO and RSH samples follow the differentiation path of the whole rocks from the literature (Figure 6.8) (Katsui and Yamamoto, 1981; Katsui et al., 1979; Yamamoto, 1988) for OO, and (Ikeda et al., 1990; Ishimoto et al., 2006; Ishizuka, 1999; Ishizuka and Nakagawa, 1999; Katsui, 1953; Katsui et al., 1978; Kuritani, 1998; Kuritani, 1999a; Kuritani, 2001; Kuritani et al., 2005; Kuritani and Nakamura, 2006; Moriguti et al., 2004; Shibata and Nakamura, 1997; Shimaoka et al., 2016; Shuto et al., 2004; Yoshida et al., 1981) for RSH, with deviation towards lower FeO_T contents. Fe-loss was corrected by

adjusting the FeO_T content of corrected MIs to fit the MgO vs FeO_T trend of the whole rocks. The group of OO MIs with low Fo and reverse zoning shows a different level of Fe enrichment compared to the rest of the MIs and the main whole rock trend (Figure 6.8a). These MIs are interpreted as xencrysts which may have suffered complete Fe-Mg re-equilibration during long storage, increasing the FeO_T content of the MIs. Fe-loss correction was not applied to these MIs. All results of the PEC-correction models can be found in Appendix 4. The trends in Figure 6.8 indicate that Ol was the only phase crystallizing during entrapment of most MIs in both samples. A group of MIs from RSH with the lowest MgO contents show a decrease in Al_2O_3 and CaO (not shown), indicating that Pl crystallization started at an MgO content of *c*. 5.5 wt%.

The corrected H_2O-CO_2 composition and estimated P-T (saturation pressure) conditions are shown in Figure 6.7 and overlap with the values of the arc front melts from Brahm et

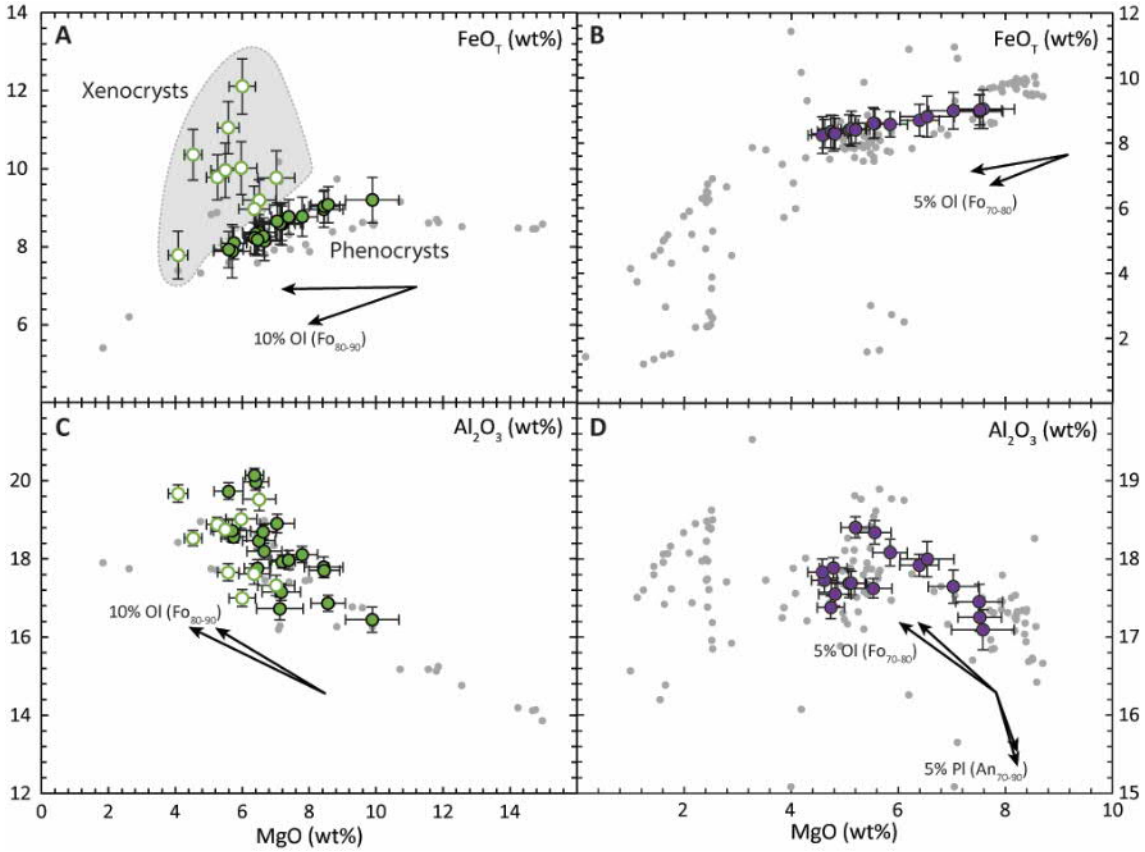

Figure 6.8. Variation diagrams for MIs from (A and C) OO and (B and D) RSH corrected for PEC and Fe-loss. Error bars indicate 1σ error. Grey dots are whole rock data from literature (see text). White symbols with green outlines in (A) and (C) correspond to MIs hosted in high-Fo Ol hosts of OO interpreted as xenocrysts. Black arrows indicate the fractionation models for Ol and/or Pl. The two arrows for each phase indicates the compositional variation of said phase.

al. (in review) (Chapter 5). OO MIs show a wide range of H_2O contents between *c*. 3.2 to

c. 9.3 H_2O, which translate into P and T ranges of *c*. 100 to *c*. 450 MPa and *c*. 970 to *c*. 1170 °C. High Fe MIs have higher H_2O and P and lower T estimations. The PT range of OO MIs overlaps the range of all arc front MIs. RSH estimations of H_2O have a narrower range than OO (*c*. 4.4 to *c*. 6.4 wt% H_2O), which also narrows down the P and T estimates (*c*. 120 to *c*. 300 MPa and *c*. 1010 to *c*. 1110 °C).

6.6.2 Halogen and sulphur loss

The halogens Cl and F have the highest solubilities relative to their abundance in basaltic melts (Carroll and Webster, 1994) and they are expected to not have suffered any degassing in glassy MIs. The tight compositional ranges of halogens within each sample and the positive correlation between Cl and F (Figure 6.6) indicates that the halogens indeed have not suffered any degassing in the samples investigated here. The highest halogen contents are found in OO with a wider compositional range, where some MI compositions are displaced from the main Cl vs F trends towards higher F concentrations at *c*. 2000 ppm Cl. This wide distribution of F compositions (*c*. 500 – 1500 ppm F) at similar Cl contents is unlikely to be caused by Cl saturation as MIs with similar major element compositions have almost twice the Cl concentrations (up to *c*. 3800 ppm). Therefore, the heterogeneous halogen compositions in OO are interpreted to reflect heterogeneous halogen contents in the primary melts.

As with H_2O and CO_2, S has the potential to be exsolved from the melt before and after MI entrapment. The multiple oxidation states of S make its solubility behaviour strongly affected by f_{O_2} conditions and S can be produced by sulphate or sulphide mineral precipitation, immiscible liquid separation and degassing (e.g., Ariskin et al., 2013; Moretti and Baker, 2008; Oppenheimer et al., 2011b; Wallace and Carmichael, 1992). After entrapment S can exsolve into shrinkage bubbles as a gas phase and/or precipitate in minerals in the bubble boundary. The lack of reliable estimations of f_{O_2} conditions for the arc front melts makes it difficult to estimate expected S solubilities, but analysing the

correlation of S variations with a known conservative element during magmatic fractionation and MI post-entrapment processes can help to identify S loss.

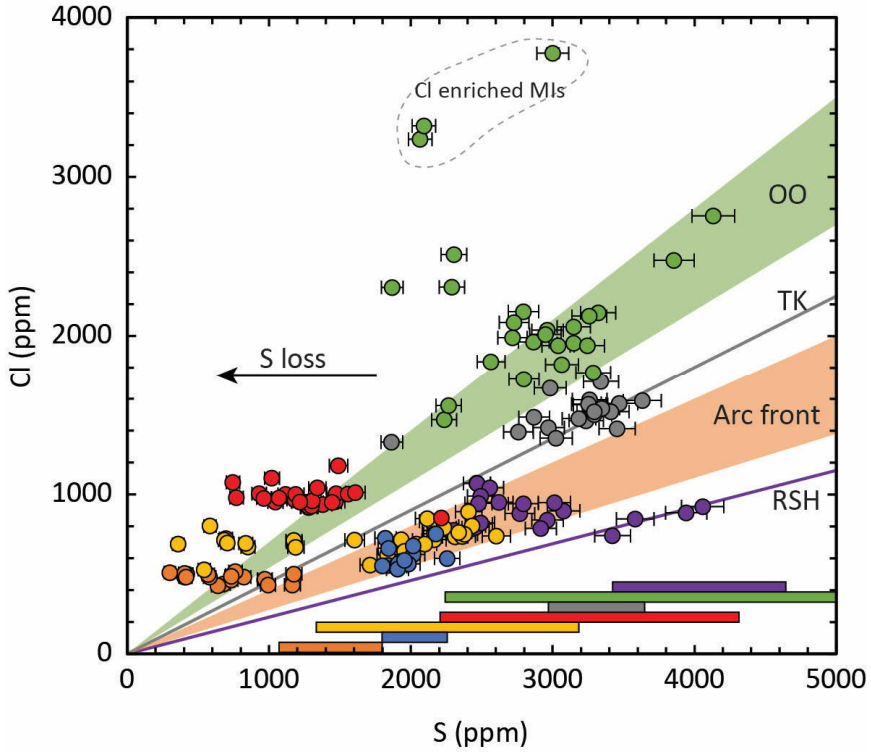

Figure 6.9. Measured Cl and S compositions of the MIs. Colour scheme as in Figure 6.1. Marked ranges of Cl/S indicates the estimated fields for each sample and the coloured rectangles at the bottom indicates estimated S contents before S loss for each sample.

Figure 6.9 shows the concentrations of S and Cl. If the MIs within each sample are produced by the same slab fluid under similar conditions and S is behaving conservatively, the Cl vs S trends should follow a linear correlation that passes through the origin. The observed displacement to lower S concentrations at the same Cl contents observed in AK, TT, AKN, TK and RSH are thus interpreted to be caused by S loss. The highest S MIs in AKN, TK, HK, OO and RSH appear to behave conservatively as they follow a line that passes through the origin. Then it can safely be interpreted that those S contents have not been affected by degassing. The S systematics of AK and TK MIs do not show conservative behaviour, indicating that the highest S content of each sample can be taken as a minimum S initial content. The MI from TT with the highest S is displaced from all others TT MIs and overlaps with the Cl/S ratio of HK and AKN. The highest S content of AK is very close to the Cl/S ratios of the rest of the arc front samples (except TK). Therefore, the original S contents of the arc front samples can be interpreted to be

following similar Cl/S ratios (*c.* 0.28 – 0.40), as it is observed for the Cl/S ratios in Figure 6.9. The Cl/S ratios increase towards the back-arc, with values of *c.* 0.45 for TK and *c.* 0.55 – 0.70 for OO. The Cl/S drops for RSH to *c.* 0.23 due to the Cl depletion observed in that sample.

6.6.3 Modelled slab-dehydration/melting conditions

The PT plot of Figure 6.10 summarizes the expected stability fields of relevant hydrous minerals in the different layers of the slab, estimated by the combination of thermodynamic modelling, experimental data and geodynamic models. The estimated PT conditions of the slab surface below each volcano are indicated by the coloured circles. The PT paths of each slab layer surface were taken from the lookup tables in the Arc Basalt Simulator version 5 spreadsheet (Kimura, 2017), which were obtained by the models D80 of Syracuse et al. (2010). The models selected correspond to the north Honshu and south Kuril sections. Conditions between 6 and 8 GPa were obtained by a quadratic extrapolation based on the shape of the curves at high pressures (*c.* 4-6 GPa).
The conditions of the slab below each volcanic system were estimated by combining the information of crustal depth (LITHO1.0; Pasyanos et al., 2014), slab depth (Slab2; Hayes et al., 2018) and slab surface P-T path (Syracuse et al., 2010) models. Using known values of crustal and mantle densities, the pressure of the slab below each volcanic system is estimated, and the slab P-T path model indicates the temperature of the slab surface.
Stability fields and H_2O content at saturated conditions for DMM (Workman and Hart, 2005a) and MORB (Hacker, 2008; Moyen and Stevens, 2006) were calculated with Perple_X version 6.9.1 (Connolly and Kerrick, 1987; Connolly and Petrini, 2002) for sub-solidus conditions, using the hp62ver.dat data file (Green et al., 2016; Holland and Blundy, 1994). Stability fields at sub-solidus and super-solidus conditions, H_2O at saturation and melt proportion of SED (pelite; Hacker, 2008) for the range of 1-6 GPa was taken from the lookup tables in the Arc Basalt Simulator version 5 spreadsheet (Kimura, 2017), which combines Perple_X calculations for subsolidus conditions with

experimental results (Hermann and Spandler, 2008; Schmidt et al., 2004) for the solidus liquidus interval.

Pressure increase, vertically from the slab surface to the Moho below the slab, is estimated to be <0.2 GPa using a simple lithostatic pressure model. PT conditions of the different slab layers can thus be approximated by assuming constant pressure and projecting the temperature for the geothermal gradient for each layer, as the small pressure difference has no major effect in the estimation of phase relations. The following analysis does not include the probable occurrence of accessory minerals (e.g., allanite, monazite, rutile, zircon, apatite). The slab component released to the mantle wedge is referred as slab liquid when the nature of the liquid is not defined, slab melt when it is a hydrous silicate melt and slab fluid when it is an aqueous fluid.

The phase relations for the sediments (Figure 6.10a) show that for the arc front volcanoes with lower T_{slab} (AKN, HK and AK), partial melting of sediments is probable. The PT conditions of the slab surface indicates 5 – 10 % melting of sediments if the slab liquid is released vertically into the mantle wedge. However, the slab component could be sourced from a shallower part of the slab and pushed westward by corner flow if ascent is less rapid. In this case, PT conditions might be closer to the wet solidus, and the slab component may reflect lower degrees of melting. Sediment melting conditions of TT and TK are close to 10 %. TT could produce melts of *c*. 5 % if the slab melt is sourced from a shallower level, whereas TK is predicted to have 10 % melting even if it is sourced at a shallower depth. The PT path towards the back-arc is steeper than the solidus, thus at pressures beyond 3.5 GPa, the slab PT conditions move closer to the solidus. Then, OO is predicted to produce about 5 % melt if segregated vertically and a little higher (<10 %) if segregated from a shallower depth. Melts and fluids generated at all depths for these six volcanoes are in equilibrium with residual Grt + Cpx + Phen. Below RSH, the slab is expected to be in equilibrium with a supercritical liquid (Kessel et al., 2005; Schmidt et al., 2004), but the possible amount of liquid generated at this depth is hard to estimate.

In the arc front, fluid influx from deeper zones of the slab is generated by amphibole breakdown in the deeper levels of the oceanic crust (MORB), and talc and Law breakdown in shallower levels. Dehydration conditions at deeper levels are similar to the other arc magmas. Further from the trench (in TT and TK) and towards the back-arc (OO

and RSH) fluids are sourced at all oceanic crust depths by Law breakdown and in lower proportion talc breakdown at deeper levels.

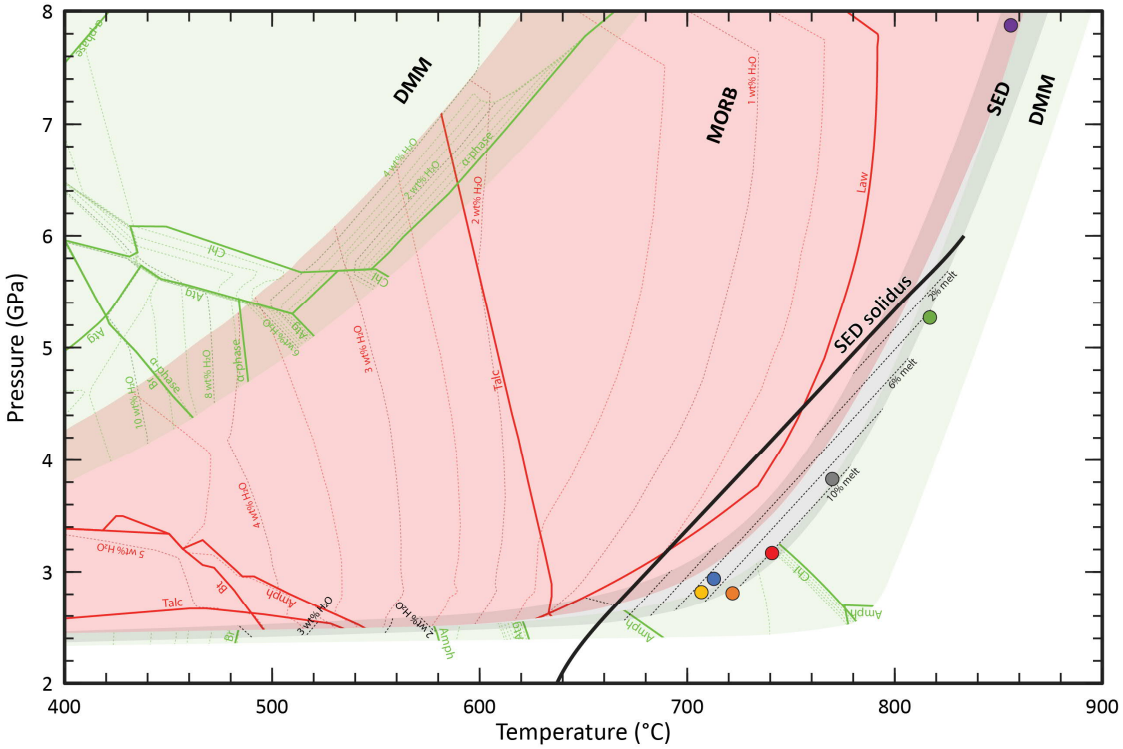

Figure 6.10. PT plot showing the relationship between the PT paths of the different layers of the slab and the expected stability fields of relevant hydrous mineral phases and the amount of water at saturated conditions. For a detailed description of the models used to estimate the slab PT paths and the stability fields of each protolith, see the methods section. Green indicates the hydrated DMM composition (in the lithospheric mantle and the hydrated mantle wedge above the slab). Red indicates the saturated MORB composition of the oceanic crust. Grey indicates the sediment

The lithospheric mantle below the subducting slab can be heavily hydrated by H_2O infiltration during the formation of extensive faults in the outer rise (Contreras-Reyes et al., 2008; Grevemeyer et al., 2007; Ranero et al., 2003; Ranero and Sallarès, 2004; Tilmann et al., 2008). Serpentinization of the lithospheric mantle has been proposed as an important source of fluids for arc magmatism (Debret et al., 2013; John et al., 2011; Kendrick et al., 2020). In the PT plot for DMM (Figure 6.10c) the possibility of fluid influx from the lithospheric mantle is assessed assuming H_2O saturation. This plot also indicates the phase assemblage expected at the hydrated mantle layer above the slab. Chlorite (Chl) and Serp are stable at the PT conditions below all six volcanoes (with the exception of RSH), and extensive dehydration by Chl and Serp breakdown is thus not expected at arc front depths. Extensive dehydration of the mantle, mainly by Serp

breakdown, is expected only for OO. The lithospheric mantle reaches Grt equilibration conditions at greater depths than below OO (*c*. 5.5 GPa at the Moho). The overlying mantle is expected to be hydrated in the arc front until Chl breakdown between TT and TK slab depths. The lower-T_{slab} arc magmas are very close to the biotite breakdown limit. Depending on the PT path of the lithospheric mantle, it can retain up to c. 4 wt H2O for colder subduction zones or be completely dehydrated at hotter subduction zones avobe c. 6 GPa. Either way there is no more fluid expected to be extracted beyond this point, after Serp and Chl exhaustion, which would be the case for RSH.

6.6.4 Correlation between trace/volatile signatures and slab conditions.

6.6.4.1 Rare Earth Elements (REEs)

The steepness of the REE patterns, represented by the ratios of LREEs to Yb, LREE/Yb, is associated to selective retention of HREEs over LREEs in the slab source. The dehydration/melting experiments of eclogites by Kessel et al. (2005) reproduced the high LREE/HREE ratios, which increased with temperature of the melt and related them to the high HREE distribution coefficient of Grt. In these experiments there is no report of the presence of accessory phases like allanite or apatite. The experiments of eclogite dehydration by Tsay et al. (2017) includes the appearance of allanite. For low-T experiments the fluid shows a flat REE pattern or even displays a slight increase towards the HREE. Allanite and monazite incorporate most of the LREE- and Th-budget of metabasites or metapelites (Hermann, 2002; Hermann and Rubatto, 2009), and this means that, in presence of Grt and allanite, all REEs are retained in the residue. Thus, the LREE/HREE ratios are controlled by the solubility of allanite, which has been shown to be T-dependent and P-independent (Hermann and Rubatto, 2009). Then, the increasing trends of LREE/HREE with T_{slab} (Figure 6.11) can be tied to progressive allanite dissolution. Apatite also has an affinity to LREEs and if present can be involved in forming the REE pattern.

Another indicator that the LREE/Yb increase towards the back-arc is caused by dissolution of allanite and/or monazite is the lower U/Th ratio seen in the back-arc compared with the arc front (Figure 6.12). With the exception of some low ratios in HK,

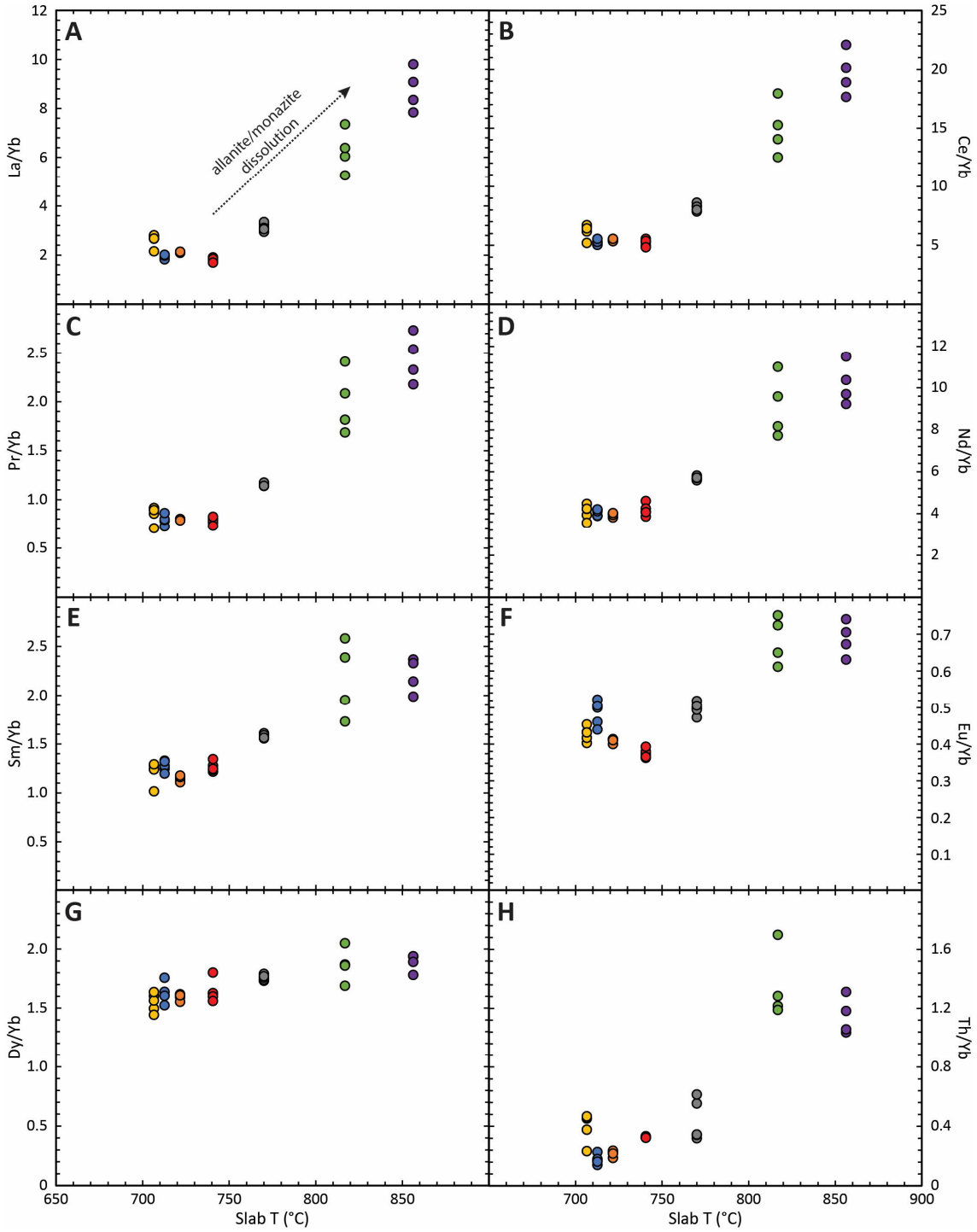

Figure 6.11. REE/Yb and Th/Yb variations in MIs with estimated T_{slab}. Colour scheme as in Figure 6.10. Dashed line in (A) indicates the process of LREE enrichment towards the back-arc.

all low T_{slab} melts up to TT have overlapping U/Th ratios > 0.32, whereas all high T_{slab} melts from TK to RSH have U/Th ratios <0.33. Allanite and monazite preferentially incorporate Th over U (Hermann and Rubatto, 2009; Tsay et al., 2017), producing a high U/Th fluid when these phases start to dissolve in the slab liquid.

The strongly negative Ti and Zr anomalies of the OO melts (Figure 6.5e) indicate that the HREEs and middle REEs (MREEs) have been enriched in the slab liquid and are not related solely to low degrees of melting. This enrichment is also probable for RSH, where Zr and Ti anomalies are absent due to enrichment of HFSEs in the slab, as discussed below. There are two processes that can explain HREE enrichment in the slab: (1) the mobility of all trace elements, including HREEs, is enhanced at higher temperatures Kessel et al. (2005), and (2) the Grt stability limit is parallel to the wet solidus, such that as the slab surface moves towards the solidus in the back-arc, some Grt breaks down, releasing HREEs.

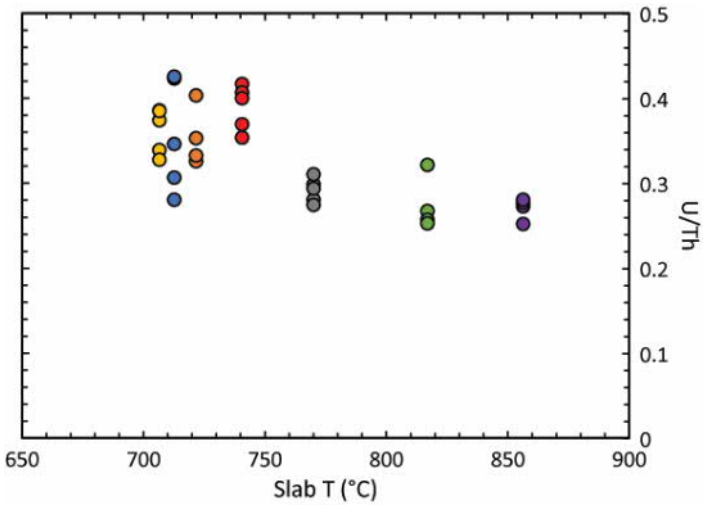

Figure 6.12. U/Th vs T_{slab} for the MIs. Colour scheme as in Figure 6.10.

6.6.4.2 High Field Strength Elements (HFSEs)

The characteristic depletion of HFSEs (Nb, Ta, Zr and Ti; Figure 6.13) compared to Large Ion Lithophile Elements (LILEs) in arc melts has usually been explained by their retention in residual rutile in the slab (Bernini et al., 2013a; Chen et al., 2018b; Foley et al., 2000; Xiong et al., 2011). Generation of HFSE-enriched residual F-OH-Ti-clinohumite intergrowths in olivine as a product of serpentinite-breakdown in the lithospheric mantle has also been invoked as a probable source of the high LILE/HFSE signature (Garrido et al., 2005). HFSE enrichment of some slab liquids are thought to be mostly controlled by

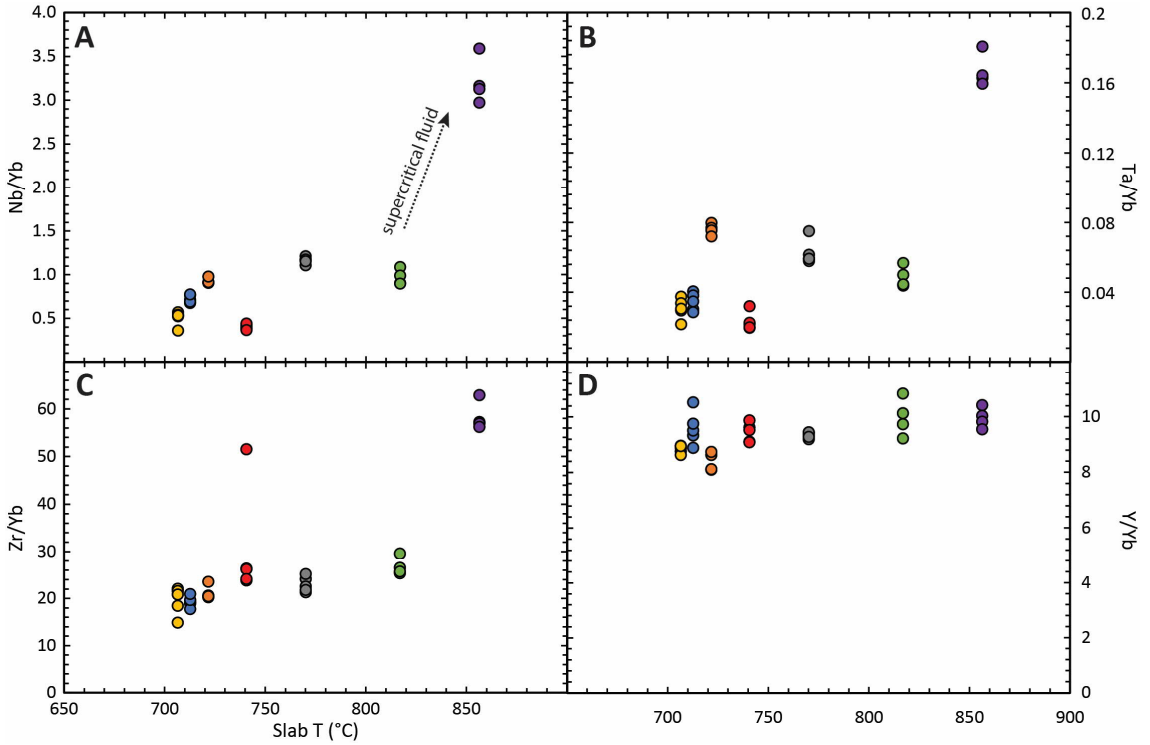

Figure 6.13. HFSE/Yb variations in MIs with estimated T_{slab}. Colour scheme as in Figure 6.10. Dashed line in (A) indicates the process involved in HFSE enrichment in RSH.

the dissolution of residual phases in the slab source (e.g., rutile, zircon; Hermann and Rubatto, 2009). Figure 6.14 shows Zr/Yb versus Nb/Yb for the seven volcanoes compared to the anhydrous melting models of DMM and enriched DMM (Workman and Hart, 2005a). Some Nb enrichment of the slab liquid in the arc melts is evidenced by the lower degrees of melting estimated for AK in Figure 6.14 compared to previously estimated melting degree for the same sample (c. 14% melting; Kuritani et al., 2019), even if assuming an enriched mantle source. Nb and Ta enrichment in AK is also seen in Figure 6.13, where the Nb/Yb and Ta/Yb ratios of AK have higher values than the other arc melts, comparable TK and OO that have hotter T_{slab} conditions. From Figure 6.14 it can be deduced that the slab liquids from AKN, HK, AK and TK are not enriched in Zr, whereas OO and TT are enriched in Zr sourced from the slab liquid. There is one extremely high Zr melt composition in TT, also visible in the spider diagram with a positive Zr anomaly. RSH shows extremely high Nb/Yb and Zr/Yb ratios, which are indicative of a slab liquid that is significantly enriched in HFSEs. The Zr composition of the slab liquid is almost exclusively controlled by the presence of zircon in the slab source (Bernini et al., 2013a; Hermann and Rubatto, 2009). The reduction of the amount of

residual zircon with higher T_{slab} in the back-arc is expected and it also explains the slightly higher Zr/Yb ratios observed in OO (Figure 6.14). The almost vertical trend between the extremely Zr-enriched TT composition and the other TT MIs mimics the Zr-enrichment trends found in glasses from the Sumisu rift in the Izu arc (Hirai et al., 2018), which indicates a slab source without residual zircon. As experimental results show that temperatures should exceed 900 °C for zircon to break down (Hermann and Rubatto, 2009), an anomalously high T_{slab} would be needed to explain this Zr enrichment in TT, but there is no other indication that the slab liquids from TT are sourced at high temperatures (e.g., low LREE/HREE). Further investigations on the variables affecting zircon stability in the slab will be required to explain this anomaly without a T_{slab} increase.

As with the reduction of residual zircon to generate Zr enrichment in TT, Nb enrichment with some of the arc magmas would require the dissolution of rutile in the slab source. As with zircon, rutile solubility increase has been shown to be tied to increasing temperatures (Hermann and Rubatto, 2009), but this does not explain the selective enrichment of some arc melts with low T_{slab}. The extremely high HFSE (Zr, Nb, Ta, Ti) enrichment observed in RSH (Figure 6.13 and Figure 6.14) is consistent with enhanced solubilities due to the supercritical nature of the liquid expected at pressures above 6 GPa

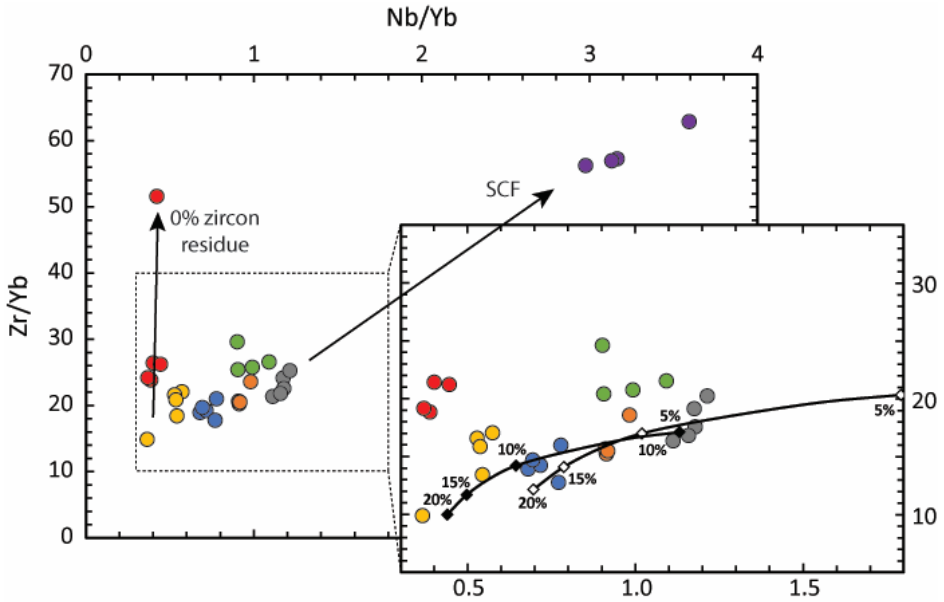

Figure 6.14. Zr/Nb vs Nb/Yb plot for MIs. Colour scheme as Figure 6.10. Trends in close-up are dry melting models from a DMM (black diamonds) and enriched DMM (white diamonds) from (Workman and Hart, 2005a). Percentages indicate the degree of partial melting at the diamond symbols. Black arrows indicate enrichment from the slab liquid. SCF = super critical fluid.

(Kessel et al., 2005; Schmidt et al., 2004; Taniuchi et al., 2020), resulting in dissolution of the main HFSE carriers (rutile and zircon).

6.6.4.3 Large Ion Lithophile Element (LILE) enrichment

All LILEs are strongly partitioned into Phen (Hermann and Rubatto, 2009; Tamura et al., 2007) and Serp (Scambelluri et al., 2001; Scambelluri et al., 2004), whereas Sr and Pb have a higher affinity with Law (Martin et al., 2014). The (Rb, Ba, K)/Yb ratio variations with increasing T_{slab} decrease then increase within arc melts (**Error! Reference source not found.**), forming a valley in the HK-AK samples. The ratios increase by a factor of about four in OO and then drop again towards RSH. LILE/LREE ratios (e.g., Ba/La; Figure 6.15a) have historically been used as a proxy for slab input in arc magmas, and decreasing trends with slab depth have been interpreted to reflect a reduction in slab input towards the back-arc (e.g., Patino et al., 1997; Sadofsky et al., 2008; Wade et al., 2006; Walker et al., 1995), whereas the LREE/HREE increase has been related to decreasing degrees of melting. As discussed above, the LREE/HREE increase is related to LREE enrichment due to increased allanite/monazite solubility with increasing temperature and not the degree of melting. Thus, Ba/La decrease can be tied to a stronger LREE enrichment from allanite dissolution for similar LILE inputs from the slab. The decreasing trends of Ba/La are different for the NE Japan and Kuril arcs, with the former having a steeper decrease, which might be related to differences in the composition and thicknesses of the sediment cover that also have an effect on the Rb/Ba ratios (see below). The increase of Ba/La in OO indicates a new source for LILE further down the slab, which enriches LILEs to a higher degree than LREEs, which are also enriched towards the back arc. As mentioned above, Phen is the main carrier of LILEs in the slab, and it is expected to be a major component in metapelites and a minor component in metabasites. Phen is stable in the metapelites and metabasites at depths from arc-front to back-arc, and only small amounts of Phen breakdown are expected at arc-front depths, where the thermal gradient is higher. No Phen breakdown is expected towards the back-arc, as the thermal gradient diminishes, and the PT path of the slab follows a subparallel path to the Phen stability field. This means that Phen has a limited potential to be there source of

LILEs in the slab liquid. Breakdown of Serp is a better candidate for a constant LILE supply from low to high T_{slab} in the arc front slab liquids, keeping LILE/Yb ratios within a narrow range. Abundant Serp is expected to be present in the hydrated lithospheric mantle under the arc front, but the low-T conditions of the lithospheric mantle under the arc front limits its availability for fluid release to the low-T_{slab} arc melts. Lower amounts of Serp, in combination with Law breakdown, in the oceanic crust can account for the LILE budgets at arc front depths. The small differences in LILE/Yb abundances within the arc front melts are probably related to variable degrees of melting, affecting the HREE abundances. The increased enrichment of LILEs in OO compared to TK can be explained by initiation of extensive Serp (and to a lesser extent Chl) breakdown from the hydrated lithospheric mantle, as the stability limit for Serp and Chl is approached below OO in the lithospheric mantle (Figure 6.10c).

Pb and Sr behave differently to other LILEs (**Error! Reference source not found.**). Neither a four-fold increase of Pb/Yb and Sr/Yb towards OO nor a drop of these ratios in RSH are observed. The lowest Pb/Yb ratios are actually found in OO and the highest Sr/Yb in RSH. The low Sr/Yb values found in AK and TT might have been affected by significant Pl fractionation expected for these melts (Brahm et al, in review, Chapter 5). When normalized to LREEs (e.g., Pb/Ce; Figure 6.15b), these LILEs show overlapping ratios within arc samples, and a decreasing trend towards the back arc (TK showing intermediate values). In contrast to the other LILE/LREE ratios (e.g., Ba/La), there is no Pb/Ce and Sr/Ce enrichment in OO. This can be explained by Pb and Sr being provided by Law breakdown occurring in the basalts (MORB layer) and at progressively greater slab depths towards the back-arc. It appears that there is a steady fluid input originating from Law breakdown across the arc, because Law is present in the slab at all depths, providing a constant input of Sr and Pb, whereas LREEs progressively increase due to allanite dissolution. Any extra Pb and Sr input added during extensive Serp breakdown from the lithospheric mantle under OO can be captured by interaction with Law in the oceanic crust. This is in agreement with the overlap of absolute Pb concentrations of the back-arc with the concentrations in the arc-front (Figure 6.5). As with Ba/La, Pb/Ce ratios have been used as a proxy of fluid influx (e.g., Bénard et al., 2018; Churikova et al., 2001; Jacques et al., 2013; Wehrmann et al., 2014a) and a Pb/Ce decrease towards the back-arc has been interpreted to reflect reduced fluid input. Here, Pb/Ce decrease is instead interpreted as a steady input of fluids from the breakdown of Law at increasing T_{slab}.

As with the HFSEs, LILEs mobility is enhanced in supercritical fluids (Kessel et al., 2005), so the drop in (Rb, Ba, K)/Yb observed in RSH (**Error! Reference source not found.**) cannot be explained by the changes in the nature of the slab liquid. There are two possible explanations for this behaviour. First, Serp breakdown is exhausted after OO depths and only minor sources of LILE remain in Phen and Law, which are predicted to still be present at *c*. 8 GPa (Schmidt and Poli, 1998). The second possibility is that the supercritical fluid released by the slab is separated into a hydrous silicate melt and an aqueous fluid during ascent in the mantle wedge, when ascending beyond the second critical point. Separation of the supercritical fluids has been invoked to explain the petrogenesis of melts with contrasting geochemistry in RSH (Taniuchi et al., 2020) Preferential partitioning of all trace elements into the silicate melt (as opposed to the aqueous fluid) is expected (Kessel et al., 2005), which could cause depletion of LILEs in the aqueous fluids that led to the generation of the RSH melts. Nevertheless, enhanced mobility of HREEs and HFSEs in silicate melts is higher than for LILEs (Kessel et al., 2005) and these elements are enriched and not depleted in RSH. Thus, exhaustion of Serp in the lithospheric mantle is the most probable explanation for LILE depletion in RSH. In addition, no such depletion is observed in Sr and Pb, which can be continuously sourced from Law-breakdown in the slab deeper MORB layer until depths of *c*. 8 GPa (Schmidt and Poli, 1998). Further, Law and Phen breakdown could act as the source of the somewhat lower enrichment of the other LILE (Rb, Ba, K) observed in RSH.

The Rb/Ba ratio has been interpreted to depend on the relative amount of sediment and basaltic components of the slab liquid (Kelley et al., 2003; Plank and Langmuir, 1998; Staudigel et al., 1996). The Rb/Ba ratio increases with increasing input from the oceanic basalts. This ratio does not appear to correlate with T_{slab} for the arc front melts (Figure 6.15). Instead, it appears to indicate that greater amounts of sediment are subducted beneath the NE Japan arc volcanoes compared to those of the Kuril arc. The back-arc melts have higher Rb/Ba ratios, likely indicating a higher amount of oceanic crust component as the sediment source is exhausted or higher amounts of slab fluids are fluxed with progressive slab subduction. These variations agree with the available Pb isotopic data from AK and AKN (Kuritani et al., 2019; Kuritani et al., 2021), predicting an increased sediment source for AK compared to AKN and also predicting a decreasing sediment source towards the back-arc at AK latitudes.

6.6.4.4 Halogens

The general behaviour of Cl and F with progressive subduction is similar to what is observed for the LILEs and MREEs, respectively. Cl/Yb ratios increase by a factor of 3-4 from the arc front to OO and drop again in RSH, whereas F/Yb ratios double from the arc front to OO, with similar values in RSH.

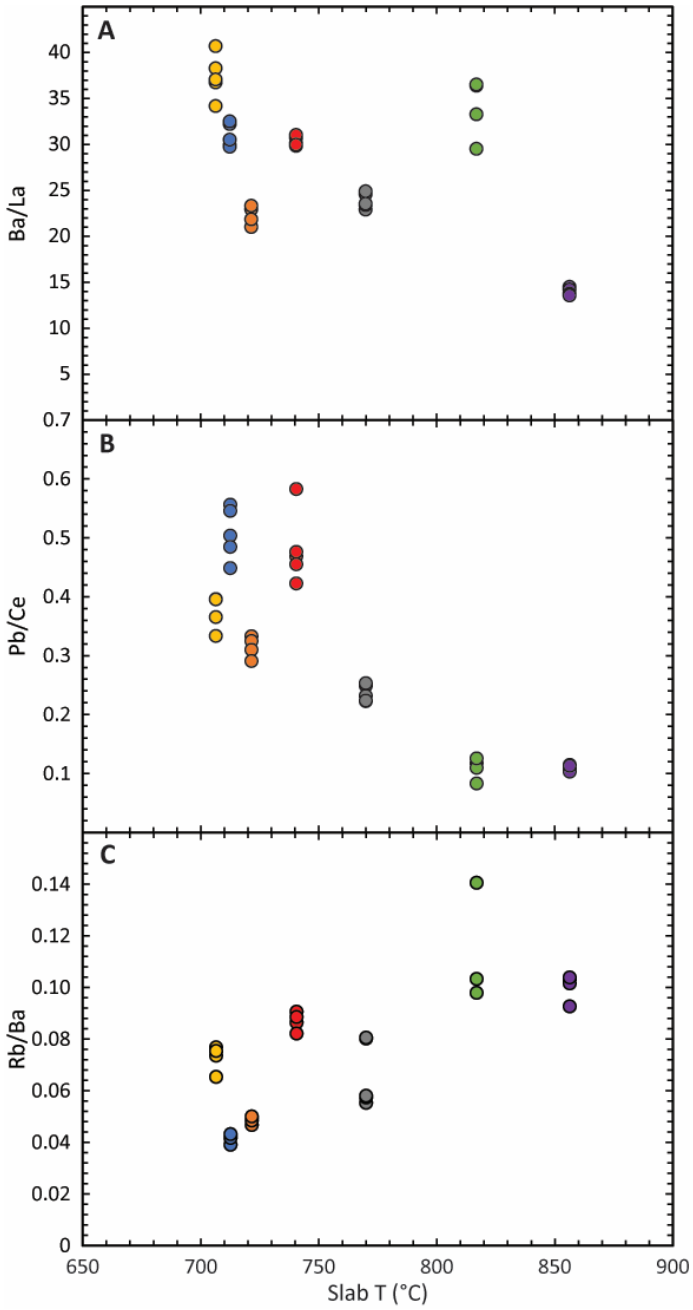

Figure 6.15. Variations of (A and B) LILE/HREE ratios and (C) Rb/Ba ratios in MIs with estimated T_{slab}. Colour scheme as in Figure 6.10.

Cl is more fluid mobile than F (e.g., Bernini et al., 2013b), and it is thought that most Cl is recycled through subduction, whereas a significant amount of F is retained in the slab

(Straub and Layne, 2003a). It has been proposed on the basis of halogen (F, Cl, I and Br) ratios and isotopic data that the most probable source of halogens in arc magmas are subducted Serp (John et al., 2011; Kendrick et al., 2020). Lower Cl/F ratios are found in eclogites and subducted serpentinites than in altered oceanic crust and oceanic (pre-subduction) serpentinites (Hughes et al., 2018; John et al., 2011), indicating preferential loss of Cl during early dehydration of the slab below the forearc (Straub and Layne, 2003a). This enriches the halogen sources of slab liquids at arc depths closer to the Cl/F ratios observed in arc melts (John et al., 2011; Kendrick et al., 2020). Enrichment of F has been observed in subducted Law (Pagé et al., 2016), which makes it a good candidate for F retention of fluids percolating through the oceanic crust, but also a source of F-enriched fluid during its breakdown.

The behaviour of Cl and F in these phases can explain the observed halogen/HREE and Cl/F variations across the arc. Roughly constant ratios are observed along the arc front, where there is a common source of fluids from Serp and Law breakdown in the oceanic crust. Cl/Yb and a slight F/Yb increase starts in TK with initial breakdown of lithospheric mantle Serp, which is enhanced towards the back-arc reaching the most enriched Cl and LILE compositions in OO. After exhaustion of Serp, the source of LILEs and halogens is reduced to Law breakdown. This produces a drop in LILE and Cl, but the preferential F enrichment of Law keeps F concentrations higher, generating the clear drop of Cl/F ratios in RSH.

The MIs with extremely high F and Cl observed in OO (>3000 ppm Cl) correspond to the group of low-Fo olivine hosts with reverse zoning. This enrichment is correlated with enrichment of phosphorus and all trace elements, which is seen in the spider diagram of the OO compositions with positive phosphorus anomalies (Figure 6.5e). These melts represent a different melting event, as their host disequilibrium indicates they are picked-up xenocrysts. These melts were produced by a slab liquid enriched by apatite dissolution, the only phase available that would explain the correlated phosphorus and halogen enrichment. In addition, apatite hosts similar amounts of LREEs and MREEs to allanite, which can provide the enriched REE source. Enriched LILEs, HFSEs and HREEs can be explained by an enriched slab liquid and/or by lower degrees of melting.

The wide variation of Cl and F for the rest of the OO MIs shows a wide range of slab fluid compositions and/or melting conditions not observed in the other volcanic samples. The fact that most MIs in arc front samples show evidence of long storage histories (Brahm et al., in review, Chapter 5) may indicate that any initial local heterogeneities resulting from the melting process are homogenized in long lived magma reservoirs at crustal depths, providing an "averaged" slab liquid and/or melting signature. In comparison, OO MIs are very primitive and thus have short storage histories, preserving local heterogeneities introduced by flux melting.

6.6.4.5 Sulphur

Walters et al. (2020) modelled the release of sulphur in the slab fluid from the AOC as subduction progresses in the arc front for the Honshu PT path (Syracuse et al., 2010) using Perple_X. The main reaction affecting the S budget at these conditions is progressive pyrite oxidation forming anhydrite, which releases oxidised S species (HSO_4^- and SO_4^{2-}). These species, transported in the slab liquid to the mantle source, are believed to be the main oxidation agents in arc magmas (e.g., Evans et al., 2012; Kelley and Cottrell, 2009). S solubility in rhyolitic melts produced by sediment melting under conditions relevant for arc front depths has shown to be high under reduced and oxidized conditions (Li et al., 2021), where minimum solubilities are found c. QFM+1, increasing towards lower and higher f_{O_2} conditions.

The constant Cl/S observed in the arc front indicates that the fluid composition released along the arc has the same S and halogen contents, suggesting that these sulphide oxidation reactions in the slab at arc front depths are similar along the NE Japan arc and Kuril arc. This suggests similar degrees of alteration, oxidation states, sulphide/sulphate contents of the oceanic crust and sediments for both arcs. The S content variation within arc front melts then follows the same behaviour than the halogen contents and can be related to the amount of slab liquid in the primary melt (see below).

The higher amounts of S estimated towards the back-arc can be tied to Serp breakdown. The antigorite breakdown reaction produces a highly oxidized fluid (Debret and Sverjensky, 2017), which enhances the mobility of sulphur, as sulphides buffer the oxidation process through dissolution of S into oxidised species. In addition, salinity increase produced by Cl released from Serp also enhances sulphur mobility (Newton and

Manning, 2005). The higher Cl/S ratios in TK and OO appear to be caused by a higher increase of Cl than S from the Serp breakdown at these locations. In addition, melting experiments have shown that S solubility (as sulphur content at sulphide saturation, SCSS, or at anhydrite saturation, SCAS) increases with temperature (Jégo and Dasgupta, 2013; Jégo and Dasgupta, 2014; Prouteau and Scaillet, 2012), consistent with increased S contents in back-arc melts.

The higher S contents in RSH than at the arc front, despite Serp exhaustion, which stops the production of highly oxidized saline fluids, might be related to the dissolution of sulphides or sulphates at these PT conditions or enhanced mobility of S in supercritical fluids. Wallace (2005) predicts that significant amounts of S survive slab dehydration/melting at arc/back-arc depths and return to the deep mantle. This indicates that there are significant amounts of S carrier phases are still present at c. 8 GPa in the slab, providing as a source of S to RSH.

6.6.5 Halogen behaviour during mantle melting

Highly variable F and Cl abundances, and Cl/F ratios of melts in arc settings can mainly be tied to variations in slab liquid compositions, but some variations can also be achieved by changes in flux melting conditions for a constant slab liquid composition. Dalou et al. (2014) calculated the partitioning of F and Cl in mantle minerals and identified contrasting behaviour in the variation of the partition coefficients with changes in the concentration of H_2O in the melt. F partitioning in the mineral phases decreases with H_2O addition, whereas Cl partitioning increases with H_2O addition. These changes in the compatibility of halogens affect the final F and Cl concentrations in the generated primary melts and their Cl/F ratios. Here, the flux-melting model applied by Dalou et al. (2014) is reproduced and compared to the halogen systematics of the melts in this study, to account for inter-volcanic and intra-volcanic variations. The model is used in a semiquantitative manner, to explain the general behaviour of the variation in halogen contents by changes in fluid composition and melting conditions.

The model is based on the flux-induced melting model of Stolper and Newman (1994) and Eiler et al. (2000), modified for non-modal melting using the equation of Johnson et al. (1990). The model is defined by the following equation (Dalou et al., 2014):

$$C_i^{melt} = \frac{C_i^{DMM} + \alpha\chi\left(C_{H_2O}^{slab}\right)^{-1}\left(C_i^{slab} - C_i^{DMM}\right)}{D_i^{lherzolite/melt} + \chi\left(1 - P_i^{lherzolite/melt}\right)}, \qquad \text{(Eq. 6.1)}$$

with:

$$D_i^{lherzolite/melt} = \left[D_0^{bulk} - \left(P_i^{bulk} \cdot \chi\right)\right]/(1-\chi), \qquad \text{(Eq. 6.2)}$$

$$D_0^{bulk} = \sum D_i^{mineral/melt} \cdot X^{mineral}, \qquad \text{(Eq. 6.3)}$$

$$P_i^{bulk} = \sum D_i^{mineral/melt} \cdot p^{mineral}, \qquad \text{(Eq. 6.4)}$$

where C_i^{melt} is the composition of the element i in primary arc melt, C_i^{DMM} is the composition of the mantle source, C_i^{slab} is the composition of the slab fluid, $C_{H_2O}^{slab}$ is the H_2O content of the slab fluid, $D_i^{lherzolite/melt}$ is the mineral proportion weighted partition coefficients, $P_i^{lherzolite/melt}$ is the weighted partition coefficient of the melt, χ is the degree of melting, $D_i^{mineral/melt}$ is the partition coefficient i into each mineral phase, $X^{mineral}$ is the weight proportion of each mineral in the mantle lherzolite and $p^{mineral}$ is the stochiometric coefficient of the mineral for the spinel lherzolite melting reaction. α is a factor that represents the rate of flux melting, defined as the amount of H_2O added to the source mantle divided by the degree of partial melting.

The modal mineralogy of the spinel lherzolite of Workman and Hart (2005a) is used here. The stochiometric coefficients for spinel lherzolite melting reactions in hydrous conditions are taken from Gaetani and Grove (1998). The halogen composition of the anhydrous lherzolite is taken from the depleted upper mantle of Saal et al. (2002), and three slab fluid compositions are used (Le Voyer et al., 2010; Straub and Layne, 2003a). Partition coefficients are taken from Dalou et al. (2014), producing a H_2O-dependent function by applying a linear regression of the partition coefficients data for the different H_2O contents of the melting experiments.

The results are shown in Figure 6.16, where they are compared to the PEC-corrected MI composition of all samples. Most of the variation in F and Cl abundances at similar Cl/F ratios within each sample can be explained by different levels of fractionation suffered by the MIs. Primary melt compositions are expected to have lower F and Cl contents than the ones plotted in Figure 6.16. The arc melts can be reproduced using the H_2O-poorer medium-level Cl/F ratio slab liquid (L2; Le Voyer et al., 2010) with 10-20% degree melting and α values from 0.02 to 0.06. It indicates that the similar Cl/F ratios of the arc magmas is produced by similar slab melts at similar degrees of melting and that the abundance of F and Cl concentrations is controlled by the amount of slab liquid being fluxed into the source mantle. At higher T_{slab}, the liquid with higher H_2O and Cl/F (L1; Straub and Layne, 2003a) is required to reproduce increased halogen contents of TK and OO. The higher Cl/F makes it possible to have higher Cl/F ratios in melts produced at lower degrees of melting. In addition, most of the spread in halogen contents of OO can be explained by local heterogeneities during melting at different amounts of fluid addition and degrees of melting, which is also consistent with the highly variable estimated H_2O contents of the MIs. Towards the back-arc, the increasing Cl/F and H_2O in the slab melt is consistent with increasing H_2O and Cl fluxed from Serp breakdown from the lithospheric mantle and reduced SiO_2 due to lower expected degrees of melting of the slab sediments. Progressive transition of the slab liquid composition from arc to back-arc (L2 to L1 in Figure 6.16) is expected as increasing Serp breakdown occurs and TK was probably produced by a slab liquid with compositions between the arc and the back-arc.

As discussed above, the drop in Cl and Cl/F in RSH can be explained by the exhaustion of Serp and the continued breakdown of Law. The halogen compositions of RSH are remarkably similar to one group of MIs from Mt Shasta (L3; Le Voyer et al., 2010), which have Cl/F ratios close to 1. Le Voyer et al. (2010) states that these particular slab liquid compositions could be explained by the presence of supercritical liquid but discards this option as the liquid is segregated at <6 GPa. Nonetheless, the present study indicates that a particularly low Cl/F signature is generated by Serp exhaustion, which may also be the case below Mt. Shasta, as high-T slab conditions have been postulated there.

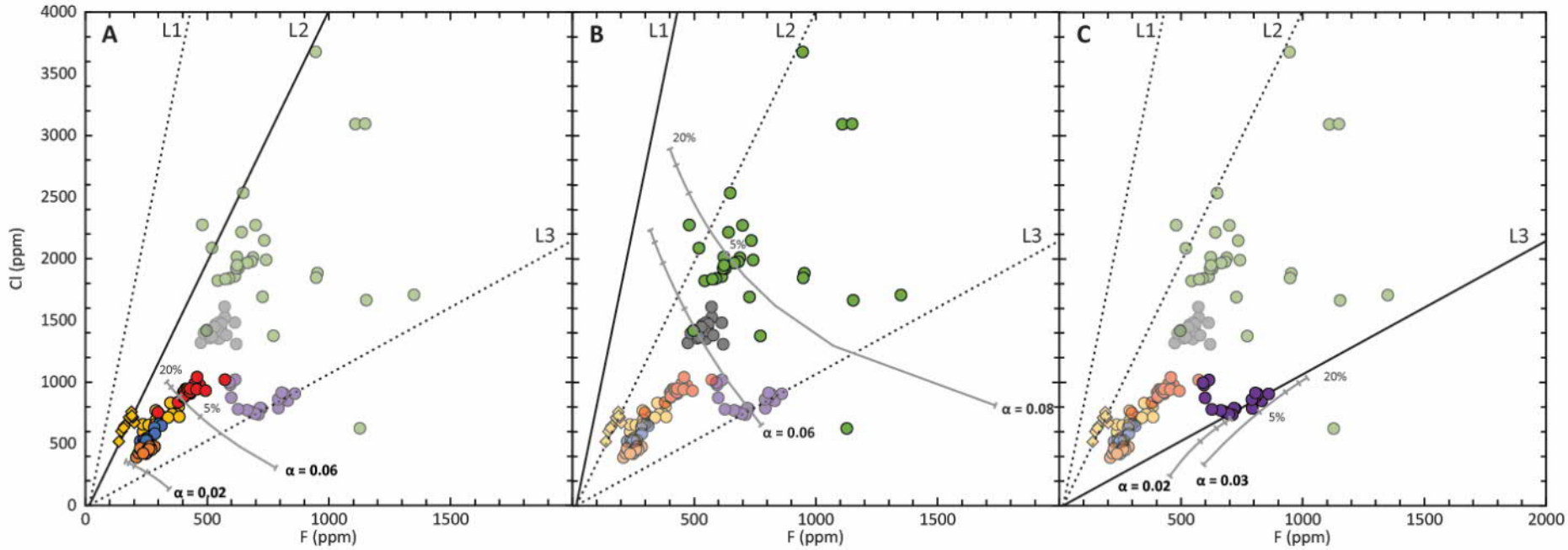

Figure 6.16. Flux-melting models compared to the Cl and F compositions of the PEC-corrected MIs. Color scheme as in Figure 6.10. Continuous black lines indicate the mixing line between DMM and the slab fluid used in the model. Dotted lines are the mixing lines for the other slab fluids used (L2 and L3 from Le Voyer et al., 2010; L1 from Straub and Layne, 2003a). Gray lines with marks are the melting modes indicating the 1%, 5%, 10%, 15% and 20% marks. The value of α of each model is indicated in the plots. (A) Reproduction of arc-front melts with L2. (B) Reproduction of TK and OO with L1. (C) Reproduction of RSH with L3.

6.7 Conclusions

Low degrees of melting of the sediment layer (<10 %) are expected at arc front depths, and melt production is reduced towards the back-arc. Trace element systematics of arc magmas across the subduction zone in northern Japan agrees with the involvement of predicted breakdown of metamorphic phases in the slab:

(1) A regular supply of Rb, Ba, K and halogens is provided through Serp breakdown at progressively deeper layers in the basaltic oceanic crust from arc front to back-arc. Some Phen breakdown is possible only at the low-T_{slab} of the arc front, restricting its capacity as LILE source for slab liquids. These LILEs and halogens are enriched in the back-arc when breakdown of lithospheric mantle Serp starts. Exhaustion of Serp at depths of *c*. 8 GPa produces depletion of these elements in the slab liquid released. Regular supply of Pb, Sr and F is controlled by Law breakdown at progressively deeper layers of the basaltic oceanic crust, continuing to depths of *c*. 8 GPa.

(2) Volatile elements (S, Cl and F) behave similarly to most LILE, increasing with input of Serp fluids. Cl is decoupled from S and F behaviour after Serp exhaustion, when its concentration decreases in the slab liquid. S and F continue to be provided from Law and suphide/sulphates available at depths c. 8 GPa.

(3) The LREE supply in arc magmas is governed by the accessory phases allanite and monazite, with their stability controlled mainly by temperature. Progressive increase of T_{slab} across arc produces a steady increase of LREEs in back-arc slab liquids.

(4) Common slab liquid proxies of the type LILE/LREE (e.g., Ba/La, Pb/Ce) do not represent a change in the supply of the slab component across-arc, but instead reflect the enrichment of LREEs with increasing T_{slab} with steady supplies of LILEs from Serp and Law breakdown.

(5) HFSE enrichment in slab liquids is mainly controlled by the solubility of accessory phases (zircon for Zr, rutile for Ti, Nb and Ta), which are typically thought to be controlled by temperature. Anomalous enrichments of HFSE in arc front melts (e.g., Zr in TT, Nb in AK) may indicate that additional variables also

influence the stability of these phases. As expected, HFSE mobility is enhanced in deeply sourced supercritical liquids (*c*. 8 GPa in RSH).

Homogeneous trace and volatile element compositions in most volcanic systems (especially in the arc) are probably caused by homogenization and “averaging” of variations in slab liquid and melting conditions during long-term storage in crustal magma reservoirs. In contrast, rapid ascent and eruption of primitive melts can preserve local variations in fluid flux melting conditions, recorded by halogen abundances and ratios variations.

Chapter 7

Synthesis

This thesis focuses on the application of olivine-hosted MIs for the study of magmatic processes in an arc system, from magma genesis to differentiation and storage processes. In Chapter 4, the problem of olivine re-equilibration is identified, which negates the possibility of recovering syn-entrapment melt compositions for long stored, antecrystic hosts. The algorithm MushPEC is developed as a first attempt to recover these compositions that cannot be obtained by classic PEC correction schemes. In Chapter 5, it is identified that most olivine crystals in the arc setting of northern Japan studied here are antecrystic. The analysis of the MIs and the application of the MushPEC algorithm to these MI populations helps to identify that HFC process cannot account for the compositional trend followed by the MI populations and that for these arc front melts BLF is the preponderant differentiation mechanism. Finally, in Chapter 6, the variation of trace element and volatile compositions of the seven samples from arc to back-arc are related to the metamorphic reactions occurring in the slab and their effect on the slab components of the arc melts at different slab depths.

7.1 The problem of olivine re-equilibration and the reasoning behind MushPEC

The classic methodologies of PEC correction identify a disequilibrium condition (Mg# disequilibrium between composition of the glass and the olivine-host) and use a reverse crystallization scheme to model the crystallization process until reaching the last equilibrium stage, where the melt was in Mg# equilibrium with the olivine (e.g., Danyushevsky et al., 2000). It is usually assumed that this calculated equilibrium stage corresponds to the composition of the melt at the moment of entrapment. Chapters 4 and 5 shows that this is not always true. Most MIs from all arc front volcanoes in northern Japan show evidence of being re-equilibrated to a narrow range of Mg# for a wide range of SiO_2 contents, showing no correlation between the degree of differentiation and Mg#

(Figure 7.1a), in contrast to the back-arc MIs (and a subgroup of AKN MIs) which show clear increasing SiO_2 with decreasing olivine host Fo content (Figure 7.1b). The first important highlight of Chapter 4 is the widespread equilibration of olivine-host and MIs with more evolved interstitial melts during long storage indicating it is a common process in long lived magmatic systems. It homogenizes all compositions of a MI population to a constant Mg# independent of the level of differentiation of the melt, as exemplified with

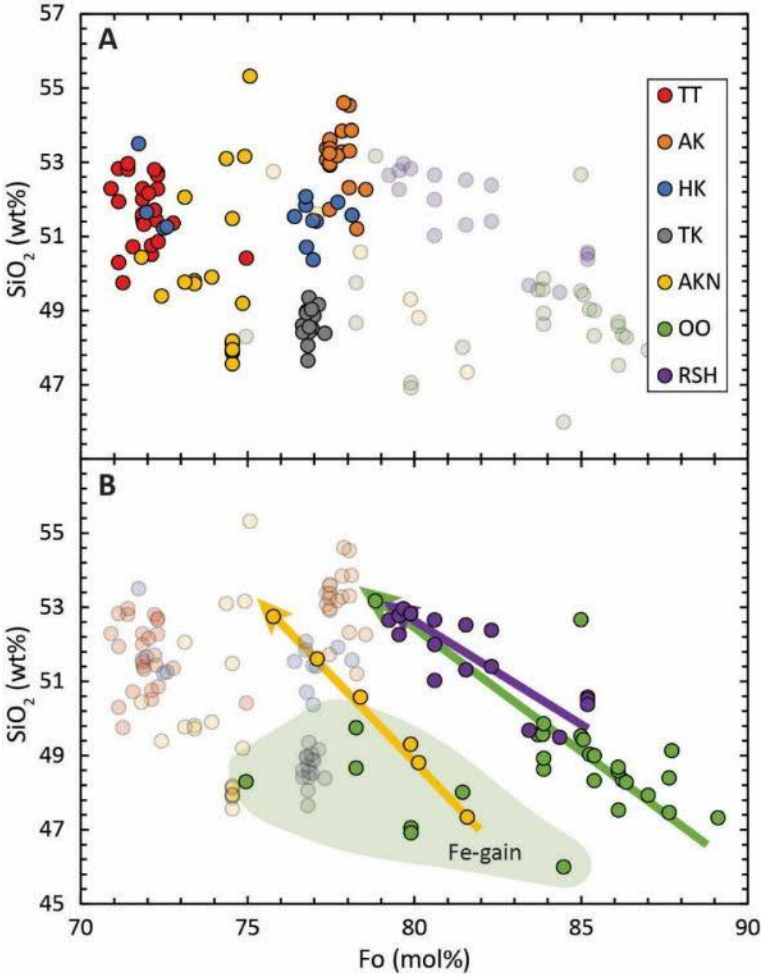

Figure 7.1. SiO_2 (wt%) vs olivine host composition (mol% of Fo) of PEC-corrected MIs of all studied samples in this thesis. (A) Arc-front MIs which do not correlate with the degree of differentiation of the olivine host are highlighted. These are evidence for re-equilibration of the olivine and MI to a narrow Mg# composition of the interstitial melt during long storage times. (B) Highlights MI populations that follow a differentiation trend reflecting the decrease of host Fo content with progressive crystallization are highlighted. These include the back-arc samples and a subgroup of the AKN MIs. The green field shows OO MIs that contain high amounts of Fe, which are in disequilibrium with the carrier melt (inverse zoning) and could represent re-equilibrated MIs xenocrysts or a different MI trend at higher Fe content.

the model in Figure 7.2. Discussion about the possible loss of information from original

syn-entrapment composition of MIs has been previously proposed by Gaetani and Watson (2000); Gaetani and Watson (2002), but the possibility of this process affecting olivine-hosted MI populations is usually not discussed in MI studies (Kelley et al., 2010; Portnyagin et al., 2007; Rowe et al., 2009; Rowe et al., 2011b; Sadofsky et al., 2008; Vigouroux et al., 2012; Wade et al., 2006; Watt et al., 2013; Wehrmann et al., 2014b; Weller and Stern, 2018). Many of the cited publications use the MI data to estimate primary magma compositions, and these estimates could be strongly affected if some of the MIs have suffered widespread Fe-Mg re-equilibration during storage.

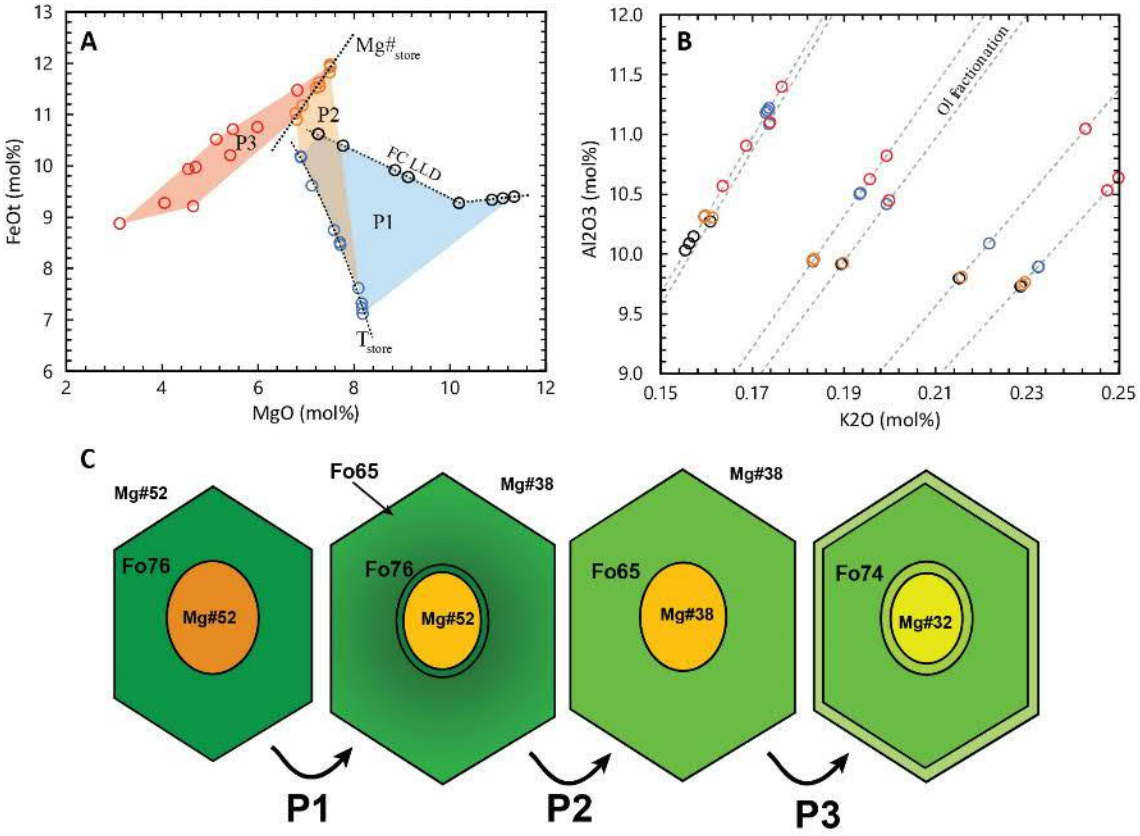

Figure 7.2. Forward model of post-entrapment compositional changes in long stored MIs (Figure 4.1). (a) MgO vs FeO_T variation diagram for the MIs. Black circles are the original MI compositions trapped during the fractional crystallization differentiation process of a magma batch. Blue circles are the composition of the MIs after P1 (PEC and Fe-loss during slow cooling) till reaching storage temperature T_{store}. Orange circles are the MI compositions after P2 (re-equilibration to $Mg\#_{store}$) and red circles are the final MI compositions after P3 (PEC and Fe-loss during ascent and eruption). (b) K_2O vs Al_2O_3 variation diagram for the MIs. Grey dashed lines indicate the olivine addition/subtraction trend of the MIs. Symbol colors are the same as (a). (c) Schematic cartoon of the evolution of one of the MIs with each phase of the post-entrapment history.

Given this process is common in the northern Japan arcs, equilibration should be explicitly assessed for and discussed in olivine-hosted MI studies, especially for low Fo olivine populations in long-lived magmatic arc systems with evidence of magmatic storage at crustal depths.

The advantage of olivine-hosted MIs for recording primary melt compositions is reduced to magmatic systems where storage timescales for olivine hosts are significantly less than the required time for total Fe-Mg re-equilibration. An example of the timescale of olivine re-equilibration is shown in (Figure 7.3; Wallace et al., 2021). The MushPEC program was built with the aim to recover the major element composition of the MIs at the moment of entrapment for long-stored, completely re-equilibrated antecrystic olivine-hosts. Succeeding in this objective would allow more MI populations to be suitable studies of magmatic petrogenesis. Recovering the original MI composition at entrapment of crystallization models to be produced to estimate primary magma compositions from geochemical data unaffected by crystal accumulation processes that commonly affect whole rock compositions, in addition to the possibility of recovering primary volatile concentrations.

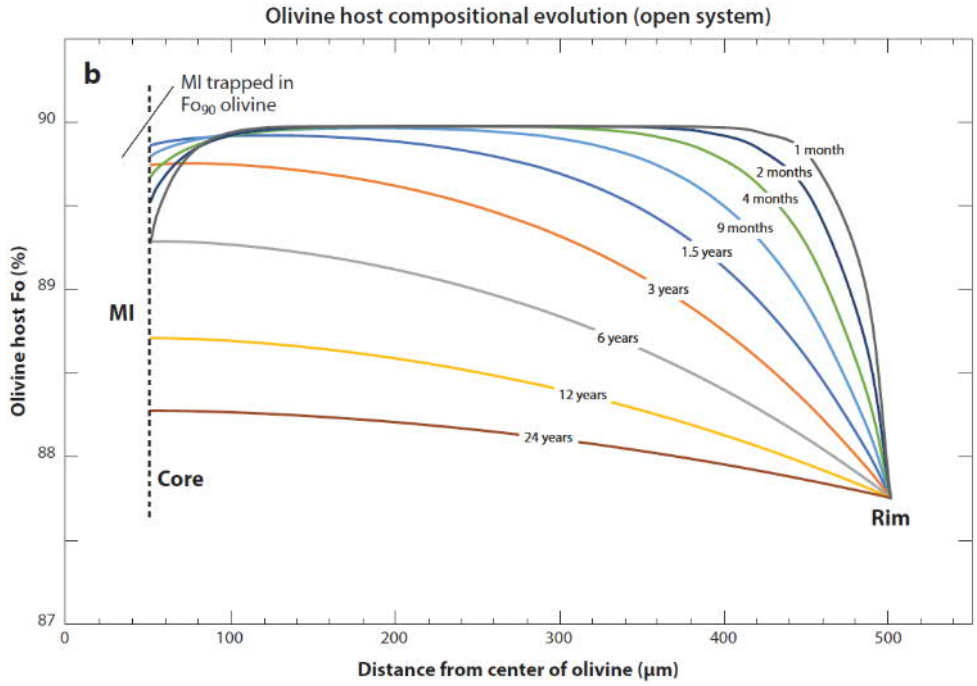

Figure 7.3. Composition profiles showing model of Fe-Mg diffusion of olivine host from MI boundary to crystal rim (Gaetani and Watson, 2000; Gaetani and Watson, 2002; Wallace et al., 2021).

7.2 MushPEC performance

MushPEC is a first attempt to recover original compositions of re-equilibrated MIs, and currently has a series of limitations, mainly related to its reliance on modelled homogeneous fractional or equilibrium crystallization liquid lines of decent. The performance of the algorithm can be improved as the thermodynamic models of mineral-melt equilibrium are improved. The reaching of a new equilibrium state during long storage makes it impossible to infer the original composition by reversing crystallization and diffusion processes suffered by the MI. MushPEC can recover the original composition of the MI by fitting the MI trend to a series of forward crystallization models, and freely adjusting MI composition through compositional vectors defined by olivine crystallization or melting. The compositional vectors are calculated in mol% with FeO_T and MgO summed together as the amount of Fe-Mg interchange is unknown but does not affect the total FeO_T+MgO. This means that the evaluation of the original Mg# of the melt is made on basis of the effect that the Fe-Mg distribution in the melt has on the LLD generated, which seems to be small compared to other parameters like pressure or H_2O content. This makes it necessary to have external constraints on the initial Mg# of the melt. The Fe-Mg distribution is also closely correlated with the f_{O_2} conditions of the melt, making it possible to further constrain the Mg# conditions by having information on the f_{O_2}.

Even though in Chapter 4 the AK sample seems to agree with the fractional crystallization model produced, further analysis of this sample in Chapter 5, in addition to the other arc front samples, indicates that HFC is not the main differentiation process. As discussed in Chapter 5, the lower H_2O content estimated by fitting the AK MI data to a fractional crystallization model compared to the H_2O content estimated by the Ca-in-olivine hygrometer (Gavrilenko et al., 2016a) is caused mainly by the decreasing Al_2O_3 trend with SiO_2 increase in the MIs. A decreasing Al_2O_3 trend predicts an early incorporation of plagioclase in the crystallization assemblage when modelling the FC process, which is tied to low H_2O in the magma (Almeev et al., 2012). Nonetheless, decreasing Al_2O_3 can also be generated by BLF at higher H_2O contents, as widespread plagioclase fractionation occurs in the solidification front. In addition to the trends of minor elements like P_2O_5 and TiO_2 as indicators of the process of fractionation occurring, higher H_2O estimated

with hygrometry than with HFC modelling may also indicate BLF or mixing are probable differentiation processes instead of HFC. Further, applying the Ca-in-olivine hygrometer to PEC-corrected MIs before attempting to use MushPEC helps to reduce the range of

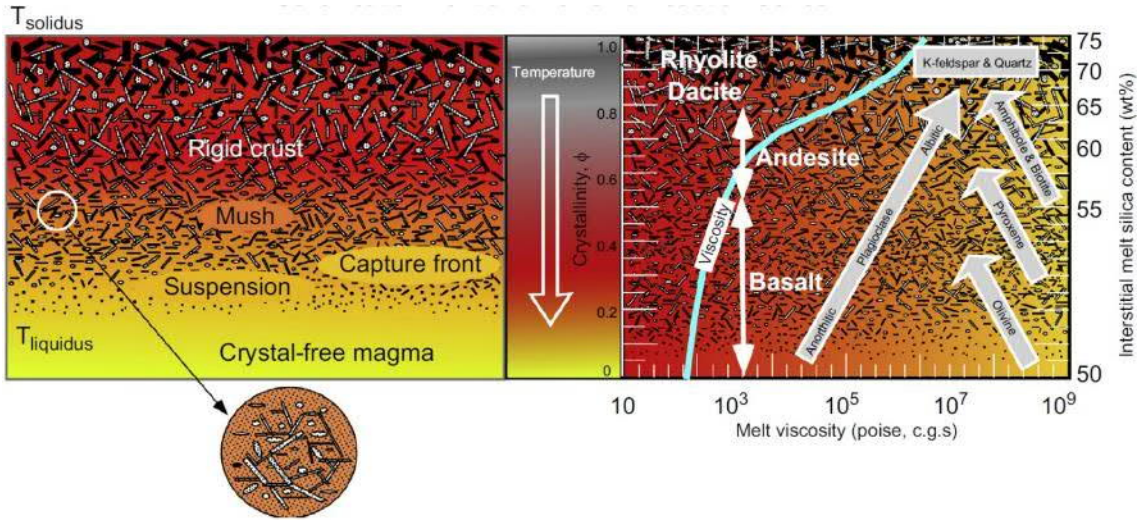

Figure 7.4. Solidification front model from Marsh (2015). The left side shows the solidification front in the ceiling of the magma body. The top is located at the solidus (interstitial melt is absent above this point) and the absence of crystals indicates the liquidus on the bottom. The middle figure indicates how the temperature variation from boundary to centre of the magma chambers correlates with the crystallinity. The right side shows the relationship between the interstitial melt composition, its viscosity and its relationship with the Bowen's reaction series, with the distance to the solidus (downward temperature increase.

H_2O contents for the initial parameters defined during the MushPEC run, reducing processing times.

The BLF or in-situ crystallization model was initially developed by Langmuir (1989) and further parametrized in the model of Nielsen and DeLong (1992), but it is also intimately related to the concept of the solidification front (Figure 7.4) (e.g., Marsh, 1996), which describes the stratification expected at a magma chamber – wall-rock boundary of high crystallinity caused by the thermal gradient of decreasing T towards the wallrock (Figure 7.4 and Figure 7.5a). Extraction of the differentiated interstitial melt from the solidification front can be extracted and incorporated into the main melt in incremental amounts, producing a differentiation trend that can be described as a combination of iterative steps of FC and mixing (Figure 7.6).

The findings in Chapter 5 highlight the widespread occurrence of BLF as a controlling process of magmatic differentiation for hydrous magmas in arc settings. Estimated

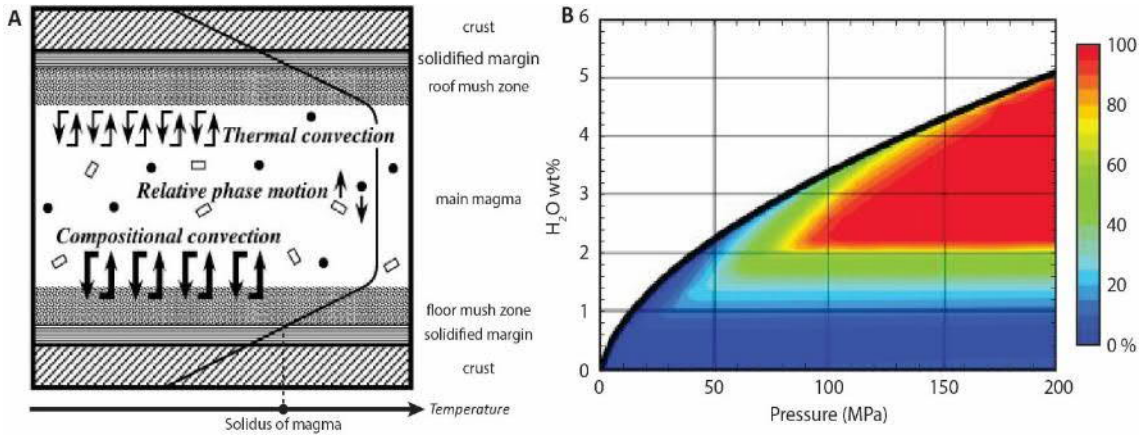

Figure 7.5. (A) Schematic from Kuritani (2009)of magma chamber representing the BLF model, indicating the temperature increase towards the centre of the magma chamber and the mixing process between the extracted melt from the floor mush zone. (B) Efficiency of BLF process as a function of H_2O content and pressure of the melt from the model results of Kuritani (2009).

pressure and H_2O contents for the arc magmas are in agreement witg conditions that promote BLF over FC based on the model of Kuritani (2009) (>100 MPa and >3 H_2O wt%; Figure 7.5b), indicating that this process may be the most common differentiation process affecting arc magmas in general. The BLF signal in AK is the smallest, represented by the upward trend in TiO_2 vs K_2O (Figure 5.9), coincident with the lowest H_2O (*c.* 3 – 5 wt%) and P values (90 – 180 MPa) estimated for this sample.

MushPEC can be applied as a method for PEC correction of re-equilibrated MIs in cases of low H_2O contents, which are not common in arc magmas but are expected in other tectonic settings such as hot spots or divergent margins. The applicability of MushPEC can be updated as new differentiation models are developed, which can be directly implemented into the algorithm as an alternative to the current rhyolite-MELTS model.

7.3 Storage histories of arc front vs back-arc

The identification of mainly re-equilibrated antecrystic hosts in the arc front and phenocrystic hosts in the back-arc are indicative of the expected conditions of transport and storage for these two settings. Oshima-Oshima is located southwest of Hokkaido, in the Japan Sea, where the crust is only *c.* 20 km thick. A thinner crust facilitates magma ascent from source to surface, allowing for highly primitive melts to be extruded without

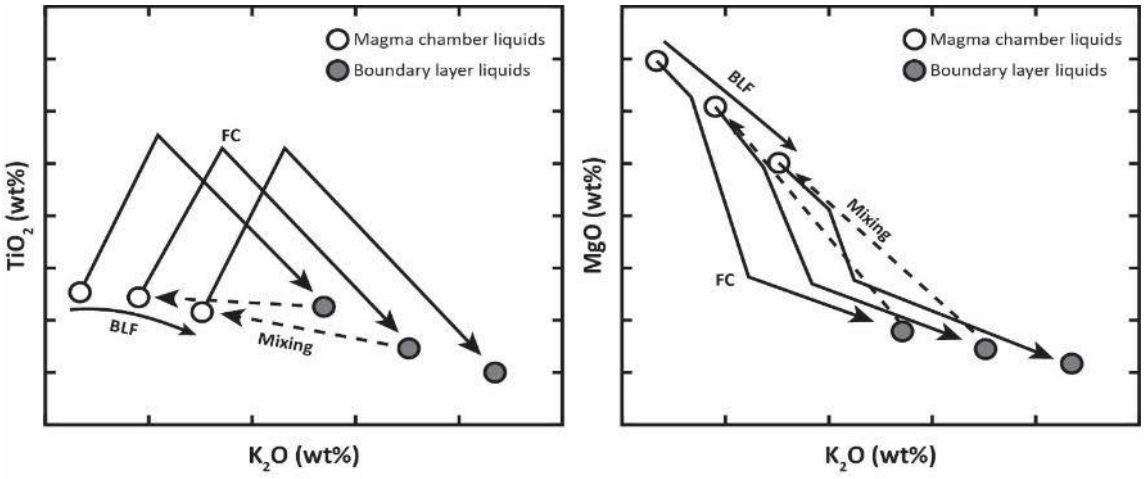

Figure 7.6. Schematic model of boundary layer fractionation (modified from Nielsen and DeLong, 1992). White circles indicate the composition of the magma chamber liquid after each step of mixing with the boundary layer liquids. Grey circles indicate the composition of the boundary layer liquid that is extracted and incorporated in the magma chamber liquid. Black arrows indicate the differentiation directions from fractional crystallization at each step (FC) and boundary layer fractionation as the resultant melt evolves in the magma chamber (BLF). The dashed arrows indicate the mixing between the boundary layer liquid generated at each step with the magma chamber liquid.

much storage time. Of course, this does not mean that no magma storage and evolution occur in the crust under OO, as more differentiated melts also exist in this volcano (Katsui and Yamamoto, 1981; Katsui et al., 1979; Yamamoto, 1988), but it increases the likelihood of magmatic batches not stalling in the crust. The difference between the arc front and OO samples lies not only in the level of differentiation and the degree of olivine re-equilibration, but also in the heterogeneities found related to the flux melting process. As shown in Chapter 6, OO is the only sample showing heterogeneous in volatile concentrations. This includes measured halogen contents (Figure 6.6) and estimated H_2O and CO_2 compositions using the Gavrilenko et al. (2016a) hygrometer and MIMiC software for the bubble correction scheme (Rasmussen et al., 2020). As explained in Chapter 6, the variable halogen compositions of the OO MIs can be explained by local heterogeneities in the process of flux melting, including the amount of fluid added to the mantle and the degree of melting of the mantle. These heterogeneities during flux melting are expected to occur in any magmatic system, but it does not get recorded in the arc melts, as magma ponding in the crust can homogenize the source signal and provide an "averaged" melting signature.

The lack of strong heterogeneities in the RSH sample might indicate longer storage times than for the OO sample, as well as differentiation in the crust, generating some level of homogenization of the melting signature for this particular sample.

The TT sample from Kunashir Island northeast of Hokkaido. Under this volcanic island the crust is *c*. 25 km thick, which is between OO (*c.* 20 km) and RSH (*c*. 28 km). Even though the crust is thinner than in the other arc front systems investigated here, the TT sample is the most differentiated sample of the seven analysed samples in this study, indicating a history of storage and differentiation that agrees with the narrow range of volatile compositions and re-equilibrated olivine compositions, which are the common characteristics within the arc front volcanic samples.

7.4 Across-arc variations of trace and volatile elements

Chapter 6 focuses on the analysis of trace and volatile element variations from arc to back-arc in northern Japan, correlating element ratio variations with the progressive increase of slab P-T towards the back-arc, estimated from subduction models. By following the expected metamorphic reactions that occur in each slab layer with progressive subduction (oceanic sediment, basaltic crust and hydrated lithospheric mantle) and by understanding the partitioning behaviour of the different elements between the mineral phases and the slab fluid or melt, the compositional variations can be explained by progressive dehydration reactions in the slab.

General overlapping in trace element ratios (LILE/HREE or LREE/HREE) and similar Cl/F ratios in the low slab temperature arc front volcanoes (AKN, HK, AK and TT; c. 700 to 740 °C), can be explained by a common slab liquid composition generated by the LILE input of Law and Serp dehydration from the basaltic crust in addition to probable low degrees of partial melting occurring in the sediment cover. As the slab temperature increases towards the back-arc, first in TK (770℃) and then OO (817°C), characteristic LREE/HREE and LILE/HREE increase is tied to two different processes. LREE is hosted in accessory minerals like allanite and monazite (Hermann and Rubatto, 2009), with T-

dependent and P-independent stability. Dissolution of these accessory phases in the sediment cover and basaltic crust with progressive increase in T produces the observed increasing trend in LREE/HREE ratios with progressive subduction. The observed LILE increase, on the other hand, cannot be tied to these phases, and it also cannot be tied to Phen breakdown in the sediment cover, because the P increase towards the back-arc bring slab surface conditions closer to the solidus, thereby reducing the degree of melting. As Law breakdown is expected to continue steadily towards the back-arc, it cannot account for the LILE enrichment. Breakdown of abundant Serp in the hydrated lithospheric mantle is then the most probable source of LILE enrichment towards the back-arc. This also agrees with the contrasting behaviour of Pb and Sr (which are LILEs). These elements behave differently from the rest of the LILEs, as their release from the slab is controlled by Law breakdown from the oceanic crust.

The drop of LILE/HREE and Cl/F ratios in RSH are caused by the exhaustion of lithospheric Serp, and the continuation of Law breakdown at pressures close to 8 GPa. Law is enriched in Pb, Sr and F compared with the other LILEs and Cl, which are enriched in Serp. At these depths the slab liquid is expected to be a supercritical liquid, but this does not appear to affect the mobility of LILE as these trace element signatures can be explained just by changes in the dehydration metamorphic reactions. The enriched HFSEs (Nb, Ta, Zr, Ti) in RSH can be explained by their increased mobility in supercritical liquids or by the dissolution of accessory minerals like zircon and rutile.

The HFSEs are generally depleted in the arc front melts, but some anomalous enrichments are identified in some of the samples. TT is enriched in Zr with respect to a depleted mantle source and the other arc melts. AK is enriched in Nb, showing a high Nb/Yb ratio that predicts lower degrees of melting than those calculated by Kuritani et al. (2019). In addition, some MIs of the OO sample are extremely enriched in Cl, F and P.

The enrichment of these elements is tied to the dissolution of the accessory minerals zircon, rutile and apatite. Melting experiments (Hermann and Rubatto, 2009) indicate that the stability of these phases in the slab are controlled by temperature, but the anomalous enrichment of some samples, unrelated to slab temperature increase, may indicate that there are other variables involved.

The interpretation of this study indicates that the amount of slab liquids is not reduced towards the back-arc but is actually enhanced due to the incorporation of lithospheric serpentinite as a source of abundant fluid input to the slab component. The decrease of classic slab fluid proxies like Pb/Ce are interpreted to be caused by dissolution of allanite/monazite with increasing slab temperature at constant Pb input sourced mainly from Law breakdown. Other LILE/LREE ratios like Ba/La that are also used as slab fluid component proxies overlap with arc front samples from OO, indicating that the LREE enrichment is compensated by additional LILE enrichment towards the back-arc sourced by the lithospheric hydrated mantle. Increasing fluid input is also recorded by the increased abundance of halogens towards the back-arc.

Across-arc trace element variations were also studied in the Izu-Bonin arc (Tollstrup et al., 2010), where a progressive increase of LREE toward the back-arc is observed. Estimation of primary melt compositions and degree of melting estimations were obtained from glass data using the method of Kelley et al. (2006). The correlation of La and La/Yb with degree of melting for the back-arc compositions and the inverse correlation in the arc front compositions was interpreted to indicate aqueous fluid involvement in the arc front and hydrous melts or supercritical fluids involvement in the back-arc (Figure 7.7). Progressively higher La and Th concentrations are observed in primary melts with distance from the Izu-Bonin trench, indicating that LREE increase with slab surface temperature, as observed in northern Japan, related to allanite/monazite dissolution. Pb concentrations in primary melts are higher in the arc front but overlap towards the back-arc, following similar positive correlations with degree of melting at different distances from the Izu-Bonin trench, indicating that the Pb source is homogeneous once the slab liquid is composed of a hydrous melt, as interpreted for northern Japan in this study. Ba on the other hand is similar in the Izu-Bonin arc front and the western seamounts which are the melts further from the Izu-Bonin trench (green symbols in Figure 7.7) and in between. The Ba increase in the western seamounts, furthest from the trench, can be related to the same process that produces the LILE increase in OO: input of fluids from antigorite breakdown from the lithospheric mantle. The Izu-Bonin arc appears to follow similar trace element variations across-arc with the difference that the Izu Bonin volcanic front has a signature of aqueous fluid input, that contrasts with

the hydrous melt inputs towards the back-arc, whereas the northern Japan arc front appears to be already affected by slab melts instead of aqueous fluids.

Portnyagin et al. (2007) identified an increase in Ba, Cl and F with slab depth in melts from Kamchatka within the same ranges as AKN and OO (100 – 180 km), which is not as pronounced as the enrichment in OO. Also, they observed no clear increasing trend of LREE/HREE is with distance from the Kuril-Kamchatka trench either, with similar ratios to those at the NE Japan and Kuril arc front measured in this study. These discrepancies may be related to lesser involvement of lithospheric serpentinites towards the back-arc as a source of LILE and along arc variations in the PT path which would affect the release of LREE from the slab.

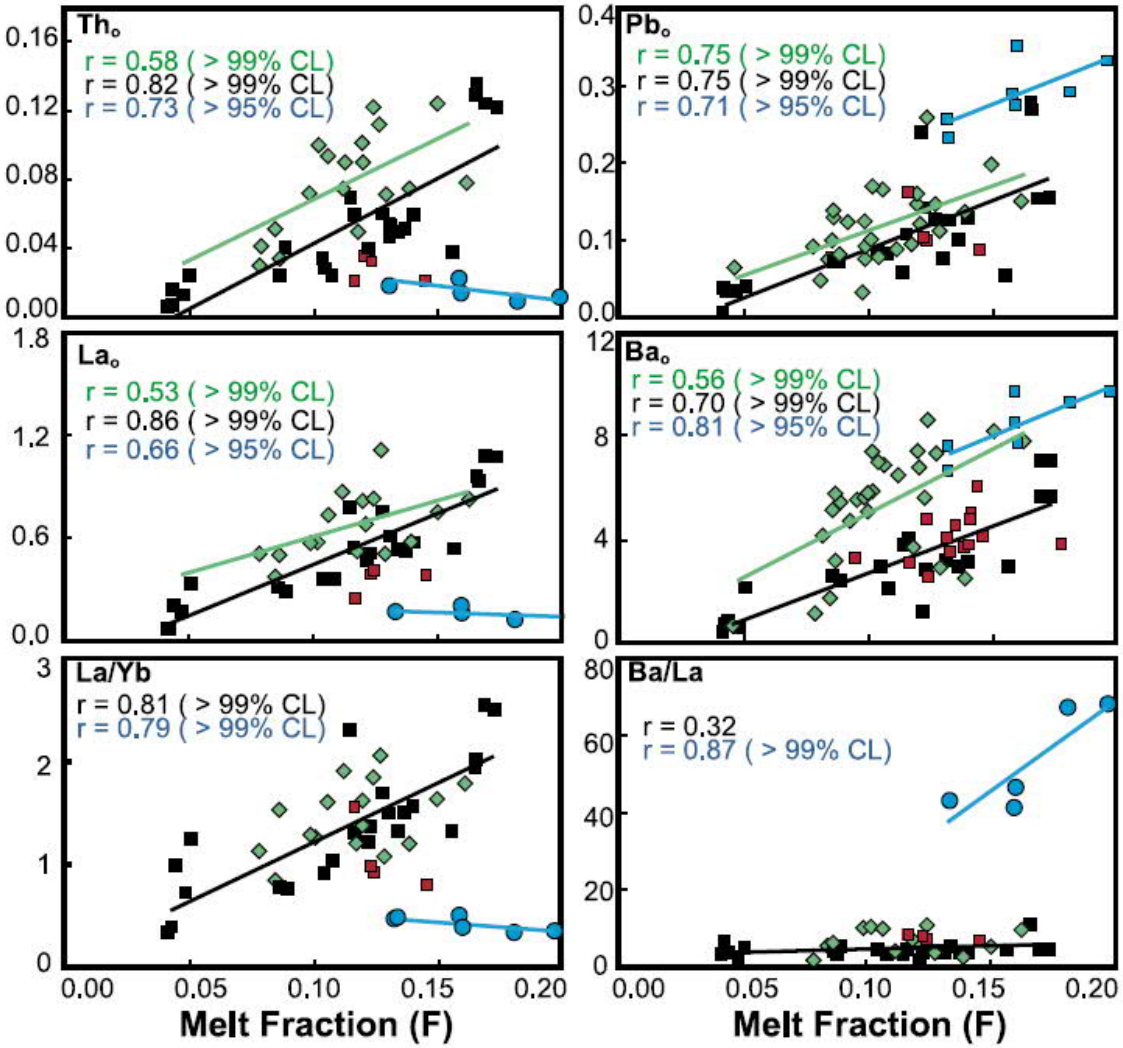

Figure 7.7. Correlation between fluid-mobile and fluid-immobile elements with the degree of melting of primary melts from the Izu-Bonin arc (Tollstrup et al., 2010). The colors define groups of melts at different distances from the trench. From closer to further from the trench: blue, red, black and green.

Across-arc variations in trace element from whole rock data from the South Volcanic Zone of the Andes (SVZ) also differ with the variations observed in northern Japan (Jacques et al., 2013; Jacques et al., 2014). Ce/Pb and Nb/U have a very good correlation in the SVZ forming an array between the trench sediments composition and the MORB source, indicating high slab fluid input in the arc front and low fluid input in the back-arc for a constant slab fluid composition. In northern Japan, these trace element ratios are not correlated and form different clusters: (1) low Ce/Pb and low Nb/U for AKN and TT, (2) low Ce/Pb and high Nb/U for TK, AK and HK, (3) high Ce/Pb and low Nb/U in OO and high Ce/Pb and high Nb/U in RSH. This indicates variability in the composition of the slab fluid. Also, back-arc ratios in northern Japan are close to the arc front ratios for SVZ compared with the very high Ce/Pb and Nb/U ratios in the back-arc of the SVZ, indicating that the back-arc melts in northern Japan have an increased fluid input compared with the SVZ back-arc.

The participation of lithospheric Serp dehydration towards the back-arc (antigorite breakdown) in the generation of arc and/or back-arc magmatism is controlled by the level of hydration of the lithospheric mantle during faulting in the outer rise and the PT path followed by the lithospheric mantle. Halogen and LILE enrichment (except for Sr and Pb) are expected at a distance from the trench equivalent to the initiation of the antigorite breakdown reaction. From the studies cited above it appears that this effect is distinguishable in island arc settings (Japan and Izu-Bonin) but is absent in continental arcs (Kamchatka and SVZ)

Chapter 8

Conclusions and Outlook

8.1 Conclusions

This thesis focused on the OHMIs from seven volcanic systems distributed along and across the arcs in northern Japan, which includes the arc front and back-arc of the northernmost NE Japan arc and the southernmost Kuril arc. This work resulted in the generation of three scientific manuscripts: Chapter 4 has been published in Frontiers in Earth Science, Chapter 5 is in review at the Journal of Petrology, and Chapter 6 is aimed for submission to Geochimica et Cosmochimica Acta. The main conclusions of this thesis are summarized here:

- Olivine antecrysts are ubiquitous in the arc front magmas. Antecrystic olivines are identified by the narrow compositional range and the composition of the MIs they host they host in them (e.g., no correlation between olivine composition and SiO_2 of the melt). This is currently not considered in most MI studies, despite it having strong repercussions for the interpretation of petrogenetic processes.
- The development of the MushPEC algorithm allows the original MI compositions of a cogenetic population that are related to each other by homogeneous fractional crystallization hosted in olivine antecrysts to be estimated. MushPEC helps expand the available MI populations for petrogenetic studies.
- The discrepancies between the MI trends within each arc front sample and the rhyolite-MELTS fractional crystallization models generated with MushPEC found in all arc front samples indicates that most hydrous basalts in arc systems differentiate through boundary layer fractionation or in-situ crystallization, agreeing with predictions of previous numerical models.
- Geochemical variations from arc front to back-arc in northern Japan are mainly controlled by enrichments in LILE and halogens due to second dehydration reaction in lithospheric serpentinites (antigorite breakdown) and by the LREE

enrichment produced by the dissolution of allanite and monazite with increasing temperature of the slab. The influx and composition of slab fluid components towards the back-arc is controlled by the level of hydration of the lithospheric mantle and the PT path of the slab, which control the location and amount of antigorite breakdown. The back-arc Rishiri volcanic system records the exhaustion of lithospheric serpentinite reflected by the drop in LILEs, halogens and Cl/F ratios in relation to Oshima-Oshima, closer to the arc front, and the change in slab liquid from a hydrous melt to a supercritical liquid by the enrichment of HFSEs.

- An increase in slab or sediment melting with temperature of the subducted slab is only expected for arc front melts, as the pressure increase of the slab towards the back-arc hinders slab or sediment melting. The slab fluid is expected to be enriched in H_2O-richer towards the back-arc as a result of antigorite breakdown starting in the lithospheric mantle.
- Strong increases in LREEs towards the back-arc are controlled by decreases in the solubility of accessory phases with temperature (allanite and monazite) and this effect controls LILE/LREE ratios, such as Pb/Ce, which are tied to increases in LREEs with temperature of the slab and not to a decrease in slab fluid as is commonly interpreted.

8.2 Outlook

This research will facilitate further study of magma generation and differentiation through assessment of OHMIs. The ideas behind the MushPEC correction, the concept of MI re-equilibration in antecrysts and the involvement of the hydrated lithospheric mantle in the generation of back-arc magmatism can all be expanded in future work.

1) Other applications for the MushPEC algorithm

The MushPEC algorithm has room for several improvements:

- A friendly user interface, with functions for data input and output analysis would make the program accessible to a wider audience.

- Application of better optimization techniques will reduce modelling times.
- The development of realistic numerical models of boundary layer fractionation will allow the MushPEC algorithm to be applied to a wider range of MI populations.

The development of the MushPEC algorithm also provides a new statistical tool for compositional data, which can be applied to automatically evaluate model fittings of other types of geochemical data. For example, the same principle of Aitchison distance minimization can be applied to fit iterative forward models of glass or whole rock data. In this case, the goodness of fit can be evaluated without the compositional adjustment of olivine addition/subtraction needed during PEC corrections. It is also possible to test for crystal accumulation effects by defining compositional vectors for different mineral phases that can be adjusted to fit the modelled trends.

2) Focus on textural analysis of MIs.

During the development of this thesis it became increasingly clear that a very good knowledge of the textures and 3D geometry of each MI was important. Accurate estimations of corrected H_2O and CO_2 contents require accurate measurements of the volumes of the MIs, their shrinkage bubbles and olivine hosts. Prioritizing more sample preparation time for MI imaging and dimension measurement in different phases would significantly reduce uncertainties generated by CO_2 correction using the MIMiC program. Application of x-ray tomography 3D imaging is always preferable when access and funding are available. In addition, prioritizing analysis time on the EPMA to generate compositional profiles of major (e.g., Fe, Mg) elements in a subset of MIs, from the MI centre through the glass-olivine boundary into the olivine could provide better constraints on the Fe-loss process (Danyushevsky et al., 2000) so one would not have to rely as much on external constrains for Fe-loss corrections. The prioritization of detailed characterization of the MI geometry and the analysis of compositional profiles will require a compromise between the amount and quality of the data, as a detailed characterization of sample geometry and the analysis of compositional profiles will considerably increases analytical time and costs.

In addition to providing an independent constraint on the Fe-loss process, the diffusion analysis of compositional profiles of the MI and host olivine, will provide reliable estimations of ascent rates for MIs hosted in antecrystic olivines. As the MIs are in Fe-

Mg equilibrium with the host and the interstitial melt, in most cases the perturbation from equilibrium can be expected to reflect the ascent and eruption of the magma, including any events of magma recharge, providing timescales for the ascent of magma that has not been affected by previous disequilibrium effects, which would be expected for MIs hosted in phenocrysts.

3) Estimating mantle source and slab component compositions

The back-arc samples in this study (Oshima-Oshima and Rishiri) differ from the arc front samples because the MIs are more primitive and are hosted in non-re-equilibrated phenocrystic olivine hosts. This means that estimates of primary magma compositions are calculated and the flux-melting process can be quantitatively modelled, allowing for slab liquid composition and mantle source to be estimated (e.g., Kelley et al., 2006; Straub and Layne, 2003b). Estimations of mantle and slab component compositions in Rishiri are made difficult by the mobility of HFSEs in the supercritical liquid, as usually these elements are assumed to be immobile to estimate the melting degree and degree of depletion of the mantle source (e.g., Kelley et al., 2006). The strong negative anomalies of HFSEs shown in the Oshima-Oshima sample makes it a better candidate to quantify the melting conditions and slab liquid composition.

Obtaining appropriate estimates of melting degree and H_2O content during melting would provide additional constraints that would allow the actual change of halogen compositions between arc front and back-arc slab liquids to be estimated, as the degree of melting could be incorporated as a known variable in the melting model of Dalou et al. (2014).

4) Providing further evidence of the involvement of lithospheric dehydration in back-arc melt generation.

The LILE and halogen enrichment towards the back-arc found in this study could be further tested by comparing the geochemical signatures in arc melts from other subduction settings in a similar way to what has been done here, by comparing the estimated PT conditions of the slab below each volcano to identify if this enrichment is towards back-arcs across the globe associated with antigorite breakdown elsewhere. Further predictions of the level of lithospheric hydration from seismic tomographic

studies (e.g., Grevemeyer et al., 2018) could be assessed to interpret the incorporation of fluids in the back-arc of different subduction systems.

Isotopic analyses of the MIs studied here could provide further evidence of shifts of sources of the slab liquid as subduction progresses. For example, Barnes et al. (2008) compare the $\delta^{37}Cl$ of melts along and across the arc in the Izu-Bonin-Mariana arc with $\delta^{37}Cl$ measured in slab sources (sediments, oceanic crust and serpentinites. Serpentinites have a distinctly enriched $\delta^{37}Cl$ compared to oceanic sediments and crust. This signature is observed in the forearc serpentines, tied to the early breakdown of lizardite-antigorite transition of the lithospheric serpentinites which provides the fluids for the forearc hydration (e.g., Straub and Layne, 2003b). Arc front samples have a wide range of $\delta^{37}Cl$ which overlaps with the sediments and oceanic crust signatures, indicating that in the arc front that the main control in the production of slab liquid are sediment and oceanic crust dehydration/melting reactions. Magmas from towards the back-arc of the Guguan cross-chain in the Izu-Bonin-Mariana arc also have enriched $\delta^{37}Cl$ signature overlapping with the measured seafloor serpentinite $\delta^{37}Cl$, reflecting the fluid input from antigorite breakdown.

Measurements of other halogens (I and Br) in the MIs could provide further evidence of the source of the fluid input. Br/Cl and I/Cl ratios have the potential to record source compositions as they are not strongly affected by melting and differentiation processes, in contrast to Cl/F which is strongly affected by the melting degree as shown in the flux melting model of Chapter 6. Kendrick et al. (2014) identified high I/Cl ratios in glass samples of the Manus Basin, Valu Fa Ridge and the Tonga Arc, which they interpreted as being produced by fluid from the breakdown of I-rich serpentinites.

Studying $\delta^{34}S$ variations across-arc to see if they correlate with the S and halogen increase towards the back-arc may also help to identify changes in source and characteristic of the slab fluid. For example, Alt et al. (2012) analysed natural subduction serpentinites (*c.* 5.0‰ $\delta^{34}S$) and their dehydration products (1.2‰ $\delta^{34}S$), estimating that the $\delta^{34}S$ of the released fluid should have very high $\delta^{34}S$ (*c.* 14.5‰). Bulk AOC generally has a less enriched $\delta^{34}S$ signature (0.5 – 0.9‰ $\delta^{34}S$; Alt, 1995; Alt and Shanks, 2010). An increase in $\delta^{34}S$ towards the back-arc, correlated with the S increase, may be compatible with a shift from an AOC source to a serpentinite source for the slab fluids with increasing slab PT conditions in the back-arc.

Bibliography

Abdelwahed, M.F. and Zhao, D., 2005. Waveform modelling of local earthquakes in southwest Japan. Earth Planets Space, 57(11): 1039-1054.

Abdelwahed, M.F. and Zhao, D., 2007. Deep structure of the Japan subduction zone. Phys. Earth Planet. Inter., 162(1-2): 32-52.

Acocella, V., Yoshida, T., Yamada, R. and Funiciello, F., 2008. Structural control on late Miocene to Quaternary volcanism in the NE Honshu arc, Japan. Tectonics, 27(5).

Aitchison, J., 1986. The statistical analysis of compositional data. Chapman and Hall, London; New York.

Aizawa, K. and Yoshida, T., 2000. Laccolith-type magmatic chamber-contact between collapsed caldera and granite body. Earth Monthly, 22: 387-392.

Alletti, M., Burgisser, A., Scaillet, B. and Oppenheimer, C., 2014. Chloride partitioning and solubility in hydrous phonolites from Erebus volcano: A contribution towards a multi-component degassing model. GeoResJ, 3-4(1): 27-45.

Almeev, R.R., Holtz, F., Koepke, J. and Parat, F., 2012. Experimental calibration of the effect of H_2O on plagioclase crystallization in basaltic melt at 200 MPa. Am. Mineral., 97(7): 1234-1240.

Almeev, R.R., Holtz, F., Koepke, J., Parat, F. and Botcharnikov, R.E., 2007. The effect of H_2O on olivine crystallization in MORB: Experimental calibration at 200 MPa. Am. Mineral., 92(4): 670-674.

Alt, J.C., 1995. Sulfur isotopic profile through the oceanic crust: Sulfur mobility and seawater-crustal sulfur exchange during hydrothermal alteration. Geology, 23(7): 585-588.

Alt, J.C., Garrido, C.J., Shanks III, W.C., Turchyn, A., Padrón-Navarta, J.A., Sánchez-Vizcaíno, V.L., Pugnaire, M.T.G. and Marchesi, C., 2012. Recycling of water, carbon, and sulfur during subduction of serpentinites: A stable isotope study of Cerro del Almirez, Spain. Earth and Planetary Science Letters, 327: 50-60.

Alt, J.C. and Shanks, W.C., 2010. Sulfur exchange between seawater and oceanic basement, Geochimica et Cosmochimica Acta, pp. A15-A15.

Aoki, K.I., 1971. Petrology of mafic inclusions from Itinome-gata, Japan. Contributions to Mineralogy and Petrology, 30(4): 314-331.

Ariskin, A.A., 1999. Phase equilibria modeling in igneous petrology: Use of COMAGMAT model for simulating fractionation of ferro-basaltic magmas and the genesis of high-alumina basalt. Journal of Volcanology and Geothermal Research, 90(1-2): 115-162.

Ariskin, A.A. and Barmina, G.S., 2004. COMAGMAT: Development of a magma crystallization model and its petrological applications. Geochem. Int., 42(SUPPL.): S1-S157.

Ariskin, A.A., Bychkov, K.A., Nikolaev, G.S. and Barmina, G.S., 2018. The COMAGMAT-5: Modeling the Effect of Fe–Ni Sulfide Immiscibility in Crystallizing Magmas and Cumulates. Journal of Petrology, 59(2): 283-298.

Ariskin, A.A., Danyushevsky, L.V., Bychkov, K.A., McNeill, A.W., Barmina, G.S. and Nikolaev, G.S., 2013. Modeling solubility of Fe-Ni sulfides in basaltic magmas: The effect of nickel. Econ. Geol., 108(8): 1983-2003.

Ariskin, A.A., Frenkel, M.Y., Barmina, G.S. and Nielsen, R.L., 1993. Comagmat: a Fortran program to model magma differentiation processes. Comput. Geosci., 19(8): 1155-1170.

Asimow, P.D. and Ghiorso, M.S., 1998. Algorithmic modifications extending MELTS to calculate subsolidus phase relations. Am. Mineral., 83(9): 1127-1132.

Aster, E.M., Wallace, P.J., Moore, L.R., Watkins, J., Gazel, E. and Bodnar, R.J., 2016. Reconstructing CO_2 concentrations in basaltic melt inclusions using Raman analysis of vapor bubbles. Journal of Volcanology and Geothermal Research, 323: 148-162.

Bachmann, O. and Bergantz, G.W., 2004. On the origin of crystal-poor rhyolites: Extracted from batholithic crystal mushes. Journal of Petrology, 45(8): 1565-1582.

Bachmann, O. and Bergantz, G.W., 2006. Gas percolation in upper-crustal silicic crystal mushes as a mechanism for upward heat advection and rejuvenation of near-solidus magma bodies. Journal of Volcanology and Geothermal Research, 149(1-2): 85-102.

Bali, E., Audétat, A. and Keppler, H., 2011. The mobility of U and Th in subduction zone fluids: an indicator of oxygen fugacity and fluid salinity. Contributions to Mineralogy and Petrology, 161(4): 597-613.

Barnes, J.D., Sharp, Z.D. and Fischer, T.P., 2008. Chlorine isotope variations across the Izu-Bonin-Mariana arc. Geology, 36(11): 883-886.

Behrens, H., Ohlhorst, S., Holtz, F. and Champenois, M., 2004. CO_2 solubility in dacitic melts equilibrated with H_2O-CO_2 fluids: Implications for modeling the solubility of CO_2 in silicic melts. Geochimica et Cosmochimica Acta, 68(22): 4687-4703.

Bénard, A., Klimm, K., Woodland, A.B., Arculus, R.J., Wilke, M., Botcharnikov, R.E., Shimizu, N., Nebel, O., Rivard, C. and Ionov, D.A., 2018. Oxidising agents in sub-arc mantle melts link slab devolatilisation and arc magmas. Nature Communications, 9(1): 3500.

Bénard, A., Koga, K.T., Shimizu, N., Kendrick, M.A., Ionov, D.A., Nebel, O. and Arculus, R.J., 2017. Chlorine and fluorine partition coefficients and abundances in sub-arc mantle xenoliths (Kamchatka, Russia): Implications for melt generation and volatile recycling processes in subduction zones. Geochimica et Cosmochimica Acta, 199: 324-350.

Berlo, K., Gardner, J.E. and Blundy, J.D., 2010. Timescales of Magma Degassing. In: A. Dosseto, S.P. Turner and J.A. Van Orman (Editors), Timescales of Magmatic Processes: From Core to Atmosphere. John Wiley and Sons, pp. 231-255.

Bernini, D., Audétat, A., Dolejš, D. and Keppler, H., 2013a. Zircon solubility in aqueous fluids at high temperatures and pressures. Geochimica et Cosmochimica Acta, 119: 178-187.

Bernini, D., Wiedenbeck, M., Dolejš, D. and Keppler, H., 2013b. Partitioning of halogens between mantle minerals and aqueous fluids: implications for the fluid flow regime in subduction zones. Contrib Mineral Petrol, 165: 117–128.

Best, M.G., 2013. Igneous and metamorphic petrology. John Wiley & Sons.

Bird, P., 2003. An updated digital model of plate boundaries. Geochem. Geophys. Geosyst., 4(3).

Blake, S., 1984. Volatile oversaturation during the evolution of silicic magma chambers as an eruption trigger. J. Geophys. Res. B Solid Earth, 89(B10): 8237-8244.

Blake, S. and Fink, J.H., 1987. The dynamics of magma withdrawal from a density stratified dyke. Earth and Planetary Science Letters, 85(4): 516-524.

Blank, J.G. and Brooker, R.A., 1994. Experimental studies of carbon-dioxide in silicate melts - solubility, speciation, and stable carbon-isotope behavior. Volatiles in Magmas, 30: 157-186.

Blundy, J. and Cashman, K., 2001. Ascent-driven crystallisation of dacite magmas at Mount St Helens, 1980-1986. Contributions to Mineralogy and Petrology, 140(6): 631-650.

Blundy, J., Cashman, K.V., Rust, A. and Witham, F., 2010. A case for CO_2-rich arc magmas. Earth and Planetary Science Letters, 290(3-4): 289-301.

Bowen, N.L., 1915. The Later Stages of the Evolution of the Igneous Rocks. Geological Magazine, 23(8): 91.

Bowen, N.L., 1928. The Evolution of the Igneous Rocks. Geological Magazine, 66(11): 523-525.

Brahm, R., Parada, M.A., Morgado, E., Contreras, C. and McGee, L.E., 2018. Origin of Holocene trachyte lavas of the Quetrupillán volcanic complex, Chile: Examples of residual melts in a rejuvenated crystalline mush reservoir. Journal of Volcanology and Geothermal Research, 357: 163-176.

Brahm, R., Zellmer, G.F., Kuritani, T., Coulthard, D., Nakagawa, M., Sakamoto, N., Yurimoto, H. and Sato, E., 2021. MushPEC: Correcting Post-entrapment Processes Affecting Melt Inclusions Hosted in Olivine Antecrysts. Front. Earth Sci., 8: 731.

Browne, B. and Szramek, L., 2015. Rates of Magma Ascent and Storage. In: H. Sigurdsson (Editor), The Encyclopedia of Volcanoes (Second Edition). Academic Press, Amsterdam, pp. 203-214.

Burgisser, A., Alletti, M. and Scaillet, B., 2015. Simulating the behavior of volatiles belonging to the C–O–H–S system in silicate melts under magmatic conditions with the software D-Compress. Computers & Geosciences, 79: 1-14.

Cannatelli, C., Doherty, A.L., Esposito, R., Lima, A. and De Vivo, B., 2016. Understanding a volcano through a droplet: A melt inclusion approach. Journal of Geochemical Exploration, 171: 4-19.

Caricchi, L., Sheldrake, T.E. and Blundy, J., 2018. Modulation of magmatic processes by CO_2 flushing. Earth and Planetary Science Letters, 491: 160-171.

Carroll, M.R. and Webster, J.D., 1994. Solubilities of sulfur, noble gases, nitrogen, chlorine, and fluorine in magmas. Volatiles in Magmas, 30: 231-279.

Chen, K.-X., Gung, Y., Kuo, B.-Y. and Huang, T.-Y., 2018a. Crustal Magmatism and Deformation Fabrics in Northeast Japan Revealed by Ambient Noise Tomography. J. Geophys. Res. B Solid Earth, 123(10): 8891-8906.

Chen, W., Xiong, X., Wang, J., Xue, S., Li, L., Liu, X., Ding, X. and Song, M., 2018b. TiO2 Solubility and Nb and Ta Partitioning in Rutile-Silica-Rich Supercritical Fluid Systems: Implications for Subduction Zone Processes. J. Geophys. Res. B Solid Earth, 123(6): 4765-4782.

Churakov, S. and Gottschalk, M., 2003. Perturbation theory based equation of state for polar molecular fluids: II. Fluid mixtures. Geochimica et Cosmochimica Acta, 67(13): 2415-2425.

Churikova, T., Dorendorf, F. and Wörner, G., 2001. Sources and fluids in the mantle wedge below Kamchatka, evidence from across-arc geochemical variation. Journal of Petrology, 42(8): 1567-1593.

Connolly, J.A.D. and Kerrick, D.M., 1987. An algorithm and computer program for calculating composition phase diagrams. Calphad, 11(1): 1-55.

Connolly, J.A.D. and Petrini, K., 2002. An automated strategy for calculation of phase diagram sections and retrieval of rock properties as a function of physical conditions. J. Metamorph. Geol., 20(7): 697-708.

Contreras-Reyes, E., Grevemeyer, I., Flueh, E. and Reichert, C., 2008. Upper lithospheric structure of the subduction zone offshore of southern Arauco peninsula, Chile, at~ 38 SJ Geophys. Res. 113, B07303.

Costa, F., Chackraborty, S. and Dohmen, R., 2003. Diffusion coupling between trace and major elements and a model for calculation of magma residence times using plagioclase. Geochimica et Cosmochimica Acta, 67(12): 2189 - 2200.

Cruz-Uribe, A.M., Marschall, H.R., Gaetani, G.A. and Le Roux, V., 2018. Generation of alkaline magmas in subduction zones by partial melting of mélange diapirs—An experimental study. Geology, 46(4): 343-346.

Dalou, C., Koga, K.T., Le Voyer, M. and Shimizu, N., 2014. Contrasting partition behavior of F and Cl during hydrous mantle melting: implications for Cl/F signature in arc magmas. Progress in Earth and Planetary Science, 1(1): 26.

Dalou, C., Koga, K.T., Shimizu, N., Boulon, J. and Devidal, J.-L., 2012. Experimental determination of F and Cl partitioning between lherzolite and basaltic melt. Contributions to Mineralogy and Petrology, 163(4): 591-609.

Danyushevsky, L.V., 2001. The effect of small amounts of H_2O on crystallisation of mid-ocean ridge and backarc basin magmas. Journal of Volcanology and Geothermal Research, 110(3-4): 265-280.

Danyushevsky, L.V., Della-Pasqua, F.N. and Sokolov, S., 2000. Re-equilibration of melt inclusions trapped by magnesian olivine phenocrysts from subduction-related magmas: Petrological implications. Contributions to Mineralogy and Petrology, 138(1): 68-83.

Danyushevsky, L.V., Leslie, R.A.J., Crawford, A.J. and Durance, P., 2004. Melt inclusions in primitive olivine phenocrysts: The role of localized reaction processes in the origin of anomalous compositions. Journal of Petrology, 45(12): 2531-2553.

Danyushevsky, L.V., McNeill, A.W. and Sobolev, A.V., 2002a. Experimental and petrological studies of melt inclusions in phenocrysts from mantle-derived magmas: An overview of techniques, advantages and complications. Chemical Geology, 183(1-4): 5-24.

Danyushevsky, L.V. and Plechov, P., 2011. Petrolog3: Integrated software for modeling crystallization processes. Geochem. Geophys. Geosyst., 12(7).

Danyushevsky, L.V., Sokolov, S. and Falloon, T.J., 2002b. Melt inclusions in olivine phenocrysts: using diffusive re-equilibration to determine the cooling history of a crystal, with implications for the origin of olivine-phyric volcanic rocks. Journal of Petrology, 43(9): 1651-1671.

Debret, B., Koga, K.T., Nicollet, C., Andreani, M. and Schwartz, S., 2013. F, Cl and S input via serpentinite in subduction zones: implications for the nature of the fluid released at depth. Terra Nova, 26: 96-101.

Debret, B. and Sverjensky, D., 2017. Highly oxidising fluids generated during serpentinite breakdown in subduction zones. Sci. Rep., 7(1): 1-6.

Demouchy, S. and Mackwell, S., 2006. Mechanisms of hydrogen incorporation and diffusion in iron-bearing olivine. Phys Chem Minerals, 33(5): 347-355.

Dixon, J.E., 1997. Degassing of alkalic basalts. Am. Mineral., 82(3-4): 368-378.

Dixon, J.E., Clague, D.A., Wallace, P. and Poreda, R., 1997. Volatiles in alkalic basalts from the North Arch volcanic field, Hawaii: Extensive degassing of deep submarine-erupted alkalic series lavas. Journal of Petrology, 38(7): 911-939.

Dixon, J.E. and Stolper, E.M., 1995. An experimental study of water and carbon dioxide solubilities in mid-ocean ridge basaltic liquids. part II: Applications to degassing. Journal of Petrology, 36(6): 1633-1646.

Dixon, J.E., Stolper, E.M. and Holloway, J.R., 1995. An experimental study of water and carbon dioxide solubilities in mid-ocean ridge basaltic liquids. part I: Calibration and solubility models. Journal of Petrology, 36(6): 1607-1631.

Donovan, A., Blundy, J., Oppenheimer, C. and Buisman, I., 2018. The 2011 eruption of Nabro volcano, Eritrea: perspectives on magmatic processes from melt inclusions. Contributions to Mineralogy and Petrology, 173(1): 23.

Drignon, M.J., Nielsen, R.L., Tepley III, F.J. and Bodnar, R.J., 2019. Reequilibration Processes Occurring in Plagioclase-Hosted Melt Inclusions From Plagioclase Ultraphyric Basalts. Geochem. Geophys. Geosyst., 20(1): 109-119.

Duan, X., 2014. A general model for predicting the solubility behavior of H_2O–CO_2 fluids in silicate melts over a wide range of pressure, temperature and compositions. Geochimica et Cosmochimica Acta, 125: 582-609.

Dufek, J. and Bachmann, O., 2010. Quantum magmatism: Magmatic compositional gaps generated by melt-crystal dynamics. Geology, 38(8): 687-690.

Edmonds, M. and Woods, A.W., 2018. Exsolved volatiles in magma reservoirs. Journal of Volcanology and Geothermal Research, 368: 13-30.

Eiler, J.M., Schiano, P., Kitchen, N. and Stolper, E.M., 2000. Oxygen-isotope evidence for recycled crust in the sources of mid-ocean-ridge basalts. Nature, 403(6769): 530-534.

Evans, K., Elburg, M. and Kamenetsky, V., 2012. Oxidation state of subarc mantle. Geology, 40(9): 783-786.

Fall, A., Tattitch, B. and Bodnar, R.J., 2011. Combined microthermometric and Raman spectroscopic technique to determine the salinity of H_2O–CO_2–NaCl fluid inclusions based on clathrate melting. Geochimica et Cosmochimica Acta, 75(4): 951-964.

Ferriss, E., Plank, T. and Walker, D., 2016. Site-specific hydrogen diffusion rates during clinopyroxene dehydration. Contributions to Mineralogy and Petrology, 171(55): 24.

Fine, G. and Stolper, E., 1985. The speciation of carbon dioxide in sodium aluminosilicate glasses. Contributions to Mineralogy and Petrology, 91(2): 105-121.

Foley, S.F., Barth, M.G. and Jenner, G.A., 2000. Rutile/melt partition coefficients for trace elements and an assessment of the influence of rutile on the trace element characteristics of subduction zone magmas. Geochimica et Cosmochimica Acta, 64(5): 933-938.

Ford, C.E., Russell, D.G., Craven, J.A. and Fisk, M.R., 1983. Olivine-liquid equilibria: temperature, pressure and composition dependence of the crystal/liquid cation partition coefficients for Mg, Fe^{2+}, Ca and Mn. Journal of Petrology, 24(3): 256-265.

Forni, F., Bachmann, O., Mollo, S., De Astis, G., Gelman, S.E. and Ellis, B.S., 2016. The origin of a zoned ignimbrite: Insights into the Campanian Ignimbrite magma chamber (Campi Flegrei, Italy). Earth and Planetary Science Letters, 449: 259-271.

Frost, T.P. and Mahood, G.A., 1987. Field, chemical, and physical constraints on mafic-felsic magma interaction in the Lamarck Granodiorite, Sierra Nevada, California. GSA Bulletin, 99(2): 272-291.

Fujinawa, A., Iwasaki, M., Honda, K., Nagao, A. and Wachi, T., 2004. Eruption history in the post-caldera stage of Akita-Komagatake Volcano, Northeastern Japan Arc:

correlation between eruptives constituting volcanic edifices and air-fall tephra layers. Kazan, 49(6): 333-354.
Fukuyama, H., 1985. Gabbroic inclusions of Ichinomegata tuff cone: Bulk chemical composition. J. Fac. Sci., Univ. Tokyo, Sect. 2, 21: 67-80.
Gaetani, G.A. and Grove, T.L., 1998. The influence of water on melting of mantle peridotite. Contributions to Mineralogy and Petrology, 131(4): 323-346.
Gaetani, G.A., Kent, A.J., Grove, T.L., Hutcheon, I.D. and Stolper, E.M., 2003. Mineral/melt partitioning of trace elements during hydrous peridotite partial melting. Contributions to Mineralogy and Petrology, 145(4): 391-405.
Gaetani, G.A. and Watson, E.B., 2000. Open system behavior of olivine-hosted melt inclusions. Earth and Planetary Science Letters, 183(1-2): 27-41.
Gaetani, G.A. and Watson, E.B., 2002. Modeling the major-element evolution of olivine-hosted melt inclusions. Chemical Geology, 183(1-4): 25-41.
Garrido, C.J., López Sánchez-Vizcaíno, V., Gómez-Pugnaire, M.T., Trommsdorff, V., Alard, O., Bodinier, J.L. and Godard, M., 2005. Enrichment of HFSE in chlorite-harzburgite produced by high-pressure dehydration of antigorite-serpentinite: Implications for subduction magmatism. Geochem. Geophys. Geosyst., 6(1).
Gavrilenko, M., Herzberg, C., Vidito, C., Carr, M.J., Tenner, T. and Ozerov, A., 2016a. A Calcium-in-Olivine Geohygrometer and its Application to Subduction Zone Magmatism. Journal of Petrology, 57(9): 1811-1832.
Gavrilenko, M., Ozerov, A., Kyle, P.R., Carr, M.J., Nikulin, A., Vidito, C. and Danyushevsky, L., 2016b. Abrupt transition from fractional crystallization to magma mixing at Gorely volcano (Kamchatka) after caldera collapse. Bull. Volcanol., 78(7).
Gelman, S.E., Deering, C.D., Gutierrez, F.J. and Bachmann, O., 2013. Evolution of the Taupo Volcanic Center, New Zealand: Petrological and thermal constraints from the Omega dacite. Contributions to Mineralogy and Petrology, 166(5): 1355-1374.
Ghiorso, M.S. and Gualda, G.A.R., 2015. An H_2O–CO_2 mixed fluid saturation model compatible with rhyolite-MELTS. Contributions to Mineralogy and Petrology, 169(6).
Ghiorso, M.S., Hirschmann, M.M., Reiners, P.W. and Kress, V.C., 2002. The pMELTS: A revision of MELTS for improved calculation of phase relations and major element partitioning related to partial melting of the mantle to 3 GPa. Geochem. Geophys. Geosyst., 3(5): 1030.
Ghiorso, M.S. and Sack, R.O., 1995. Chemical mass transfer in magmatic processes IV. A revised and internally consistent thermodynamic model for the interpolation and extrapolation of liquid-solid equilibria in magmatic systems at elevated temperatures and pressures. Contributions to Mineralogy and Petrology, 119: 197-212.
Gill, J.B., 1981. Orogenic Andesites and Plate Tectonics. Springer, Berlin, Heidelberg, XIV, 392 pp.
Gonnermann, H.M., 2015. Magma Fragmentation. Annual Review of Earth and Planetary Sciences, 43(1): 431-458.
Gorman, P.J., Kerrick, D.M. and Connolly, J.A.D., 2006. Modeling open system metamorphic decarbonation of subducting slabs. Geochem. Geophys. Geosyst., 7(4).
Green, E.C.R., White, R.W., Diener, J.F.A., Powell, R., Holland, T.J.B. and Palin, R.M., 2016. Activity–composition relations for the calculation of partial melting equilibria in metabasic rocks. J. Metamorph. Geol., 34(9): 845-869.

Green, T.H., Blundy, J.D., Adam, J. and Yaxley, G.M., 2000. SIMS determination of trace element partition coefficients between garnet, clinopyroxene and hydrous basaltic liquids at 2-7.5 GPa and 1080-1200°C. Lithos, 53(3-4): 165-187.

Grevemeyer, I., Ranero, C.R., Flueh, E.R., Kläschen, D. and Bialas, J., 2007. Passive and active seismological study of bending-related faulting and mantle serpentinization at the Middle America trench. Earth and Planetary Science Letters, 258(3-4): 528-542.

Grevemeyer, I., Ranero, C.R. and Ivandic, M., 2018. Structure of oceanic crust and serpentinization at subduction trenches. Geosphere, 14(2): 395-418.

Grove, T., Parman, S., Bowring, S., Price, R. and Baker, M., 2002. The role of an H_2O-rich fluid component in the generation of primitive basaltic andesites and andesites from the Mt. Shasta region, N California. Contributions to Mineralogy and Petrology, 142(4): 375-396.

Grove, T.L., Baker, M.B., Price, R.C., Parman, S.W., Elkins-Tanton, L.T., Chatterjee, N. and Müntener, O., 2005. Magnesian andesite and dacite lavas from Mt. Shasta, northern California: products of fractional crystallization of H_2O-rich mantle melts. Contributions to Mineralogy and Petrology, 148(5): 542-565.

Grove, T.L., Chatterjee, N., Parman, S.W. and Médard, E., 2006. The influence of H_2O on mantle wedge melting. Earth and Planetary Science Letters, 249(1-2): 74-89.

Grove, T.L. and Kinzler, R.J., 1986. Petrogenesis of andesites. Annual Review of Earth & Planetary Sciences, 14: 417-454.

Grove, T.L., Till, C.B. and Krawczynski, M.J., 2012. The role of H_2O in subduction zone magmatism. Annual Review of Earth and Planetary Sciences, 40: 413-439.

Gualda, G.A.R., Ghiorso, M.S., Lemons, R.V. and Carley, T.L., 2012. Rhyolite-MELTS: A modified calibration of MELTS optimized for silica-rich, fluid-bearing magmatic systems. Journal of Petrology, 53(5): 875-890.

Hacker, B.R., 2008. H_2O subduction beyond arcs. Geochem. Geophys. Geosyst., 9(3).

Harker, A., 1909. The Natural History of Igneous Rocks. Cambridge University Press, Cambridge.

Hartley, M.E., Maclennan, J., Edmonds, M. and Thordarson, T., 2014. Reconstructing the deep CO_2 degassing behaviour of large basaltic fissure eruptions. Earth and Planetary Science Letters, 393: 120-131.

Hartley, M.E., Neave, D.A., Maclennan, J., Edmonds, M. and Thordarson, T., 2015. Diffusive over-hydration of olivine-hosted melt inclusions. Earth and Planetary Science Letters, 425: 168-178.

Hartley, M.E., Shorttle, O., Maclennan, J., Moussallam, Y. and Edmonds, M., 2017. Olivine-hosted melt inclusions as an archive of redox heterogeneity in magmatic systems. Earth and Planetary Science Letters, 479: 192-205.

Hasegawa, A. and Nakajima, J., 2004. Geophysical constraints on slab subduction and arc magmatism. In: C.J. Hawkesworth and R.S.J. Sparks (Editors), Geophysical Monograph Series. Blackwell Publishing Ltd, pp. 81-93.

Hauri, E., 2002. SIMS analysis of volatiles in silicate glasses, 2: Isotopes and abundances in Hawaiian melt inclusions. Chemical Geology, 183(1-4): 115-141.

Hayes, G., 2018. Slab2 - A Comprehensive Subduction Zone Geometry Model, U.S. Geological Survey data release.

Hayes, G.P., Moore, G.L., Portner, D.E., Hearne, M., Flamme, H., Furtney, M. and Smoczyk, G.M., 2018. Slab2, a comprehensive subduction zone geometry model. Science, 362(6410): 58-61.

Hermann, J., 2002. Allanite: thorium and light rare earth element carrier in subducted crust. Chemical Geology, 192(3): 289-306.
Hermann, J. and Green, D.H., 2001. Experimental constraints on high pressure melting in subducted crust. Earth and Planetary Science Letters, 188(1-2): 149-168.
Hermann, J. and Rubatto, D., 2009. Accessory phase control on the trace element signature of sediment melts in subduction zones. Chemical Geology, 265(3): 512-526.
Hermann, J. and Spandler, C.J., 2008. Sediment melts at sub-arc depths: An experimental study. Journal of Petrology, 49(4): 717-740.
Herzberg, C., 2011. Identification of source lithology in the Hawaiian and Canary Islands: Implications for origins. Journal of Petrology, 52(1): 113-146.
Herzberg, C. and Asimow, P.D., 2008. Petrology of some oceanic island basalts: PRIMELT2.XLS software for primary magma calculation. Geochem. Geophys. Geosyst., 9(9).
Hess, P.C., 1992. Phase equilibria constraints on the origin of ocean floor basalts. In: J.P. Morgan, D.K. Blackman and J.M. Sinton (Editors), Mantle Flow and Melt Generation at Mid-Ocean Ridges, pp. 67-102.
Hirai, Y., Yoshida, T., Okamura, S., Tamura, Y., Sakamoto, I. and Shinjo, R., 2018. Breakdown of residual zircon in the Izu arc subducting slab during backarc rifting. Geology, 46(4): 371-374.
Hirschmann, M.M., Asimow, P.D., Ghiorso, M.S. and Stolper, E.M., 1999. Calculation of peridotite partial melting from thermodynamic models of minerals and melts. III. Controls on isobaric melt production and the effect of water on melt production. Journal of Petrology, 40(5): 831-851.
Holland, T. and Blundy, J., 1994. Non-ideal interactions in calcic amphiboles and their bearing on amphibole-plagioclase thermometry. Contributions to Mineralogy and Petrology, 116(4): 433-447.
Honda, S. and Yoshida, T., 2005. Application of the model of small-scale convection under the island arc to the NE Honshu subduction zone. Geochem. Geophys. Geosyst., 6(1).
Huang, Z. and Zhao, D., 2013. Mechanism of the 2011 Tohoku-Oki earthquake (Mw 9.0) and tsunami: insight from seismic tomography. J. Asian Earth Sci., 70-71(1): 160-168.
Huang, Z., Zhao, D., Umino, N., Wang, L., Matsuzawa, T., Hasegawa, A. and Yoshida, T., 2010. P-wave tomography, anisotropy and seismotectonics in the eastern margin of Japan Sea. Tectonophysics, 489(1-4): 177-188.
Huang, Z., Zhao, D. and Wang, L., 2011. Seismic heterogeneity and anisotropy of the Honshu arc from the Japan Trench to the Japan Sea. Geophys. J. Int., 184(3): 1428-1444.
Hughes, L., Burgess, R., Chavrit, D., Pawley, A., Tartèse, R., Droop, G., Ballentine, C.J. and Lyon, I., 2018. Halogen behaviour in subduction zones: Eclogite facies rocks from the Western and Central Alps. Geochimica et Cosmochimica Acta, 243: 1-23.
Iacono-Marziano, G., Morizet, Y., Le Trong, E. and Gaillard, F., 2012. New experimental data and semi-empirical parameterization of H_2O-CO_2 solubility in mafic melts. Geochimica et Cosmochimica Acta, 97: 1-23.
Ihinger, P.D., Hervig, R.L. and McMillan, P.F., 1994. Analytical methods for volatiles in glasses. Volatiles in Magmas, 30: 67-121.
Ikeda, Y., Kagami, H., Katsui, Y. and Kurasawa, H., 1990. Variations in Nd and Sr isotope ratios of Quaternary volcanic rocks from the southwestern Kurile arc: an

implication for migration of fluid phases in the subduction zone. Journal of mineralogy, petrology and economic geology, 85(1): 1-9.

Ishimoto, H., Shuto, K. and Goto, Y., 2006. Middle Miocene to Quaternary primary basalt and high magnesian andesite magmas of North Hokkaido, Japan: source mantle characteristics and degrees of partial melting. Isl. Arc, 15(2): 251-268.

Ishizuka, Y., 1999. Eruptive history of Rishiri volcano, northern Hokkaido, Japan. Kazan, 44(1): 23-40.

Ishizuka, Y. and Nakagawa, M., 1999. Petrological evolution of Rishiri volcano, northern Hokkaido, Japan. J. Mineral. Petrol. Econ. Geol, 94: 279-294.

Ishizuka, Y., Nakagawa, M. and Fujiwara, S.y., 2010. Geological Map of Tokachidake Volcano, Geological Map of Volcanoes. Geological Survey of Japan, AIST.

Itaya, T., Nagao, K., Nishido, H. and Ogata, K., 1984. K-Ar age determination of late pleistocene volcanic rocks. The Journal of the Geological Society of Japan, 90(12): 899-909.

Jacques, G., Hoernle, K., Gill, J., Hauff, F., Wehrmann, H., Garbe-Schönberg, D., van den Bogaard, P., Bindeman, I. and Lara, L.E., 2013. Across-arc geochemical variations in the Southern Volcanic Zone, Chile (34.5-38.0°S): Constraints on mantle wedge and slab input compositions. Geochimica et Cosmochimica Acta, 123: 218-243.

Jacques, G., Hoernle, K., Gill, J., Wehrmann, H., Bindeman, I. and Lara, L.E., 2014. Geochemical variations in the Central Southern Volcanic Zone, Chile (38-43°S): The role of fluids in generating arc magmas. Chemical Geology, 371: 27-45.

Jégo, S. and Dasgupta, R., 2013. Fluid-present melting of sulfide-bearing ocean-crust: Experimental constraints on the transport of sulfur from subducting slab to mantle wedge. Geochimica et Cosmochimica Acta, 110: 106-134.

Jégo, S. and Dasgupta, R., 2014. The fate of sulfur during fluid-present melting of subducting basaltic crust at variable oxygen fugacity. Journal of Petrology, 55(6): 1019-1050.

Jerram, D.A. and Martin, V.M., 2008. Understanding crystal populations and their significance through the magma plumbing system. Geological Society, London, Special Publications, 304(1): 133.

Jochum, K.P., Nohl, U., Herwig, K., Lammel, E., Stoll, B. and Hofmann, A.W., 2005. GeoReM: a new geochemical database for reference materials and isotopic standards. Geostandards and Geoanalytical Research, 29(3): 333-338.

John, T., Scambelluri, M., Frische, M. and Barnes, J.D., 2011. Dehydration of subducting serpentinite: Implications for halogen mobility in subduction zones and the deep halogen cycle. Earth Planet Sci Lett, 308: 65-76.

Johnson, J., Nielsen, R.L. and Fisk, M.R., 1996. Plagioclase-hosted melt inclusions in the Steens Basalt, southeastern Oregon. Petrology, 4(3): 247-254.

Johnson, K.T.M., Dick, H.J.B. and Shimizu, N., 1990. Melting in the oceanic upper mantle: an ion microprobe study of diopsides in abyssal peridotites. Journal of Geophysical Research, 95(B3): 2661-2678.

Jugo, P.J., Wilke, M. and Botcharnikov, R.E., 2010. Sulfur K-edge XANES analysis of natural and synthetic basaltic glasses: Implications for S speciation and S content as function of oxygen fugacity. Geochimica et Cosmochimica Acta, 74(20): 5926-5938.

Kagami, H., 2005. Formative periods and source materials of Cretaceous-Paleogene granitoids from Honshu Arc. Journal of the Geological Society of Japan, 111: 441-457.

Kagami, H., Kawano, Y., Ikawa, H., Ishioka, J., Kagashima, S., Shimura, T., Shuto, K., Iizumi, S., Imaoka, T., Owada, M., Osanai, Y., Tainosho, Y., Tanaka, H., Tsuchiya, N. and Yuhara, M., 2000. Regional variation of eSr and eNd initial ratios in the Late Cretaceous - Paleogene felsic igneous rocks from Honshu Arc, Japan. Earth Monthly, 30(Spec. issue): 185-190.

Kamenetsky, V.S. and Gurenko, A.A., 2007. Cryptic crustal contamination of MORB primitive melts recorded in olivine-hosted glass and mineral inclusions. Contributions to Mineralogy and Petrology, 153(4): 465-481.

Kamenetsky, V.S., Zelenski, M., Gurenko, A., Portnyagin, M., Ehrig, K., Kamenetsky, M., Churikova, T. and Feig, S., 2017. Silicate-sulfide liquid immiscibility in modern arc basalt (Tolbachik volcano, Kamchatka): Part II. Composition, liquidus assemblage and fractionation of the silicate melt. Chemical Geology, 471: 92-110.

Katsui, Y., 1953. Petro-chemical study on the lavas from Volcano Rishiri, Hokkaido, Japan. Journal of the Faculty of Science, Hokkaido University. Series 4, Geology and mineralogy, 8(3): 245-258.

Katsui, Y., Ōba, Y., Ando, S., Nishimura, S., Masuda, Y., Kurasawa, H. and Fujimaki, H., 1978. Petrochemistry of the Quaternary volcanic rocks of Hokkaido, north Japan. 北海道大学理学部紀要, 18(3): 449-484.

Katsui, Y. and Satoh, H., 1970. Geology of the Oshima-Oshima district. Geological Survey of Japan, 16(4).

Katsui, Y. and Yamamoto, M., 1981. The 1741-1742 activity of Oshima-Ōshima volcano, north Japan. 北海道大学理学部紀要= Journal of the Faculty of Science, Hokkaido University. Series 4, Geology and mineralogy, 19(4): 527-536.

Katsui, Y., Yamamoto, M., Nemoto, S. and Niida, K., 1979. Genesis of calc-alkalic andesites from Oshima-Ōshima and Ichinomegata volcanoes, North Japan. 北海道大学理学部紀要, 19(1-2): 157-168.

Katz, R.F., Spiegelman, M. and Langmuir, C.H., 2003. A new parameterization of hydrous mantle melting. Geochem. Geophys. Geosyst., 4(9).

Kawakatsu, H. and Watada, S., 2007. Seismic evidence for deep-water transportation in the mantle. Science, 316(5830): 1468-1471.

Kelley, K.A. and Cottrell, E., 2009. Water and the oxidation state of subduction zone magmas. Science, 325(5940): 605-607.

Kelley, K.A., Plank, T., Grove, T.L., Stolper, E.M., Newman, S. and Hauri, E., 2006. Mantle melting as a function of water content beneath back-arc basins. J. Geophys. Res. B Solid Earth, 111(9).

Kelley, K.A., Plank, T., Ludden, J. and Staudigel, H., 2003. Composition of altered oceanic crust at ODP Sites 801 and 1149. Geochem. Geophys. Geosyst., 4(6).

Kelley, K.A., Plank, T., Newman, S., Stolper, E.M., Grove, T.L., Parman, S. and Hauri, E.H., 2010. Mantle melting as a function of water content beneath the Mariana arc. Journal of Petrology, 51(8): 1711-1738.

Kendrick, M.A., Arculus, R.J., Danyushevsky, L.V., Kamenetsky, V.S., Woodhead, J.D. and Honda, M., 2014. Subduction-related halogens (Cl, Br and I) and H_2O in magmatic glasses from Southwest Pacific Backarc Basins. Earth and Planetary Science Letters, 400: 165-176.

Kendrick, M.A., D'Andres, J., Holden, P. and Ireland, T., 2018. Halogens (F, Cl, Br, I) in Thirteen USGS, GSJ and NIST International Rock and Glass Reference Materials. Geostandards and Geoanalytical Research, 42(4): 499-511.

Kendrick, M.A., Danyushevsky, L.V., Falloon, T.J., Woodhead, J.D., Arculus, R.J. and Ireland, T., 2020. SW Pacific arc and backarc lavas and the role of slab-bend serpentinites in the global halogen cycle. Earth and Planetary Science Letters, 530: 115921.

Kendrick, M.A., Hémond, C., Kamenetsky, V.S., Danyushevsky, L., Devey, C.W., Rodemann, T., Jackson, M.G. and Perfit, M.R., 2017. Seawater cycled throughout Earth's mantle in partially serpentinized lithosphere. Nature Geoscience, 10(3): 222-228.

Kent, A.J.R., 2008. Met inclusions in basaltic and related volcanic rocks. In: K.D. Putirka and F.J. Tepley III (Editors), Reviews in Mineralogy and Geochemistry, pp. 273-331.

Kessel, R., Schmidt, M.W., Ulmer, P. and Pettke, T., 2005. Trace element signature of subduction-zone fluids, melts and supercritical liquids at 120–180 km depth. Nature, 437(7059): 724-727.

Kimura, G., 1986. Oblique subduction and collision: forearc tectonics of the Kuril arc (Pacific). Geology, 14(5): 404-407.

Kimura, G., 1994. The latest Cretaceous-early Paleogene rapid growth of accretionary complex and exhumation of high pressure series metamorphic rocks in northwestern Pacific margin. Journal of Geophysical Research, 99(B11): 22,147-122,164.

Kimura, G., 1996. Collision orogeny at arc-arc junctions in the Japanese Islands. Isl. Arc, 5(3): 262-275.

Kimura, J.I., 2017. Modeling chemical geodynamics of subduction zones using the Arc Basalt Simulator version 5. Geosphere, 13(4): 992-1025.

Kimura, J.I. and Ariskin, A.A., 2014. Calculation of water-bearing primary basalt and estimation of source mantle conditions beneath arcs: PRIMACALC2 model for WINDOWS. Geochem. Geophys. Geosyst., 15(4): 1494-1514.

Kimura, J.I., Gill, J.B., Kunikiyo, T., Osaka, I., Shimoshioiri, Y., Katakuse, M., Kakubuchi, S., Nagao, T., Furuyama, K., Kamei, A., Kawabata, H., Nakajima, J., Van Keken, P.E. and Stern, R.J., 2014. Diverse magmatic effects of subducting a hot slab in SW Japan: Results from forward modeling. Geochem. Geophys. Geosyst., 15(3): 691-739.

Kimura, J.I., Gill, J.B., Skora, S., van Keken, P.E. and Kawabata, H., 2016. Origin of geochemical mantle components: Role of subduction filter. Geochem. Geophys. Geosyst., 17(8): 3289-3325.

Kimura, J.I., Hacker, B.R., Van Keken, P.E., Kawabata, H., Yoshida, T. and Stern, R.J., 2009. Arc Basalt Simulator version 2, a simulation for slab dehydration and fluid-fluxed mantle melting for arc basalts: Modeling scheme and application. Geochem. Geophys. Geosyst., 10(9).

Kimura, J.I., Kent, A.J.R., Rowe, M.C., Katakuse, M., Nakano, F., Hacker, B.R., Van Keken, P.E., Kawabata, H. and Stern, R.J., 2010. Origin of cross-chain geochemical variation in Quaternary lavas from the northern Izu arc: Using a quantitative mass balance approach to identify mantle sources and mantle wedge processes. Geochem. Geophys. Geosyst., 11(10).

Kimura, J.I. and Yoshida, T., 2006. Contributions of slab fluid, mantle wedge and crust to the origin of quaternary lavas in the NE Japan arc. Journal of Petrology, 47(11): 2185-2232.

King, P.L., Vennemann, T.W., Holloway, J.R., Hervig, R.L., Lowenstern, J.B. and Forneris, J.F., 2002. Analytical techniques for volatiles: A case study using intermediate (andesitic) glasses. Am. Mineral., 87(8-9): 1077-1089.

Kita, S., Hasegawa, A., Nakajima, J., Okada, T., Matsuzawa, T. and Katsumata, K., 2012. High-resolution seismic velocity structure beneath the Hokkaido corner, northern Japan: Arc-arc collision and origins of the 1970 M 6.7 Hidaka and 1982 M 7.1 Urakawa-oki earthquakes. Journal of Geophysical Research B: Solid Earth, 117(12).

Kita, S., Nakajima, J., Hasegawa, A., Okada, T., Katsumata, K., Asano, Y. and Kimura, T., 2014. Detailed seismic attenuation structure beneath Hokkaido, northeastern Japan: Arc-arc collision process, arc magmatism, and seismotectonics. J. Geophys. Res. B Solid Earth, 119(8): 6486-6511.

Kita, S., Okada, T., Hasegawa, A., Nakajima, J. and Matsuzawa, T., 2010. Existence of interplane earthquakes and neutral stress boundary between the upper and lower planes of the double seismic zone beneath Tohoku and Hokkaido, northeastern Japan. Tectonophysics, 496(1-4): 68-82.

Kobayashi, T., 1987. Geology of Rishiri volcano. Journal of Geological Society of Japan, 93: 749-760.

Krenn, E., Harlov, D.E., Finger, F. and Wunder, B., 2012. LREE-redistribution among fluorapatite, monazite, and allanite at high pressures and temperatures. Am. Mineral., 97(11-12): 1881-1890.

Kress, V.C. and Carmichael, I.S.E., 1991. The compressibility of silicate liquids containing Fe_2O_3 and the effect of composition, temperature, oxygen fugacity and pressure on their redox states. Contributions to Mineralogy and Petrology, 108(1-2): 82-92.

Kress, V.C. and Ghiorso, M.S., 2004. Thermodynamic modeling of post-entrapment crystallization in igneous phases. Journal of Volcanology and Geothermal Research, 137(4): 247-260.

Kudo, T. and Hoshizumi, H., 2006. Catalog of eruptive events within the last 10,000 years in Japan, database of Japanese active volcanoes. Geol Surv Japan, AIST.

Kudo, T., Okuno, M. and Nakamura, T., 2003. Eruptive history of Kita-Hakkoda volcanic group during the last 6000 years, Northeast Japan. Chishitsugaku Zasshi = Journal of the Geological Society of Japan, 109(3): 151-165.

Kudo, T., Okuno, M., Ohba, T., Kitade, Y. and Nakamura, T., 2000. The eruptive products from Jigoku-numa hot pool in Kita-Hakkoda volcano group, northeast Japan: Eruption style, magnitude and age. Kazan, 45(6): 315-322.

Kudo, T., Takarada, S. and Sasaki, M., 2004. Geology and volcanic history of Kita-Hakkoda volcanic group, northeast Japan. Journal of the Geological Society of Japan, 110(5): 271-289.

Kuno, H., 1959. Origin of Cenozoic petrographic provinces of Japan and surrounding areas. Bull Volcanol, 20(1): 37-76.

Kuritani, T., 1998. Boundary layer crystallization in a basaltic magma chamber: evidence from Rishiri Volcano, northern Japan. Journal of Petrology, 39(9): 1619-1640.

Kuritani, T., 1999a. Boundary layer fractionation constrained by differential information from the Kutsugata lava flow, Rishiri Volcano, Japan. J. Geophys. Res. B Solid Earth, 104(B12): 29401-29417.

Kuritani, T., 1999b. Thermal and compositional evolution of a cooling magma chamber by boundary layer Fractionation: model and its application for primary magma estimation. Geophys. Res. Lett., 26(13): 2029-2032.

Kuritani, T., 2001. Replenishment of a mafic magma in a zoned felsic magma chamber beneath Rishiri Volcano, Japan. Bull. Volcanol., 62(8): 533-548.

Kuritani, T., 2009. The relative roles of boundary layer fractionation and homogeneous fractionation in cooling basaltic magma chambers. Lithos, 110(1-4): 247-261.

Kuritani, T., Kanai, C., Yamashita, S. and Nakagawa, M., 2019. Magma generation conditions at the Akita-Komagatake volcano, Northeast Japan arc: Implications of across-arc variations in mantle melting parameters. Lithos, 348-349: 105197.

Kuritani, T., Kitagawa, H. and Nakamura, E., 2005. Assimilation and fractional crystallization controlled by transport process of crustal melt: implications from an alkali basalt–dacite suite from Rishiri Volcano, Japan. Journal of Petrology, 46(7): 1421-1442.

Kuritani, T. and Nakagawa, M., 2016. Origin of ultra rear-arc magmatism at Rishiri Volcano, Kuril Arc. Geochemistry Geophysics Geosystems, 17(10): 4032-4050.

Kuritani, T. and Nakamura, E., 2006. Elemental fractionation in lavas during post-eruptive degassing: Evidence from trachytic lavas, Rishiri Volcano, Japan. Journal of Volcanology and Geothermal Research, 149(1): 124-138.

Kuritani, T., Sato, E., Wada, K., Matsumoto, A., Nakagawa, M., Zhao, D., Shimizu, K. and Ushikubo, T., 2021. Conditions of magma generation at the Me-akan volcano, northern Japan. Journal of Volcanology and Geothermal Research, 417: 107323.

Kuritani, T., Tanaka, M., Yokoyama, T., Nakagawa, M. and Matsumoto, A., 2016. Intensive Hydration of the Wedge Mantle at the Kuril Arc-NE Japan Arc Junction: Implications from Mafic Lavas from Usu Volcano, Northern Japan. Journal of Petrology, 57(6): 1223-1240.

Kuritani, T., Yokoyama, T. and Nakamura, E., 2007. Rates of thermal and chemical evolution of magmas in a cooling magma chamber: a chronological and theoretical study on basaltic and andesitic lavas from Rishiri Volcano, Japan. Journal of Petrology, 48(7): 1295-1319.

Kuritani, T., Yokoyama, T. and Nakamura, E., 2008. Generation of rear-arc magmas induced by influx of slab-derived supercritical liquids: Implications from alkali basalt lavas from Rishiri Volcano, Kurile arc. Journal of Petrology, 49(7): 1319-1342.

Kusunoki, K. and Kimura, G., 1998. Collision and extrusion at the Kuril-Japan arc junction. Tectonics, 17(6): 843-858.

Lambart, S., Laporte, D., Provost, A. and Schiano, P., 2012. Fate of pyroxenite-derived melts in the peridotitic mantle: Thermodynamic and experimental constraints. Journal of Petrology, 53(3): 451-476.

Lange, R.A., 1997. A revised model for the density and thermal expansivity of K_2O-Na_2O-CaO-MgO-Al_2O_3-SiO_2 liquids from 700 to 1900 K: extension to crustal magmatic temperatures. Contributions to Mineralogy and Petrology, 130(1): 1-11.

Lange, R.A., Frey, H.M. and Hector, J., 2009. A thermodynamic model for the plagioclase-liquid hygrometer/thermometer. Am. Mineral., 94(4): 494-506.

Lange, R.L. and Carmichael, I.S.E., 1990. Thermodynamic properties of silicate liquids with emphasis on densiy, thermal expansion and compressibility. In: P.H. Ribbe (Editor), Rev Mineral. Mineralogical Society of America, Washington, D.C., pp. 25-64.

Langmuir, C.H., 1989. Geochemical consequences of in situ crystallization. Nature, 340(6230): 199-205.

Langmuir, C.H., Klein, E.M. and Plank, T., 1992. Petrological systematics of mid-ocean ridge basalts: Constraints on melt generation beneath ocean ridges. Mantle Flow and Melt Generation at Mid-Ocean Ridges, 71: 183-280.

Le Voyer, M., Rose-Koga, E.F., Laubier, M. and Schiano, P., 2008. Petrogenesis of arc lavas from the Rucu Pichincha and Pan de Azucar volcanoes (Ecuadorian arc): Major, trace element, and boron isotope evidences from olivine-hosted melt inclusions. Geochem. Geophys. Geosyst., 9(12).

Le Voyer, M., Rose-Koga, E.F., Shimizu, N., Grove, T.L. and Schiano, P., 2010. Two contrasting H_2O-rich components in primary melt inclusions from Mount Shasta. J Petrol, 51(7): 1571-1595.

Lesne, P., Kohn, S.C., Blundy, J., Witham, F., Botcharnikov, R.E. and Behrens, H., 2011. Experimental simulation of closed-system degassing in the system basalt-H_2O-CO_2-S-Cl. Journal of Petrology, 52(9): 1737-1762.

Li, H. and Hermann, J., 2017. Chlorine and fluorine partitioning between apatite and sediment melt at 2.5 GPa, 800 C: A new experimentally derived thermodynamic model. Am. Mineral., 102(3): 580-594.

Li, H., Zhang, L., Bao, X., Wykes, J.L. and Liu, X., 2021. High sulfur solubility in subducted sediment melt under both reduced and oxidized conditions: With implications for S recycling in subduction zone settings. Geochimica et Cosmochimica Acta, 304: 305-326.

Li, X., Zhang, C., Almeev, R.R. and Holtz, F., 2020. GeoBalance: An Excel VBA program for mass balance calculation in geosciences. Geochemistry, 80(2): 125629.

Liu, X. and Zhao, D., 2016. P and S wave tomography of Japan subduction zone from joint inversions of local and teleseismic travel times and surface-wave data. Phys. Earth Planet. Inter., 252: 1-22.

Lowenstern, J.B., 1995. Applications of silicate-melt inclusions to the study of magmatic volatiles. Magmas, fluids, and ore deposits, 23: 71-99.

Maclennan, J., 2017. Bubble formation and decrepitation control the CO_2 content of olivine-hosted melt inclusions. Geochem. Geophys. Geosyst., 18(2): 597-616.

Manning, C.E., 2004. The chemistry of subduction-zone fluids. Earth and Planetary Science Letters, 223(1-2): 1-16.

Markhinin, E.K., Anikiev, Y.A. and Grannik, V.M., 1974. The eruption of Tyatya Volcano on the Kuril Islands in July 1973. Geol. Geofiz(10): 22-32.

Marks, M.A.W., Kendrick, M.A., Eby, G.N., Zack, T. and Wenzel, T., 2017. The F, Cl, Br and I Contents of Reference Glasses BHVO-2G, BIR-1G, BCR-2G, GSD-1G, GSE-1G, NIST SRM 610 and NIST SRM 612. Geostandards and Geoanalytical Research, 41(1): 107-122.

Marschall, H.R. and Schumacher, J.C., 2012. Arc magmas sourced from mélange diapirs in subduction zones. Nature Geoscience, 5(12): 862-867.

Marsh, B.D., 1996. Solidification fronts and magmatic evolution. Mineral. Mag., 60(1): 5-40.

Marsh, B.D., 2007. Magmatism, Magma, and Magma Chambers. In: G. Schubert (Editor), Treatise on Geophysics. Elsevier, Amsterdam, pp. 275-333.

Marsh, B.D., 2015. Magma chambers, The encyclopedia of volcanoes. Elsevier, pp. 185-201.

Martin, A.K., 2011. Double saloon door tectonics in the Japan Sea, Fossa Magna, and the Japanese Island Arc. Tectonophysics, 498(1): 45-65.

Martin, L., Hermann, J.r., Gauthiez-Putallaz, L., Whitney, D., Vitale Brovarone, A., Fornash, K. and Evans, N.J., 2014. Lawsonite geochemistry and stability–

implication for trace element and water cycles in subduction zones. J. Metamorph. Geol., 32(5): 455-478.

Maruyama, S. and Send, T., 1986. Orogeny and relative plate motions: Example of the Japanese Islands. Tectonophysics, 127(3-4): 305-329.

Médard, E. and Grove, T.L., 2008. The effect of H_2O on the olivine liquidus of basaltic melts: experiments and thermodynamic models. Contributions to Mineralogy and Petrology, 155(4): 417-432.

Mercier, M., Muro, A.D., Métrich, N., Giordano, D., Belhadj, O. and Mandeville, C.W., 2010. Spectroscopic analysis (FTIR, Raman) of water in mafic and intermediate glasses and glass inclusions. Geochimica et Cosmochimica Acta, 74(19): 5641-5656.

Métrich, N. and Wallace, P.J., 2008. Volatile abundances in basaltic magmas and their degassing paths tracked by melt inclusions. In: K.D. Putirka and F.J. Tepley III (Editors), Reviews in Mineralogy and Geochemistry, pp. 363-402.

Mollo, S., Giacomoni, P.P., Coltorti, M., Ferlito, C., Iezzi, G. and Scarlato, P., 2015. Reconstruction of magmatic variables governing recent Etnean eruptions: Constraints from mineral chemistry and P–T–fO_2–H_2O modeling. Lithos, 212-215: 311-320.

Moore, G., Vennemann, T. and Carmichael, I.S.E., 1995. Solubility of water in magmas to 2 kbar. Geology, 23(12): 1099-1102.

Moore, G., Vennemann, T. and Carmichael, I.S.E., 1998. An empirical model for the solubility of H_2O in magmas to 3 kilobars. Am. Mineral., 83(1-2): 36-42.

Moore, L.R., Gazel, E., Tuohy, R., Lloyd, A.S., Esposito, R., Steele-MacInnis, M., Hauri, E.H., Wallace, P.J., Plank, T. and Bodnar, R.J., 2015. Bubbles matter: An assessment of the contribution of vapor bubbles to melt inclusion volatile budgets. Am. Mineral., 100(4): 806-823.

Moore, L.R., Mironov, N., Portnyagin, M., Gazel, E. and Bodnar, R.J., 2018. Volatile contents of primitive bubble-bearing melt inclusions from Klyuchevskoy volcano, Kamchatka: Comparison of volatile contents determined by mass-balance versus experimental homogenization. Journal of Volcanology and Geothermal Research, 358: 124-131.

Moretti, R. and Baker, D.R., 2008. Modeling the interplay of fO_2 and fS_2 along the FeS-silicate melt equilibrium. Chemical Geology, 256(3-4): 285-297.

Moriguti, T., Shibata, T. and Nakamura, E., 2004. Lithium, boron and lead isotope and trace element systematics of Quaternary basaltic volcanic rocks in northeastern Japan: mineralogical controls on slab-derived fluid composition. Chemical Geology, 212(1-2): 81-100.

Morse, S.A., 1994. Basalts and Phase Diagrams: An introduction to the Quantitative use of Phase Diagrams in Igneous Petrology. Krieger, 493 pp.

Moyen, J.F. and Stevens, G., 2006. Experimental Constraints on TTG Petrogenesis: Implications for Archean Geodynamics. Archean Geodynamics and Environments, 164: 149-175.

Müller, T., Dohmen, R., Becker, H.W., ter Heege, J.H. and Chakraborty, S., 2013. Fe–Mg interdiffusion rates in clinopyroxene: experimental data and implications for Fe–Mg exchange geothermometers. Contributions to Mineralogy and Petrology, 166(6): 1563-1576.

Nagashima, K., Kunihiro, T., Takayanagi, I., Nakamura, J., Kosaka, K. and Yurimoto, H., 2001. Output characteristics of stacked CMOS-type active pixel sensor for charged particles. Surface and Interface Analysis, 31(2): 131-137.

Nakagawa, M., 1985. Geochemical study of lavas from Akita-Komagatake volcano, northeast Japan-Chemical compositional variation of island-arc tholeiitic series. Res. Rep. Lab. Nuc. Sci. Tohoku Univ., 18: 351-365.

Nakagawa, M., Ishizuka, Y., Kudo, T., Yoshimoto, M., Hirose, W., Ishizaki, Y., Gouchi, N., Katsui, Y., Solovyow, A.W., Steinberg, G.S. and Abdurakhmanov, A.I., 2002. Tyatya Volcano, southwestern Kuril arc: Recent eruptive activity inferred from widespread tephra. Isl. Arc, 11(4): 236-254.

Nakagawa, M., Matsumoto, A., Kobayashi, K. and Wada, K., 2019. Comparative Petrological Studies of 1962 and 1988–1989 Eruptions of Tokachidake Volcano, Japan: A Case Study for Understanding the Relationship Between Eruption Style and Magma Processes. Journal of Disaster Research, 14(5): 766-779.

Nakajima, J., Hada, S., Hayami, E., Uchida, N., Hasegawa, A., Yoshioka, S., Matsuzawa, T. and Umino, N., 2013. Seismic attenuation beneath northeastern Japan: Constraints on mantle dynamics and arc magmatism. J. Geophys. Res. B Solid Earth, 118(11): 5838-5855.

Nakajima, J. and Hasegawa, A., 2003. Estimation of thermal structure in the mantle wedge of northeastern Japan from seismic attenuation data. Geophys. Res. Lett., 30(14): SDE 6-1 - 6-4.

Nakajima, J., Matsuzawa, T., Hasegawa, A. and Zhao, D., 2001. Three-dimensional structure of Vp, Vs and Vp/Vs beneath northeastern Japan: Implications for arc magmatism and fluids. J. Geophys. Res. B Solid Earth, 106(B10): 21843-21857.

Nakajima, J., Takei, Y. and Hasegawa, A., 2005. Quantitative analysis of the inclined low-velocity zone in the mantle wedge of northeastern Japan: A systematic change of melt-filled pore shapes with depth and its implications for melt migration. Earth and Planetary Science Letters, 234(1-2): 59-70.

Newcombe, M.E., Fabbrizio, A., Zhang, Y., Ma, C., Le Voyer, M., Guan, Y., Eiler, J.M., Saal, A.E. and Stolper, E.M., 2014. Chemical zonation in olivine-hosted melt inclusions. Contributions to Mineralogy and Petrology, 168(1): 1030.

Newman, S. and Lowenstern, J.B., 2002. VOLATILECALC: A silicate melt-H_2O-CO_2 solution model written in Visual Basic for excel. Comput. Geosci., 28(5): 597-604.

Newton, R.C. and Manning, C.E., 2005. Solubility of anhydrite, $CaSO_4$, in NaCl–H_2O solutions at high pressures and temperatures: applications to fluid–rock interaction. Journal of Petrology, 46(4): 701-716.

Nielsen, R.L., 1990. Modern Methods of Igneous Petrology. In: N. James and R. Kelly (Editors), Simulation of Igneous Differentiation Processes. De Gruyter, pp. 65-106.

Nielsen, R.L. and DeLong, S.E., 1992. A numerical approach to boundary layer fractionation: application to differentiation in natural magma systems. Contributions to Mineralogy and Petrology, 110(2): 355-369.

Nielsen, S.G. and Marschall, H.R., 2017. Geochemical evidence for mélange melting in global arcs. Science advances, 3(4): e1602402.

Nikolaev, G.S., Ariskin, A., Barmina, G., Nazarov, M. and Almeev, R., 2016. Test of the Ballhaus–Berry–Green Ol–Opx–Sp oxybarometer and calibration of a new equation for estimating the redox state of melts saturated with olivine and spinel. Geochem. Int., 54(4): 301-320.

Nishimoto, S., Ishikawa, M., Arima, M., Yoshida, T. and Nakajima, J., 2008. Simultaneous high P-T measurements of ultrasonic compressional and shear wave velocities in Ichino-megata mafic xenoliths: Their bearings on seismic velocity perturbations in lower crust of northeast Japan arc. J. Geophys. Res. B Solid Earth, 113(12).

Niu, X., Zhao, D. and Li, J., 2018. Precise relocation of low-frequency earthquakes in Northeast Japan: new insight into arc magma and fluids. Geophys. J. Int., 212(2): 1183-1200.

Northrup, C.J., Royden, L.H. and Burchfie, B.C., 1995. Motion of the Pacific plate relative to Eurasia and its potential relation to Cenozoic extension along the eastern margin of Eurasia. Geology, 23(8): 719-722.

O'Hara, M.J. and Fry, N., 1996. Geochemical Effects of Small Packet Crystallization in Large Magma Chambers—Further Resolution of the Highly Compatible Element Paradox. Journal of Petrology, 37(4): 891-925.

Ochs III., F.A. and Lange, R.A., 1997. The partial molar volume, thermal expansivity, and compressibility of H_2O in $NaAlSi_3O_8$ liquid: new measurements and an internally consistent model. Contributions to Mineralogy and Petrology, 129(2): 155-165.

Ohguchi, T., Yoshida, T. and Okami, K., 1989. Historical change of the Neogene and Quaternary volcanic field in the Northeast Honshu Arc, Japan. Mem. Geol. Soc. Jpn., 32: 431-455.

Okada, T., Umino, N. and Hasegawa, A., 2010. Deep structure of the ou mountain range strain concentration zone and the focal area of the 2008 Iwate-Miyagi Nairiku earthquake, NE Japan-seismogenesis related with magma and crustal fluid. Earth Planets Space, 62(3): 347-352.

Oppenheimer, C., Moretti, R., Kyle, P.R., Eschenbacher, A., Lowenstern, J.B., Hervig, R.L. and Dunbar, N.W., 2011a. Mantle to surface degassing of alkalic magmas at Erebus volcano, Antarctica. Earth and Planetary Science Letters, 306(3-4): 261-271.

Oppenheimer, C., Scaillet, B. and Martin, R.S., 2011b. Sulfur degassing from volcanoes: Source conditions, surveillance, plume chemistry and earth system impacts, Reviews in Mineralogy and Geochemistry, pp. 363-421.

Ozawa, K. and Shimizu, N., 1995. Open-system melting in the upper mantle: constraints from the Hayachine-Miyamori ophiolite, northeastern Japan. Journal of Geophysical Research, 100(B11): 22,315-322,335.

Pagé, L. and Hattori, K., 2017. Tracing halogen and B cycling in subduction zones based on obducted, subducted and forearc serpentinites of the Dominican Republic. Sci. Rep., 7(1): 17776.

Pagé, L., Hattori, K., de Hoog, J.C.M. and Okay, A.I., 2016. Halogen (F, Cl, Br, I) behaviour in subducting slabs: A study of lawsonite blueschists in western Turkey. Earth and Planetary Science Letters, 442: 133-142.

Papale, P., 1999. Modeling of the solubility of a two-component H2O + CO2 fluid in silicate liquids. Am. Mineral., 84(4): 477-492.

Papale, P., Moretti, R. and Barbato, D., 2006. The compositional dependence of the saturation surface of H_2O + CO_2 fluids in silicate melts. Chemical Geology, 229(1-3): 78-95.

Pasyanos, M.E., Masters, T.G., Laske, G. and Ma, Z., 2014. LITHO1.0: An updated crust and lithospheric model of the Earth. J. Geophys. Res. B Solid Earth, 119(3): 2153-2173.

Patino, L.C., Carr, M.J. and Feigenson, M.D., 1997. Cross-arc geochemical variations in volcanic fields in Honduras CA: progressive changes in source with distance from the volcanic front. Contributions to Mineralogy and Petrology, 129(4): 341-351.

Patton, C., Hellstrom, J., Paul, B., Woodhead, J.H. and Hergt, J., 2011. Iolite: freeware for the visualization and processing of mass spectrometry data. Journal of Analytical Atomic Spectrometry, 26: 2508-2518.

Pawlowsky-Glahn, V., Egozcue, J.J. and Tolosana-Delgado, R., 2015. Linear models. In: V. Barnett (Editor), Modelling and Analysis of Compositional Data. John Wiley & Sons Ltd, pp. 149-171.

Pearce, J.A., 1983. Role of the sub-continental lithosphere in magma genesis at active continental margins. Continental Basalts and Mantle Xenoliths: 230-249.

Pearce, J.A., Stern, R.J., Bloomer, S.H. and Fryer, P., 2005. Geochemical mapping of the Mariana arc-basin system: Implications for the nature and distribution of subduction components. Geochem. Geophys. Geosyst., 6(7).

Perfit, M.R., Gust, D., Bence, A.E., Arculus, R. and Taylor, S.R., 1980. Chemical characteristics of island-arc basalts: implications for mantle sources. Chemical Geology, 30(3): 227-256.

Petrelli, M., El Omari, K., Spina, L., Le Guer, Y., La Spina, G. and Perugini, D., 2018. Timescales of water accumulation in magmas and implications for short warning times of explosive eruptions. Nature Communications, 9(1): 770.

Pistone, M., Blundy, J. and Brooker, R.A., 2017. Water transfer during magma mixing events: Insights into crystal mush rejuvenation and melt extraction processes. Am. Mineral., 102(4): 766-776.

Plank, T. and Langmuir, C.H., 1998. The chemical composition of subducting sediment and its consequences for the crust and mantle. Chemical Geology, 145(3-4): 325-394.

Poli, S. and Schmidt, M.W., 1995. H_2O transport and release in subduction zones: experimental constraints on basaltic and andesitic systems. Journal of Geophysical Research, 100(B11): 22,299-222,314.

Pollitz, F.F., 1986. Pliocene change in Pacific-plate motion. Nature, 320(6064): 738-741.

Portnyagin, M., Duggen, S., Hauff, F., Mironov, N., Bindeman, I., Thirlwall, M. and Hoernle, K., 2015. Geochemistry of the late Holocene rocks from the Tolbachik volcanic field, Kamchatka: Quantitative modelling of subduction-related open magmatic systems. Journal of Volcanology and Geothermal Research, 307: 133-155.

Portnyagin, M., Hoernle, K., Plechov, P. and Mironov, N., 2007. Constraints on mantle melting and composition and nature of slab components in volcanic arcs from volatiles (H_2O, S, Cl, F) and trace elements in melt inclusions from the Kamchatka Arc. Earth Planet Sci Lett, 255.

Prouteau, G. and Scaillet, B., 2012. Experimental constraints on sulphur behaviour in subduction zones: implications for TTG and adakite production and the global sulphur cycle since the Archean. Journal of Petrology, 54(1): 183-213.

Putirka, K.D., 2008. Thermometers and barometers for volcanic systems. In: K.D. Putirka and F.J. Tepley III (Editors), Reviews in Mineralogy and Geochemistry, pp. 61-120.

Putirka, K.D., Perfit, M., Ryerson, F.J. and Jackson, M.G., 2007. Ambient and excess mantle temperatures, olivine thermometry, and active vs. passive upwelling. Chemical Geology, 241(3-4): 177-206.

Pyle, D.M. and Mather, T.A., 2009. Halogens in igneous processes and their fluxes to the atmosphere and oceans from volcanic activity: A review. Chemical Geology, 263(1-4): 110-121.

Ranero, C.R., Phipps Morgan, J., McIntosh, K. and Relchert, C., 2003. Bending-related faulting and mantle serpentinization at the Middle America trench. Nature, 425(6956): 367-373.

Ranero, C.R. and Sallarès, V., 2004. Geophysical evidence for hydration of the crust and mantle of the Nazca plate during bending at the north Chile trench. Geology, 32(7): 549-552.

Rasmussen, D.J., Plank, T.A., Wallace, P.J., Newcombe, M.E. and Lowenstern, J.B., 2020. Vapor-bubble growth in olivine-hosted melt inclusions. Am. Mineral., 105(12): 1898-1919.

Reiners, P.W., Hammond, P.E., McKenna, J.M. and Duncan, R.A., 2000. Young basalts of the central Washington Cascades, flux melting of the mantle, and trace element signatures of primary arc magmas. Contributions to Mineralogy and Petrology, 138(3): 249-264.

Reubi, O. and Blundy, J., 2009. A dearth of intermediate melts at subduction zone volcanoes and the petrogenesis of arc andesites. Nature, 461(7268): 1269-1273.

Reubi, O., Blundy, J. and Varley, N.R., 2013. Volatiles contents, degassing and crystallisation of intermediate magmas at Volcan de Colima, Mexico, inferred from melt inclusions. Contributions to Mineralogy and Petrology, 165(6): 1087-1106.

Robidoux, P., Frezzotti, M.L., Hauri, E.H. and Aiuppa, A., 2018. Shrinkage Bubbles: The C–O–H–S Magmatic Fluid System at San Cristóbal Volcano. Journal of Petrology, 59(11): 2093-2122.

Roedder, E., 1979. Origin and significance of magmatic inclusions. Bull. Mineral, 102: 487-510.

Rose-Koga, E.F., Koga, K.T., Hamada, M., Hélouis, T., Whitehouse, M.J. and Shimizu, N., 2014. Volatile (F and Cl) concentrations in Iwate olivine-hosted melt inclusions indicating low-temperature subduction. Earth Planets Space, 66(1): 81.

Rose-Koga, E.F., Koga, K.T., Moreira, M., Vlastelic, I., Jackson, M.G., Whitehouse, M.J., Shimizu, N. and Habib, N., 2017. Geochemical systematics of Pb isotopes, fluorine, and sulfur in melt inclusions from São Miguel, Azores. Chemical Geology, 458: 22-37.

Rowe, M.C., Kent, A.J.R. and Nielsen, R.L., 2009. Subduction influence on oxygen fugacity and trace and volatile elements in basalts across the cascade volcanic arc. Journal of Petrology, 50(1): 61-91.

Rowe, M.C. and Lassiter, J.C., 2009. Chlorine enrichment in central Rio Grande Rift basaltic melt inclusions: Evidence for subduction modification of the lithospheric mantle. Geology, 37(5): 439-442.

Rowe, M.C., Peate, D.W. and Newbrough, A., 2011a. Compositional and thermal evolution of olivine-hosted melt inclusions in small-volume basaltic eruptions: A "simple" example from Dotsero Volcano, NW Colorado. Contributions to Mineralogy and Petrology, 161(2): 197-211.

Rowe, M.C., Peate, D.W. and Peate, I.U., 2011b. An investigation into the nature of the magmatic plumbing system at Paricutin Volcano, mexico. Journal of Petrology, 52(11): 2187-2220.
Saal, A.E., Hauri, E.H., Langmuir, C.H. and Perfit, M.R., 2002. Vapour undersaturation in primitive mid-ocean-ridge basalt and the volatile content of earth's upper mantle. Nature, 419(6906): 451-455.
Sadofsky, S.J., Portnyagin, M., Hoernle, K. and van den Bogaard, P., 2008. Subduction cycling of volatiles and trace elements through the Central American volcanic arc: evidence from melt inclusions. Contributions to Mineralogy and Petrology, 155(4): 433-456.
Sakuyama, M., 1983. Phenocryst assemblages and H_2O content in circum-Pacific arc magmas. Geodynamics of the Western Pacific-Indonesian Region, 11: 143-158.
Sasaki, Y., 1986. Geochemical study of the eruptive rocks of stage 1 and stage 2 in Hakkoda volcanic group. Research Report of the Laboratory of Nuclear Science of Tohoku University, 19: 288-299.
Sasaki, Y., 1987. Geochemical study of the tholeiitic magma of stage 1 in Hakkoda volcanic group. Research Report of the Laboratory of Nuclear Science of Tohoku University, 20: 363-374.
Sasaki, Y., Yoshida, T. and Aoki, K., 1985. Geochemistry of Kita-Hakkoda volcanic group, northeastern Japan. Res. Rep. Lab. Nucl., Tohoku Univ, 18: 175-188.
Sato, E. and Sato, H., 2009. Study of effect of magma pocket on mixing of two magmas with different viscosities and densities by analogue experiments. Journal of Volcanology and Geothermal Research, 181(1): 115-123.
Sato, H. and Hasegawa, A., 1996. Mapping of partial melt zone in the upper mantle beneath northeastern Japan - ascent of magma in island arc. Kazan, 41: 115-125.
Sato, H. and Yoshida, T., 1993. Relationship between Late Cenozoic large scale caldera formations and tectonics, northeast Japan. Earth Monthly, 15: 721-724.
Scambelluri, M., Bottazzi, P., Trommsdorff, V., Vannucci, R., Hermann, J., Gòmez-Pugnaire, M.T. and Vizcaìno, V.L.-S., 2001. Incompatible element-rich fluids released by antigorite breakdown in deeply subducted mantle. Earth and Planetary Science Letters, 192(3): 457-470.
Scambelluri, M., Fiebig, J., Malaspina, N., Müntener, O. and Pettke, T., 2004. Serpentinite subduction: implications for fluid processes and trace-element recycling. Int. Geol. Rev., 46(7): 595-613.
Schmidt, M.W. and Poli, S., 1998. Experimentally based water budgets for dehydrating slabs and consequences for arc magma generation. Earth and Planetary Science Letters, 163(1-4): 361-379.
Schmidt, M.W., Vielzeuf, D. and Auzanneau, E., 2004. Melting and dissolution of subducting crust at high pressures: The key role of white mica. Earth and Planetary Science Letters, 228(1-2): 65-84.
Shibata, T. and Nakamura, E., 1997. Across-arc variations of isotope and trace element compositions from Quaternary basaltic volcanic rocks in northeastern Japan: Implications for interaction between subducted oceanic slab and mantle wedge. J Geophys Res, 102(B4): 8051-8064.
Shimaoka, A., Imamura, M. and Kaneoka, I., 2016. Beryllium isotopic systematics in island arc volcanic rocks from northeast Japan: Implications for the incorporation of oceanic sediments into island arc magmas. Chemical Geology, 443: 158-172.
Shoji, S., Nanzyo, M. and Dahlgren, R.A., 1993. Volcanic Ash Soils: Genesis, Properties and Utilization. Elsevier Science, 287 pp.

Shuto, K., Hirahara, Y., Ishimoto, H., Aoki, A., Jinbo, A. and Goto, Y., 2004. Sr and Nd isotopic compositions of the magma source beneath north Hokkaido, Japan: comparison with the back-arc side in the NE Japan arc. Journal of Volcanology and Geothermal Research, 134(1-2): 57-75.

Simura, R. and Ozawa, K., 2011. Magmatic Fractionation by Compositional Convection in a Sheet-like Magma Body: Constraints from the Nosappumisaki Intrusion, Northern Japan. Journal of Petrology, 52(10): 1887-1925.

Sisson, T.W. and Grove, T.L., 1993. Experimental investigations of the role of H_2O in calc-alkaline differentiation and subduction zone magmatism. Contributions to Mineralogy and Petrology, 113(2): 143-166.

Smith, P.M. and Asimow, P.D., 2005. Adiabat-1ph: A new public front-end to the MELTS, pMELTS, and pHMELTS models. Geochem. Geophys. Geosyst., 6(2).

Sorensen, S.S., Grossman, J.N. and Perfit, M.R., 1997. Phengite-hosted LILE enrichment in eclogite and related rocks: implications for fluid-mediated mass transfer in subduction zones and arc magma genesis. Journal of Petrology, 38(1): 3-34.

Sours-Page, R., Nielsen, R.L. and Batiza, R., 2002. Melt inclusions as indicators of parental magma diversity on the Northern East Pacific Rise. Chemical Geology, 183(1-4): 237-261.

Spandler, C., Mavrogenes, J. and Hermann, J., 2007. Experimental constraints on element mobility from subducted sediments using high-P synthetic fluid/melt inclusions. Chemical Geology, 239(3): 228-249.

Sparks, R.S.J. and Marshall, L.A., 1986. Thermal and mechanical constraints on mixing between mafic and silicic magmas. Journal of Volcanology and Geothermal Research, 29(1): 99-124.

Staudigel, H., Plank, T., White, B. and Schmincke, H.U., 1996. Geochemical fluxes during seafloor alteration of the basaltic upper oceanic crust: DSDP sites 417 and 418. In: G.E. Bebout, D.W. Scholl, S.H. Kirby and J.P. Platt (Editors), Geophysical Monograph Series. Blackwell Publishing Ltd, pp. 19-38.

Stolper, E. and Newman, S., 1994. The role of water in the petrogenesis of Mariana trough magmas. Earth and Planetary Science Letters, 121(3-4): 293-325.

Straub, S.M. and Layne, G.D., 2003a. Decoupling of fluids and fluid-mobile elements during shallow subduction: Evidence from halogen-rich andesite melt inclusions from the Izu arc volcanic front. Geochem. Geophys. Geosyst., 4(7).

Straub, S.M. and Layne, G.D., 2003b. The systematics of chlorine, fluorine, and water in Izu arc front volcanic rocks: Implications for volatile recycling in subduction zones. Geochimica et Cosmochimica Acta, 67(21): 4179-4203.

Sun, S.S. and McDonough, W.F., 1989. Chemical and isotopic systematics of oceanic basalts: Implications for mantle composition and processes, Geological Society Special Publication, pp. 313-345.

Sutō, S. and Ishii, T., 1987. Geology of the Shizukuishi district. Geological Survey of Japan.

Syracuse, E.M., van Keken, P.E., Abers, G.A., Suetsugu, D., Bina, C., Inoue, T., Wiens, D. and Jellinek, M., 2010. The global range of subduction zone thermal models. Phys. Earth Planet. Inter., 183(1-2): 73-90.

Takagi, D., Sato, H. and Nakagawa, M., 2005. Experimental study of a low-alkali tholeiite at 1–5 kbar: optimal condition for the crystallization of high-An plagioclase in hydrous arc tholeiite. Contributions to Mineralogy and Petrology, 149(5): 527-540.

Takahashi, E., 1986. Origin of basaltic magmas-implications from peridotite melting experiments and an olivine fractionation model. Bulletin of the Volcanological Society of Japan, 30(30): S17-S40.
Takarada, S. and Muraoka, H., 2004. Geology of the Hakkoda San District. Quadrangle Series, 1(50,000).
Tamaki, K., Suyehiro, K., Allan, J., Ingle Jr, J.C. and Pisciotto, K.A., 1992. Tectonic synthesis and implications of Japan Sea ODP drilling. Proc. scientific results, ODP, Legs 127/128, Japan Sea: 1333-1348.
Tamura, Y., Tani, K., Chang, Q., Shukuno, H., Kawabata, H., Ishizuka, O. and Fiske, R.S., 2007. Wet and dry basalt magma evolution at Torishima Volcano, Izu–Bonin Arc, Japan: the possible role of phengite in the downgoing Slab. Journal of Petrology, 48(10): 1999-2031.
Tamura, Y., Tatsumi, Y., Zhao, D., Kido, Y. and Shukuno, H., 2002. Hot fingers in the mantle wedge: New insights into magma genesis in subduction zones. Earth and Planetary Science Letters, 197(1-2): 105-116.
Taniuchi, H., Kuritani, T., Yokoyama, T., Nakamura, E. and Nakagawa, M., 2020. A new concept for the genesis of felsic magma: the separation of slab-derived supercritical liquid. Sci. Rep., 10(1): 8698.
Tatsumi, Y., 1986. Formation of the volcanic front in subduction zones. Geophys. Res. Lett., 13(8): 717-720.
Tatsumi, Y., 1989. Migration of fluid phases and genesis of basalt magmas in subduction zones. Journal of Geophysical Research, 94(B4): 4697-4707.
Tatsumi, Y., Hamilton, D.L. and Nesbitt, R.W., 1986. Chemical characteristics of fluid phase released from a subducted lithosphere and origin of arc magmas: Evidence from high-pressure experiments and natural rocks. Journal of Volcanology and Geothermal Research, 29(1-4): 293-309.
Thomson, A. and Maclennan, J., 2013. The Distribution of Olivine Compositions in Icelandic Basalts and Picrites. Journal of Petrology, 54(4): 745-768.
Tilmann, F.J., Grevemeyer, I., Flueh, E.R., Dahm, T. and Goßler, J., 2008. Seismicity in the outer rise offshore southern Chile: indication of fluid effects in crust and mantle. Earth and Planetary Science Letters, 269(1-2): 41-55.
Tollstrup, D., Gill, J., Kent, A., Prinkey, D., Williams, R., Tamura, Y. and Ishizuka, O., 2010. Across-arc geochemical trends in the Izu-Bonin arc: Contributions from the subducting slab, revisited. Geochem. Geophys. Geosyst., 11(1).
Tong, P., Zhao, D. and Yang, D., 2012. Tomography of the 2011 Iwaki earthquake (M 7.0) and Fukushima nuclear power plant area. Solid Earth, 3(1): 43-51.
Toplis, M.J., 2005. The thermodynamics of iron and magnesium partitioning between olivine and liquid: criteria for assessing and predicting equilibrium in natural and experimental systems. Contributions to Mineralogy and Petrology, 149(1): 22-39.
Tsay, A., Zajacz, Z., Ulmer, P. and Sanchez-Valle, C., 2017. Mobility of major and trace elements in the eclogite-fluid system and element fluxes upon slab dehydration. Geochimica et Cosmochimica Acta, 198: 70-91.
Tsuji, Y., Nakajima, J. and Hasegawa, A., 2008. Tomographic evidence for hydrated oceanic crust of the Pacific slab beneath northeastern Japan: Implications for water transportation in subduction zones. Geophys. Res. Lett., 35(14).
Turner, M., Turner, S., Blatter, D., Maury, R., Perfit, M. and Yogodzinski, G., 2017a. Water contents of clinopyroxenes from sub-arc mantle peridotites. Isl. Arc, 26(5).
Turner, M., Turner, S., Mironov, N., Portnyagin, M. and Hoernle, K., 2017b. Can magmatic water contents be estimated from clinopyroxene phenocrysts in some

lavas? A case study with implications for the origin of the Azores Islands. Chemical Geology, 466: 436-445.

Ueki, K. and Iwamori, H., 2017. Geochemical differentiation processes for arc magma of the Sengan volcanic cluster, Northeastern Japan, constrained from principal component analysis. Lithos, 290-291: 60-75.

Van Horne, A., Sato, H. and Ishiyama, T., 2017. Evolution of the Sea of Japan back-arc and some unsolved issues. Tectonophysics, 710-711: 6-20.

Van Keken, P.E., Hacker, B.R., Syracuse, E.M. and Abers, G.A., 2011. Subduction factory: 4. Depth-dependent flux of H_2O from subducting slabs worldwide. J. Geophys. Res. B Solid Earth, 116(1).

Vaughan, D.J. and Corkhill, C.L., 2017. Mineralogy of sulfides. Elements, 13(2): 81-87.

Venugopal, S., Schiavi, F., Moune, S., Bolfan-Casanova, N., Druitt, T. and Williams-Jones, G., 2020. Melt inclusion vapour bubbles: the hidden reservoir for major and volatile elements. Sci. Rep., 10(1): 9034.

Vigouroux, N., Wallace, P.J., Williams-Jones, G., Kelley, K., Kent, A.J.R. and Williams-Jones, A.E., 2012. The sources of volatile and fluid-mobile elements in the Sunda arc: A melt inclusion study from Kawah Ijen and Tambora volcanoes, Indonesia. Geochem. Geophys. Geosyst., 13(9).

Wachi, T. and Koshiya, S., 1997. Tephra stratigraphy and eruptive activities of the Akita-Komagatake volcano. Kazan, 42(1): 17-34.

Wada, K., 1997. Eruption history of Me-akan Volcano, eastern Hokkaido, during the last 12000 years. Fall session of the Volcanological Society of Japan, 1997.

Wada, K., Ikegami, H. and Inaba, T., 1998. Chemical compositions of the rocks from Me-akan volcano Eastern Hokkaido Japan: Compositional variety of eruptive magmas. Rep. Taisetsuzan Inst. Sci., 32: 43-59.

Wade, J.A., Plank, T., Melson, W.G., Soto, G.J. and Hauri, E.H., 2006. The volatile content of magmas from Arenal volcano, Costa Rica. Journal of Volcanology and Geothermal Research, 157(1-3): 94-120.

Walker, J., Carr, M., Patino, L., Johnson, C., Feigenson, M. and Ward, R., 1995. Abrupt change in magma generation processes across the Central American arc in southeastern Guatemala: Flux-dominated melting near the base of the wedge to decompression melting near the top of the wedge. Contributions to Mineralogy and Petrology, 120(3): 378-390.

Wallace, P. and Carmichael, I.S.E., 1992. Sulfur in basaltic magmas. Geochimica et Cosmochimica Acta, 56(5): 1863-1874.

Wallace, P.J., 2005. Volatiles in subduction zone magmas: Concentrations and fluxes based on melt inclusion and volcanic gas data. Journal of Volcanology and Geothermal Research, 140(1-3): 217-240.

Wallace, P.J., Kamenetsky, V.S. and Cervantes, P., 2015. Melt inclusion CO_2 contents, pressures of olivine crystallization, and the problem of shrinkage bubbles. Am. Mineral., 100(4): 787-794.

Wallace, P.J., Plank, T., Bodnar, R.J., Gaetani, G.A. and Shea, T., 2021. Olivine-Hosted Melt Inclusions: A Microscopic Perspective on a Complex Magmatic World. Annual Review of Earth and Planetary Sciences, 49(1): 465-494.

Walters, J., Cruz-Uribe, A. and Marschall, H., 2020. Sulfur loss from subducted altered oceanic crust and implications for mantle oxidation. Geochemical Perspectives Letters, 13: 36-41.

Wang, J. and Zhao, D., 2013. P-wave tomography for 3-D radial and azimuthal anisotropy of tohoku and kyushu subduction zones. Geophys. J. Int., 193(3): 1166-1181.
Watanabe, S., Widom, E., Ui, T., Miyaji, N. and Roberts, A.M., 2006. The evolution of a chemically zoned magma chamber: The 1707 eruption of Fuji volcano, Japan. Journal of Volcanology and Geothermal Research, 152(1-2): 1-19.
Waters, L.E. and Lange, R.A., 2015. An updated calibration of the plagioclase-liquid hygrometer-thermometer applicable to basalts through rhyolites. Am. Mineral., 100(10): 2172-2184.
Watt, S.F.L., Pyle, D.M., Mather, T.A. and Naranjo, J.A., 2013. Arc magma compositions controlled by linked thermal and chemical gradients above the subducting slab. Geophys. Res. Lett., 40(11): 2550-2556.
Webster, J.D., 2004. The exsolution of magmatic hydrosaline chloride liquids. Chemical Geology, 210(1): 33-48.
Wehrmann, H., Hoernle, K., Garbe-Schönberg, D., Jacques, G., Mahlke, J. and Schumann, K., 2014a. Insights from trace element geochemistry as to the roles of subduction zone geometry and subduction input on the chemistry of arc magmas. Int. J. Earth Sci., 103(7): 1929-1944.
Wehrmann, H., Hoernle, K., Jacques, G., Garbe-Schönberg, D., Schumann, K., Mahlke, J. and Lara, L.E., 2014b. Volatile (sulphur and chlorine), major, and trace element geochemistry of mafic to intermediate tephras from the Chilean Southern Volcanic Zone (33–43°S). Int. J. Earth Sci., 103(7): 1945-1962.
Weller, D.J. and Stern, C.R., 2018. Along-strike variability of primitive magmas (major and volatile elements) inferred from olivine-hosted melt inclusions, southernmost Andean Southern Volcanic Zone, Chile. Lithos, 296-299: 233-244.
Wieser, P.E., Edmonds, M., Maclennan, J., Jenner, F.E. and Kunz, B.E., 2019. Crystal scavenging from mush piles recorded by melt inclusions. Nature Communications, 10(1): 5797.
Wilson, M., 1995. Magmatic differentiation. Geological Society, London, Memoirs, 16(1): 205-218.
Witham, F., Blundy, J., Kohn, S.C., Lesne, P., Dixon, J., Churakov, S.V. and Botcharnikov, R., 2012. SolEx: A model for mixed COHSCl-volatile solubilities and exsolved gas compositions in basalt. Comput. Geosci., 45: 87-97.
Workman, R.K. and Hart, S.R., 2005a. Major and trace element composition of the depleted MORB mantle (DMM). Earth and Planetary Science Letters, 231.
Workman, R.K. and Hart, S.R., 2005b. Major and trace element composition of the depleted MORB mantle (DMM). Earth and Planetary Science Letters, 231(1-2): 53-72.
Wotzlaw, J.-F., Bindeman, I.N., Watts, K.E., Schmitt, A.K., Caricchi, L. and Schaltegger, U., 2014. Linking rapid magma reservoir assembly and eruption trigger mechanisms at evolved Yellowstone-type supervolcanoes. Geology, 42(9): 807-810.
Xiong, X., Keppler, H., Audétat, A., Ni, H., Sun, W. and Li, Y., 2011. Partitioning of Nb and Ta between rutile and felsic melt and the fractionation of Nb/Ta during partial melting of hydrous metabasalt. Geochimica et Cosmochimica Acta, 75(7): 1673-1692.
Yamada, R. and Yoshida, T., 2002. Relationship between the evolution of the Neogene volcanism and the Kuroko mineralization in the vicinity of the Hokuroku district, NE Japan -A chronological study. Shigen Chishitsu, 52: 97-110.

Yamada, R. and Yoshida, T., 2011. Relationships between Kuroko volcanogenic massive sulfide (VMS) deposits, felsic volcanism, and island arc development in the northeast Honshu arc, Japan. Miner. Deposita, 46(5): 431-448.

Yamamoto, M., 1988. Picritic primary magma and its source mantle for Oshima-Ōshima and back-arc side volcanoes, Northeast Japan arc. Contributions to Mineralogy and Petrology, 99(3): 352-359.

Yokoyama, I., Katsui, Y., Ehara, S. and Koide, K., 1976. Meakandake. Volcano geology, eruption history, current activities and disaster prevention measures (in Japanese). Hokkaido Disaster Management Council, Sapporo.

Yoshida, T., 2001. The evolution of arc magmatism in the NE Honshu arc, Japan. Tohoku Geophys. J., 36(2): 131-149.

Yoshida, T., Aizawa, K., Nagahashi, Y., Sato, H., Ohguchi, T., Kimura, J. and Ohira, H., 1999a. The formation of late Cenozoic caldera swarm in the island arc volcanic period of Northeast Honshu arc. Earth Monthly, 27: 123-129.

Yoshida, T. and Aoki, K.I., 1984. Geochemistry of major and trace elements in the Quaternary volcanic rocks from northeast Honshu, Japan. Science Reports of the Tohoku Imperial University, 3rd Series, 16(1): 1-34.

Yoshida, T., Kimura, J., Ohguchi, T. and Sato, H., 1997. Structure and evolution of magma plumbing systems of island arc. Bulletin of the Volcanology Society of Japan, 42: S189-S207.

Yoshida, T., Kimura, J.I., Yamada, R., Acocella, V., Sato, H., Zhao, D., Nakajima, J., Hasegawa, A., Okada, T., Honda, S., Ishikawa, M., Ardiansyah Prima, O.D., Kudo, T., Shibazaki, B., Tanaka, A. and Imaizumi, T., 2014. Evolution of late cenozoic magmatism and the crust-mantle structure in the NE japan arc, Geological Society Special Publication, pp. 335-387.

Yoshida, T., Nakajima, J., Hasegawa, A., Sato, H., Nagahashi, Y., Kimura, J., Tanaka, A., Prima, O.D.A. and Ohguchi, T., 2005. Evolution of late Cenozoic magmatism in the NE Honshu Arc and its relation to the crust-mantle structures. Quat. Res, 44(4): 195-216.

Yoshida, T., Tsumura, N., Hasegawa, A., Okamura, S., Zhao, D. and Kimura, J., 1999b. Structure and evolution of upper mantle in the Northeast Honshu arc, Japan. Earth Monthly, 21: 179-193.

Yoshida, T., Yamaguchi, T. and Kawasaki, Y., 1981. Internal structure of Kutsugata lava flow, Rishiri Volcano. The Journal of the Japanese Association of Mineralogists, Petrologists and Economic Geologists, 76(6): 181-194.

Yurimoto, H., Nagashima, K. and Kunihiro, T., 2003. High precision isotope micro-imaging of materials. Appl Surf Sci, 203-204: 793-797.

Zashu, S., Kaneoka, I. and Aoki, K.I., 1980. Sr isotope study of mafic and ultramafic inclusions from Itinome-gata, Japan. Geochem. J., 14(3): 123-128.

Zellmer, G.F., Chen, K.-X., Gung, Y., Kuo, B.-Y. and Yoshida, T., 2019. Magma Transfer Processes in the NE Japan Arc: Insights From Crustal Ambient Noise Tomography Combined With Volcanic Eruption Records. Front. Earth Sci., 7(40).

Zellmer, G.F., Edmonds, M. and Straub, S.M., 2015. Volatiles in subduction zone magmatism. Special Publication - Geological Society of London, 410(1): 1-17.

Zellmer, G.F., Pistone, M., Iizuka, Y., Andrews, B.J., Gomez-Tuena, A., Straub, S.M. and Cottrell, E., 2016. Petrogenesis of antecryst-bearing arc basalts from the Trans-Mexican Volcanic Belt: Insights into along-Arc variations in magma-mush

ponding depths, H2O contents, and surface heat flux. Am. Mineral., 101(11): 2405-2422.
Zellmer, G.F., Sakamoto, N., Iizuka, Y., Miyoshi, M., Tamura, Y., Hsieh, H.H. and Yurimoto, H., 2014. Crystal uptake into aphyric arc melts: Insights from two-pyroxene pseudo-decompression paths, plagioclase hygrometry, and measurement of hydrogen in olivines from mafic volcanics of SW Japan, Geological Society Special Publication, pp. 161-184.
Zen, E.-a., 1986. Aluminum Enrichment in Silicate Melts by Fractional Crystallization: Some Mineralogic and Petrographic Constraints. Journal of Petrology, 27(5): 1095-1117.
Zhang, C., Holtz, F., Ma, C., Wolff, P.E. and Li, X., 2012. Tracing the evolution and distribution of F and Cl in plutonic systems from volatile-bearing minerals: A case study from the Liujiawa pluton (Dabie orogen, China). Contributions to Mineralogy and Petrology, 164(5): 859-879.
Zhao, D., 2015. The 2011 Tohoku earthquake (Mw 9.0) sequence and subduction dynamics in Western Pacific and East Asia. J. Asian Earth Sci., 98: 26-49.
Zhao, D., Huang, Z., Umino, N., Hasegawa, A. and Yoshida, T., 2011. Seismic imaging of the Amur-Okhotsk plate boundary zone in the Japan Sea. Phys. Earth Planet. Inter., 188(1-2): 82-95.
Zhao, D., Niu, X. and Li, J., 2017. Precise relocation of low-frequency earthquakes in Northeast Japan: new insight into arc magma and fluids. Geophys. J. Int., 212(2): 1183-1200.
Zhao, D., Yanada, T., Hasegawa, A., Umino, N. and Wei, W., 2012. Imaging the subducting slabs and mantle upwelling under the Japan Islands. Geophys. J. Int., 190(2): 816-828.

Appendices

Appendix 1

Forward model of post-entrapment processes in long stored MIs

The forward model of post-entrapment processes suffered by a MI set is based on the equations describing the PEC and Fe-loss processes of (Danyushevsky et al., 2000). To simplify calculations, the model assumes a close system for f_{O_2}, where Fe^{3+} is taken as an incompatible element during olivine crystallization. The effect of H_2O concentrations on olivine liquidus temperature are not considered, and liquidus temperatures calculated with the model of (Ford et al., 1983) are used to derive temperature variations between each calculation step, instead of absolute temperatures.

After MI selection from the FC LLD generated with rhyolite-MELTS, each of the MI compositions is modified by the three phases of post-entrapment processes described in the main text.

Phase 1: Olivine host composition during entrapment and initial liquidus temperature of the MI are calculated with the model of (Ford et al., 1983). To calculate a step of PEC the following equation is used (Danyushevsky et al., 2000):

$$MIwt_i = MIwt_{i+1} * (1 - \Delta x) + Olwt_{i+1} * \Delta x \qquad \text{(Eq. A1)}$$

Where $MIwt_i$ is the current MI composition (in wt%), $MIwt_{i+1}$ is the MI composition after the PEC step, which is in equilibrium with $Olwt_{i+1}$, the olivine composition calculated with (Ford et al., 1983). Δx is the fraction of olivine crystallization in each step (0.0001 or 0.01 wt%). $MIwt_{i+1}$ is found by iteratively solving equation A1.

After each PEC step, the Fe-loss step is calculated by iterating steps of Fe-Mg exchange followed by smaller steps of PEC to compensate for the increase in olivine liquidus temperature with MgO gain.

$$XFe^{2+}_{i+1} = XFe^{2+}_{i} - \Delta x_1 \qquad \text{(Eq. A2)}$$

$$XMg_{i+1} = XMg_{i} + \Delta x_1 \qquad \text{(Eq. A3)}$$

Where XFe^{2+}_{i} and XMg_{i} are cation fractions of the MI after the previous PEC step, XFe^{2+}_{i+1} and XMg_{i+1} are cation fractions of the melt after Fe-Mg exchange and Δx_1 indicates the amount of Fe-Mg exchange for each step, set as $\Delta x/128$. After each step of Fe-Mg exchange, the extra PEC is calculated using equation (A1) with fractionation steps of $\Delta x_2 = \Delta x/512$, until reaching the same liquidus temperature as prior to Fe-Mg exchange. The Fe-Mg exchange and extra PEC steps are repeated until the MI reaches equilibrium with Fo_{rim}, defined as:

$$Fo_{rim} = Fo_2 + (Fo_1 - Fo_2) * (Y/100) \qquad \text{(Eq. A4)}$$

Where Fo_1 is the olivine composition in equilibrium with the melt before phase 1, Fo_2 is the olivine composition in equilibrium with the melt after phase 1 and Y indicates the degree of re-equilibration (as %). In the first stage of this model, Y is set randomly between 90 and 100% to simulate the slow cooling process, where the Fe-loss degree is expected to be close to maximum. The PEC and Fe-loss iterations stop when all MIs reach olivine liquidus temperatures 10 °C below that of the most differentiated MI, to simulate all MIs evolving under similar conditions during the FC process.

Phase 2: To model complete re-equilibration during the second stage, the calculations are inversed. The re-equilibration temperature is set as the temperature where the first stage stops, and the interstitial melt Mg# is taken from the FC LLD at 10 °C below the temperature of entrapment of the most differentiated MI, to simulate the simplified case where crystals are stored in the same magma that they were fractionated from. As re-equilibration of the olivine host reaches the vicinity of the MI, the MI start exchanging Fe-Mg with the olivine as Fo content of the olivine starts dropping. This is simulated by the following equations.

$$XFe^{2+}_{i+1} = XFe^{2+}_{i} + \Delta x_3 \qquad \text{(Eq. A5)}$$

$$XMg_{i+1} = XMg_i - \Delta x_3 \qquad \text{(Eq. A6)}$$

These equations are the inverse of equations A2 and A3, and Δx_3 is set to 0.01. After each re-equilibration step, the higher Fe content of the MI decreases the liquidus temperature of olivine, triggering melting on the MI walls. Olivine melting is modelled by applying the following equation:

$$MI_{i+1}\,(wt\%) = MI_i\,(wt\%) * (1 - \Delta x_4) + Ol_i\,(wt\%) * \Delta x_4 \qquad \text{(Eq. A7)}$$

Where MI_i is the MI composition after Fe gain and before melting, MI_{i+1} is the MI composition after one step of melting, Ol_i is the composition of the olivine after the Fe-gain step. The melting step Δx_4 corresponds to $\Delta x_3/1024$. Equation A7 is repeated until the olivine liquidus temperature reaches the liquidus temperature before the Fe-gain step. The melting process increases the Mg# of the melt, counteracting the effect of Fe-gain, so equations A5 and A6 are applied again with a step $\Delta x_5 = \Delta x_3/4096$. Fe-gain and melting equations are iterated until the MI composition is in thermal and compositional equilibrium with the new host olivine composition. This process is repeated for each Δx_3 step of re-equilibration until the MI is in equilibrium with the olivine that is in turn in equilibrium with the interstitial melt.

Phase 3: The third and final step models the post-entrapment processes occurring during ascent and eruption. PEC and Fe-loss is modelled with the same equation as stage 1, by setting the amount of PEC randomly between 0% and 10% and the degree of re-equilibration between 0% and 50%.

Test of rhyolite-MELTS crystallization sequence for hydrous basalts

Before applying the rhyolite-MELTS algorithm to generate the crystallization models used by MushPEC, its capability to reproduce the crystallization behaviour of hydrous basic magmas needs to be assessed. For the model to successfully reproduce the cotectic behaviour of magmas, the liquidus temperature of each of the mineral phases involved must be accurately reproduced. The rhyolite-MELTS algorithm has been successfully

applied to reproduce the crystallization sequence of low H_2O basic magmas, like MORBs or OIBs. It has been shown by several studies that H_2O content of the melt has a strong effect of depressing liquidus temperatures of silicate mineral phases (e.g., Almeev et al., 2012; Danyushevsky, 2001; Médard and Grove, 2008; Sisson and Grove, 1993; Waters and Lange, 2015). Therefore, it is necessary to check if the liquidus temperature of the minerals of interest are correctly modelled by rhyolite-MELTS. For hydrous basic magmas, the mineral phases involved during crystallization are usually olivine, plagioclase, clino- and orthopyroxene and spinel (titanomagnetite).

Models of the depression olivine and plagioclase liquidi as a function of water content have been developed from experimental data (Almeev et al., 2012; Médard and Grove, 2008). Comparison of rhyolite-MELTS behaviour with the empirical models shows that rhyolite-MELTS liquidus depression is slightly lower for both phases (Figure A1). Even though temperatures of hydrous melts will be slightly overestimated by rhyolite-MELTS, the cotectic relationship between both phases should not be affected as both liquidi are displaced by similar amounts.

As to date empirical models have not been developed modelling the depression of clino-

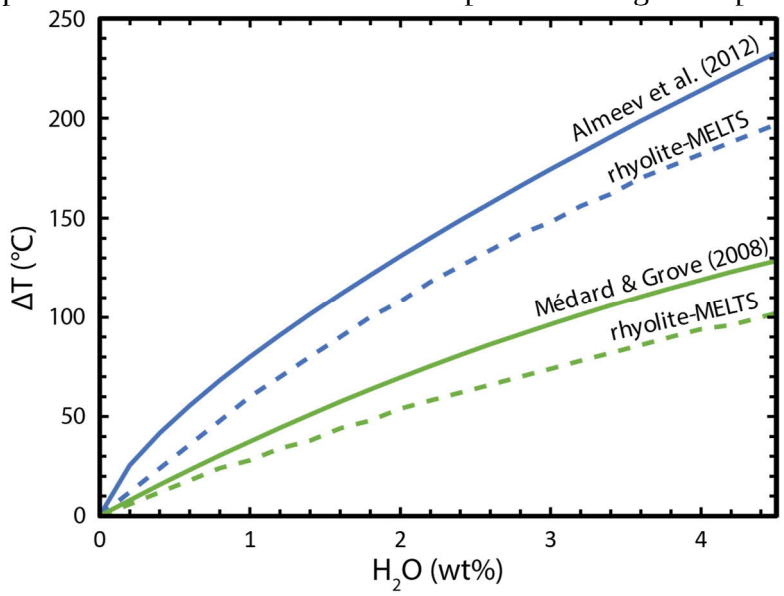

Figure A1. Effect of melt H_2O concentration in liquidus temperature suppression (ΔT). Green and blue lines indicate the ΔT for olivine and plagioclase, respectively. Dashed lines are the ΔT obtained from rhyolite-MELTS, whereas continuous lines represent the ΔT empirical models from (Almeev et al., 2012; Médard and Grove, 2008).

and orthopyroxene liquidi as a function of H_2O content,, a different approach is needed to analyse the behaviour of the crystallization sequence when these phases are involved.

(Takagi et al., 2005) conducted a series of equilibrium crystallization experiments at 100, 200 to 500 MPa with variable H_2O contents on a sample from Iwate volcano. Iwate volcano is the closest stratovolcano to Akita-Komagatake volcano (km) and the composition used by (Takagi et al., 2005) (IWL16) is very similar to the AK melt used in this study (a low-alkali hydrous tholeiite). For the experimental runs, two types of initial bulk material were used with slightly different compositions, a glass powder produced by previous melting of the IWL16 whole rock composition, and a powder produced directly from the whole rock material. Buffer conditions in the experimental runs were estimated to be NNO + 1 (±1) Here, the crystallization sequence produced by the experimental runs was compared with rhyolite-MELTS equilibrium crystallization models.

(Takagi et al., 2005) estimated the bulk H_2O contents of the experiments based on the water added before the experiment and the volatile loss determined by weighing the experimental capsule before and after the experiments. No direct H_2O analyses were made of the glasses after the experiments and the water contents of the glasses were estimated using the difference method for unsaturated experiments and using the solubility model of (Moore et al., 1995) for saturated experiments. Water content estimations were checked here using the (Waters and Lange, 2015) plagioclase-melt hygrometer for runs where glass and plagioclase compositions were available. The degree of crystallization of the runs was estimated by least square mass balance calculations with the Geobalance program (Li et al., 2020) using the compositions of all phases in the experimental run. Bulk H_2O contents were then estimated by mass balance using the glass H_2O content calculated with the hygrometer and the degree of crystallinity. Uncertainties of these new H_2O estimations are *c.* ±0.5 wt% H_2O (1σ). Results show that a lot of experiments had unaccounted for loss of H_2O and that H_2O values were thus overestimated, especially for experiments at 500 MPa and 100 MPa. The H_2O estimates of experimental runs at 200 MPa are usually within error for H_2O contents <2.5 wt%. Some samples with low H_2O contents are seen to slightly underestimate water contents. H_2O corrections could only be

made to experiments in which plagioclase was present and compositions for all phases were available.

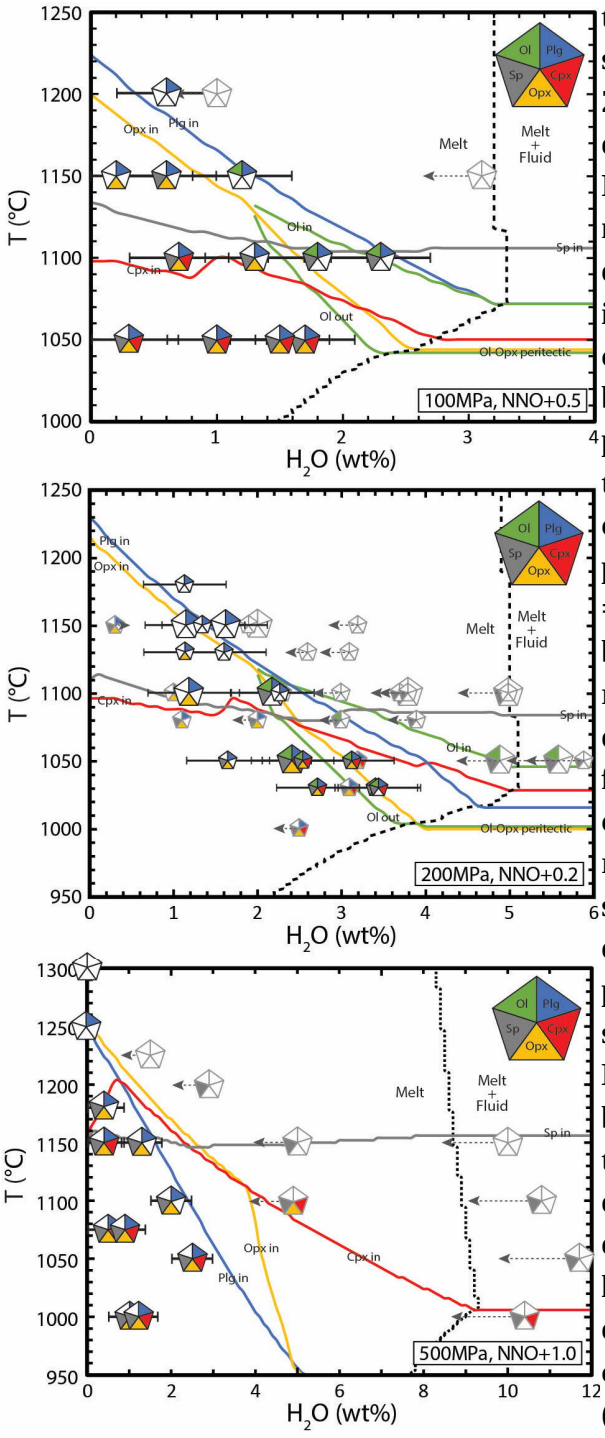

Figure A2. Phase diagrams showing the phase equilibria for the IWL16 sample experiments (Takagi et al., 2005) and the rhyolite-MELTS equilibrium crystallization models. Pentagon symbols indicates the mineral assemblage observed in the experimental runs and curves indicates the phases entering or the crystallization sequence reproduced by rhyolite-MELTS. Line and pentagon colour code is indicated by the large pentagon at the top left corner of each plot (Ol = olivine, Plg = plagioclase, Cpx = clinopyroxene, Opx = orthopyroxene, Sp = spinel). Dashed black line indicates fluid saturation in rhyolite-MELTS. Big pentagons are experimental runs using glass powder from IWL16, which correspond to the composition used to generate the rhyolite-MELTS models, whereas smaller pentagons in (b) are experimental runs of whole rock powder from IWL16, which has a slightly different composition. Experimental runs with corrected bulk H_2O concentrations are shown as the pentagons with black lines and error bars, whereas uncorrected experiments are shown with light grey lines. Dashed grey arrows indicate the expected displacement of bulk H_2O contents from the values given in (Takagi et al., 2005).

Equilibrium crystallization models were run using alphaMELTS2 with the rhyolite-MELTS 1.2.0 model for different water contents at 100, 200 and 500 MPa. Different buffer conditions were tested between the estimated values of the experimental runs (NNO to NNO + 2). Figure A2 shows the experimental results for all runs compared to

the best fit models. The equilibrium crystallization models match the corrected H_2O contents of the experimental data very well. In rhyolite-MELTS, there is usually an interplay between the appearance of orthopyroxene and low-Ca pyroxene (pigeonite), the latter not appearing in the experimental runs. In the comparison between experiments and models, low-Ca pyroxene is taken as orthopyroxene, as it is closer in composition to it, and it will have a similar effect as orthopyroxene on the liquid line of decent.

Experimental data are well reproduced within uncertainties at 100 MPa, with relatively small temperature discrepancies for the appearance of spinel and olivine in runs at 1150°C. Corrected H_2O concentrations for the experiment at 200 MPa also fit the rhyolite-MELTS models very well within the uncertainties in bulk H_2O contents of the experiments. In particular, rhyolite-MELTS captures the small T-H_2O space were olivine and orthopyroxene coexist in equilibrium. Again, small discrepancies are found in the appearance of spinel at high temperatures for a nearly anhydrous experiment and the absence of clinopyroxene in experiments at low water and temperature conditions. Experiments at 500 MPa also present few discrepancies with the rhyolite-MELTS models. Here, the absence of olivine equilibration at high pressures is reproduced by the models, in addition to the increase in the pyroxene liquidus temperature in relation to that for plagioclase. As in lower pressure experiments, some runs at low water content did not crystallize clinopyroxene, predicted by the rhyolite-MELTS algorithm.

It is concluded that rhyolite-MELTS appears to reproduce the cotectic relationships during crystallization of hydrous basalts, including phases with less well understood behaviour, like pyroxenes and Fe-Ti oxides. Small discrepancies are only found at low water contents (<2 wt%), at conditions where olivine is unstable, and are thus not applicable to this study.

Appendix 2

Appendix 2 contains to all compositional data from the MIs and whole rock samples obtained from the analytical technics and corresponds to the excel file named "**Appendix2.xlsx**" of the complementary files.

1. Appendix 2.1: Major element EPMA analyses of olivine cores hosting MIs.
2. Appendix 2.2: Major element EPMA analyses of the MI glasses.
3. Appendix 2.3: Volatile element SIMS analyses of the MI glasses.
4. Appendix 2.4: H_2O-CO_2 composition of standard glasses measured with micro-FTIR.
5. Appendix 2.5: Sulphur contents of glass standards measured with EPMA.
6. Appendix 2.6: Trace element LA ICP-MS analyses of MI glasses.
7. Appendix 2.7: Trace element LA ICP-MS analyses of glass beads from whole rock samples.
8. Appendix 2.8: Major element XRF analyses of glass beads from whole rock samples.

Appendix 3

Appendix 3 contains all compositional data from EPMA analysis of thin sections and corresponds to the excel file named "**Appendix3.xlsx**" of the complementary files.

1. Appendix 3.1: Major element EPMA analyses of glass from the thin sections.
2. Appendix 3.2: Major element EPMA analyses of plagioclase from the thin sections.
3. Appendix 3.3: Major element EPMA analyses of olivine from the thin sections.
4. Appendix 3.4: Major element EPMA analyses of pyroxene from the thin sections.
5. Appendix 3.5: Major element EPMA analyses of Fe-Ti oxides from the thin sections.

Appendix 4

Appendix 4 contains the input and output parameters of the post-entrapment corrections using the modified MIMiC software and corresponds to the excel file named "**Appendix4.xlsx**" of the complementary files.

1. Appendix 4.1: Original major and volatile MI compositions and dimensions of host crystal, MI and shrinkage bubbles.
2. Appendix 4.2: Corrected major and volatile compositions of the MIs.

MASSEY UNIVERSITY
TE KUNENGA KI PŪREHUROA
UNIVERSITY OF NEW ZEALAND

GRADUATE RESEARCH SCHOOL

STATEMENT OF CONTRIBUTION
DOCTORATE WITH PUBLICATIONS/MANUSCRIPTS

We, the candidate and the candidate's Primary Supervisor, certify that all co-authors have consented to their work being included in the thesis and they have accepted the candidate's contribution as indicated below in the *Statement of Originality*.

Name of candidate:	Raimundo Brahm Scott
Name/title of Primary Supervisor:	Georg F. Zellmer
In which chapter is the manuscript /published work:	4

Please select one of the following three options:

(●) The manuscript/published work is published or in press

- Please provide the full reference of the Research Output:

Brahm, R., Zellmer, G.F., Kuritani, T., Coulthard, D., Nakagawa, M., Sakamoto, N., Yurimoto, H. and Sato, E., 2021. MushPEC: Correcting Post-entrapment Processes Affecting Melt Inclusions Hosted in Olivine Antecrysts. Front. Earth Sci., 8(731)

( ) The manuscript is currently under review for publication – please indicate:

- The name of the journal:

- The percentage of the manuscript/published work that was contributed by the candidate:

- Describe the contribution that the candidate has made to the manuscript/published work:

( ) It is intended that the manuscript will be published, but it has not yet been submitted to a journal

Candidate's Signature:	Raimundo Brahm Firmado digitalmente por Raimundo Brahm Fecha: 2021.06.23 13:37:38 +12'00'
Date:	23-jun-2021
Primary Supervisor's Signature:	Georg F. Zellmer Digitally signed by Georg F. Zellmer DN: cn=Georg F. Zellmer, c=NZ, o=Massey University, ou=School of Agriculture and Environment, email=g.f.zellmer@massey.ac.nz Date: 2021.07.16 08:10:58 +12'00'
Date:	16-Jul-2021

This form should appear at the end of each thesis chapter/section/appendix submitted as a manuscript/ publication or collected as an appendix at the end of the thesis.

MASSEY UNIVERSITY
TE KUNENGA KI PŪREHUROA
UNIVERSITY OF NEW ZEALAND

GRADUATE RESEARCH SCHOOL

STATEMENT OF CONTRIBUTION
DOCTORATE WITH PUBLICATIONS/MANUSCRIPTS

We, the candidate and the candidate's Primary Supervisor, certify that all co-authors have consented to their work being included in the thesis and they have accepted the candidate's contribution as indicated below in the *Statement of Originality*.

Name of candidate:	Raimundo Brahm Scott
Name/title of Primary Supervisor:	Georg F. Zellmer
In which chapter is the manuscript /published work:	5

Please select one of the following three options:

○ The manuscript/published work is published or in press

- Please provide the full reference of the Research Output:

◉ The manuscript is currently under review for publication – please indicate:

- The name of the journal:

Journal of Petrology

- The percentage of the manuscript/published work that was contributed by the candidate: 85.00
- Describe the contribution that the candidate has made to the manuscript/published work:

The candidate made all sample preparation, compositional analysis, geochemical modelling and manuscript writting (with comments and corrections from other co-authors).

○ It is intended that the manuscript will be published, but it has not yet been submitted to a journal

Candidate's Signature:	Raimundo Brahm Firmado digitalmente por Raimundo Brahm Fecha: 2021.06.23 13:53:51 +12'00'
Date:	23-Jun-2021
Primary Supervisor's Signature:	Georg F. Zellmer Digitally signed by Georg F. Zellmer DN: cn=Georg F. Zellmer, c=NZ, o=Massey University, ou=School of Agriculture and Environment, email=g.f.zellmer@massey.ac.nz Date: 2021.07.16 08:09:16 +12'00'
Date:	26-Jul-2021

This form should appear at the end of each thesis chapter/section/appendix submitted as a manuscript/ publication or collected as an appendix at the end of the thesis.

MASSEY UNIVERSITY
TE KUNENGA KI PŪREHUROA
UNIVERSITY OF NEW ZEALAND

GRADUATE RESEARCH SCHOOL

STATEMENT OF CONTRIBUTION
DOCTORATE WITH PUBLICATIONS/MANUSCRIPTS

We, the candidate and the candidate's Primary Supervisor, certify that all co-authors have consented to their work being included in the thesis and they have accepted the candidate's contribution as indicated below in the *Statement of Originality*.

Name of candidate:	Raimundo Brahm Scott
Name/title of Primary Supervisor:	Georg F. Zellmer
In which chapter is the manuscript /published work:	6

Please select one of the following three options:

○ The manuscript/published work is published or in press

- Please provide the full reference of the Research Output:

○ The manuscript is currently under review for publication – please indicate:

- The name of the journal:

- The percentage of the manuscript/published work that was contributed by the candidate:

- Describe the contribution that the candidate has made to the manuscript/published work:

◉ It is intended that the manuscript will be published, but it has not yet been submitted to a journal

Candidate's Signature:	Raimundo Brahm Firmado digitalmente por Raimundo Brahm Fecha: 2021.06.23 13:56:15 +12'00'
Date:	23-jun-2021
Primary Supervisor's Signature:	Georg F. Zellmer Digitally signed by Georg F. Zellmer DN: cn=Georg F. Zellmer, c=NZ, o=Massey University, ou=School of Agriculture and Environment, email=g.f.zellmer@massey.ac.nz Date: 2021.07.16 08:10:22 +12'00'
Date:	16-Jul-2021

This form should appear at the end of each thesis chapter/section/appendix submitted as a manuscript/ publication or collected as an appendix at the end of the thesis.